공학박사 학위논문

Improving Electrochemical Performance in Lithium-Sulfur Batteries using Carbonaceous Materials

탄소질 물질을 이용한 리튬-황 배터리의 전기화학적 성능 향상

2015년 8월

서울대학교 대학원
화학생물공학부
박 정 진

Abstract

Improving Electrochemical Performance in Lithium-Sulfur Batteries using Carbonaceous Materials

Jungjin Park

School of Chemical and Biological Engineering

The Graduate School

Seoul National University

Recently, the increment of energy consumption of high technological advancement and the requirement of environmentally-friendly energy sources make a necessity of new conceptual energy source. Notably, among various approaches for promising energy sources, electrochemical energy storage system seems appealing for its high energy conversion efficiency and low product of pollutant. Lithium-sulufur secondary battery is one of the most promising electrochemical redox couple system for storage chemical energy directly to electrical energy. Although a plenty of research has been conducted in this field, several issues still remain, including its low electrical conductivity, irreversible

loss of polysulfides and volume expansion during battery cycling. In this thesis, the various carbonaceous materials was controlled to solve this issues.

In chapter 1, the electrochemical conversion system based on lithium anode and sulfur cathode is introduced. The selected terminologies are formally refered, and the history of lithium based secondary battery is briefly explained. In addition, the advantage and drawback of lithium sulfur battery system are mentioned and its theoretical reaction mechanism based on previous studies also simply noticed. Moreover, there are the concepts of various research papers and its solving approaches. Finally, the experimental conditions of conventional battery test and advanced mesaurements are reported in this thesis.

In chapter 2, the electrochemically critical parameters in the Li-S battery, the overpotential (ΔV), the capacity from the dissolution region (Q_1), and the capacity from the precipitation region (Q_2), are identified to trace the electrochemical behavior of the electrode during the charge/discharge operation, which can aid in the deep understanding of the enhancement mechanism in the different model situation. The effect of cycling rate, conductive additive content, and oxygen functional group on the battery performance has been studied as the model systems. In this study, it is suggested that cycling conditions should be carefully considered and critical parameters are derived when exploring the performance of Li-S battery or designing batteries based on a new concept or novel architecture.

In chapter 3, we have synthesized GO-S/CB composites that micron-sized sulfur particles are encapsulated by GO sheets. The structural properties and chemical properties of GO-S/CB composites were characterized by various microscopic and spectroscopic techniques. Various electrochemical analyses were conducted to elucidate the role of GO that has rich oxygen functional groups and its effect on the electrochemical properties. The charge-discharge profiles revealed the significantly enhanced cycling and rate performance of the GO-S/CB electrode, indicating that GO plays a key role in trapping dissolved polysulfide and in improving electronic conductivity.

Therefore, in chapter 4, we have designed GQDs-S/CB composites as a high-performance cathode material for Li-S batteries. The nano-sized GQDs induce a tightly packed structure via charge interaction with S and CB, which results in enhanced conductivity by shortened electron conduction paths. Furthermore, C-S bonding is generated in-situ during the operation of the battery, which originates from the high functional-edge density of the GQDs. Thus, loss of active materials into the electrolyte is minimized. The adsorption of nano-sized sulphur particles onto the GQD interfaces by C-S bonding was confirmed by TEM, and further supported by XPS and Raman analysis and DFT calculations. The GQDs-S/CB composites significantly improve cycling and rate performances, with high reversible capacities at both high and low current density. This excellent cycling behavior was demonstrated through the analysis of discharge profiles. We believe that our results provide a new avenue for material scientists to tailor

oxygen-rich functional groups of nano-sized carbon for the application in various batteries.

In chapter 5, the synthesis of sulfur copolymers via inverse vulcanization for enhanced cathode materials in Li−S batteries is reported. We demonstrate that this inexpensive, bulk copolymerization can sufficiently modify the properties of sulfur to improve the battery performance without the need for nanoscopic synthesis or processing. This system also demostrates for the first time that high capacity polymeric electrodes can be fabricated while also suppressing capacity fading after extended battery performance to 500 cycles.

In chapter 6, the SDrGO chemically synthesized the DIB and sulfur with reduced graphene oxide. To make uniformly incorporated structure, oleylamine (OLA) functionalities are applied on the synthesis method. The S-C boning from DIB support the wrapping of soluble polysulfides and reduced grapehene oxide support the increased electrical conductivity, which make improved cycling and rate performance. Various electrochemical techniques support the deeply understanding for analysing reaction phenomena on this system.

In chapter 7, the structural integrity at the nanoscale of S-P3HT/CB accounts for the enhanced rate capability by shortened diffusion length of reactant. In summary, we introduced the copolymerization of allyl-terminated P3HT with sulfur enabled by a radical reaction between the allyl end-group and a radical sulfur species. This approach

allows the covalent linkage of sulfur and P3HT yielding in S-P3HT copolymer homogeneously distributed in a sulfur matrix. The homogeneous incorporation of this semiconducting polymer lowers the electrical resistance, thus, an improved battery performance can be observed for S-P3HT copolymer containing electrodes.

In chapter 8, PEO/PAA multilayers on sulfur electrode effectively improved the capacity retention of lithium-sulfur batteries, by successful protection of polysulfide from irreversible loss. This simple and inexpensive method is expected to be widely utilized in various types of electrochemical devices. Future work for further optimization of electrochemical performance is currently underway by nanostructural tailoring of surface layers.

Keywords: lithium sulfur battery, carbonaceous materials, inverse vulcanization, polymeric sulfur, carbon sulfur interaction, electrochemistry

Student Number: 2011-31304

Contents

List of Tables

List of Figures

Chapter 1.

Chapter 2.

Chapter 3.

The peaks in this figure correspond to the various functional groups in the GQDs and CB. SEM images of d, GQDs-S, and g, GQDs-S/CB. e, HRTEM images of the GQDs-S composites and GQD pattern (yellow circle). A Moiré pattern (red circle) is clearly visible in these TEM images, which is created by a superposition of the GQDs and S crystalline lattices , and f, Raman spectrum of GQDs-S composites, which shows that the GQDs are formed on the sulphur particles. The strong peaks at 218.16 and 472.75 cm^{-1} arise from sulphur, and the D (disorder) and G (graphitic) peaks arise from the GQDs. Schematic diagrams show the structure, h, and the magnified structure, i, of GQDs-S/CB.

Fig. 4.2. (Color) Schematic diagrams and SEM images of S/CB and GQDs-S/CB in a Li-S battery. a,b, schematic configuration of S/CB and GQDs-S/CB employed as a cathode in a Li-S battery. The sulphur (yellow) is wrapped with carbon black (S/CB) and compactly covered with graphene quantum dots and carbon black (GQDs-S/CB). Polysulphides were dissolved into solvent and the color changed to orange. c,d, SEM images of GQDs-S/CB and S/CB.

Fig. 4.3. (Color) Electrochemical properties of S/CB and GQDs-S/CB electrodes. a, Schematic illustration of the discharge profile of a conventional Li-S battery. High order-polysulphides (S_n^{2-}, n=8-4) and low order-polysulphides (S_n^{2-}, n=2-1) are abbreviated as HO-PSs and LO-PSs. The onset potential (*U*) and the capacity (*Q*) in the dissolution and precipitation regime are noted, which facilitates the analysis of the electrochemical properties of each sample. b,

Fig. 4.S13. (Color) High resolution S 2*p* X-ray photoelectron spectroscopy and cycle performance. a,b**,** S 2*p* spectrum of the CB and GQDs electrodes, in the charge state, after 20 cycles. These electrodes were cycled in the Li_2S_8 catholyte. Each spectrum was fitted with functions corresponding to different valencies of sulphur (navy line) and the sum of these fitted curves (violet dots) is consistent with the raw data (black solid line). **c,** Cycle retention of GQDs/CB and CB electrodes in Li_2S_8 catholyte over 100 cycles.

Fig. 4.S14. (Color) The relative energies for the reactant and product in binding of polysulphides to GQDs. A plot of the relative energies for the reactant and product in binding of polysulphides to GQDs, versus the sulphur chain length. The functional groups on GQDs enhance the binding of polysulphides to the carbon due to the substitution of **a**, –OH (C-OH) to S_n^{2-} and **b**, –OH (C-COOH) for S_n^{2-}. Yellow, red, white, and gray represents S, O, H, and C atoms, respectively.

Fig. 4.S15. (Color) TEM and SEM images with EELS and EDX on the GQDs and the CB electrodes in Li_2S_8 catholyte after 20 cycles. a,e Bright field STEM images of the GQDs and CB electrodes. b-d,f-h, Electron energy loss spectroscopy maps of C, S, and O of the GQDs and CB electrode in the Li_2S_8 catholyte. i,m, SEM images of the GQDs and CB electrodes in the Li_2S_8 catholyte after cycling. j-l,n-p, C, S, and O EDX maps of the GQDs and CB electrodes.

Fig. 4.S16. (Color) HRTEM (high-resolution transmission electron microscopy) images of nano-sized sulphur on GQDs electrode in Li_2S_8 catholyte after 20 cycles. a,

Chapter 1. Introduction

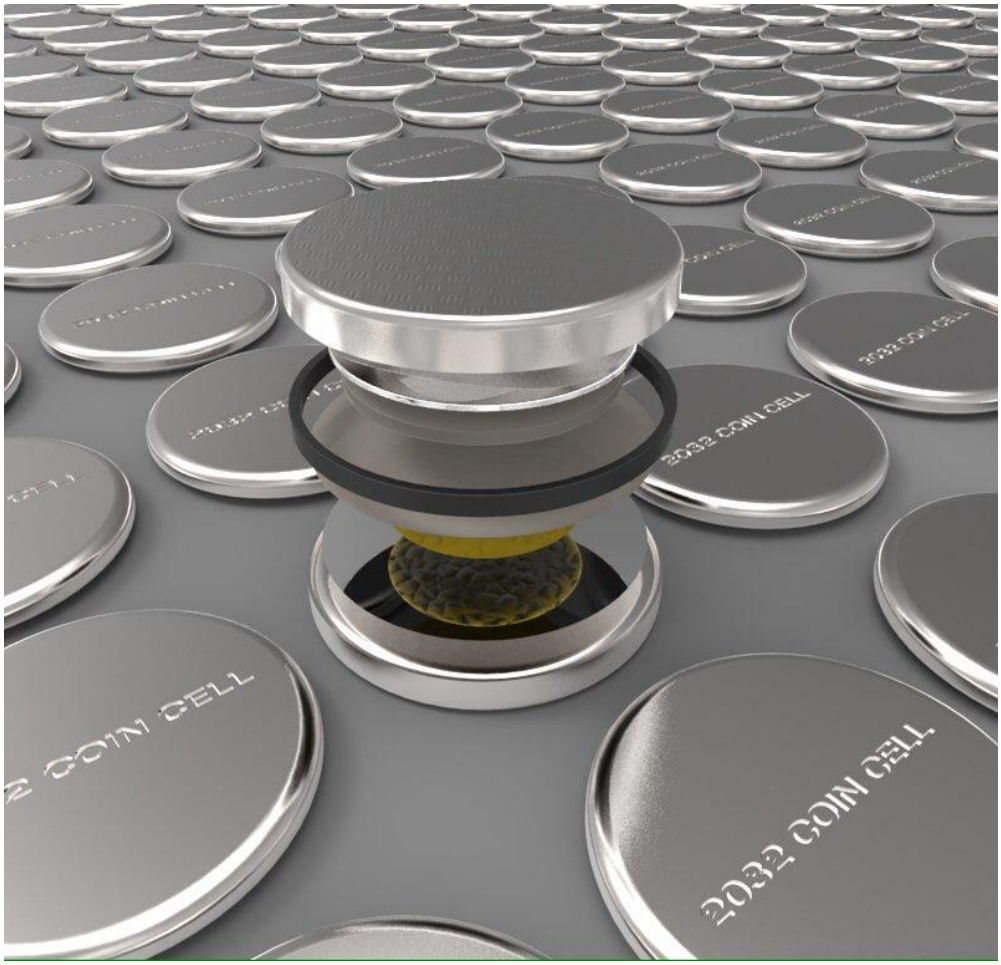

Fig. 1.T. (Color) Schematic illustration of conventional 2032 coin cells

1.1. Building better batteries

Recently, the idea of making high power and energy electric vehicle is everywhere, and a plenty of scientific researches on electric energy storage system are funded in this area. Electric storage in automotive is not new and various electrified-vehicles are now reaching the world-wide markets. The technology of automobile are forced by the legislation, to raise fuel efficiency and to lower carbon dioxide (CO_2) emissions. Today, most of the cars are often equipped with internal battery management system for reducing CO_2 emission by proposing regenerative braking or stop-start function. The hybrid electric vehicles (HEV) are clearly distinguished with electric vehicles (EV). HEV still used a combustion engine, but incorporate a battery system. The firstly introduced HEV was the Prius in 1997 (Toyota Mortors), which pursued the minimized fuel consumption up to exceed 30%. In contrast, the EV does not manage any internal combustion engine, which is fully operated by the battery. However, the possible drive range of EVs does not enough to compare with combustion engine. In addition, there are the critical requirements to satisfying EV system as upper mentioned: safety, cost, gravimetric and volumetric power/energy, capacity retention in Figure 1.1[1].

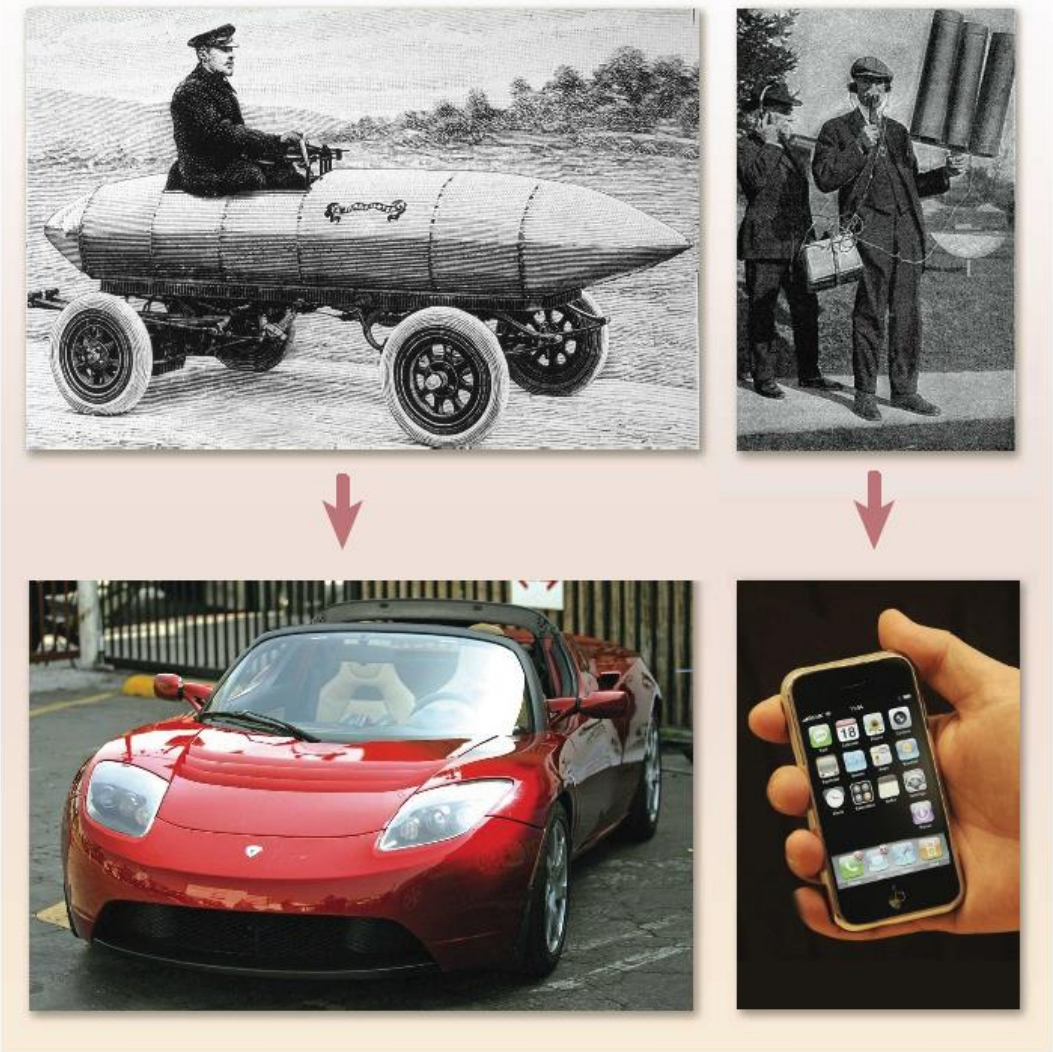

Fig. 1.1. (Color) Revisiting the Past. In 1899 a Belgian car, La jamais contente (top left), equipped with lead–acid batteries, reached a speed of 30 metres per second. In the same year, at a car competition in Paris, the only petrol-driven car was disqualified for having unpractically high consumption. Inside the United States, between 1900 and 1920, the proportion of electrical cars produced fell from 60% to 4% of the total. One century

later, fully electrical cars, such as the Tesla roadster (bottom left), are coming back into the picture. Meanwhile, the first wireless communication took place in Pennsylvania in 1920 (top right). Nearly 100 years later, the latest mobile phones (bottom right) can perform a wide range of functions.Sketch of the electrochemical conversion system with hydrogen oxidation and oxygen reduction and with methanol oxidation and oxygen reduction, as the combination of anode reaction and cathode reaction.[1]

1.2. Terminology

An electrochemistry is the reaction of converting chemical energy into electrical energy and *vice versa*. The electrochemical cell consists the lithium metal thin film as a anode and sulfur and carbon composites as a cathode, which independently separated by a porous polymer layer that has properties of ionic conductor and electric insulator. The anode side react the oxidation, while the cathode side is where a reduction occurs. During battery cycling, these notification should switch when reverse reaction occurs between charge and discharge. In the literature of lithium-sulfur batteries as a lithium metal secondary battery, the positive electrode have to be sulfur and carbon composites electrode and the negative electrode should be lithium metal, avoiding the disorganization. The open circuit potential (OCV) has origins from differences between the chemical potential of the active material of each electrode. In thin work, the several terminologies are introduced to promoting understanding.

- Specific capacity: It is equal to the total amount of coulomb (C) when the battery is fully charge/discharge from (up to) *x* Li:

$Q = 1000 \, x \, F/3600 \, M$,

Where F is the Faraday constant and M is the molecular mass of the active materials

- Voltage window: The cell is running inside it. The potential *vs*. Li^+/Li is set to 0.00 V. Difference active materials are set as the cell shows the different redox potentials. The high voltage window is an important factor to obtain high energy. In practice, the voltage window used is controlled by user to obtain the best desired performance. It is make sure that decomposition of electrolyte will evolves if potential window go wide of the stable ranges, oxidation over the potential/ reduction below the potential.
- The gravimetric/volumetric power: These are the power available when the battery is discharged at a certain discharge current, which can be normalized by the mass of active materials and the volume, respectively. The unit is Watts (W) (=I x V)
- The gravimetric/volumetric energy: These are the total amount of Watt x hours available when the battery is discharged at a certain discharge current, which can be normalized by the mass of active materials and the volume, respectively. The unit is Joule (J) (=W x time)
- Columbic efficiency: It means that the ratio of discharged capacity over the charged capacity at the same cycle. It indicates that reversibility of charge/discharge redox process.

- Cell polarization (overpotential): It means that the differences of discharged potential over the charged potential at the same cycle when a certain current is flowing. It indicates that extra coulomb is needed to fully react reduction/oxidation on the operation. The reason generated the cell polarization/overpotential evolves the energy loss by heating, and possibly to side reactions, and low electronic/ionic conductivity
- Rate capability: It means the response capability of a cell to an various electrical current applied, depending on its magnitude. The current normally expresses in term of "*C*-rate". The *C* is defined as the current required to fully charge/discharge the electrode per 1 hour, considering the theoretical capacity.

In addition, all of gravimetric values are normalized by the amount of elemental sulfur in this work.

1.3. Secondary battery based on lithium

The lithium metal extremity used their ultimate advantage: its light weight and small atomic size results in the highest gravimetric capacity and fast ion kinetics in electrolyte while its electronegativity provides the highest possible cell voltage against any given positive electrode materials. Conclusively, this gives rise to the highest power and energy densities on the contrast to all commercially available rechargeable battery as shown in figure 1.2.[2] On these day, Li-ion battery is the most promising candidate to replace nickel based batteries and to take over the auto mobile market in the recent years.

In addition, Li-ion rechargeable battery can easily apply for wide range of applications, from those advantages. Unfortunately, A plenty of batteries present on the market for concumer application (mobile device, bio-medical equipment, etc.) do not fulfill the energy storage system (ESS) and electric vehicle (EV) field requirements in terms of safety, energy, and power issues.

A conventional Li-ion cell firstly introduced by Sony corp. (Japan) in 1991, which consist of graphite as the anode/negative electrode and transition metal based lithium host ($LiCoO_2$) as the cathode/positive electrode, respectively. The common electrolyte used is based on carbonate type solvent with lithium salt such as $LiPF_6$. In discharged step, the negative electrode releases Li^+ ions (oxidation reaction) which diffuse into positive electrode through electrolyte. Electrons flow the positive electrode through the external circuit, then reacts the Li^+ and active materials (reduction reaction), so call “lithiation”. In charged step, the reverse processes generates upon external power supply, so call “delithiation”. Despite their attractive points, many problems arise from the use of lithium-ion batteries in the electric vehicles (EVs). Present, the researcher reported lithium ion batteries is reached in limitation of the theoretical energy and power density. Increasing the battery performance of electric vehicles as well as decreasing the battery cost hard to attain with current material nature. There have to be needed to new concepts or materials as a next generation candidates for the future.

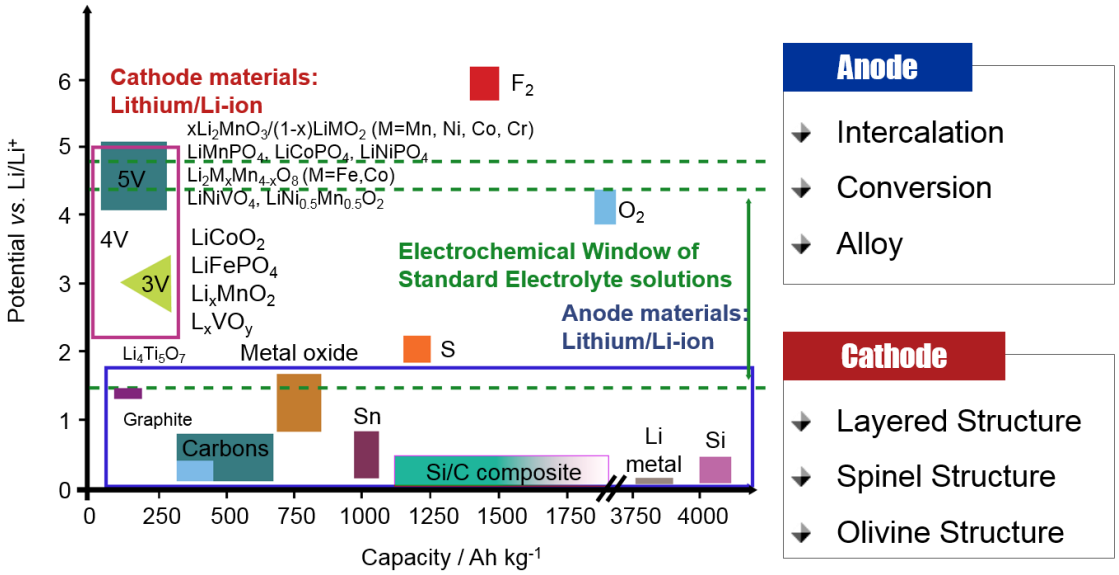

Fig. 1.2. (Color) Plot of capacity and potential window of cathode and anode materials[2]

1.4. Introduction of lithium sulfur battery

Sulfur elements is normally produced by petroleum refinements process, which means abundant and economical cost in figure 1.3.[3] Lithium sulfur battery consists of lithium metal as the negative electrode and sulfur as the positive electrode, which has very attractive system due to its high gravimetric capacity/energy and material cost.

The lithium-sulfur cell has a 1,675 mAh/g theoretical gravimetric capacity, 2,500 Wh/kg theoretical energy density based on weight, and 2,800 Wh/L based on volume.[4,5], which has 5 times higher than conventional lithium-ion batteries [graphite-LiCoO2]. Although those theoretical advantages are achieved, actual energy density would not exceed the current level of lithium-ion battery because the fraction of active materials proposed in previous reports present below 60 wt.% with porosity regulary above 30%. in cathode.[6]

The figure 1.4 shows the reaction mechanim of lithium sulfur battery. the sulfur particles exist the octa-cyclo sulfur structure (S_8), which is most stable phase at room temperature atmosphere. In discharged state, the S_8 ring reacts electrons and lithium ions (heterogeneous reaction) so that the structure converts to ring open. After that, the linear sulfur chain converts from longer chain to shorter chain subsequently. In charged state, the lithium sulfide atoms generate electrons, lithium ions and polysulfide ions from oxidization, and lithium ions migrate back to the negative electrode through electrolyte and electrons also migrate back to the same electrode through external power supply.

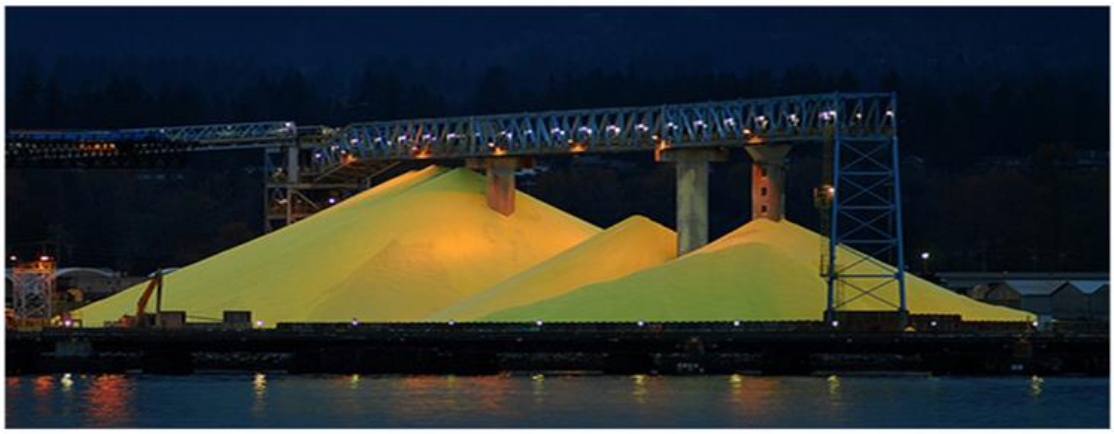

Fig. 1.3. (Color) Example of an exposed deposit of elemental sulfur from hydrodesulfurization in petroleum refining processes. The large abundance of sulfur points to an important opportunity to use this Li-S battery[3]

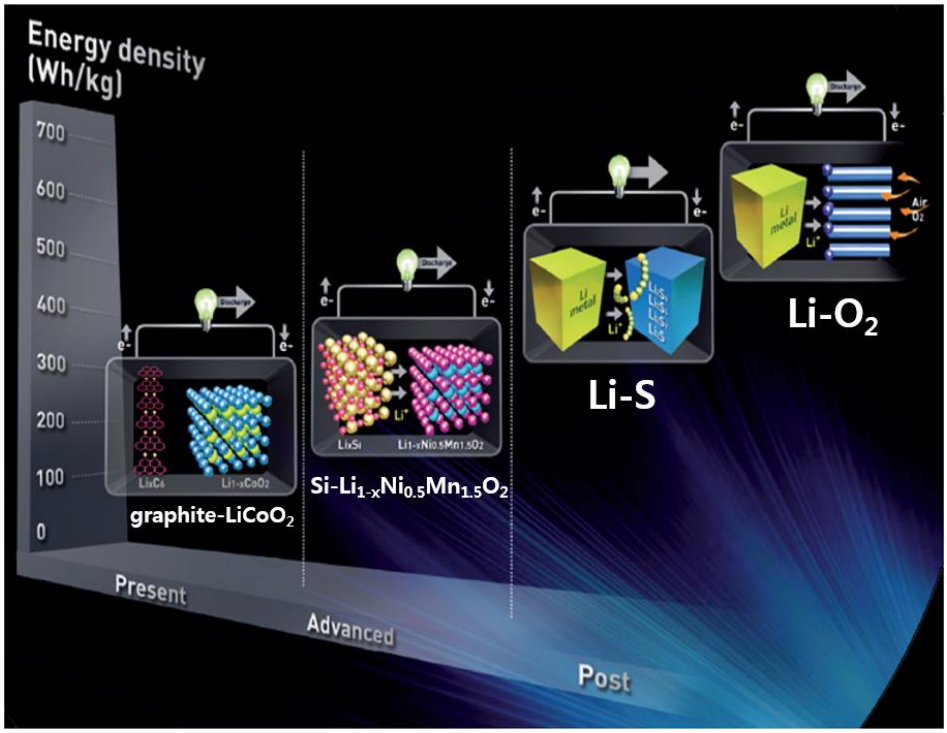

Fig. 1.4. (Color) Plot of redox couples for high energy density batteries[4]

1.5. Theoretical analysis of charge/discharge profile

Figure 1.5 exhibits a conventional charge/discharge profile of Li-S battery. The voltage window controlled from 1.5 V to 3.0 V and applied constant current. The black and grey line means the charge and discharge profile, respectively. First of all, when the discharge reaction starts, elemental sulfur (S_8) consisted of ring type molecule is gradually reduced to the soluble sulfide anion (S_8^{2-}) with electrons and lithium ions defined "upper plateau region". Then, continuous reduction leads to the conversion of dissolved S_8^{2-} to S_n^{2-} (n = 6, 4) defined "slope region". Since these high-order LiPSs (HO-LiPSs, (S_n^{2-}, n=8-4)) reactions are generated in the liquid electrolyte, the loss of active materials can occur simultaneously with this electrochemical reaction. The summation of the upper plateau and slope regions can be defined as the "dissolution region". Once the composition of S_4^{2-} is reached, low-order LiPSs (LO-LiPSs, (S_n^{2-}, n=2-1)) are converted to Li_2S through the reduction of S_4^{2-} (lower plateau region, defined as precipitation region). Finally, Li_2S results from the complete reduction of S_8, which induces ~80% (compared to S_8) theoretical volume expansion. The charge reaction will generate from Li_2S to S in the inverse direction.

The overall reduction/oxidation is below.

$$S_8 + 16\ Li^+ \leftrightarrow 8Li_2S \text{ (16 electrons process)}$$

Representative points Q_1, Q_2, U_1, U_2, U_3, and ΔV are marked in the profile which will support deeply understanding electrochemical analysis of Li-S cell properties in figure 1.6. Where U_1, and U_2, indicate the onset reaction potentials of the dissolved and precipitated species in discharge profile (from S_8 to Li_2S), respectively, while U_3 denotes

onset over-potential of the re-dissolved Li_2S and then a long slopping curve in charge profile (from Li_2S to S_8). The both syncline point in discharge process and anticline point in charge process arise from the supersaturated soluble polysulfides and extra energy (activation energy barrier) for oxidation of insoluble and insulating Li_2S, respectively.

The Q_1 and Q_2 are the capacities corresponding to dissolution and precipitation region, respectively. The Q1 is 419 mAh/g estimated from the reaction, S_8 (s) + $4Li^+$ + $4e^-$ ↔ $2Li_2S_4$ (l). Meanwhile, Q_2 is 1,256 mAh/g which is achieved by the reduction of higher order to lower order polysulfides, $2Li_2S_4$ (l) + $12Li^+$ ↔ $8Li_2S$ (s). The charge-discharge potential difference (ΔV) shows the polarization phenomenon of each region, which exhibits the precipitation region has higher overpotential compared with dissolution region.

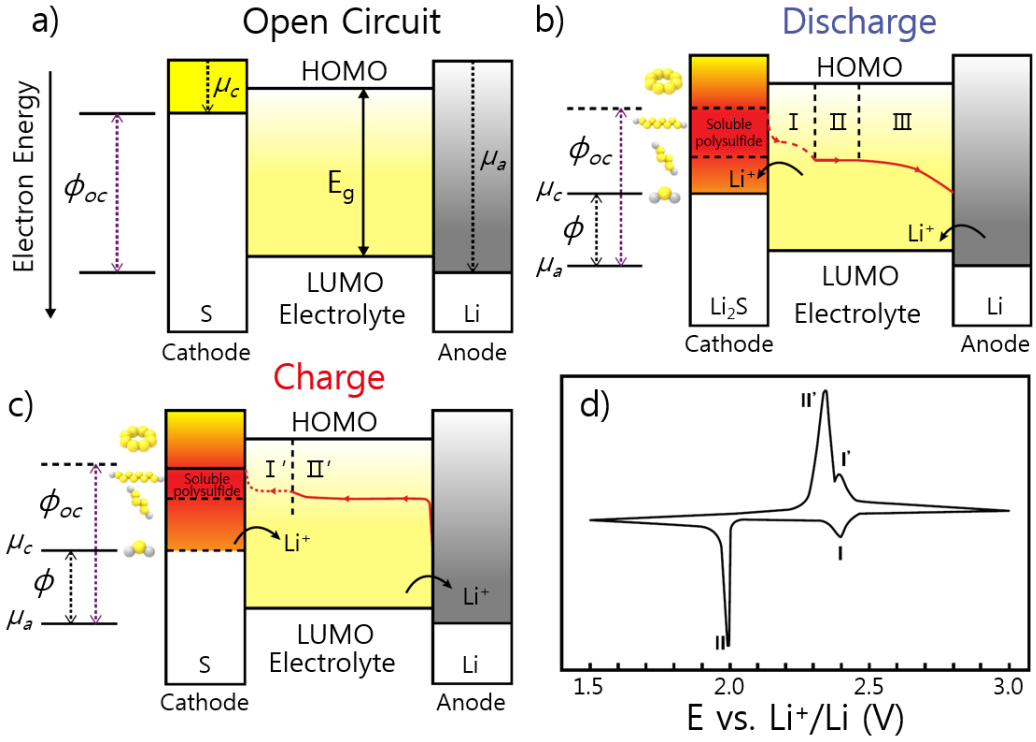

Fig. 1.5. (Color) Electrochemistry of the Li-S battery at different stage[5]

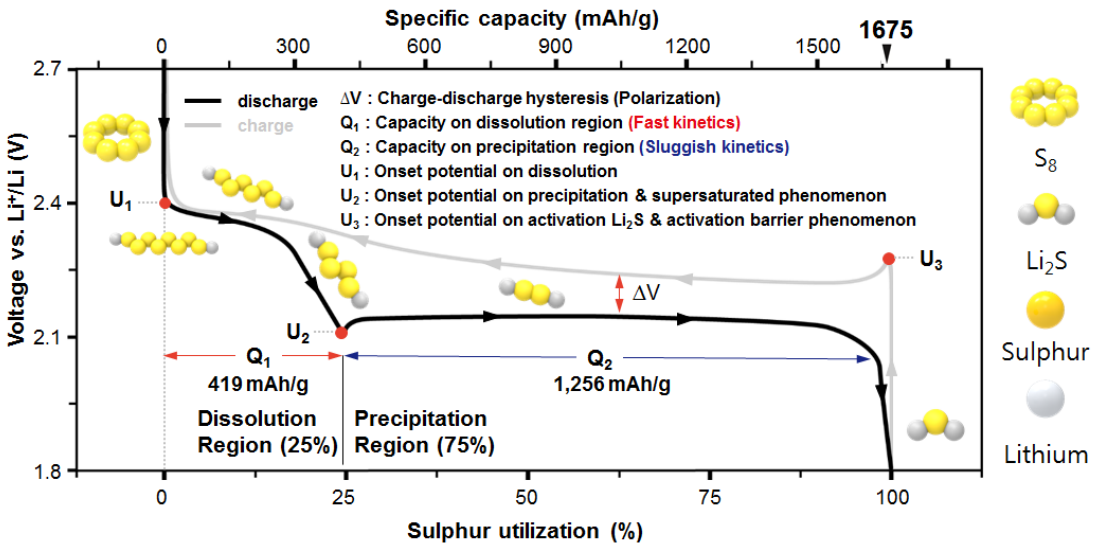

Fig. 1.6. (Color) Charge/discharge profile of Li-S cell

1.6. Challenges of designing lithium sulfur batteries

There are three obvious issues arising for the use of elemental sulfur as an cathode material in an electrochemical device in figure 1.7. First of all, the insulating behavior for ionic and electronic conductivity.[6] The products of its reduction also expected to be insulative property, especially the final product Li_2S. Therefore, the elemental sulfur cannot be used alone as a cathode material. The cathode normally is constructed composites of elemental sulfur and carbon mixture, which supports to highly utilize the sulfur material (reduction/oxidation). Such mixture is problematic to gain high sulfur loading level for high energy density. In addition, the final product (Li_2S, 1.66 g/cm^3) shows a relative lower density than initial product (S, 2.05 g/cm^3) which expects that the formation of Li_2S result in an increased volume change in positive electrode (fully discharged state).[7] This expansion can generate mechanical strain/stress the structural failure of cathode during charge/discharge process.[8] Furthermore, the unique charge/discharge mechanism (dissolution/precipitation) results in irreversibly agglomerated active materials on the surface of the positive electrode, which becomes electrochemically inaccessible.[9,10] And still most of the problems caused the actual chemistry of sulfur intermediates. Its complexity and thus the lack of understanding are deeply issue to develop Li-S battery as an alternative energy storage system. The overall equation of the conversion of sulfur to lithium sulfide does not clarify because various intermediate species Li_2S_n, $2 \leq n \leq 8$, fully unknown and their stability is still controversial in the previous reports. The fact that these intermediate species are highly soluble into the electrolyte, and thus readily diffuse out to electrochemically

inactive space.[11] If they reach the lithium metal counter electrode surface, would be rapidly reduced further to insoluble Li2S and/or formed passivation layer[12]. Another unique behavior is a “shuttle” phenomena which shows the soluble polysulfides are reduced at the negative electrode, and then diffuse back to the positive electrode to be oxidized electrochemically in figure 1.8. This situation originates from anion (S_n^{2-}) concentration gradient and repeats continuously, and thus gives rise to decreased Coulombic efficiency and self-discharge.[13] The migration of active material in the electrolyte is also a cause of capacity fading during first cycles, even if recent studies reports that initial capacity loss does not participate in long-term capacity fading.[14,15] These un-known behavior of polysulfides is important hindrance to develop a conventional Li-S battery.

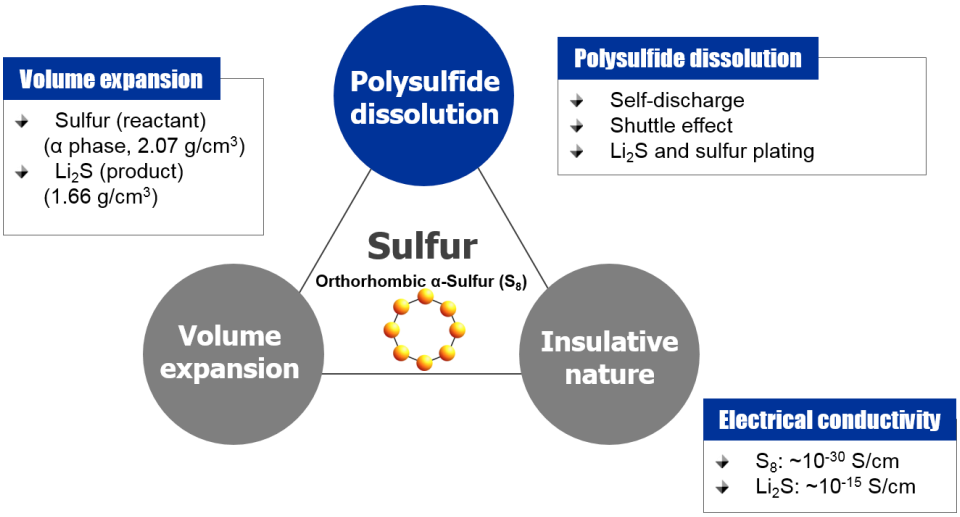

Fig. 1.7. (Color) The problems in lithium-sulfur batteries

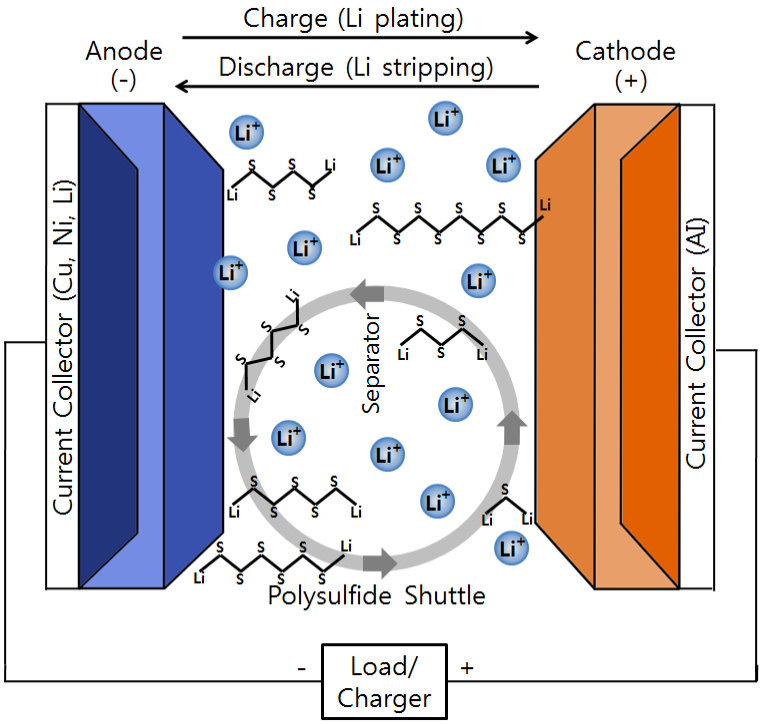

Fig. 1.8. (Color) Shuttle effect in Li-S battery

1.7. Recent understanding for Li-S battery

In recently, various trials have been reported to develop Li-S cell. Indeed, the number of publications has increased drastically as shown in figure 1.9.[16] Most of literature focuses on improving the performance and results are attaining better and better, but the deeply understanding of the mechanism is also importantly investigated; the reasons for the fading behaviors described in the previous paragraph does not still identified. Some groups tried to understand the reduction/oxidation mechanism involved during discharge contrary to the charge mechanism which is easily distinguished the reaction area. Some groups proposed a mechanim for the discharge involving Li_2S_8, Li_2S_6, Li_2S_4, and Li_2S_2 using various measurements because those soluble polysulfides are uncharacterized in the solid state, and thus making difficult the understanding of the redox mechanism. Ultra-violet (UV) visible spectroscopy[17-19] and proton[20] and lithium[21] NMR among other studies[22-24] suggest a set of equilibrium between polysulfides in solution, informing the complexity of the intermediate state of the system. In conventionally accepted description of the system is mostly based on a mathematical modeling of the galvanostatic discharge.[25] This paper reported that the modeling based on solubility constant and reaction rates gives useful information of the dominant species present during cycling. By determining the average concentrations of these species, they can model the typical electrochemical signature of the reduction. The first plateau (upper plateau) thus corresponds to the conversion of ring sulfur to linear long chain (Li_2S_8,Li_2S_6,Li_2S_4). The “downhill” on the voltage profile is properly reproduced by the maximum of the average concentration Li_2S_4. The second plateau then corresponds to the

precipitation of Li_2S_2 and Li_2S form a supersaturated solution.

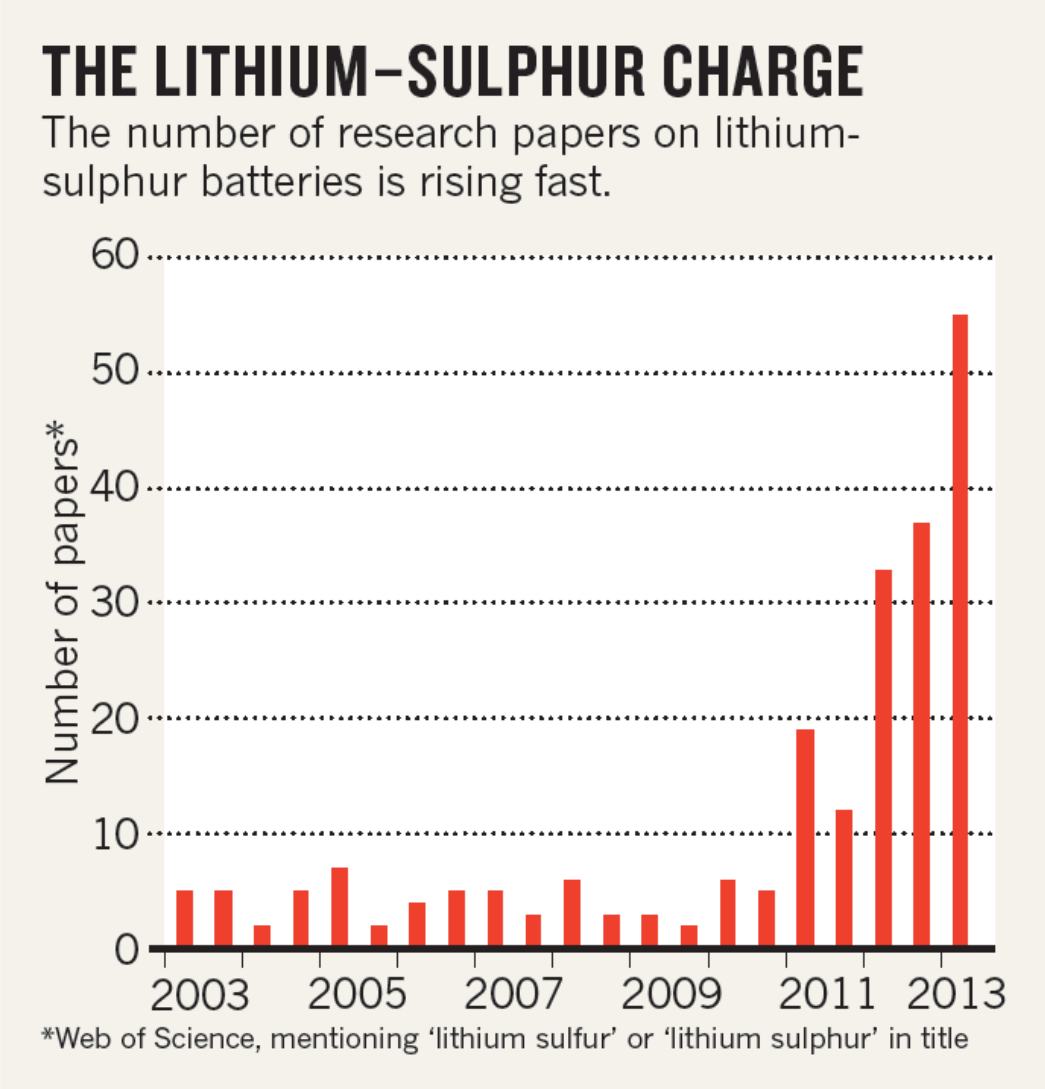

Fig. 1.9. (Color) The number of research papers on lithium-sulfur batteries is rising fast[16]

1.8. The concepts for improving Li-S batteries

1.8.1 Design of the cathode

The elemental sulfur is contained in the cathode side, which lithium metal normally used in the anode side, so call lithium metal secondary battery. The active materials needs to be lightweight and electrionic/ionic conductive in order to obtain gravimetric capacity/energy and power. The sulfur is not effective conductor but one of the lightweight element, and thus most of the recent research papers have tried to apply carbon framework and/or carbon coating layer at sulfur particle as a conducting agent in positive electrode. In very recent, the Nazar group proposed the introduction of mesoporous carbon (CMK-3) with sulfur, where sulfur is impregnated into CMK-3 and then confined. This idea explains that the mesoporous carbon host hinders the diffusion of soluble polysulfide into the bulk electrolyte, thus supporting to maintain a high reversible capacity and utilization of sulfur. After that, many studies report the use of conductive carbon structure such as carbon nanotubes, hollow carbon spheres, carbon fibers. Following this issues, graphene oxide has also been investigated for not only improving wrapping properties of irreversible loss of soluble polysulfides but also increased surface modification with oxygen functional group and soluble polysulfides. On the other side, the sulfur active materials can also be coupled with a conductive polymer coating to wrap particles and prevent any loss of active material in the electrolyte.

1.8.2 Design of the liquid electrolyte

Lithium salts have to be dissolved in an organic solvent as electrolyte because most of the lithium cation moves to anode and cathode side during battery operation. In lithium sulfur

battery system, the selection of the electrolyte is the pivotal role in battery cycles because soluble linear chain polysulfides are very reactive with conventional organic solvent, such as esters, carbonates, and phosphates. In addition, the mobility of polysulfide species are subjected to solublility of solvent, which give rise to self-discharge, i.e. chemical reactions that reduces the energy storage in the battery without any electrical connection. The conventional solvents for Li-S batteries are limited to linear and cyclic ethers, such as 1,3–dioxolane (DOL) and dimethyl ether (DME). Moreover, tetraethylene glycol dimethyl ether (TEGDME) as glymes typle are also reported in the literature. The important conditions of solvent have to contain a low viscosity and a high ionic conductivity. The DOL/DME shows a viscosity approximately 2.0 cP and an ionic conductivity around 11.0 mS/cm for an 1.0 M concentration of lithium Bis(Trifluoromethanesulfonyl)Imide (LiTFSI). The salt generally used LiTFSI in 1.0 M concentration, even if other salts like $LiPF_6$ easily react with soluble polysulfide. The use of additives in electrolytes has been intensively studied. The additives dissolve electrolyte and then form the passivation layer on thelithium anode, which passivation layer has the lithium ionic conductivity and/or protection of dissolution of polysulfides. The lithium nitrate ($LiNO_3$) is used almost all the literature. In the presence of soluble polysulfide solvent, $LiNO_3$ in solution is chemically reduced to formation of Li_xNO_y on lithium metal surface. These Li_xNO_y species hinder the possible reduction of soluble polysulfides on the lithium anode. On the based of formation of passivation layer, polysulfides do not react on the passivation layer surface and thus, the shuttle phenomenon does not occur. Unfortunately, several researchs report that $LiNO_3$ easily reduced under the 1.8 V vs.

Li^+/Li, giving rise to irreversible capacity at first cycle. The concepts for improving Li-S battery shows in figure 1.10.

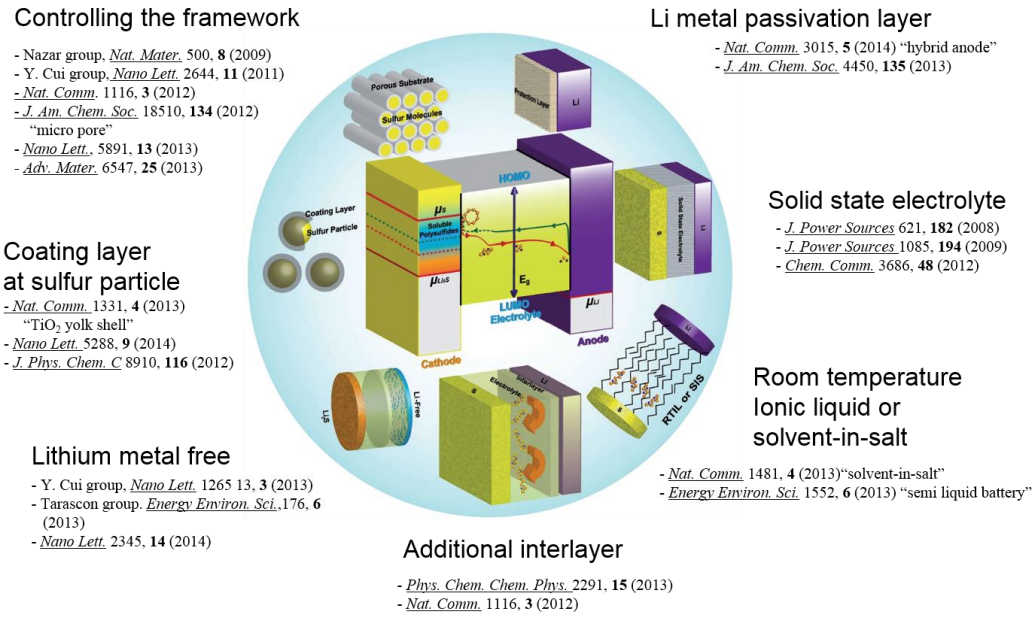

Fig. 1.10. (Color) The concepts for improving Li-S batteries[5]

1.9 Experimentals

1.9.1 design of coin cell

The 2032 type-coin cell design is shown in figure 1.11. The cell is contained within cap and bottom of stainless steel that serve both as a sealed container and as current collectors. The plastic gasket prevents electrical contact between cap and bottom and also ensure complete sealing. The cathode containing sulfur and carbon mixture casts onto an aluminum current collector, while lithium foil casts onto a spacer (stainless steel), which supports intensive electrical contact with lithium foil because of their soft stiffness and controls void space of coin cell as the negative electrode. The separator (SK innovation Corp.) consisted of microporous polypropylene is placed between the cathode and anode in order to not only prevent electrical short but also supports the fast lithium ion transport using their porosity. Finally, a spring is used to maintain a selected pressure in the cell. The cell assembly is carried out in Ar filled-glovebox with the help of a crimper. The coin cell has an advantage of effective sealing during long period, reducing the evaporation of electrolyte, and maintaining a suitable pressure.

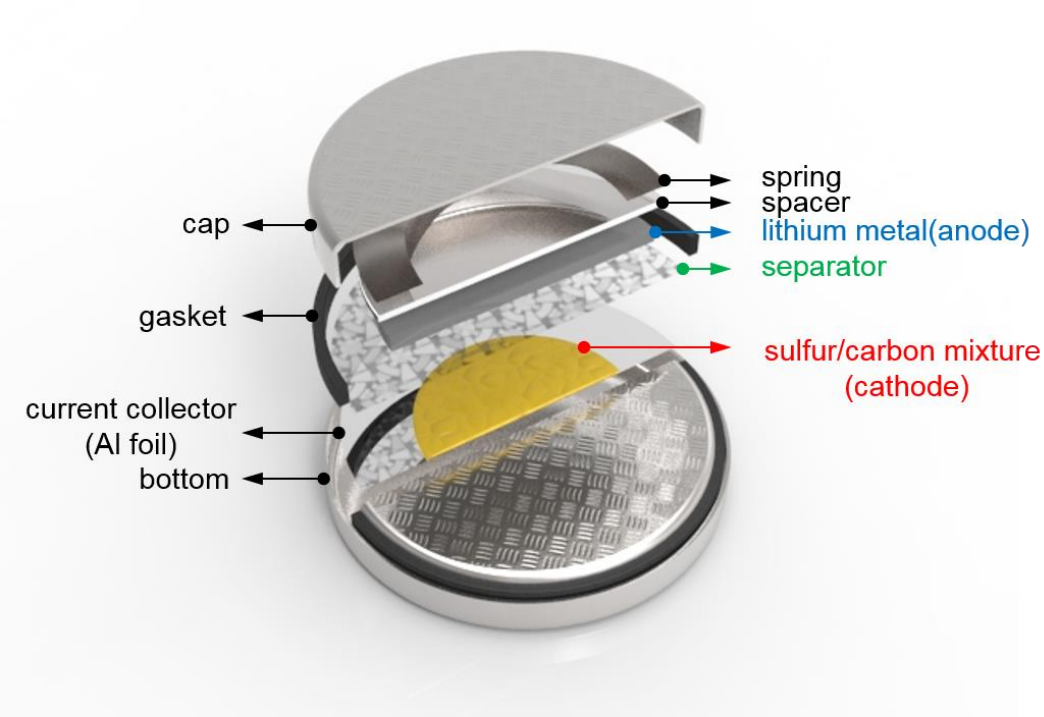

Fig. 1.11. (Color) The schematic illustration of 2032 type-coin cell configuration

1.9.2 Measurements

1.9.2.1 Electrochemical techniques

This electrochemical properties were measured with a WBCS3000 cycler (Won-A Tech, Korea) and Autolab (Metrohm Autolab, Netherlands)

1.9.2.1.1 Galvanostatic charge-discharge with potential limitation (GCDPL)

This method corresponds to the commonly used measurement to study the behavior of batteries upon operation. The galvanostatic charge and discharge current are normally expressed as a *C*-rate, calculated from the electrode capacity. The *C*-rate is a value of the rate at which a battery is fully charged or discharged relatively to its theoretical maximum capacity. For instance, a *C*-rate of 1 *C* defines that the necessary current is applied or drained from the battery to completely charge/discharge it in 1 hour. The *C*-rates multiples of 1 *C* are exploited. In this thesis, it is common to use a C-rate of 0.1C, so to charge and discharge a battery in ten hours. Moreover, the potential limitation is normally fixed from 1.5 (1.7) V to 2.8 (3.0) V. Since the capacity is expressed in Ampere per hour, estimating the current necessary to fully charge/discharge a battery is straightforward.

1.9.2.1.2 Cyclic voltammetry (CV)

Voltammetry informs the electrochemical techniques in which the current at an electrode is measured as a function of the potential applied. The potential is varied in some systematic procedure – a linear voltage lamp with time is used – and the resulting current-potential plot is called a voltammogram. “Cyclic” means to the inversion of the voltage rate when the potential reaches its positive or negative limit. This potential can be consider of as “electron pressure” which either forces a species to gain or lose the

electron. As a result, this technique allows looking at which voltage the redox reactions happen more clearly than a galvanostatic measurement. In some cases, electrochemical reaction rates can be obtained by controling the scan rate.

1.9.2.1.3 Electrochemical impedance spectroscopy (EIS)

EIS data were obtained with a Autolab from 100 kHz to 100 mHz with an AC voltage amplitude of 10 mV at the selected voltage of the cells with the Li metal foil as both auxiliary and reference electrodes.

1.9.2.2 X-ray diffraction (XRD)

XRD data were collected with a high power X-ray Diffractometer (9 kW) with Cu Kα radiation (λ) 0.15418 nm (model: Smartlab). The phase indexing in the collected XRD data was identified with the international centre for diffraction data (ICDD).

1.9.2.3 Thermogravimetric analysis (TGA)

The amount of sulfur in the composites was determined by TGA (Perkin-Elmer).

1.9.2.4 Scanning electron microscopy (SEM) and Transmission electron microscopy (TEM)

The morphology of the samples was investigated with a TEM (JEOL, model: JEM-2100F) and SEM (ZEISS, model: AURIGA), equipped with a scanning transmission electron microscope (STEM), high resolution transmission electron microscopy (HRTEM), and field emission scanning electron microscopy (FESEM).

1.9.2.5 Energy dispersive X-ray spectroscopy (EDS) and Electron Energy Loss Spectroscopy (EELS)

The elemental composition and mapping results of the samples were determined with an

EDS/EELS attached to the SEM/TEM instrument.

1.9.2.6 Raman spectroscopy

A Raman spectroscope (Jobin Yvon, model: LabRam HR) with a 514.5 nm green laser and a 50 × aperture was employed to obtain the Raman scattering spectra.

1.9.2.7 Fourier transform infra-red (FTIR) spectroscopy

A FTIR spectroscope (Thermal electron Corp., model: Nicolet 5700) was employed to obtain the IR absorption spectra.

1.9.2.8 UV-visible spectroscopy

A UV-Visible spectroscope (Perkin-Elmer, model:Lamda 20 2nm) was employed to obtain the UV-visible absorption spectra.

1.9.2.9 Near edge x-ray absorption fine structure (NEXAFS)

A NEXAFS (Pohang accelerator Laboratory (PAL), 4D beam line) was employed to obtain the X-ray absorption spectra.

1.9.2.10 X-ray photoelectron spectroscopy (XPS)

The surface analysis were examined by XPS (Thermo Scientific Corp., model: sigma probe) utilizing a monochromated Al Kα X-ray source ($h\upsilon$ = 1486.6 eV). The pressure in the analysis chamber was typically 10^{-9} torr during data acquisition. All spectra were fitted with Gaussian-Lorentzian functions and a Shirley-type background by the deconvolution software (Avantage, Software).

1.8. References

1. M. Armand and J. –M. Tarascon, "Building better batteries", *Nature* **451**, 7 (2008).

2. R. Marom, S. F. Amalraj, N. Leifer, D. Jacob, and D. Aurbach, "A review of advanced and practical lithium battery materials", *J. Mater. Chem.* **21**, 9938 (2011).

3. Chung, W. J., Griebel, J. J., et al., "The use of elemental sulfur as an alternative feedstock for polymeric materials", *Nat. Chem.* **5**, 518-524 (2013).

4. N.-S. Choi, Z. Chen, S. A. Freunberger, X. Ji, Y.-K. Sun, K. Amine, G. Yushin, L. F. Nazar, J. Cho, and P. G. Bruce, "Challenges facing lithium batteries and electrical double layer capacitors", *Angew. Chem. Int. Ed.* **51**, 9994-10024 (2012).

5. Y.-X. Yin, S. Xin, Y.-G. Guo, and L.-J. Wan, "Lithium-sulfur batteries: electrochemistry, materials, and prospects", *Angew. Chem. Int. Ed.* **52**, 2-18 (2013).

6. Hagen, M., Dörfler, S., Fanz, P., Berger, T., Speck, R., Tübke, J., Althues, H., Hoffmann, M. J., Scherr, C. & Kaskel, S. "Development and costs calculation of lithium-sulfur cells with high sulfur load and binder free electrodes." *J. Power Sources*, **224**, 260-268 (2013).

7. Dean, J,-A. Lange's Handbook of Chemistry (1985).

8. He, X., Ren, J., Wang, L., Pu, W., Jiang, C. & Wan, C. "Expansion and shrinkage of the sulfur composite electrode in rechargeable lithium batteries" *J. Power Sources*, **190**, 154-156 (2009).

9. Elazari, R., Salitra, G., Talyosed, Y., Grinblat, J., Scordilis-Kelley, C., Xiao, A.,

Affinito, J. & Aurbach, D. “Morphological and structural studies of composite sulfur electrodes upon cycling by HRTEM, AFM and Raman spectroscopy” *J. Electrochem. Soc.*, **157**, A1131-A1138 (2010).

10. Barchasz, C., Lepêtre, J.-C., Alloin, F. & Patoux, S. “New insights into the limiting paramters of the Li/S rechargeable cell” *J. Power Sources*, **199**, 322-330 (2011).

11. Cheon, S. E., Ko, K. S., Cho, J. H., Kim, S. W., Chin, E. Y. & Kim, H. T. “Rechargeable lithium sulfur battery”, *J. Electrochem. Soc.*, **150**, A796-799 (2003).

12. [Diao, Y., Xie, K., Xiong, S. & Hong, X. “Shuttle phenomenon – The irreversible oxidation mechanism of sulfur active materal in Li-S battery” *J. Power Sources*, **235**, 181-186 (2013).

13. Barchasz, C., Lepêtre, J.-C., Alloin, F. & Patoux, S. “New insights into the limiting paramters of the Li/S rechargeable cell” *J. Power Sources*, **199**, 322-330 (2011).

14. Rao, B. M. L. & Shropshire, J. A., *J. Electrochem. Soc.*, **128**, 942 (1981).

15. Diao, Y., Xie, K., Xiong, S. & Hong, X. “Analysis of polysulfide dissolved in electrolyte in discharge-charge process of Li-S battery” *J. Electrochem. Soc.*, **159**, A421-A425 (2012).

16. Richard Van Noorden “Sulphur back in vogue for batteries”, *Nature*, **498** 27, 416-417 (2013).

17. Barchasz, C., Molton, F., Duboc, C., Leprêtre, J. C., Patoux, S. & Alloin, F. “Lithium/sulfur cell discharge mechanism : an original approach for intermediate

species identification" *Anal. Chem.*, **84**, 3973-3980 (2012).

18. Tobishima, S.-I., Yamamoto, H. & Matsuda, M. "Study on the reduction species of sulfur by alkali metals in nonaqueous solvents" *Electrochimica Acta* **42**, 1019-1029 (1997).

19. Patel, M. U. M., Demir-Cakan, R., Marcrette, M., Tarascon, J.-M., Gaberscek, M. & Dominko, R. "Li-S battery analyzed by UV/Vis in Operando mode" *Chem. Sus. Chem.* DOI: 10.1002/cssc.20300142 (2013).

20. Argyropoulos, D. S., Hou, Y., Ganesaratnam, R., Harpp, D. N. & Koda, K. "Quantitative NMR analysis of alkaline polysulfide solutions". *Holzforschung*, **59**, 124-131 (2005).

21. Kimberly A. See, Michal Leskes, John M. Griffin, Sylvia Britto, Peter D. Matthews, Alexandra Emly, Anton Van der Ven, Dominic S. Wright, Andrew J. Morris, Clare P. Grey, and Ram Seshadri, "Ab initio structure search and in situ 7Li NMR studies of discharge products in the Li-S battery system", *J. Am. Chem. Soc.* **136** 16368-16377, (2014).

22. Badoz-Lambling, J., Bonnaterre, R., Cauquis, G., Delamar, M. & Demange, G. La "reduction du soufre en milieu organique" *Electrochimica Acta* **21**, 119-131 (1976).

23. Yamin, H., Gorenshtein, A., Penciner, J., Sternberg, Y. & Peled, E. "Lithium – sulfur battery. Oxidation/reduction mechanisms of polysulfides in THF solutions" *J. Electrochem. Soc.*: *Electrochem. Sc. Techno.* **135**, 1045-1048 (1988).

24. Li, Y.,Zhan, H., Liu, S., Huang, K. & Zhou, Y. “Electrochemical properties of the soluble reduction products in rechargeable Li/S battery” *J. Power Sources* **195**, 2945–2949 (2010).

25. Mikhaylik, Y. V. & Akridge, J. “Polysulfide shuttle study in the Li/S battery system” *J. electrochem. Soc.*, **151** A1969-A1976 (2004).

Chapter 2.

The Electrochemical Analysis using Critical Parameters in Li-S Battery

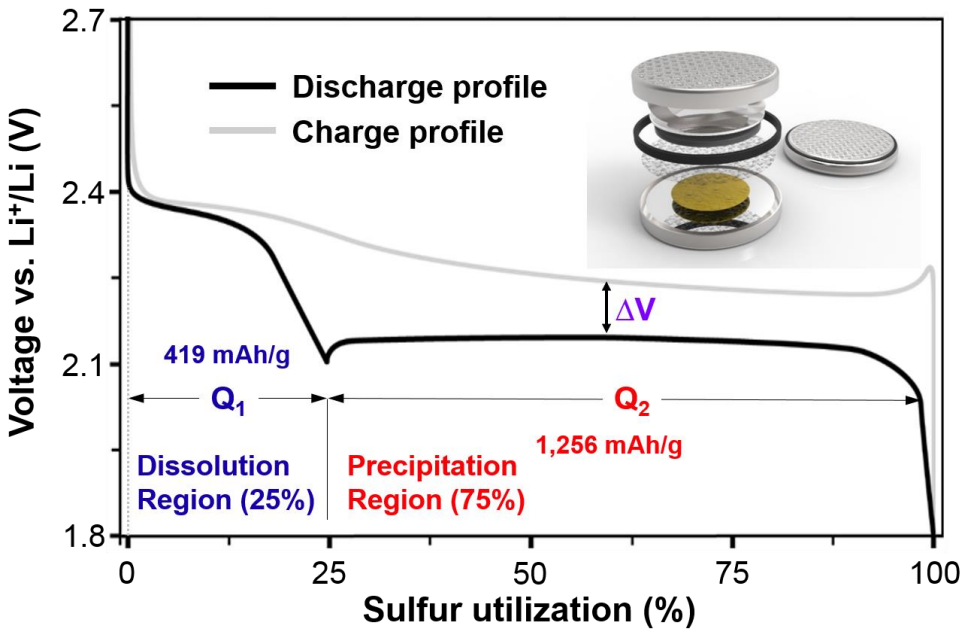

Fig. 2.T. (Color) Schematic illustration of A representative charge-discharge profile of Li-S batteries

---

* The work presented in Chap. 2 was published in *Bulletin of the Korean Chemical Society*, In-press, (2015).

"The electrochemical analysis using critical parameters in Li-S battery"

Jungjin Park†, Chunjoong Kim*, and Yung-Eun Sung*.

2.1. Introduction

2.1.1. Previous studies

Recently numerous studies have been reported to improve the performance of Li-S battery.[1] Indeed, the number of publications has increased explosively, which reported the sulfur has a potential possibility for the energy storage system with high energy density1. While sulfur is environmentally abundant and cheap, it has a high theoretical gravimetric capacity (1675 mAh/g) as a cathode for Li-S battery, which is five times higher than that of conventional lithium ion batteries using graphite and $LiCoO_2$ as an anode and a cathode, respectively.[2] Although those advantages exist, several drawbacks should be overcome for the wider commercialization of Li-S batteries. Particularly, low electrical conductivity of sulfur as initial reactant and lithium sulfide as final product, volume change of charge/discharge operation by conversion reaction, and irreversible loss of soluble polysulfides are solved in the timely manner.[3-5] To solve these problems, in-depth understanding of the charge/discharge mechanism in the Li-S battery is necessary. The previous studies reported the capacity vs. voltage profile can support to understand the reaction mechanism by dividing the dissolution and precipitation region during the discharge process.[6]

2.1.2. Material selection

In this study, we try to electrochemically analyze the model systems, control of charge/discharge rate, amount of conducting agent, and the effect of oxygen functionalized groups on the carbon blacks, which easily affects electrochemical performance. Especially, the three critical parameters, the overpotential (ΔV), the

capacity from the dissolution region (Q_1), and the capacity from the precipitation region (Q_2), are identified to trace the electrochemical behavior of the electrode during the battery operation, which can aid in the understanding of the enhancement mechanism in the different model situation.

2.2. Experimental section

Electrode preparations: The conventional sulfur powders purchased from Sigma Aldrich Corp. The electrodes of various conditions were prepared with sulfur, carbon black, and polyvinyldifluoride (PVDF) by mass ratio of 60:30:10 (S/C 2:1 sample) and 30:60:10 (S/C 1:2 sample) in N-Methylpyrrolidone (NMP) solvent to produce electrode slurry. The oxygen functionalized carbon black was prepared using O_2 plasma generator, which continuously operated on the carbon black for 12 hour. Those oxidized carbon blacks confirmed the oxygen functional groups using Fourier transform infra-red (FTIR) spectroscopy (Thermo electron Corp, NicoletTM 6700) and then applied to make oxidized CB sample (60:30:10 mass ratio). The slurry was casted onto a current collector, an aluminium foil, using a doctor blade method, and then dried for 4 h to form a working electrode. After dehydration, it was pressed by a roll press machine and then dried again for 12 h. The loading level of the active material was ~ 1.0 mg/cm^2. 2032 type coin cells assembled for the battery test. Li metal foil was used for the counter electrode. The electrolyte was 1.0 M lithium bis-trifluoro-methane sulfonylimide (LiTFSI) in 1,3-dioxolane (DOL) and 1,2-dimethoxyethane (DME) (volume ratio 1:1). Lithium nitrate ($LiNO_3$) was used as an additive into the electrolyte to stabilize Li anode. The coin cells were assembled in an Ar-filled glove box. galvanostatic cycling with potential limitation

(GCPL) technique was carried out with a WBC3000 cycler (WonA Tech, Korea) at fixed room temperature (RT).

Electrochemical measurement: galvanostatic cycling with potential limitation (GCPL) technique was applied. The potential window was chosen to be stable against electrolyte decomposition (1.7 to 2.8 V vs. Li_+/Li). The galvanostatic cycling is normally expressed as C/h, h being the number of hours at which the nominal charge will be passed through. C is defined as the total charge corresponding to the full reduction/oxidation of the sulfur hence a 1 C rate (1675 mAh/g) theoretically enables the battery to be fully (dis)charged in one hour.

2.3. Results and discussion

2.3.1. Electrochemical analysis

The representative charge-discharge profile of Li-S batteries, Figure 2.1, depicts a schematic model of reaction pathways that occur during the battery operation. This profile easily establishes the theoretical analysis for the understanding of Li-S battery performance. During the discharge reaction, the octa-cyclo sulfur molecule (S_8) as an initial reactant is reduced to the long chain linear sulfides (S_n^{2-}, n=8-4), in which the discharge profile displays the upper plateau and slope region, so-called "dissolution region". These long chain species are further reduced to short chain linear sulfides (S_n^{2-}, n=4-1), leading to the formation of lithium disulfide (Li_2S) as a final product. These reactions can occur at the lower plateau, so-called "precipitation region". During the charge process, these reactions occur with an opposite way, thus Li_2S is reoxidized to the S_8 molecule.

The overall reaction can be written as follows.

$$S_8 + 16\ Li^+ \leftrightarrow 8Li_2S \text{ (16 electron process)}^6$$

From the 16 electron process of sulfur, the sulfur cathode has a theoretical specific capacity of 1675 mAh/g. The whole reduction reaction can be separated by its reaction mechanism. The theoretical capacity at the dissolution region is 419 mAh/g expressed Q_1 by the dissolution reaction (S_8 (s) + $4Li^+ + 4e^- \leftrightarrow 2Li_2S_4$ (l)), where soluble polysulfides are generated and dissolved into the electrolyte. Meanwhile, the theoretical capacity at the precipitation region is 1256 mAh/g expressed Q_2 by the precipitation reaction ($2Li_2S_4$ (l) + $12Li^+ \leftrightarrow 8Li_2S$ (s)), where the dissolved long chain linear sulfides are precipitated as Li_2S. By the theoretical reaction pathways, the ratio of Q_2/Q_1 should be three[6]. A polarization overpotential of cathode, ΔV, represents the electrode polarization, i.e. the hysteresis between discharge and charge reaction. Q_1, Q_2, and ΔV are critical parameters to understand the electrochemical phenomenon that occurs during Li-S battery operation. These parameters are denoted in the Figure 2.1 for intuitive understanding. To better understand the electrochemical behaviours of these parameters, three model systems were applied to the Li-S battery.

Firstly, Q_1, Q_2, and ΔV as the cycling rate were investigated. The conventional Li-S batteries, which are composed of sulfur and carbon mixture as a cathode and lithium as an anode, were cycled at the different rates, 0.5 C (=837.5 mA/g) vs. 0.05 C (=83.75mA/g) (Figure 2.2a). Very interestingly, contrary to what is commonly observed in the other

electrochemical systems, slow rate cyclings showed more deteriorated cycle retention than fast rate cyclings though higher initial capacity was obtained. The first discharge capacity at 0.05 C rate cyclings was 1035.2 mAh/g while that at 0.5 C rate cyclings was 951.4 mAh/g. After 100 cycles, the electrode at the 0.5 C rate revealed 60.79% capacity retention, however, only 40.48% of capacity retention could be achieved in the electrode at the 0.05 C rate cycling s as can be seen in Figure 2.2b.

To study detailed mechanism for this behaviour, charge-discharge profiles are shown in Figure 2.3a. The overpotential (ΔV), Q_1, and Q_2 are guided for the convenience on the profiles. At the faster charge/discharge rate (0.5 C), the overpotential (ΔV) is wider than the slower charge/discharge rate (0.05 C), which informs the more polarization should be required to deliver the more charges. Meanwhile, the decay of Q_1 and Q_2 is only observed in the electrode at the 0.05 C rate cyclings, of which cycle evolution are highlighted in Figure 2.3b. The electrode at the 0.5 C rate shows lower initial specific capacity, sum of Q_1 and Q_2, but higher cycle retention than that at 0.05 C rate. At the low cycling rate (0.05 C rate), both Q_1 and Q_2 decreased fast even during 10 cycles. This decrease mostly results from the decay of Q_1. The soluble polysulfides that are generated during the dissolution reaction have a random motion in the organic electrolyte during the dissolution reaction. Unless the reaction time is short, these polysulfides are easily diffused out toward the anode side, leading to the irreversible loss of active materials. Thus gradual decrease of Q_1 results in the decrease of Q_2 as well as total capacity. Whereas, the electrode at the fast cycling rate of 0.5 C showed the stable capacity retention in both Q_1 and Q_2. The shorter elapse time in the dissolution region can

effectively decrease the chance of the polysulfide diffusing out toward the anode side. This result indicates that the cycling rate should be carefully considered since the cycle retention of Li-S battery can be adversely affected by the slow rate cycling.

The effect of the conducting agent on the Li-S battery performance is also investigated. Conducting agents are one of important constituents because they offer the electronic conductivity in order for the reaction to proceed and also provide the reaction sites. Carbon black is typically used as the conducting additive. The electrodes with different ratio of carbon black to sulfur in cathode, where the ratio of S/C is prepared as 2:1 (low carbon content electrode, S/C 2:1 electrode) and 1:2 (high carbon content electrode, S/C 1:2 electrode), are prepared (Figure 2.4a). Both of electrodes were galvanostatically cycled at a 0.5 C rate. As aforementioned, the high rate cycling is more suitable to study the intrinsic effect of carbon content on the Li-S battery by minimizing the loss of soluble sulfides during the dissolution reaction. The high carbon content electrode enables more utilization of sulfur, resulting in the higher initial capacity (Figure 2.4b). Even though larger amount of carbon black was used in the S/C 1:2 electrode, the traces of capacity decay are similar in both electrodes. This means that the carbon black is not effective against the loss of the soluble polysulfide intermediate species.

Charge-discharge profiles are presented in Figure 2.5a. It is clear that the overpotential (ΔV) of the S/C 1:2 electrode decreased compared with S/C 2:1 due to more accessible reaction sites and higher electrical conductivity by larger amount of carbon black. It is noteworthy that Q_2 values are higher in higher carbon content electrode while Q_1 values are similar regardless of carbon content. In addition, decay of Q_2 is slightly faster in lower

carbon content electrode. Cycle evolution of Q_1 and Q_2 are plotted in Figure 2.5b. Q_1 values are very stable even during repeated cycles and nearly same regardless of carbon content. Meanwhile, Q_2 values are higher in the high carbon content electrode and decreased as cycles went on. This can be ascribed to the more sluggish reaction of Q_2 (precipitation reaction) than that of Q_1 (dissolution reaction). Also, it is confirmed that Q_2 capacities highly depend on the amount of reaction sites, i.e. carbon additives since the precipitation reaction is slower than dissolution.

Recently, numerous articles reported that oxygen functionalized groups on carbon can provide the increase in an affinity between carbon and sulfur, thus leading to the improvement in the electrochemical performance of Li-S batteries[7-8]. Hydroxyl bonding on carbon can lower the formation energy of soluble polysulfide on conducting agents, which easily increase the sulfur utilization[7]. Meanwhile, C. Zu et al. reported that hydroxyl bonding on carbon can be substituted by carbon-sulfur bond (C-S bonding), which has higher affinity of the soluble sulfides to the carbon[8]. To elucidate the detailed mechanism of performance enhancement by the oxygen functional group, carbons with/without oxygen functional groups were introduced to the electrodes as the conductive additives. The schematic illustration shows the carbon and oxidized carbon that are applied to the cathode in Figure 2.6a. The Fourier transformation intra-red (FTIR) spectroscopy, Figure 6b, was studied to confirm the oxygen functional group in the oxidized carbon black. The features at 1,300 and 1,450 cm^{-1} are attributed to the C-O and C-O-C branches, respectively, which are more prominent in oxidized carbon black compared with carbon black. The increases in C-O and C-O-C branches are associated

with the formation of hydroxyl group on the carbon in the oxidized carbon black[9]. If the formation of bonding between C and S occurs owing to hydroxyl groups, this effect would be more prominent during the dissolution reaction. In this perspective, electrodes using oxidized carbon black were cycled at the low cycling rate (0.1 C), which can more clarify the stability of polysulfide. The electrode with the oxidized carbon black showed better cyclability than that with the normal carbon black as shown in Figure 2.7a. The electrode with the oxidized carbon black revealed 665.9 mAh/g while that with a normal carbon black showed only 508.2 mAh/g at 50 cycles. Q_1 and Q_2 values are plotted in Figure 2.7b to see the traces of them as repeated cycles with charge-discharge profiles in Figure 2.7c and 2-7d. The good retention of Q_1 values in the electrode in an oxidized carbon black could be observed, in contrast, Q_1 in the electrode with a normal carbon black showed gradual decrease as cycles. This confirms that hydroxyl groups can preserve the soluble polysulfides in the vicinity of them, resulting in the better cycling performance. In addition, Q_2 values from both electrodes decreased, which indicates that oxygen functional groups do not much affect the precipitation reaction. The clear decrease of Q_1 can also be found in the voltage profiles in Figure 2.7c when a normal carbon black was applied to the electrode while the Q_1 capacity is sustained in the electrode with an oxidized carbon black (Figure 2.7d). It should be noted that the electrode with an oxidized carbon black reveals the increase in the overpotential (ΔV), which corroborates the decrease of electrical conductivity owing to the oxygen functional group.

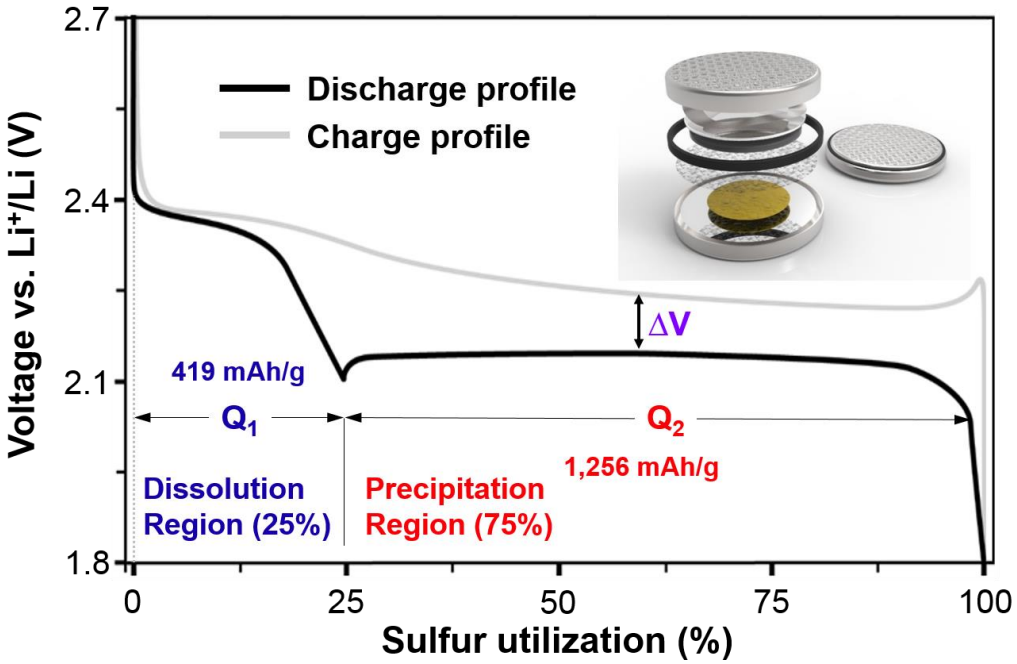

Fig. 2.1. (Color) A representative charge-discharge profile of Li-S batteries

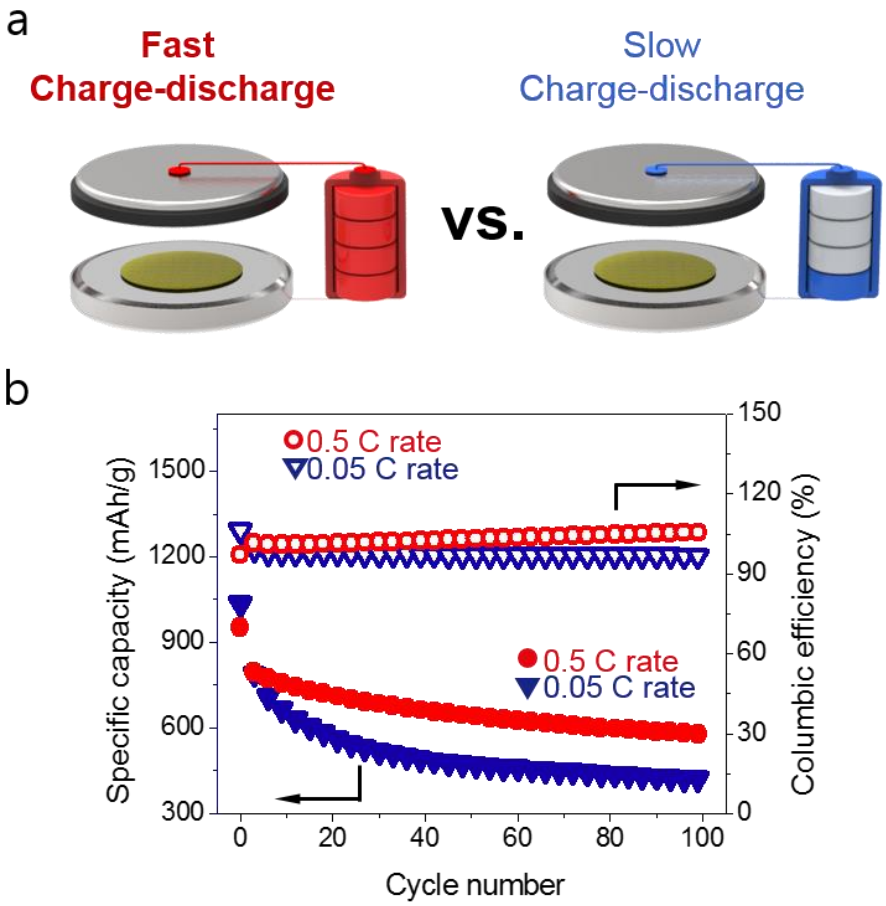

Fig. 2.2. (Color) (a) schematic illustrations showing fast (0.5 C) and slow (0.05 C) charging/discharging rate applied to the cathode of Li-S battery (b) the cycling performance as the rate for 100 cycles.

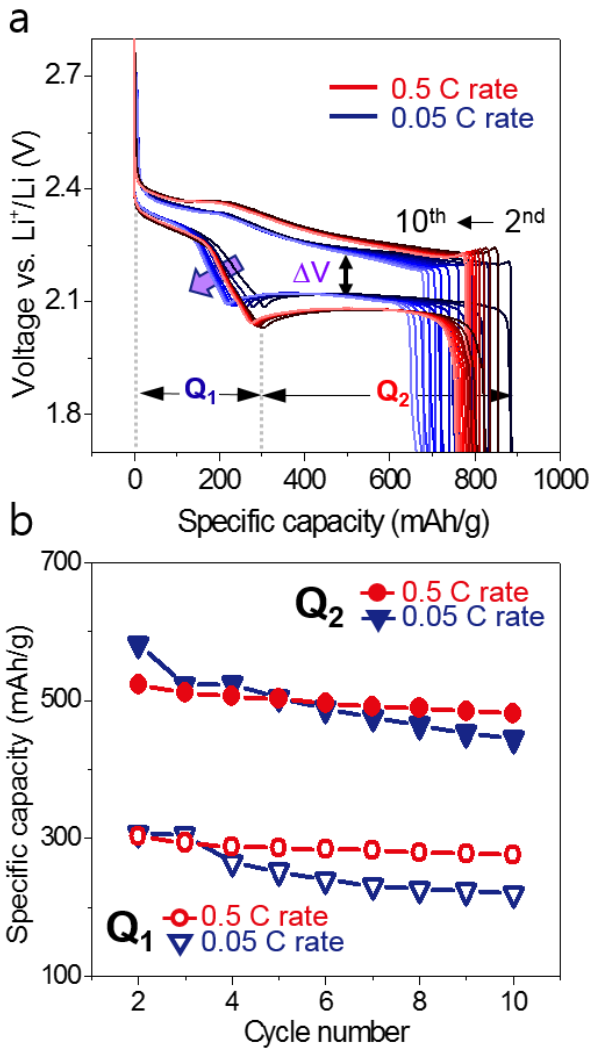

Fig. 2.3. (Color) (a) The charge-discharge profile at the different cycling rate (b) Q1 and Q2 capacity values are traced as the rate from 2nd. to 10th. cycle.

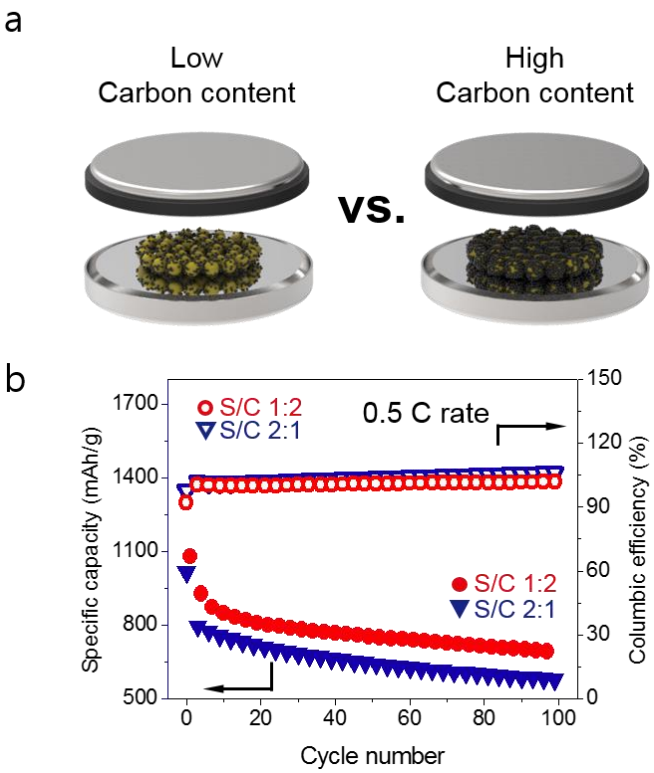

Fig. 2.4. (Color) (a) Schematic illustrations for different amount of conductive agent loading in the cathode. Electrodes with high carbon (S/C 1:2) and low carbon (2:1) content were prepared for the Li-S battery. (b) The cycling performance as the amount of carbon black for 100 cycles.

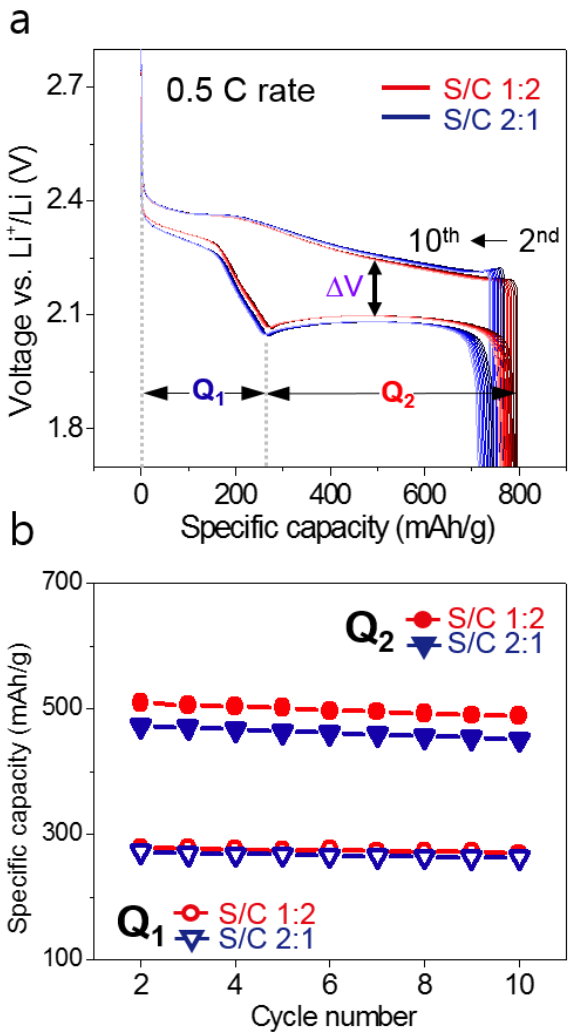

Fig. 2.5. (Color) (a) The charge-discharge profiles of the electrodes with high (S/C 1:2) and low (S/C 2:1) carbon content. A constant current of the 0.5 C rate was applied during the repeated cycles. (b) Q1 and Q2 capacity values are traced as the carbon content from 2nd to 10th cycle.

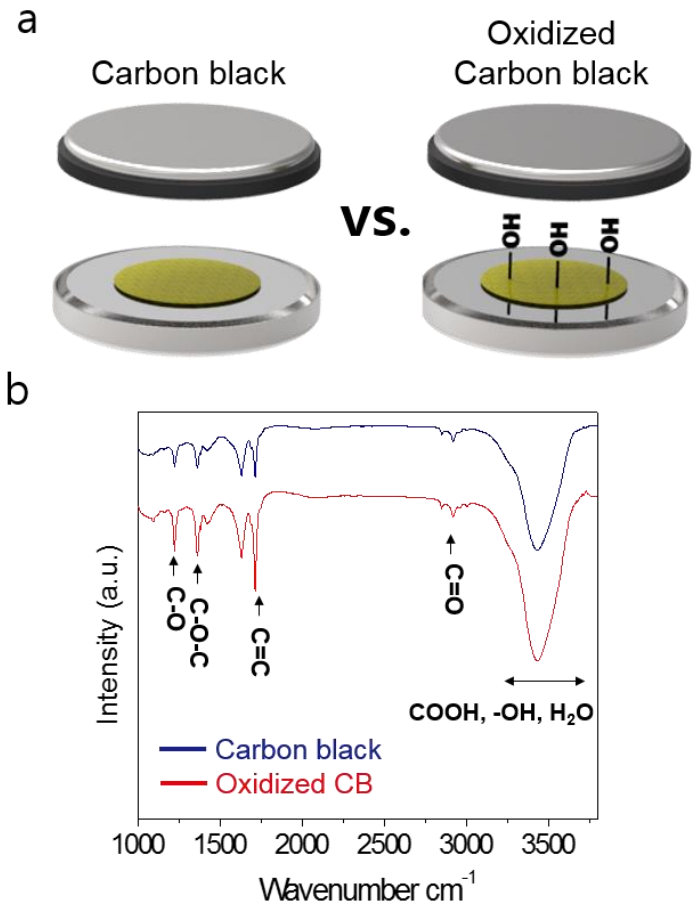

Fig. 2.6. (Color) (a) Schematic illustrations of the electrodes with untreated carbon black and oxidized carbon black. (b) The infra-red (IR) spectra to confirm the oxygen functional groups on carbon black in the oxidized carbon black.

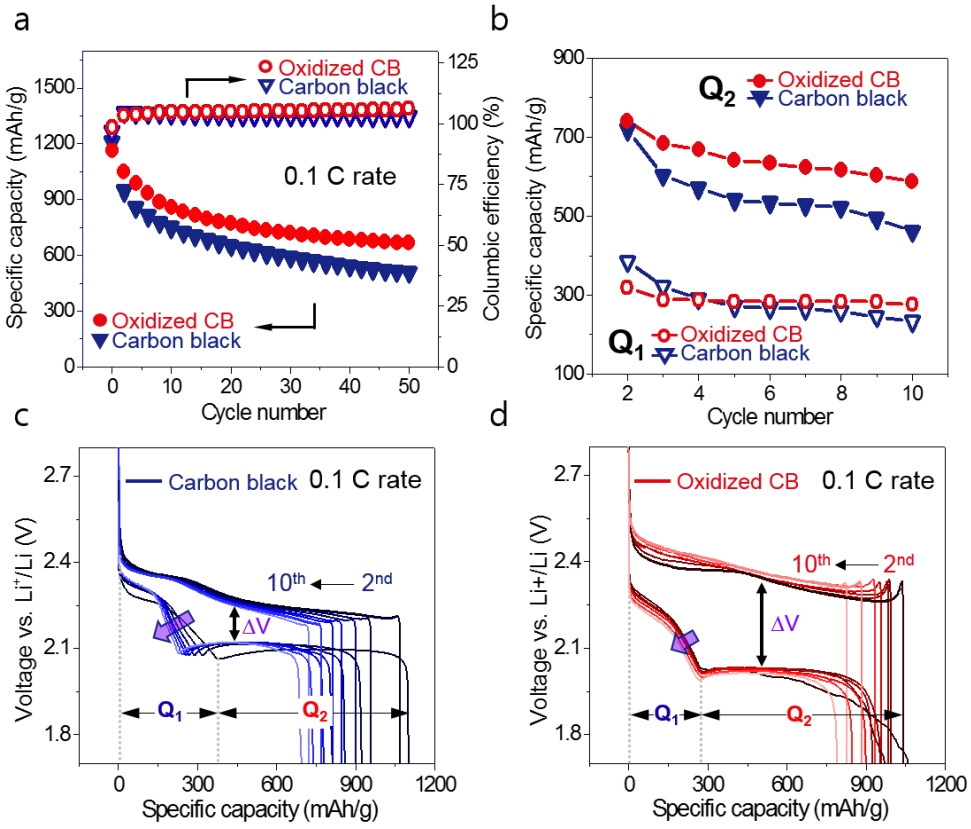

Fig. 2.7. (Color) (a) The cycling performance of electrodes with untreated carbon black and oxidized carbon black. Galvanostatic cycling was carried out at the 0.5 C rate for 50 cycles. (b) Q1 and Q2 capacity values are plotted to study the effect of oxygen functional groups on the electrochemical performance. Charge-discharge profiles of the electrode (c) with a normal carbon black and (d) with an oxidized carbon black.

2.4. Conclusions

In conclusion, we set up the series of experimental models for the in-depth understanding of the charge/discharge mechanisms. In order to study the effect of (dis)charging rate, the amount of conductive agents, and oxygen functional groups, three different model systems were studied. In each model system, Q_1, Q_2, and ΔV were traced as cycles to understand the electrochemical behaviours of them and the enhancement mechanism. Our study suggests that cycling conditions should be carefully considered and critical parameters are derived when exploring the performance of Li-S battery or designing batteries based on a new concept or novel architecture.

2.5. References

1. R. V. Noorden, *Nature* **498**, 27, 416-417 (2013).
2. D. Peramunage, and S. Licht, *Science* **261**, 1029-1032 (1993).
3. Dean, J,-A. Lange's Handbook of Chemistry (1985).
4. He, X., Ren, J., Wang, L., Pu, W., Jiang, C. & Wan, C. *J. Power Sources* **190**, 154-156 (2009).
5. Elazari, R., Salitra, G., Talyosed, Y., Grinblat, J., Scordilis-Kelley, C., Xiao, A., Affinito, J. & Aurbach, D, *J. Electrochem. Soc.* **157**, A1131-A1138 (2010).
6. Y. Su, Y. Fu, T. Cochell, and A. Manthiram, *Nature Communications* **4**, 2985 1-8 (2013).
7. L. Ji, M. Rao, H. Zheng, L. Zhang, Y. Li, W. Duan, J. Guo, E. J. Cairns, and Y. Zhang *J. Am. Chem. Soc.* **113**, 18522-18525 (2011).
8. C. Zu, and A. Manthiram, *Advanced Energy Materials* **3**, 1008-1012 (2013).
9. Socrates, G. Infrared and Raman characteristic group frequencies tables and charts: Sulphur and Selenium compounds, John Wiley & Sons Ltd, Third edition, Ch.16, (2001).

Chapter 3.

An Electrochemical Approach to Graphene Oxide Coated Sulfur for Long Cycle Life

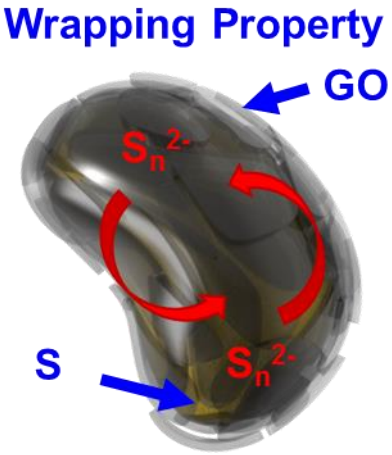

Fig. 3.T. (Color) Schematic illustration of GO-S/CB composite. The tightly coated graphene oxide support to wrapping dissolved polysulfide intermediates by physical/chemical interaction.

---

* The work presented in Chap. 3 was published in *Nanoscale*, In-press, DOI: 10.1039/c5nr01951f (2015).

"An Electrochemical Approach to Graphene Oxide Coated Sulfur for Long Cycle Life"

Joonhee Moon†, **Jungjin Park**†, Insu Jo, Seung-Ho Yu, Cheolho Jeon, Jouhahn Lee, Sung-Pyo Cho, Yung-Eun Sung*, Byung Hee Hong*

3.1. Introduction

3.1.1. Previous studies

There has been a growing demand for studies on eco-friendly and alternative energy sources to replace fossil fuels and natural gas. Lithium-based rechargeable batteries with both high volumetric and gravimetric energy have received significant attention as green power sources for portable electronics including mobile phones and laptops.[1–3] However, state-of-theart lithium rechargeable battery systems must be substantially improved to satisfy the ever-increasing energy demands of current electric vehicles for both high energy and power density.[1–3] The low specific capacity of cathode materials (~150 mAh/g for layered oxides and ~170 mAh/g for $LiFePO_4$) compared to those of the anode materials (370 mAh/g for graphite and 4200 mAh/g for silicon[4]) has spurred many researchers to develop new high capacity cathode materials.

Among the many candidates, sulfur is one of the most promising materials that can overcome the aforementioned issues. Elemental sulfur has a theoretical specific capacity of 1675 mAh/g[5,6] which is approximately five times higher than that of conventional $LiCoO_2$ cathode materials. Furthermore, sulfur has other noticeable advantages[7] as its resource is abundant, and it is inexpensive and environmentally friendly. These advantages are expected to play pivotal roles in commercializing as a next generation battery system that has a high specific energy.

However, the poor electronic conductivity of elemental sulfur (~1×10^{-30} S/cm at room temperature) limits its utilization as an active material for sulfur electrodes.[8] During

charging and discharging, the sulfur cathode is converted into lithium polysulfides (Li_2S_8, Li_2S_6, Li_2S_4 2.15–2.4 V and Li_2S_2, Li_2S ≤ 2.15 V)[8,9] dissolved in liquid organic electrolytes and deposited on lithium metal electrodes and separators, which causes irreversible loss of polysulfides. Recently, Y. V. Mikhaylik et al. reported that high-order polysulfides generated at the sulfur electrode in charge state diffuse to the lithium anode where they react directly with the lithium metal in a parasitic reaction to recreate the low-order polysulfides. Those species diffuse back to the sulfur cathode to regenerate the higher forms of polysulfide, thus creating a shuttle mechanism.[10] These losses of an active material leads to low Coulombic efficiency, poor rechargeability, and rapid fading of the capacity.[8–12] Thus, extensive research studies have been conducted in an attempt to overcome the above mentioned problems. In fact, the efforts have been focused on enhancing the electrical conductivity of sulfur by combining it with various conducting materials such as porous carbon,[13–15] one dimensional carbon,[16,17] graphene oxide (GO),[18–20] and conductive polymers.[21] In particular, the GO-based materials showed enhanced electrochemical properties because GO–sulfur composites are capable of preventing the shuttling of polysulfides. However, the role of oxygen functional groups in such an improvement has still not been completely understood.

3.1.2. Material selection

In this work, GO-wrapped sulfur (GO-S) composites were prepared and decorated with carbon black (CB), and then utilized as a cathode electrode in a lithium sulfur battery (Li-S battery). The structural properties of the cathode electrode were

characterized *via* transmission electron microscopy (TEM), scanning electron microscopy (SEM), and Raman spectroscopy. In addition, the chemical properties were determined by using Fourier transform infrared spectroscopy (FTIR) and X-ray photoelectron spectroscopy (XPS). The cyclic performance and Coulombic efficiency was analysed using various electrochemical measurement techniques.

3.2. Experimental section

Synthesis: GO used in this paper was synthesized by Hummer's method.[22] Graphite powder (10 g) was prepared in a flask in an ice bath. 7.6 g $NaNO_3$ was added into the flask which was filled with 338 ml H_2SO_4 under stirring conditions until it homogenized. In addition, 45 g of $KMnO_4$ was gradually added into the system over 1 h under magnetic stirring. The solution was removed from the ice bath after 2 h and was further stirred for 5 days. A viscous slurry was obtained which was then added to 600 ml aqueous solution over 1 h. H_2O_2 (30 wt.%) (5 ml) was then added into the mixture with stirring the system over 1 day. The brown coloured mixture was rinsed with deionized water using a centrifuge system several times. Finally, the GO aqueous solution was obtained and dried with a vacuum evaporator.[18]

GO (~4 mg/ml) was dispersed in deionized water and sonicated for 1 h. GO has hydrophilic properties because of the oxygen functional group, which helps GO to easily disperse in water. In order to increase the conductivity of the core–shell material, carbon black nanoparticles (Super P, ~50 nm diameter, CB, 40 mg) were loaded on the

graphene oxide (GO) by a simple sonication method. The mixture in the flask was sonicated for 1 h for a homogeneous suspension. For GO-S/CB composites, 1.5 g of $Na_2S_2O_3$ powder was dissolved in 250 ml deionized water and hydrochloric acid was added to the solution under magnetic stirring, which turns to yellow colour from sulfur. To decorate GO/CB on sulfur particles, Triton TX-100 aqueous solution was poured into the flask while the system was heated up to ~70 °C in an oil bath. After 20 min at ~70 °C, the prepared GO/CB suspension was added into the flask and kept for 20 min under vigorous magnetic stirring. Then, the system was cooled down to room temperature and the resulting product was collected and rinsed several times by centrifugation. The product was dried in a vacuum system.

Cell Assembly and electrochemical measurement: The GO–S composites were mixed with Super P (type of carbon black) and polyvinyldifluoride (PVDF), with mass ratio of 60 : 20 : 20, in N-methylpyrrolidone (NMP) solvent to produce electrode slurry. The slurry was loaded onto a current collector, an aluminium foil, using the doctor blade technique, and then dried for 3 h to form a working electrode. After dehydration, it was pressed using a roll press machine and then, it was dried again for 12 h. The loading level of the total material was ~1–1.2 mg/cm^2. 2032 type coin cells were used for the battery type and Li metal foil for the counter electrode. The electrolyte was 1.0 M lithium bis-trifluoro-methane sulfonylimide (LITFSI) in 1,3-dioxolane (DOL) and 1,2-dimethoxyethane (DME) (volume ratio 1 : 1). In addition, it should be noted that $LiNO_3$ was used as an additive in the electrolyte to enhance the cycle stability of the Li–S cell.

The coin cells were assembled in an Ar-filled glove box. The galvanostatic charge–discharge experiment was performed with a WBC3000 cycler (WonA Tech, Korea) at room temperature (RT). The coin cells were cycled at a constant current density of 835 mA/g (0.5 C) on cycling performance or various constant current density from 0.1 C to 1 C on rate performance with the voltage range of 1.7–2.8 V vs. Li^+/Li. All the specific capacity values were based on the mass of elemental sulfur. Coulombic efficiency is described as the charge capacity divided by discharge capacity. The cyclic voltammetry (CV) was operated from 1.5 V to 3.0 V at 0.03 mV/s scan rate, which can be converted to the constant current of 0.1 C rate. The Electrochemical Impedance Spectroscopy (EIS) was performed by applying an AC voltage of 0.005 V in the frequency range from 100 000 to 0.05 Hz.

Material characterization: The charge–discharge capacity of the Li–S cell was calculated by the sulfur content of the electrode matrix and the weight ratio of sulfur to carbon in the composite electrode was measured by thermogravimetric analysis (TGA: SDT Q600). TGA measurements were conducted under a nitrogen atmosphere from room temperature to 600 ℃ at a heating rate of 5 °C min−1. The X-ray diffraction pattern was obtained using high power XRD from Rigaku Corp. with Cu Kα radiation (λ) 0.15418 nm (model: D-MAX2500-PC). The diffraction data were recorded in the 2θ range of 20–80° with a step of 4° min−1. To determine the surface morphology, field-emission scanning electron microscopy (FE-SEM) was performed (AURIGA, Carl Zeiss).

3.3. Results and discussion

3.3.1. Materials characterization

The GO-S/CB composites were synthesized with a help of surfactants in order to increase the surface affinity between GO and sulphur. The surfactant is also useful to control the grain size in a manner similar to that of conventional sulfur particles. The GO contained both hydrophobic aromatic and hydrophilic regions which interact with carbon black (Super P, average particle size ~50 nm, CB), and polysulfides, respectively. The schematic illustration in Fig. 3.1(a) shows a sulfur particle tightly packed with GO sheets. The SEM images of GO-S/CB show a few micron-sized sulfur particles well covered with GO and CB (Fig. 3.1(b) and 3-S1(a)†), while the surface of the sulfur particles are partially exposed in the S/CB electrode as shown in Fig. 3.S1(b).† The fringes and Moiré patterns in the TEM images (Fig. 3.1(c and d)) imply that the sulphur particles are compactly wrapped with GO and CB. The corresponding GO-S/CB composites were characterized using scanning transmission electron microscopy (STEM) and energy dispersive X-ray spectroscopy (EDS). The elemental EDS mapping for carbon (orange), sulfur (blue), and oxygen (magenta) clearly shows that GO-S/CB forms a core–shell structure with oxygenrichfunctional groups (Fig. 3.1(e–h)).

The surfaces of the GO-S/CB and the S/CB electrodes were characterized via Fourier transform infrared spectroscopy (FTIR), X-ray photoelectron spectroscopy (XPS), and Raman spectroscopy, as shown in Fig. 3.2. The FTIR spectrum of GO-S/CB shows various configurations of oxygen in the structure including the vibration modes of –OH, C=O, C–O, and C–O–C at 3434 cm^{-1}, 1725 cm^{-1}, 1024–1180 cm^{-1}, and 1200 cm^{-1}, respectively; the peak at 1629 cm^{-1} results from the sp^2-hybridized C=C in-plane stretching.[23] Moreover, the O 1s spectra obtained from XPS exhibit significantly higher

intensity of the peak at 533.0 eV (C–OH) in GO-S/CB compared to that of S/CB. These results noticeably match with the FTIR and XPS spectra of each carbon material (GO and CB) as shown in Fig. 3.S2.† The Raman spectra of GO-S/CB and S/CB exhibit typical carbon peaks; i.e., two strong peaks at 1350 cm^{-1} for the D band and at 1590 cm^{-1} for the G band, which stem respectively from structural defects and the in-plane vibrational mode.[24] The Raman spectrum in the inset of Fig. 3.2(c) shows a peak corresponding to sulfur only.[25] The sulfur peak was not observed for both samples, implying that the sulfur particles are surrounded by carbon materials.

Fig. 3(a) shows the X-ray diffraction (XRD) patterns measured from the S/CB and GO-S/CB composites on the Al foil. The positions of the peaks corresponding to sulfur particles all occurred at the standard Bragg position of the orthorhombic phase with the space group Fddd (JCPDS 24-0733: S_8)[26] and no traces of other impurities were detected. The amount of GO in the GO-S composite was quantified via TGA analysis. Fig. 3.3(b) represents the TGA results of the GO-S composite from 40 to 600 ℃ under a nitrogen atmosphere, and the weight loss was shown approximately up to 84 wt.%. The loss of the sulfur-conducting material composite results mainly from the evaporation of sulfur at temperatures of ~170–250 ℃. Furthermore, the continuous and steady weight loss of the second stage above 370 ℃ is estimated to be 6 wt.%. The sulfur content of the GO–S composite was adjusted to 90 wt.% during the preparation process.

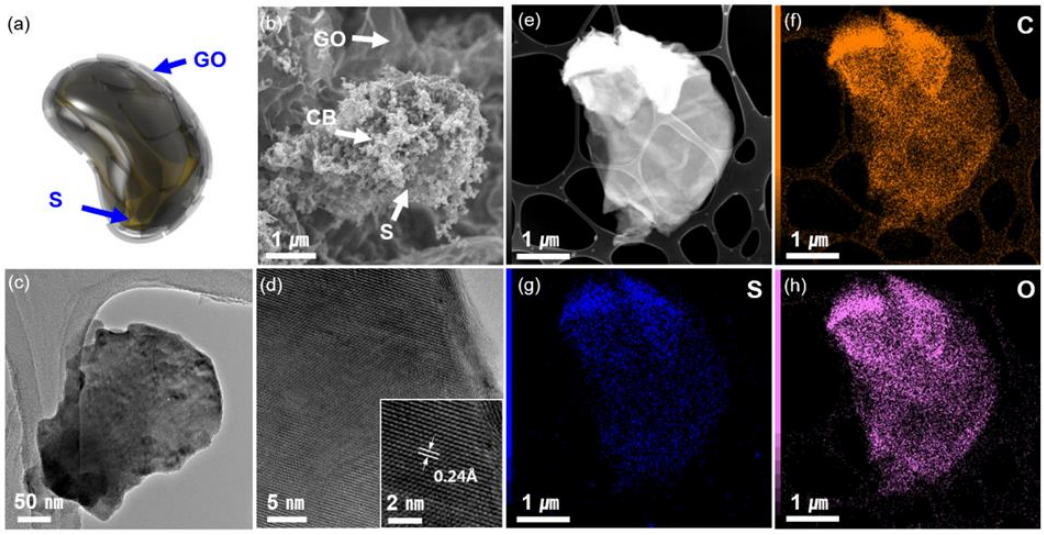

Fig. 3.1. (Color) (a) Schematic illustration and (b) scanning electron microscopy (SEM) image of GO-S/CB composites. (c) Transmission electron microscopy (TEM) image and (d) high resolution TEM image of GO-S/CB. (e) Scanning-TEM (STEM) image and (f–h) C, S, and O energy-dispersive X-ray spectroscopy (EDS) maps of the GO-S/CB composites.

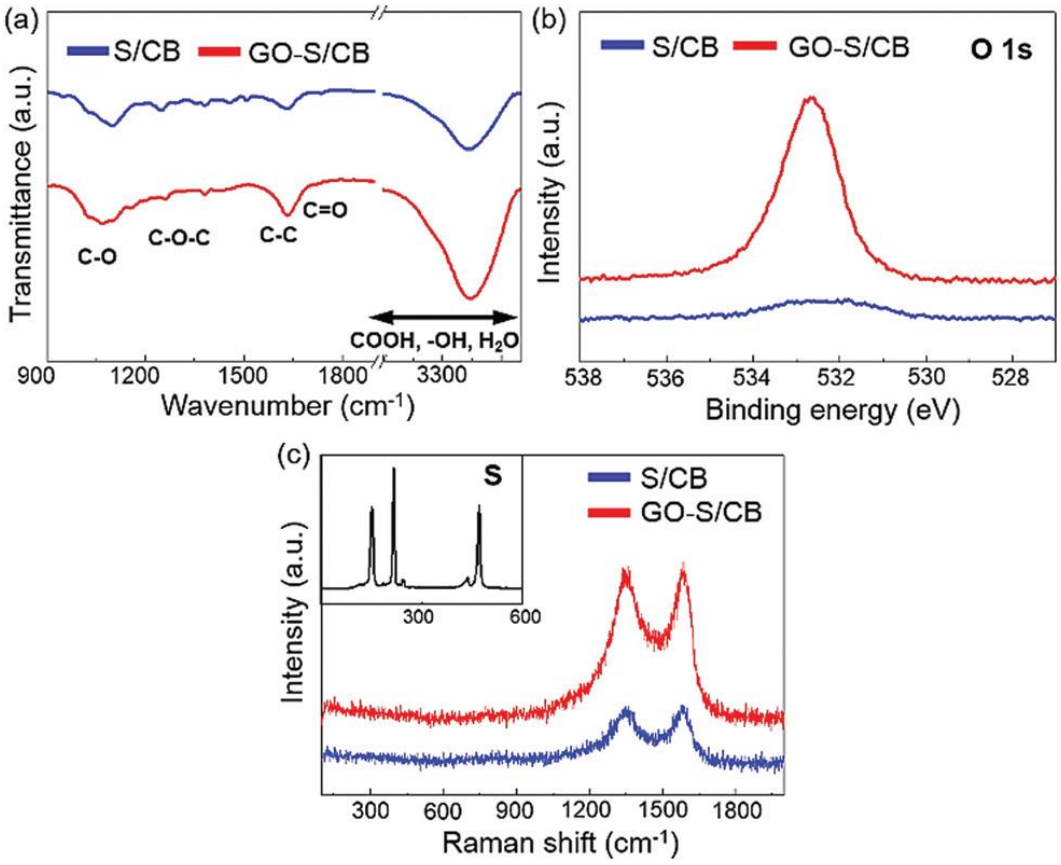

Fig. 3.2. (Color) (a) FTIR spectra of GO-S/CB and S/CB. The peaks correspond to the various functional groups in GO-S/CB and S/ CB. (b) O 1s XPS spectra and (c) Raman spectra of GO-S/CB and S/CB.

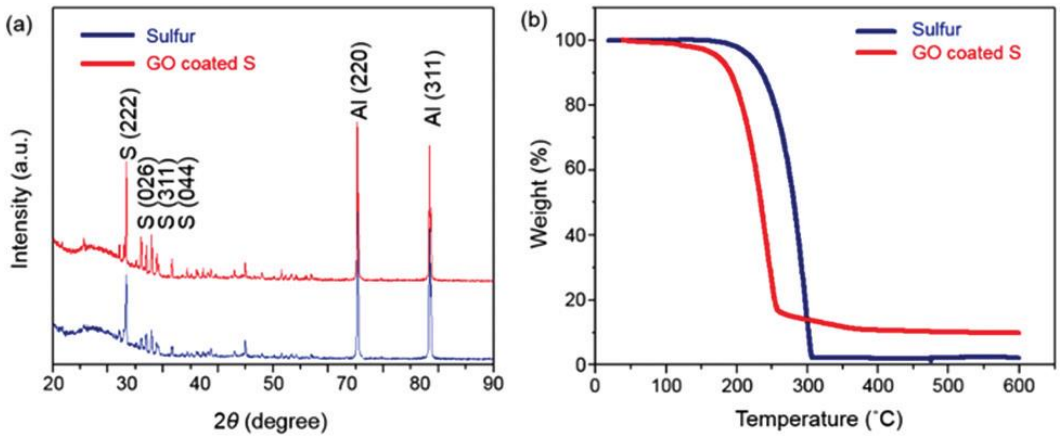

Fig. 3.3. (Color) X-ray diffraction (XRD) patterns and thermogravimetric analysis (TGA). (a) XRD spectra of S/CB and GO-S/CB on the Al foil current collector and (b) TGA spectra collected in N_2 atmosphere with a heating rate of 10 °C min−1 showing the S content of the GO-S electrodes.

3.3.2. Electrochemical analysis

Fig. 3.4(a) and (b) show conventional charge–discharge profiles of the S/CB and the GO-S/CB as a lithium sulfur battery. The cell is discharged and charged at 0.5 C rate (835 mA/g) for 20 cycles, which is sufficient for revealing variations and tendencies in the electrochemical behaviour. In the discharge profiles, two-step plateaus were generated at 2.4 V and 2.1 V due to the dissolution of sulfur to soluble high-order polysulfide and the precipitation of low-order polysulfide to lithium sulfide (polysulfides (Li_2S_8, Li_2S_6, Li_2S_4 2.15–2.4 V and Li_2S_2, Li_2S $\leq$ 2.15 V)).[8,9] In this paper, we designated three regions, Q_1, Q_2 and ΔV, which facilitate the explanation of the electrochemical properties of the GO-S/CB cathode electrode. Q_1 and Q_2 indicate capacity of the dissolution and the precipitation regions, respectively and the ΔV means overpotential between discharge and charge reactions.

In the Q_1 region, the sulfur particles as reactants are initially dissolved into electrolyte, and then, the reactants are reduced to the long-chain sulfides (S_n^{2-}, n = 8–4) in the liquid phase (dissolved state). In this regime, the lithium/polysulfide ions can easily move, leading to the fast kinetics of the reaction. However, the liquid mechanism leads to irreversible loss of soluble polysulfides due to diffusion from the polysulfide into the bulk electrolyte.[9] In the Q_2 region, long-chain polysulfides are converted to short-chain polysulfides (S_n^{2-}, n=4–1), and then finally produce the lithium sulfide (Li_2S) (precipitated state); the kinetics of this reaction are sluggish owing to the formation of lithium polysulfides, driving the high reversible cycle retention of capacity.[9] In charge

processes, the reverse reactions aforementioned occur. Q_1, Q_2, and ΔV provide insight into the origins of the unique reaction mechanism of the materials. The GO-S/CB exhibits the constant Q_1 capacity retention with increasing cycle number, while the capacity of S/CB is continuously fading due to the irreversible loss of polysulfide, which represents that GO can play a key role in reserving polysulfides.

Moreover, the slowly decreasing Q_2 value of GO-S/CB, compared to the rapidly decreasing value of S/CB indicates that GO provides reversible reaction sites with polysulfide. Previous studies assert that the oxygen-rich carbon matrix promotes the interaction of carbon with sulfides.[18,19,27] Thus, we believe that the increased electrochemical performance of GO stems from physical wrapping and chemical surface modification. The cycling performance and Coulombic efficiency of S/CB and GO-S/CB composites were measured at 0.5 C rate (1 C rate = 1675 mA/g) for 100 cycles, as shown in Fig. 3.4(c) and (d); respective initial capacities of 1003.5 mAh/g and 1142.7 mAh/g were obtained for S/CB and GO-S/CB at the first cycle. At the relatively fast C-rate, GO as a conducting agent supports electrical contact with sulfur, which shows the discharge capacities of ~723.7 mAh/g (GO-S/CB) and ~307.3 mAh/g (S/CB) at 100^{th} cycle, respectively. The fading capacity of the S/CB may be attributed to its Coulombic efficiency, i.e., the S/CB exhibits a low charge/discharge ratio in the initial cycle, but the Coulombic efficiency increased gradually due to the shuttle mechanism stemming from the irreversible loss of the polysulfide into electrolyte. This loss indicates that the structure of the S/CB does not trap the soluble polysulfide.[10]

The overpotential (ΔV) was estimated from the reaction potential of the

charge/discharge profile (Fig. 3.4(a and b)). In Fig. 3.5, the cyclic voltammetry (CV) results provide a detailed view of the reaction potential including that of the oxidized and reduced polysulfides. To exclude the effect of mass transfer of an ion in the electrolyte, a scan rate of CV at 0.03 mV/s was converted to the approximately 0.1 C rate. Moreover, to facilitate electrochemical analysis, we designated the first and second reactions of the anodic and cathodic scan as O_2 and O_1, and R_1 and R_2, respectively; i.e. solid-state sulfur (S_8) is converted to polysulfide in the R_1 region and liquid-state sulfide forms solid-state sulfur in the O_1 area. In the R_2 and O_2 regions, liquid-state sulfide is converted to solid Li_2S, and Li_2S is dissolved in polysulfide, respectively. The R_2 of S/CB and GO-S/CB exhibits similar reaction potential. In contrast, the R_1 reaction of GO-S/CB exhibits a 0.3 V higher potential shift than that of S/CB, indicative of the superior electrical contact between sulfur and the conducting agent. In the anodic scan, however, the O_1 and O_2 peaks of GO-S/CB are shifted toward negative potentials than those of S/CB. This phenomenon is consistent with the improved electrical contact of GO-S/CB, while the increased hysteresis of charge/discharge of S/CB stems from electrical contact loss. In addition, the higher intensity and sharper peaks of GO-S/CB indicate better reaction kinetics at each step, compared to those of the S/CB.

Rate capability tests were conducted at various C-rates (0.1 C to 1 C), as shown in Fig. 3.6. The GO-S/CB exhibits superior stability of rate performance in the higher C-rate conditions, which concurs with the Coulombic efficiency resulting from the irreversible loss of dissolved polysulfide with increasing current. On the other hand, the Coulombic efficiency of S/CB is significantly influenced by the constant current scale in Fig. 3.6(b).

After a rate of 1 C, the Coulombic efficiency is still sharply reduced even after recovery up to 0.1 C, which implies that the severe active-material loss at high constant results from an unstable structure. This result also indicates that the accumulated sulfide has a significant influence on the successive cycling performance; i.e., the so-called shuttle phenomena. Thus, our results suggest that GO improves the electrical conductivity and physical stability of the cathode materials during battery operation.

Electrochemical impedance spectroscopy (EIS) spectra (Fig.3-7) represent the structural stability and electrical conductivity of the cathode electrodes before and after battery operation. The Nyquist plots are composed of a semi-circle in the high-frequency region, which is related to contact and charge transfer resistance, and a short inclined line in the low-frequency regions; this line results from ion diffusion in the cathode.[29] In order to measure the precise EIS property of the cathode electrode, a symmetric type cell with lithium metal is positioned in a parallel configuration (grey dots), and the effect of lithium metal on the EIS spectra was determined. Prior to cycling, the semi-circle corresponding to GO-S/CB is smaller than its S/CB counterpart. This indicates that the electrical conductivity of the former is higher than that of the latter. Moreover, after battery operation, the diameters of both semi-circles increase owing to the formation of a passivation layer, increased resistance of the electrolyte, modified surface roughness, and so forth. The semi-circle corresponding to GO-S/CB is, however, still smaller than that of S/CB, which indicates that the GO aid in increasing the conductivity and structural stability during battery operation.

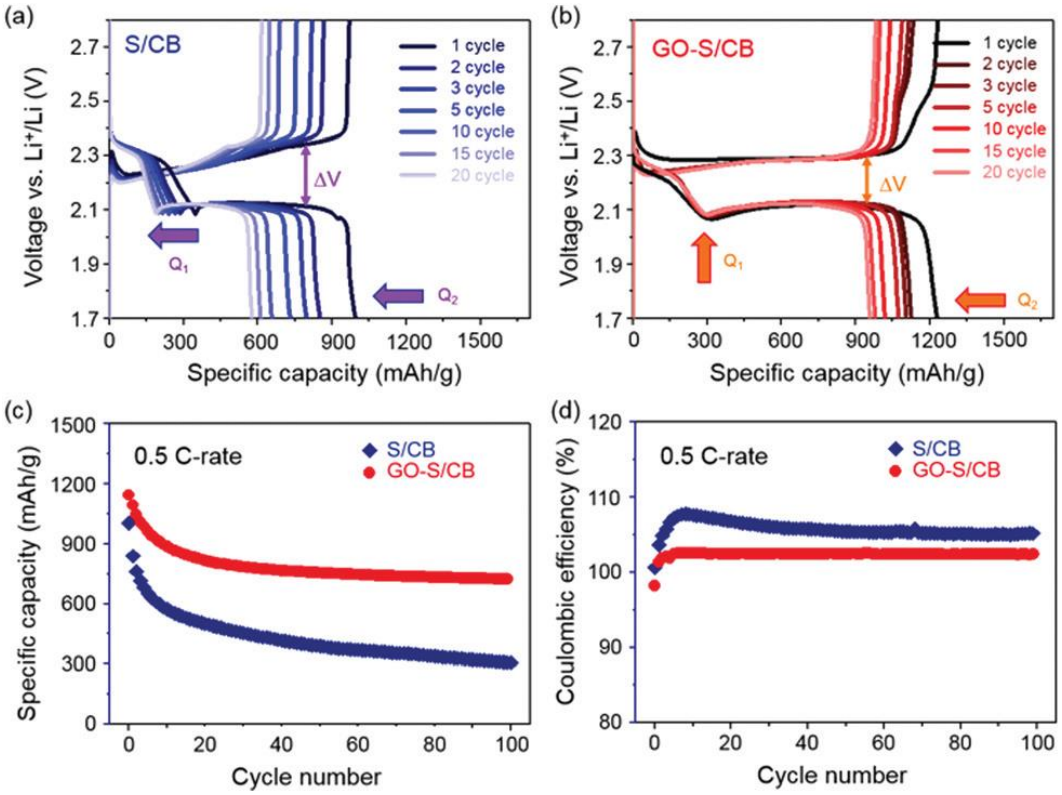

Fig. 3.4. (Color) Electrochemical characterization of S/CB and GO-S/CB cathodes. Voltage profiles for (a) S/CB and (b) GO-S/CB plotted from 1st. to 20th. cycles at 0.5 *C*. (c) Cycling performance and (d) Coulombic efficiency of S/CB and GO-S/CB at 0.5 *C* for 100 cycles.

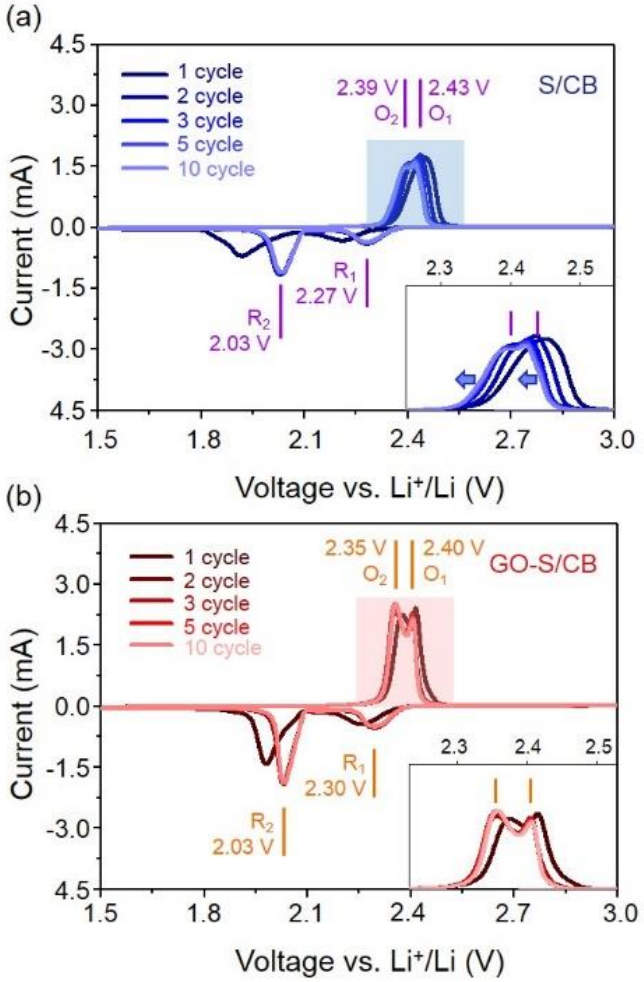

Fig. 3.5. (Color) Cyclic Voltammetry peaks of (a) S/CB and (b) GO-S/CB cathodes at 0.03 mVs^{-1} scan rate.

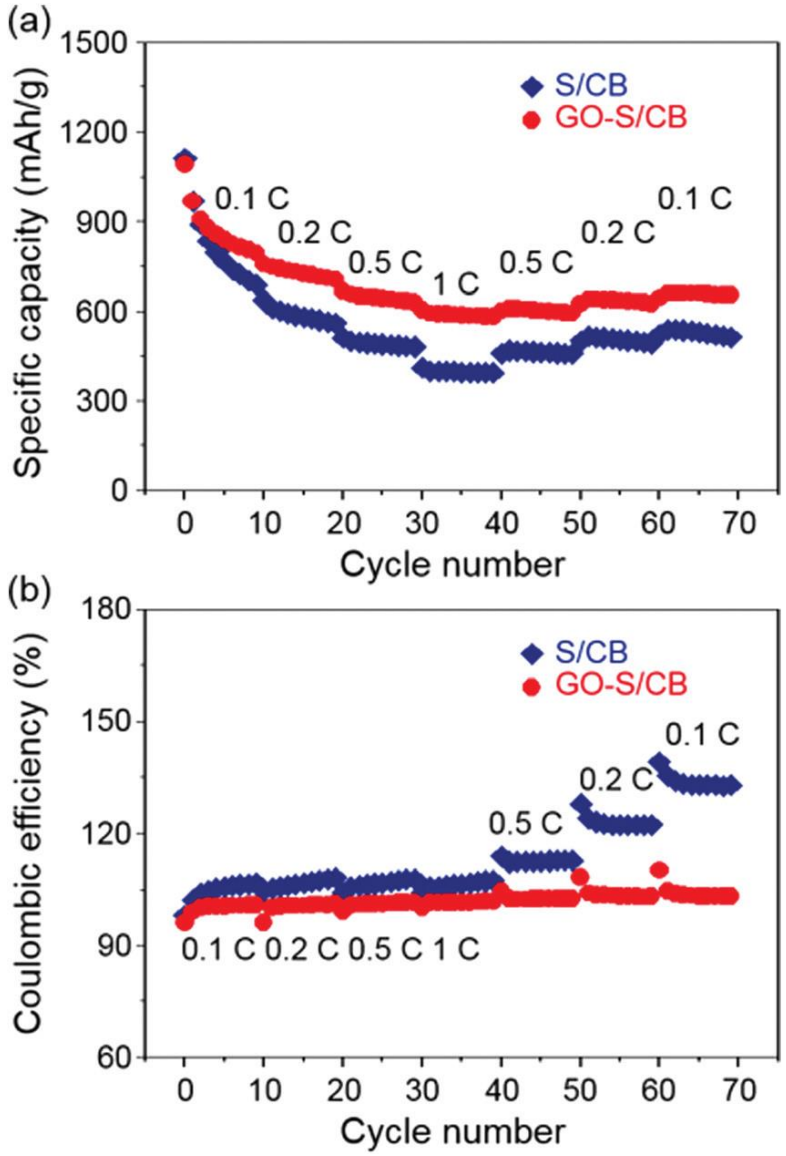

Fig. 3.6. (Color) (a) Rate performance and (b) Coulombic efficiency of S/CB and GO-S/CB composites from 0.1 *C* up to 1 *C*.

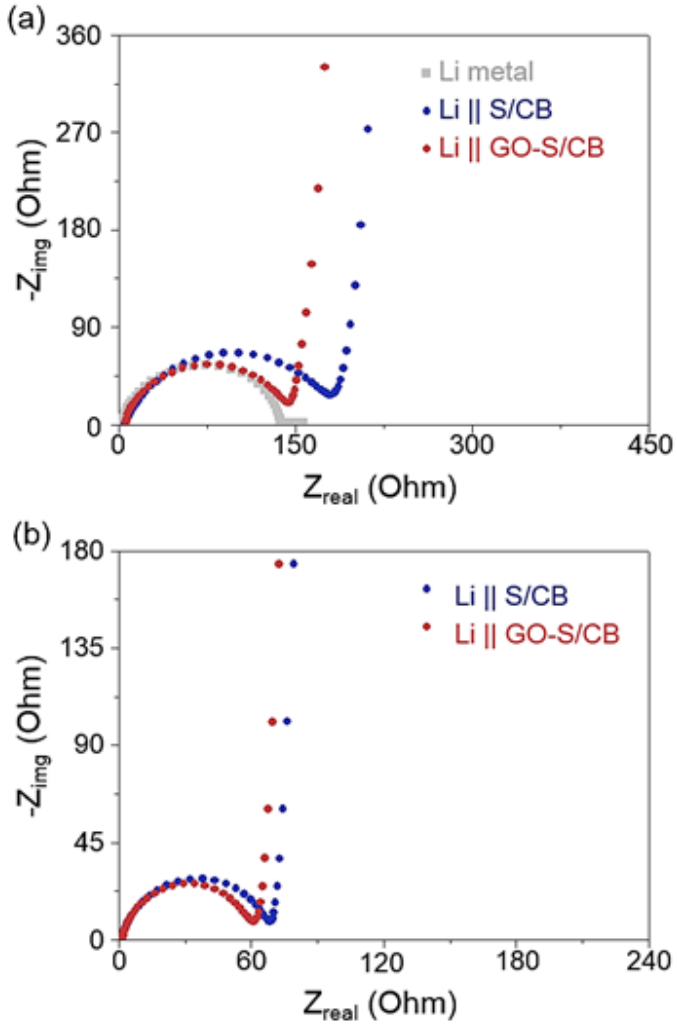

Fig. 3.7. (Color) (a) Rate performance and (b) Coulombic efficiency of S/CB and GO-S/CB composites from 0.1 *C* up to 1 *C*.

3.4. Conclusions

In summary, we have synthesized GO-S/CB composites in which micron-sized sulfur particles are encapsulated by GO sheets. The structural properties and chemical properties of GO-S/CB composites were characterized by various microscopic and spectroscopic techniques. Various electrochemical analyses were conducted to elucidate the role of GO that has rich oxygen functional groups and its effect on the electrochemical properties. The charge–discharge profiles revealed the significantly enhanced cycling and rate performance of the GO-S/CB electrode, indicating that GO plays a key role in trapping trapping dissolved polysulfide and in improving electronic conductivity. Moreover, the Columbic efficiency of the GO-S/CB electrode prevents capacity fading stemming from the dissolution and precipitation of polysulfide, and also promotes homogeneous electron flows. In addition, EIS spectra indicate that the GO-S/CB electrode has a higher electrical conductivity before/after battery cycling than the S/CB electrode, implying that the structure of the GO-S/CB electrode is maintained during battery operation. Thus, we expect that the incorporation of GO would make an important step forward to the practical applications of Li–S batteries in the future.

3.5. Supporting informations

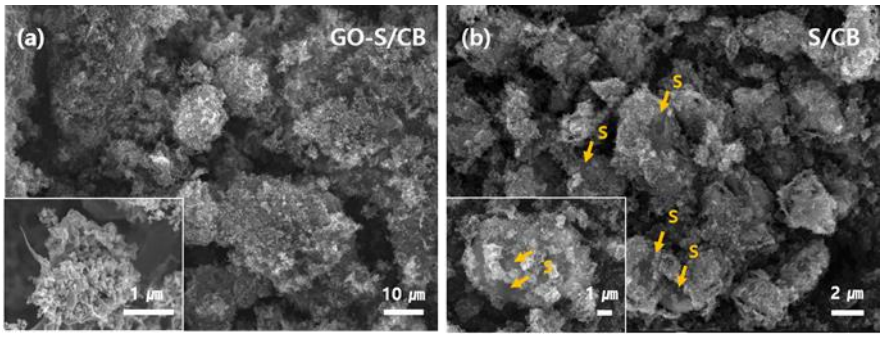

Fig. 3.S1. (Color) SEM images of (a) GO-S/CB and (b) S/CB. The insets show the magnified images of GO-S/CB and S/CB, respectively.

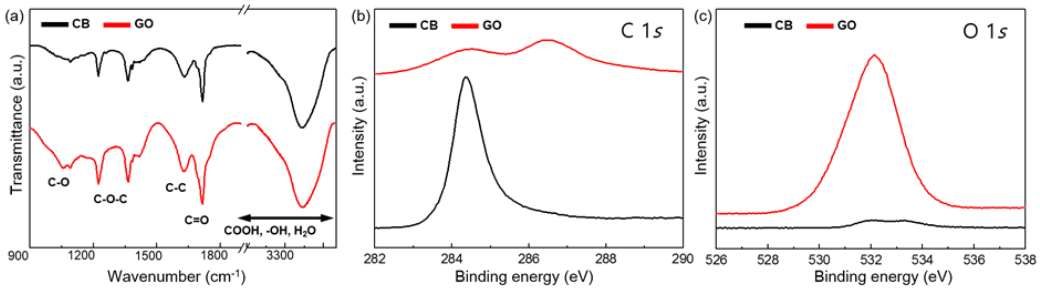

Fig. 3.S2. (Color) (a) Fourier transform infrared spectroscopy (FTIR) spectra of CB and GO. Strong peaks attributed to the characteristic vibrational mode of oxygen functional groups. X-ray photoelectron spectroscopy of CB and GO. (b) C 1s peaks and (c) O 1s peaks.

3.5. References

1. N. Choi, Z. Chem, S. A. Freunberger, X. Ji, Y.-K. Sun, K. Amine, G. Yushin, L. F. Nazar, J. Cho and P. G. Bruce, *Angew. Chem. Int. Ed.* **51**, 9994 (2012).
2. Y.-K. Sun, Z. Chen, H.-J. Noh, D.-J. Lee, H.-G. Jung, Y. Ren, S. Wang, C. S. Yoon, S.-T. Myung and K. Amine, *Nat. Mater.* **11**, 942 (2012).
3. M. Armand and J.-M. Tarascon, *Nature* **451**, 652 (2008).
4. C. K. Chan, H. Peng, G. Liu, K. McIlwrath, X. F. Zhang, R. A. Huggins and Y. Cui, *Nat. Nanotechnol.* **3**, 31 (2008).
5. J. Kim, D.-J. Lee, H.-G. Jung, Y.-K. Sun, J. Hassoun and B. Scrosati, *Adv. Funct. Mater.* **23**, 1076 (2013).
6. J. Wang, J. Yang, C. Wan, K. Du, J. Xie and N. Xu, *Adv. Funct. Mater.* **13**, 487 (2013).
7. W. J. Chung, J. J. Griebel, E. T. Kim, H. Yoon, A. G. Simmonds, H. J. Ji, P. T. Dirlam, R. S. Glass, J. J. Wie, N. A. Nguyen, B. W. Guralnick, J. Park, A. Somogy, P. Theato, M. E. Mackey, Y.-E. Sung, K. Char and J. Pyun, *Nat. Chem.* **5**, 518 (2013).
8. Y. Yang, G. Zheng and Y. Cui, *Chem. Soc. Rev.* **42**, 3018 (2013).
9. Y.-S. Su, Y. Fu, T. Cochell and A. Manthiram, *Nat. Commun.* **4**, 2985 (2013).
10. Y. V. Mikhaylik and J. R. Akridge, *J. Electrochem. Soc.* **151**, A1969 (2004).
11. R. Elazari, G. Salitra, A. Garsuch, A. Panchenko and D. Aurbach, *Adv. Mater.* 23, 5641 (2011).
12. S. S. Zjang and J. A. Read, *J. Power Sources* **200**, 77 (2012).

13. C. D. Liang, N. J. Dudney and J. Y. Howe, *Chem. Mater.* 21, 4724 (2009).
14. N. Jayaprakash, J. Shen, S. S. Moganity, A. Corona and L. A. Archer, *Angew. Chem., Int. Ed.* **50**, 5904 (2011).
15. J. L. Wang, J. Yang, J. Y. Xie, N. X. Xu and Y. Li, *Electrochem. Commun.* **4**, 499 (2002).
16. G. Zheng, Y. Yang, J. J. Cha, S. S. Hong and Y. Cui, *Nano Lett.* **11**, 4462 (2011).
17. W. Ahn, K.-B. Kim, K.-N. Jung, K.-H. Shin and C.-S. Jin, *J. Power Sources* **202**, 394 (2012).
18. H. Wang, Y. Yang, Y. Liang, J. T. Robinson, Y. Li, A. Jackson, Y. Cui and H. Dai, *Nano Lett.* 11, 2644 (2011).
19. L. Ji, M. Rao, H. Zheng, L. Zhang, Y. Li, W. Duan, J. Guo, E. J. Cairns and Y. Zhang, *J. Am. Chem. Soc.* **133**, 18522 (2011).
20. J. Liu, Y. L. Cao, X. L. Li, I. A. Aksay, J. Lemmon, Z. M. Nie and Z. G. Yang, *Phys. Chem. Chem. Phys.* **13**, 7660 (2011).
21. C. D. Dimitrakopoulos and P. R. L. Malenfant, *Adv. Mater.* **14**, 99 (2002).
22. W. S. Hummers Jr. and R. E. Offeman, *J. Am. Chem. Soc.* **80**, 1339 (1958).
23. M. Acik, G. Lee, C. Mattevi, A. Pirkle, R. M. Wallace, M. Chhowalla, K. Cho and Y. Chabal, *J. Phys. Chem. C* **115**, 19761 (2011).
24. L. G. Cancado, K. Takai, T. Enoki, M. Endo, Y. A. Kim, H. Mizusaki, A. Jorio, L. N. Coelho, R. Magalhäes-Paniago and M. A. Pimenta, *Appl. Phys. Lett.* **88**, 163106 (2006).
25. J.-T. Yeon, J.-Y. Jang, J.-G. Han, J. Cho, K. T. Lee and N.-S. Choi, *J.*

Electrochem. Soc. **159**, A1308 (2012).

26. Joint Committee in Powder Diffraction Standards (JCPDS), International Center of Diffraction Data, Swarthmore, PA.
27. X. Ji, K. T. Lee and L. F. Nazar, *Nat. Mater.* **8**, 500 (2009).
28. J. Brückner, S. Thieme, H. T. Grossmann, S. Dörfler, H. Althues and S. Kaskel, *J. Power Sources* **268**, 82 (2014).
29. Z. Dung, Z. Zhang, Y. Lai, J. Liu, J. Li and Y. Liu, *J. Electrochem. Soc.* **160**, A553 (2013) .

Chapter 4.

Graphene Quantum Dots: Induced C-S Bonding Suitable for High Sulphur/Sulphide Utilization

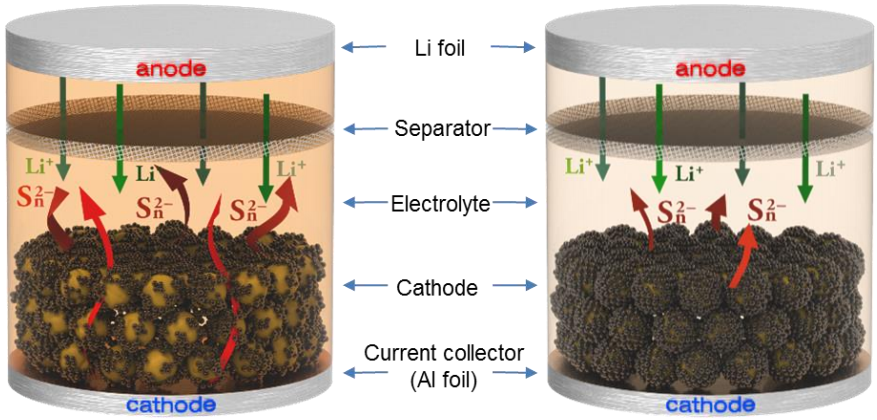

Fig. 4.T. (Color) Schematic configuration of S/CB and GQDs-S/CB employed as a cathode in a Li-S battery. The sulphur (yellow) is wrapped with carbon black (S/CB) and compactly covered with graphene quantum dots and carbon black (GQDs-S/CB), respectively. Polysulphides were dissolved into solvent and the color changed to orange

4.1. Introduction

4.1.1. Previous studies

Rechargeable lithium ion batteries (LIBs) are widely used for various applications such as portable devices, bio-medical implants, and electric vehicles because of their high energy and power density [1-4]. However, current LIBs based on graphite-transition metal oxide electrode couples have nearly reached a ceiling in their storage capability due to their electrical and crystal structural limitations. Therefore, breakthroughs with new energy storage systems that can surpass current performance barrier of LIBs should be brought about in a timely manner. Recently, systems that can operate by electrochemical transformation of sulphur (S_8) to lithium sulphide (Li_2S) have attracted great attention because elemental lithium and sulphur can be directly utilized as an anode and a cathode, respectively[5]. Sulphur (S_8) generated from petroleum refinement[6] is an ideal choice for a cathode due to its low cost, environmental friendliness, and high theoretical specific capacity (1,675 mAh/g, 16 electrons process) when it is fully transformed to Li_2S (refs 6-9). However, three main barriers limit the efficient use of sulphur as a cathode: the deleterious electrochemically induced volume expansion of lithiated from S_8 to Li_2S (~80%), the poor electronic conductivity of S_8 (~1×10^{-30} S/m) and Li_2S (~1×10^{-14} S/m), and the irreversible loss of intermediate LiPSs into the electrolyte[5,10,11]. This loss of LiPSs during cycling is responsible for the poor cycle stability, low sulphur utilization, and polysulphide-shuttle mechanism[5]. To overcome these problems, various carbonaceous materials have been integrated into the sulphur cathode matrix to take advantage of their physical properties to prevent LiPSs dissolution

into the electrolyte[12-14], sorption properties[15-17], and high electronic conductivity[18-19]. In particular, graphene oxide (GO)-sulphur composites have been reported as a new approach to prevent the loss of LiPSs by adsorption and wrapping properties of GO (refs 20-23). However, these systems were found to have poor structural integrity[24] between S and GO, which allows LiPSs to be readily lost by repeated electrochemical cycling. Furthermore, these studies focused on the characteristics of as-prepared GO-S composites, which limits understanding of the role of functional groups during battery operation.

4.1.2. Material selections

Herein, we introduce nano-sized GQDs (an average particle size of ~4 nm) with oxygen functional groups[25-27] that assemble with sulphur and carbon black (CB) to form a tightly packed structure, which provides fast charge conduction pathways while minimizing the irreversible loss of LiPSs. Oxygen functional groups also serve to preserve dissolved LiPSs by the formation of C-S bonds (the so called sulphiphilic property), as confirmed by density functional theory (DFT) calculations, whereby high sulphur/sulphide utilization is achieved even at high current densities. In order to study the mechanism of the enhanced electrochemical performance, the contribution of dissolution and precipitation to the electrochemical performance was carefully considered.

4.2. Experimental Section

Synthesis of graphene quantum dots. Carbon fibers were placed into a mixture of

H_2SO_4 and HNO_3. The solution was sonicated for 2 h, and then stirred for 24 h. The solution was then refluxed at 90℃ for 48 h with vigorous stirring. The mixture was cooled and diluted with deionized water, and the pH was adjusted to 8 with Na_2CO_3. The final product was dialyzed for 5 days and then filtered. Finally, the GQDs aqueous solution was concentrated.

Synthesis of GQDs-S composites. 1.5 g of $Na_2S_2O_3$ powder (Sigma-Aldrich) was dissolved in 250 ml deionized water, and this solution was stirred with hydrochloric acid. The GQDs-S core-shell composites were synthesized by heating a 1% Triton TX-100 (Sigma-Aldrich, average mol wt.% 625) to ~70℃, and after 20 min at ~70℃, the prepared GQDs were vigorously stirred in this solution for 20 min. A carbon black suspension was then injected into this mixture and was stirred vigorously for 20 minutes. Then, the solution was cooled to room temperature and the collected products were rinsed several times. Finally the GQDs-S composites were dried under vacuum.

Cell fabrication and electrochemical measurement.

The electrodes were fabricated from slurries that contained 60 wt.% sulphur, 20 wt.% conducting agents and 20 wt.% polyvinylidene fluoride (pvdf) binder dispersed in N-methyl-2-pyrrolidone (2 ml). The prepared slurry was cast onto an aluminum foil using a doctor blade. The prepared electrodes were transferred to an Ar-filled glove box and were assembled in a 2032 type coin cell. The mass loading of all samples was ~1mg of active material. The electrolyte was 1.0 M LiTFSI (lithium bis-trifluoromethanesulfonimide) and 0.1 M $LiNO_3$ (lithium nitrate) with DOL (dioxolane) and DME (dimethyl ether) 1:1 volume ratio (Panax Etec, Korea). The separator was supplied from SK Innovation, and

lithium metal was used as a counter electrode. Electrochemical properties were measured with a WBCS3000 cycler (Won-A Tech, Korea). The voltage window for electrochemical measurements was fixed between 1.5 - 3.0 V vs. Li^+/Li (all the voltages below are vs. Li^+/Li). The Carbon or GQDs electrodes were fabricated similarly to the aforementioned procedures from slurries that contained 80 wt.% carbon of GQDs and 20 wt.% polyvinylidene fluoride (pvdf) binder dispersed in N-methyl-2-pyrrolidone (2 ml).

Li_2S_8 catholyte was prepared by using Li_2S and S_8 powders which were inserted into the same electrolyte condition according to the stoichiometric ratio. In order to analyze the cycled electrodes the coin cells were opened in an Ar-filled glove box. All the samples were analyzed after rinsing with copious amounts of DOL/DME. The EIS measurement was performed at open circuit potential between 100 MHz to 100 mHz with fluctuations of <10mv, and the Nyquist plots were fitted from equivalent circuits.

Characterization. XRD was performed on a (Rigaku, D-MAX2500-PC) operating with Cu Ka radiation (λ=1.5406 Å) at 40 kV and 200 mA. TEM was performed on a (JEOL JEM-2100F). XPS was performed on a AXIS Ultra DLD (Kratos.Inc) using a 150 W monochromatic Al K (1486.6 eV) source at the Korea Basic Science Institute (KBSI). High resolution data was collected using a pass energy of 40 eV and 0.05 eV step. Raman spectra was obtained with a Renishaw micro-Taman spectroscope with an excitation wavelength of 514.5 nm. The spot diameter was approximately 2 ㎛.

Computational methods. We carried out density functional theory (DFT) calculations for optimizing structures and analyzing frequencies. Conventional B3LYP exchange-correlation functional[42] was used for the DFT calculations. B3LYP is a hybrid-GGA

exchange-correlation functional, which means size-consistency problem can't be considered. To more precisely describe the anion systems, we used a 6-31++G(d) basis set which added diffuse functions to all atoms. All structures in this paper are optimized which is confirmed by frequency analysis. GAUSSIAN 09 package[43] is used for all calculations.

4.3. Results and Discussion

4.3.1. Materials Characterization

To study the physical/chemical properties of GQDs, various microscopic and spectroscopic analytical tools were employed. High resolution transmission electron microscope (HRTEM) images were collected to study the morphology of the GQDs (Figs. 4.1a and 1b). The GQDs are highly crystalline and show an average size of 4.11 (±0.55) nm (the inset of Fig. 4.1b). Oxygen-rich functional groups on the edge of the GQDs where non-bonding carbons exist were identified by Fourier-transform infra-red (FTIR) spectroscopy (Fig. 4.1c). Strong peaks attributed to the characteristic vibrational modes of oxygen functional groups (–OH at 3,434 cm^{-1}, C=O at 1,725 cm^{-1}, C-O in 1,024-1,180 cm^{-1}, and C-O-C at 1,200 cm^{-1}) can be observed in GQDs, while the peak at 1,629 cm^{-1} results from sp^2-hybridized C=C (in-plane stretching)[28]. These oxygen-functional groups of GQDs can strongly bond to sulphur *via* electrostatic interaction.

The GQDs-S composites were prepared by GQDs and S that is chemically reduced from $Na_2S_2O_3$. It should be noted that surface of sulphur was mediated by a surfactant

(see the details in the Method section). The scanning electron microscopy (SEM) and TEM images in Figs. 4.1d and 1e show the morphology of the GQDs-S. Several micron-sized sulphur particles are homogeneously coated with GQDs. The uniform distribution of GQDs on the sulphur surface is confirmed by energy dispersive X-ray spectroscopy (EDX) mapping of C, O, and S (Fig. 4.S1). The graphitic characteristic of GQDs-S was established by Raman spectroscopy (Fig. 4.1f), where the peaks for carbon (D and G at 1,350 and 1,590 cm^{-1}, ref. 29) and sulphur (the four characteristic peaks below 600 cm^{-1})[30] can be clearly resolved.

The GQDs-S/carbon black (CB, average particle size of ~50 nm) composite structures were prepared from GQDs-S and CB *via* van der Waals interaction[20]. Experimental details can be found in the Methods section. The SEM image of GQDs-S/CB, Fig. 4.1g, presents that CBs are tightly bound to the GQDs-S composites. Scanning transmission electron microscopy (STEM)-EDX was used to determine the compositional distribution of C, O, and S in the GQDs-S/CB composite and shows that C, O, and S is homogeneously distributed throughout the composite structure (Fig. 4.S2). X-ray diffraction (XRD) analysis of the GQDs-S/CB composite structures reveals high S crystallinity and phase purity (Fig. 4.S3a) and the composition of GQDs-S/CB was estimated by thermogravimetric analysis (TGA) (Fig. 4.S3b) to be 70 : 20 : 10 (wt.%) in S : CB : GQD. X-ray photoelectron spectroscopy (XPS), Fig. 4.S4, analyzed the surface of the GQDs-S/CB composite and the results of the quantitative analysis are displayed in Table S1. The XPS results indicate higher intensity of C=O (286.7 eV in C 1*s* and 530.9

eV in O 1*s*) and C-OH (533 eV in O 1*s*) for GQDs-S/CB compared to S/CB due to the surfactant and oxygen functional group of the GQDs[31]. Meanwhile negligible S 2*p* signal was detected since the GQDs-S are covered with CB in the GQDs-S/CB structure (see S 2*p* in GQDs-S/CB *vs*. S/CB). The schematic illustration in Figs. 1h and 1i, shows the GQDs distributed on a sulphur particle, which can strongly bond to CB, leading to a densely coated GQDs-S/CB composite structure.

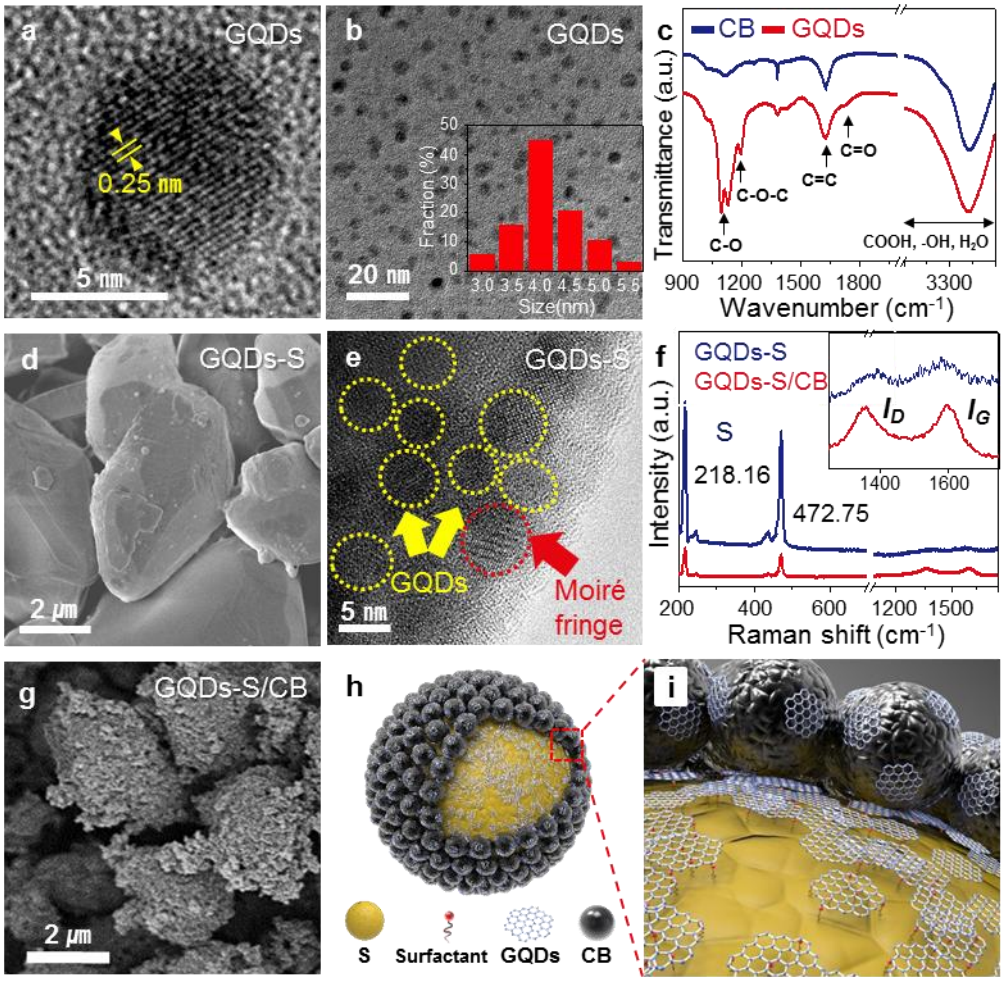

Fig. 4.1. (Color) Material characterization of GQDs-S/CB and S/CB composites. a,b, High-resolution TEM images of GQDs. The inset in Fig. 2b shows a histogram of the GQDs size distribution. c, FT-IR spectra of GQDs and CB. The peaks in this figure correspond to the various functional groups in the GQDs and CB. SEM images of d, GQDs-S, and g, GQDs-S/CB. e, HRTEM

images of the GQDs-S composites and GQD pattern (yellow circle). A Moiré pattern (red circle) is clearly visible in these TEM images, which is created by a superposition of the GQDs and S crystalline lattices , and f, Raman spectrum of GQDs-S composites, which shows that the GQDs are formed on the sulphur particles. The strong peaks at 218.16 and 472.75 cm^{-1} arise from sulphur, and the D (disorder) and G (graphitic) peaks arise from the GQDs. Schematic diagrams show the structure, h, and the magnified structure, i, of GQDs-S/CB.

4.3.2. Schemes of charge/discharge reaction dynamics

The schematic illustration in Fig. 4.2a depicts a conventional Li-S battery, where the anode is made of a metallic lithium, and the cathode is a composite of sulphur and CB. The structure of the cathode has a large impact on the irreversible loss of LiPSs into the electrolyte during battery operation. Herein, GQDs are introduced at the S/CB cathode, as shown in Fig. 4.2b. The GQDs contain both hydrophobic aromatic and hydrophilic defect regions, which can interact with CBs (ref. 20) and S_8, respectively. Scanning electron microscopy (SEM) images (Figs. 4.2c and 4-2d) confirm that the GQDs-S/CB composite electrodes are densely packed with CBs, which should increase electrochemical performance by highly preserving LiPSs in the geometric structure of GQDs-S/CB, while the surface of the sulphur particles are partially exposed in S/CB electrode. The exposure of S_8 to the electrolyte leads to the severe loss of electrochemically generated LiPSs followed by the degradation of the electrochemical performance.

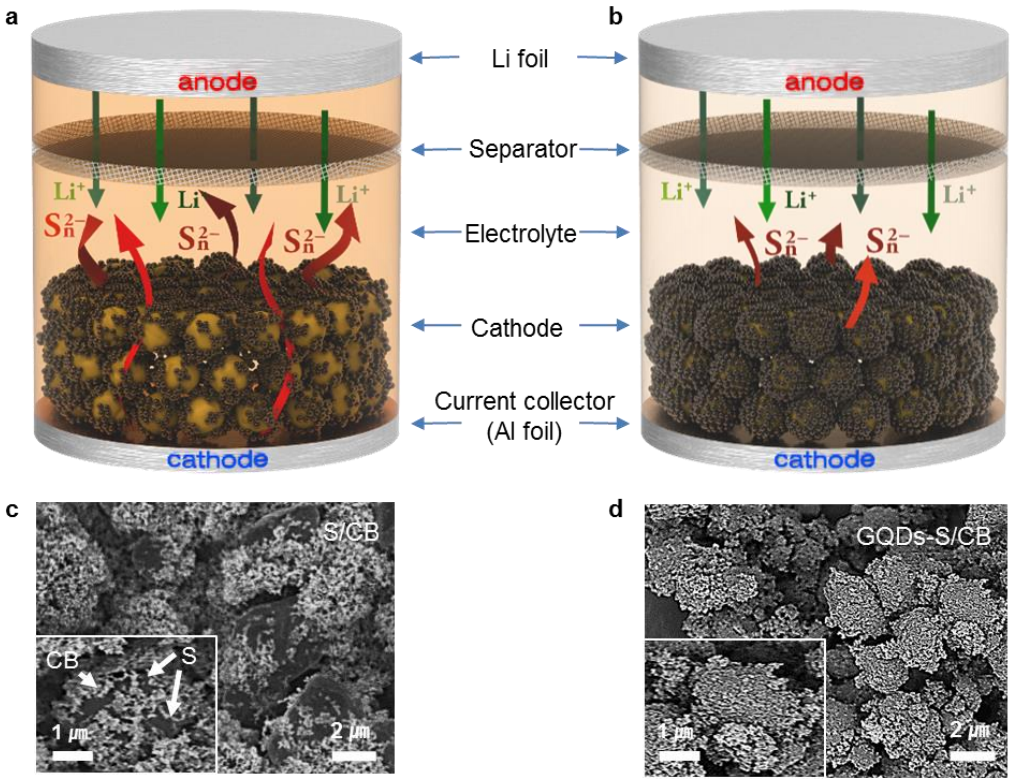

Fig. 4.2. (Color) Schematic diagrams and SEM images of S/CB and GQDs-S/CB in a Li-S battery. a,b, schematic configuration of S/CB and GQDs-S/CB employed as a cathode in a Li-S battery. The sulphur (yellow) is wrapped with carbon black (S/CB) and compactly covered with graphene quantum dots and carbon black (GQDs-S/CB). Polysulphides were dissolved into solvent and the color changed to orange. c,d, SEM images of GQDs-S/CB and S/CB.

4.3.3. Electrochemical analysis

The discharge profile in Fig. 4.3a illustrates a schematic model of possible reaction pathways that occur in a conventional Li-S battery. In the upper plateau region, elemental sulphur (S_8) is gradually reduced to the soluble sulphide anion (S_8^{2-}). Then, continuous reduction leads to the conversion of dissolved S_8^{2-} to S_n^{2-} (n = 6, 4)[32]. Since these high-order LiPSs (HO-LiPSs, (S_n^{2-}, n=8-4)) reactions are generated in the liquid electrolyte, the loss of active materials can occur simultaneously with this electrochemical reaction. The summation of the upper plateau and slope regions can be defined as the dissolution regime. Once the composition of S_4^{2-} is reached, low-order LiPSs (LO-LiPSs, (S_n^{2-}, n=2-1)) are converted to Li_2S through the reduction of S_4^{2-} (lower plateau region, defined as precipitation regime). Finally, Li_2S results from the complete reduction of S_8, which induces ~80% (compared to S_8) theoretical volume expansion. Representative points U_1, U_2, Q_1, and Q_2 are marked in the profile, where U_1 and U_2 indicate the onset reaction potentials of the dissolved and precipitated species, respectively, while Q_1 and Q_2 are the capacities corresponding to dissolution and precipitation regime, respectively. Q_1 is 419 mAh/g estimated from the reaction, S_8 (*s*) + $4Li^+ + 4e^- \leftrightarrow 2Li_2S_4$ (*l*). Meanwhile, Q_2 is 1,256 mAh/g which is achieved by the reduction of higher order to lower order polysulphides, $2Li_2S_4$ (*l*) + $12Li^+ \leftrightarrow 8Li_2S$ (*s*). Four parameters (U_1, U_2, Q_1, and Q_2) and the Q_2/Q_1 ratio (= 3) will be evaluated to understand the battery performance[32].

The cycling performance was tested at 0.5 *C*-rate (1 *C* = 1,675 mA/g assuming the reaction, $S_8 + 16Li^+ + 16e^- \leftrightarrow 8Li_2S$) in Fig. 3b. GQDs-S/CB composites exhibit superior cyclability and Coulombic efficiency compared to S/CB. A discharge capacity of ~1,000 mAh/g was achieved after 100 cycles while S/CB showed only 459.57 mAh/g. The capacity *vs*. voltage profiles at selected cycles are presented in Fig. 4.S6. The electrochemical properties of modified sulphur (surfactant coated sulphur) covered with CBs were also measured to study the effect of the surfactant on the electrochemical performance (Fig. 4.S5). Modified S/CB exhibits lower initial capacity but slightly better retention than S/CB because the surfactant on the surface of S partially protect the loss of HO-LiPSs (refs 15,20). Figure 4.3c presents the rate capabilities of GQDs-S/CB and S/CB from 0.1 *C* to 10 *C* (see Fig. 4.S7 for the capacity *vs*. voltage profiles at the different rate steps). The GQDs-S/CB shows excellent rate properties in comparison with S/CB. In Fig. 4.S8, a capacity of 540.17 mAh/g at 10 *C* was achieved (42% *vs*. capacity at *C*/10) in GQDs-S/CB. In contrast, only 120.35 mAh/g was achieved at 10 *C* (10% *vs*. that at *C*/10) in S/CB.

The onset potentials (U_1 and U_2) and capacities (Q_1 and Q_2) of GQDs-S/CB and S/CB are presented in Figs.4-3d-3g, which were derived from the capacity *vs*. voltage profiles (Figs. 4.S6 and 4-S7). These values are tabulated in Tables 4-S2-5. Firstly, these parameters are studied to analyse the electrochemical differences between GQDs-S/CB and S/CB. In the first cycle, U_1 of GQDs-S/CB is 2.33 V, which is slightly higher than that of S/CB, 2.31 V, owing to the lowered interface resistance. The better carbon

coverage in GQDs-S/CB leads to faster electron transfer kinetics (Fig. 4.3d). Electrochemical impedance spectroscopy (EIS) quantified the interfacial resistance, as shown in Fig. 4.S9. The radius of the smaller sized semi-circle (100 kHz – 1 Hz) is proportional to summation of the initial resistance and the charge transfer resistance (R_{int} + R_{ct}) based on the equivalent circuit in Fig 4-S9a (ref. 33). The U_2 value is also slightly higher in GQDs-S/CB, which indicates that HO-LiPSs are easily reduced to LO-LiPSs. After the first cycle, a slight increase of U_1 and U_2 was observed for both samples due to the decrease in overpotential resulting from the rearrangement of micron-sized sulphur[33]. U_1 and U_2 of both GQDs-S/CB and S/CB follow the same trend during 100 cycles which confirms that there is no significant change of onset potential after the first cycle.

In contrast, Q_1 and Q_2 show quite different behaviour as shown in Fig. 4.3e. For the first cycle, higher Q_1 and Q_2 are observed in GQDs-S/CB (Q_1 = 370.9 mAh/g and Q_2 = 853.24 mAh/g) compared to the S/CB (Q_1 = 354.86 mAh/g and Q_2 = 793.35 mAh/g) due to the enhanced electrical contact by the densely packed sulphur-carbon structure. However, the Q_2/Q_1 ratios are low in both GQDs-S/CB (Q_2/Q_1 = 2.30) and S/CB (Q_2/Q_1 = 2.24). Such low Q_2/Q_1 ratio for the first cycle can be attributed to the irreversible initial loss of HO-LiPSs, inefficient precipitation of LO-LiPSs, and electrolyte decomposition was followed by formation of solid electrolyte interphase (SEI). Q_1 and Q_2 values gradually decrease with extended cycling in S/CB. While the Q_1 values show relatively slow decay, severe fading of Q_2 is observed, which indicates the precipitation reaction is highly impeded by the loss of active sites. Whereas, the Q_1 and Q_2 values are maintained for

GQDs-S/CB even after 100 cycles through minimized loss of active species and preservation of active sites for facile reactions. The Q_2/Q_1 ratios in GQDs-S/CB are found to be 2.94 and 2.81, at the 10th cycle and the 100th cycle, respectively, which are close to the theoretical value (=3), while Q_2/Q_1 ratios of S/CB are 1.96 and 1.55, at the 10th and 100th cycle, respectively. Such high Q_2/Q_1 ratios strongly support that the redox reaction between S_8 and Li_2S can occur very reversibly owing to highly efficient electrode structure driven by GQDs. The GQDs can aid in capturing the PSs during the electrochemical reaction, which will be discussed in detail later. In addition, the EIS study, Fig. 4.S9 b,c, and associated discussion to support PSs capture by GQDs can be found in supplemental section.

The U_1 and U_2 values are also derived from the rate capability tests as shown in Fig. 4.3f. The GQDs-S/CB electrode shows slightly higher U_1 and U_2 values than S/CB at a relatively low rate (< 0.2 *C*). However, the U_1 and U_2 values of the S/CB electrodes significantly decrease at a rate above the 0.5 *C* rate while the U_1 and U_2 values of the GQDs-S/CB electrodes remain more stable. The higher U_1 and U_2 in GQDs-S/CB confirm that the GQDs increase the electrical conductivity of the material, whereby overpotentials that are required to initiate the dissolution (U_1) and precipitation (U_2) reactions are decreased. It should be noted that the tendency of U_1 and U_2 are similar because these values are related to the electrical contact of S_8 and HO-LiPSs, respectively. On the contrary, different behaviours are observed in Q_1 and Q_2, particularly, under the higher current density as shown in Fig. 4.3g. The reaction kinetics for formation of HO-

LiPSs is fast; thus, Q_1 is less affected by high current density[34]. However, a significant decrease is revealed in Q_2 at higher current density, which is attributed to the slow reduction due to the low electrical conductivity of LO-LiPSs or limited reaction sites. The Q_2/Q_1 ratios in S/CB are 2.36 and 1.27, at 0.1 *C* and 2 *C* rate, respectively, while higher Q_2/Q_1 ratios, 2.55 (at 0.1 *C*) and 1.75 (at 2 *C*), can be achieved in GQDs-S/CB. The larger Q_2/Q_1 ratio in GQDs-S/CB indicate superior capacity retention is available through the facile charge transfer and preserved reaction sites, which leads to faster reaction kinetics of LO-LiPSs (higher Q_2) as well as lower overpotential (higher U_1 and U_2).

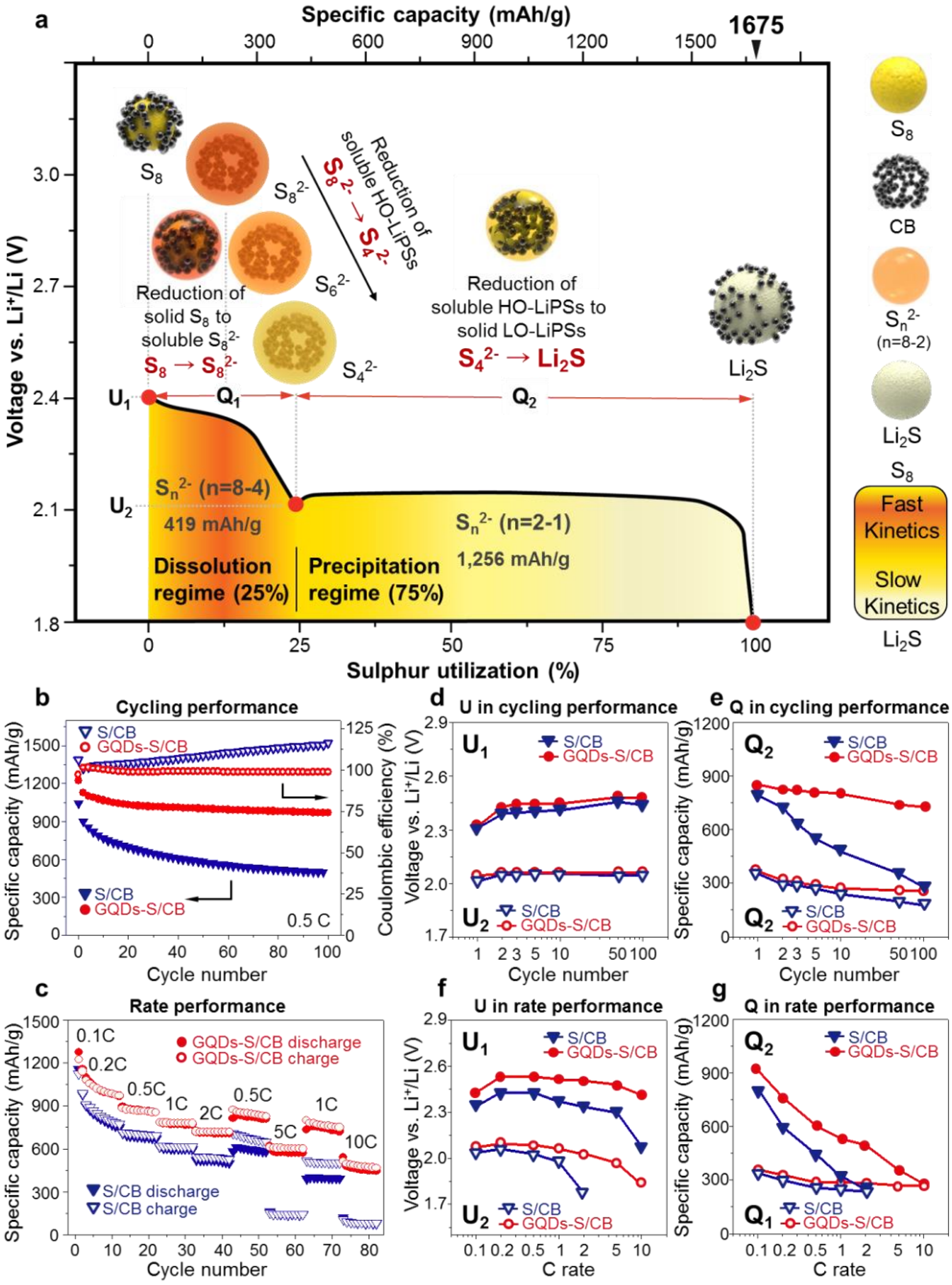

Fig. 4.3. (Color) Electrochemical properties of S/CB and GQDs-S/CB electrodes. a, Schematic illustration of the discharge profile of a conventional Li-S battery. High order-polysulphides (S_n^{2-}, n=8-4) and low order-polysulphides (S_n^{2-}, n=2-

1) are abbreviated as HO-PSs and LO-PSs. The onset potential (*U*) and the capacity (*Q*) in the dissolution and precipitation regime are noted, which facilitates the analysis of the electrochemical properties of each sample. b, Rate performance of the GQDs-S/CB and S/CB at 0.1 *C* to 10 *C*. c, cycling performance and Coulombic efficiency at 0.5 *C* of both samples for 100 cycles. d,f, Onset potential as a function of cycle number and e,g, capacity as a function of rate and capacity as a function of cycle number.

4.3.4. X-ray photoelectron spectroscopy (XPS) analysis

The chemical bonding states of S/CB and GQDs-S/CB electrodes were characterized by XPS (Fig. 4.4a-c). The C 1*s* spectra of the as-prepared electrodes (Fig. 4.4a) exhibit peaks at 283.8 eV and 284.5 eV attributed to sp^2 and sp^3 hybridized carbons[35], respectively, while the peak at 285.3 eV corresponds to C-S bonding[36]. The peak at 286.2 eV is assigned to C-OH bonding, which is more intense in the GQDs-S/CB than S/CB because the GQDs have a high density of OH surface functional groups. The two peaks that correspond to carbonyl and carboxyl groups are located at 287.0 eV and 289.0 eV, respectively. The C 1*s* spectra of the S/CB electrode obtained from the charged and discharged stages, after the 20th. cycle (Figs. 4.4b,c), shows slightly intensity loss and gain of the C-OH (286.27 eV) and C-S (285.26 eV) peaks. However, for the GQDs-S/CB electrode, the hydroxyl peak (286.2 eV) decreases noticeably while a C-S peak (285.4 eV) becomes prominent in both of the charged and discharged state. The change in the bonding nature can indicates that hydroxyl groups in the GQDs can facilitate the formation of C-S bonds during cycling. These C-S bonds can provide the reaction sites to fully reduce HO-LiPSs to LO-LiPSs, thus the Q_2/Q_1 ratio is stable at ~2.9 even after 100 cycles as shown in Fig. 4.S8. The C-F_2 peak at ~291.0 eV and C-F_3 peak at ~293.0 eV are originated from the binder (polyvinylidene fluoride, PVDF) and electrolyte salt (lithium bis(trifluoromethane)-sulfonimide , LiTFSI), respectively[37].

The S 2*p* spectra in Fig. 4.S10, collected after 20 cycles, also support the formation of C-S bonding discussed above. The C-S bonding peak (162.63 eV) in S 2*p* is assigned

to a lower binding energy than the S-S (164.0 eV) bonding[26], which has correlated with C-S bonding in C 1*s* peak. The intensity in the GQDs-S/CB electrode is higher than that in the S/CB. The S-S bonding peaks at ~164.0 eV are ascribed to the crystalline sulphur in the electrode[31]. The higher S-S peak intensity of GQDs-S/CB compared to S/CB indicates that more elemental sulphur is formed by adsorption of sulphur onto the GQDs. The adsorption processes prevents irreversible loss of the active material into the electrolyte by formation of nano-sized sulphur that is chemically favorable to bond to the GQDs as discussed later. The peaks at 167.0 eV and around 170.0 eV are attributed to sulphate, SO_2, from LiTFSI (ref. 37) and oxidized polysulphide species, SO_3, respectively.

The SEM images, Fig. 4.S11 and S12, of both anodes and cathodes after 20 cycles, respectively, were taken of GQDs-S/CB and S/CB electrodes. Due to the thick SEI layer formation, the SEM images of the cathodes, Fig. 4.S11, show flattened morphologies. Interestingly, homogenous surfaces can be observed in GQDs-S/CB, while, segregation of carbon is observed in the CB/S electrode. . This morphological difference is driven by the tightly packed structure of GQDs-S/CB during battery operation. A clean surface is observed on the GQDs-S/CB anode while the CB/S anode exhibits S and Li_2S particles on the surface (as confirmed by EDX and Raman spectroscopy as shown in Fig. 4.S12). These sulphur and LiPSs deposits result from the loss of active materials from the cathode side during repeated cycling.

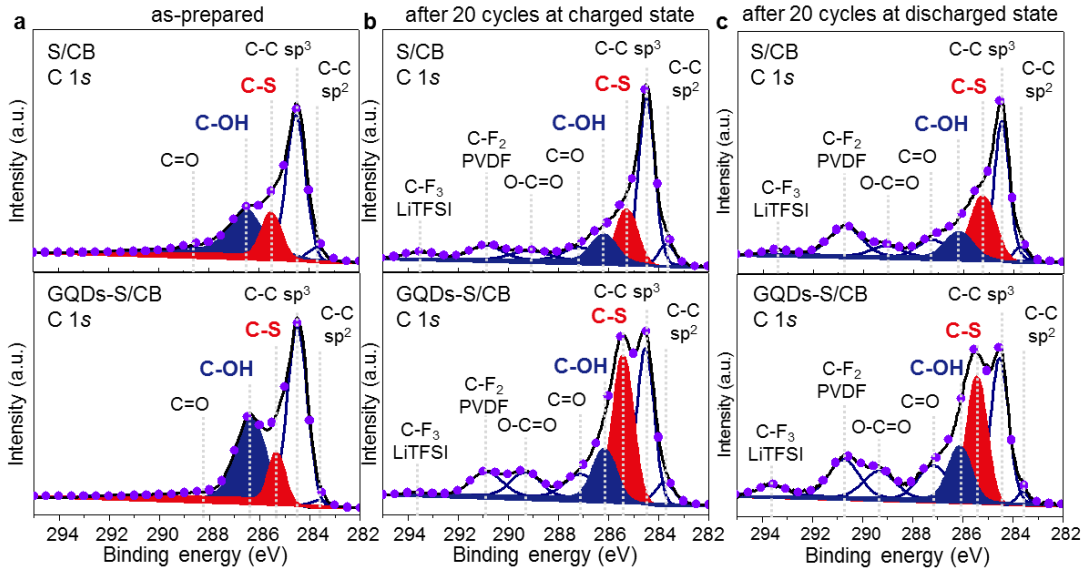

Fig. 4.4. (Color) High resolution C 1*s* X-ray photoemission spectroscopy (XPS) and computational calculations a, S and GQDs-S composites before cycling. C 1*s* high resolution spectra of the S/CB and GQDs-S/CB electrodes after 20 cycles at b, charged and c, discharged state. Each spectrum was fitted with functions corresponding to different valencies of carbon and sulphur (navy solid line) and the sum of those fitted curves (violet dots) is consistent with the raw data (black solid line).

4.3.5. The Modified surface reaction analysis

To further investigate the intrinsic surface interaction at the interface between GQDs and CB, GQDs/CB and CB electrodes without sulphur were prepared and electrochemically cycled in Li_2S_8 catholyte (Fig. 4.5a). The cycle retention of GQDs/CB is over 90% during 100 cycles while CB exhibits a capacity retention below 80% (Fig. 4.S13c). After cycling the GQDs/CB electrode, the C 1*s* and S 2*p* XPS spectra (Figs. 4.5a and 4-S13a,b) show higher S-S and C-S peaks compared with CB. Furthermore, Raman peaks for C-S aromatic bonding at 1,086 cm^{-1} and for C-S esteric bonds at 997 cm^{-1} are more intense for the GQDs/CB electrodes[38]. The carbon peaks at 1,590 cm^{-1} and 1,350 cm^{-1} are assigned to the G and D bands of carbon, respectively (Fig. 4.5b). XRD of the GQDs/CB electrodes also confirms nano-sized crystalline sulphur (Fig. 4.5c), which strongly supports that PSs are adsorbed on the oxygen functional groups of GQDs. DFT calculations were performed to clarify the formation of C-S bonding between the GQDs and sulphur species. The calculation is based on the following reaction:

$$\text{coronene\_OH} + S_n^{2-} \rightarrow (\text{coronene\_}S_n)^- + OH^- \qquad (n=1, 2, 4, 6, 8)$$

This model is used to represent the terminal edges of the GQDs (ref. 39), with one of the edges replaced by a hydroxyl group, "coronene_OH." A coronene is a polycyclic aromatic hydrocarbon comprising six peri-fused benzene rings with the chemical formula of $C_{24}H_{12}$. The relative energies calculated by DFT for the reactants and products indicate that replacing the terminal hydroxyl group by a sulphur dianion results in a lower energy state. The relative energies are shown in Fig. 4.S14a where it is clear that the energies of

the product decrease when sulphur dianions are replaced with the terminal hydroxyl group. The lower energy of the products (S_n^{2-}, n = 1, 2, 4, and 6) can provide a driving force for the reaction, thereby the formation of C-S bonds are favourable. However, the small sulphur dianions normally exist in the form of a solid crystal combined with lithium cations, such as Li_2S that cannot easily participate in C-S bonding[5]. In addition, sulphur dianions become unstable as the sulphur chain length is shortened due to the Coulombic repulsion. Meanwhile, large sulphur dianion chains (n>6) tend to disassemble into smaller chains[40]. Thus, it is speculated that the major participants in the reaction are S_2^{2-}, S_4^{2-} and S_6^{2-} ions. In addition, the same DFT calculation was performed for carboxyl group terminated coronene (coronene_COOH) (Fig. 4.S14b), showing similar results toacoronene_OH group. Our results highlight the crucial role in the formation of C-S bonds through terminal oxygen-functional groups present on the edge of GQDs.

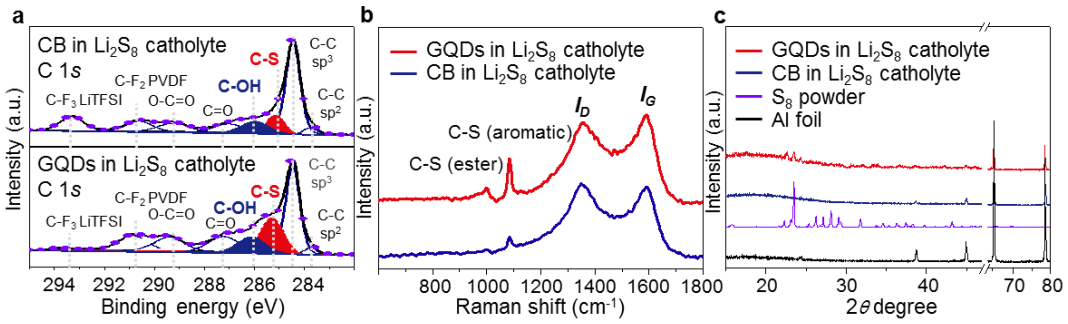

Fig. 4.5. (Color) XPS of the a, C 1*s* spectra of CB and GQDs/CB electrodes in Li_2S_8 catholyte. b, Raman spectra showing C-S bond formation within the samples. c, XRD spectra of GQDs/CB and CB electrodes in in a Li_2S_8 catholyte.

4.3.6. Nano-sized sulfur particle formation

TEM images were obtained from the GQDs/CB and CB electrodes after 20 (dis)charge cycles in Li_2S_8 catholyte. While only a small number of sulphur particles were observed on the CB electrode (Fig. 4.S15), many nano-sized sulphur particles can be observed on the GQD electrode in Figs. 4.6a-d. Nano-sized sulphur particles were covered with GQDs, which was confirmed by their lattice fringes corresponding to (111) planes. In addition, the indices of bright spots on the fast Fourier transform (FFT) image indicate sulphur is single crystalline and crystallizes in the orthorhombic structure of the alpha phase (JCPDS, No. 08-0247)[41]. The broad ring patterns in the FFT image indicate the presence of multiple GQDs with different orientations in Fig. 4.S16. The TEM-EELS and SEM-EDX analysis of the GQDs also indicates that nano-sized sulphur particles are adsorbed onto the GQDs (Figs. 4.S15 a-d,i-l). On the other hand, the CB electrode contains a low sulphur density (Figs. 4.S15 e-h,m-p) This observation implies that the oxygen functional groups in the GQDs induce preferred nucleation of sulphur onto the GQDs. Thus, sulphur can easily be adsorbed/desorbed on the GQDs as predicted by the aforementioned DFT calculation.

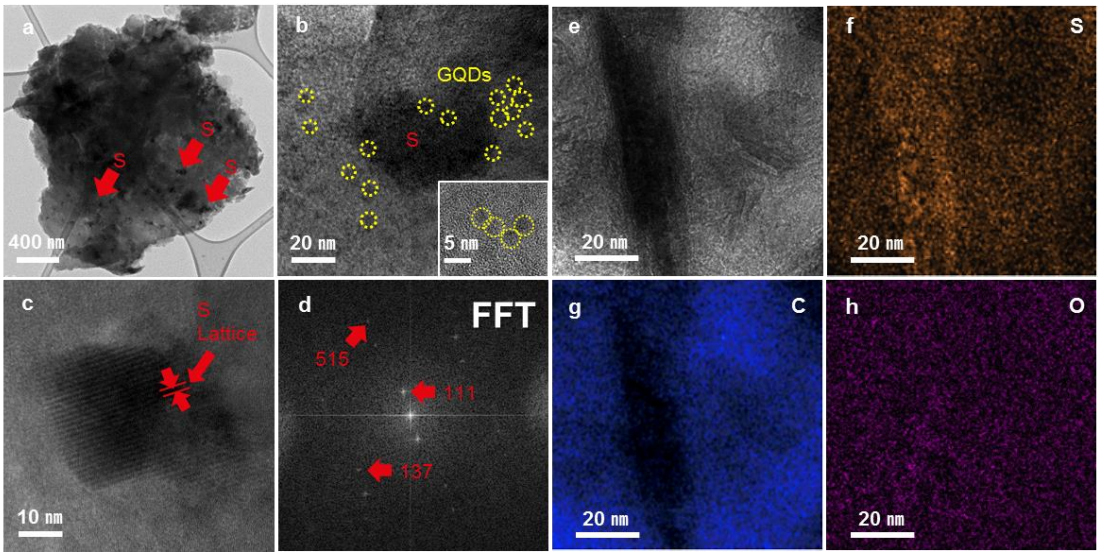

Fig. 4.6. (Color) TEM and STEM images of nano-sized sulphur on GQDs electrode in Li_2S_8 catholyte after 20 cycles. a, The low and high magnification of nano-sized sulphur in GQDs materials. The lump shows GQDs electrode with nano-sized sulphur and the small dark particles indicate the nano-sized sulphur. b, GQDs covered on nano-sized sulphur particle, c, HRTEM image shows the lattice fringes of the nano-sized sulphur and the GQDs. d, The FFT of the original HRTEM image is c in the center of the filtered image. The two bright spots represent sulphur particles and the other spot indicates GQDs lattice plane. e, STEM image of GQDs electrode in the catholyte after cycling. f-h, Electron energy loss spectroscopy maps of S, C, and O in the GQDs electrode.

4.4. Conclusions

we have designed GQDs-S/CB composites as a high-performance cathode material for Li-S batteries. The nano-sized GQDs induce a tightly packed structure via charge interaction with S and CB, which results in enhanced conductivity by shortened electron conduction paths. Furthermore, C-S bonding is generated in-situ during the operation of the battery, which originates from the high functional-edge density of the GQDs. Thus, loss of active materials into the electrolyte is minimized. The adsorption of nano-sized sulphur particles onto the GQD interfaces by C-S bonding was confirmed by TEM, and further supported by XPS and Raman analysis and DFT calculations. The GQDs-S/CB composites significantly improve cycling and rate performances, with high reversible capacities at both high and low current density. This excellent cycling behavior was demonstrated through the analysis of discharge profiles. We believe that our results provide a new avenue for material scientists to tailor oxygen-rich functional groups of nano-sized carbon for the application in various batteries.

4.5. Supporting informations

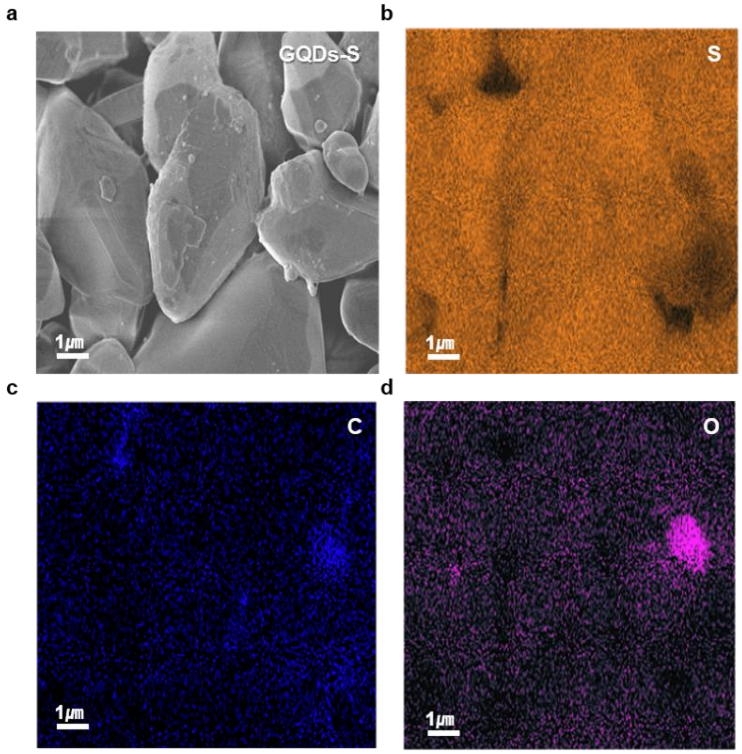

Fig. 4.S1. (Color) Scanning electron microscopy and energy-dispersive X-ray spectroscopy characterization of the GQDs-S composites. SEM images of the GQS-S composites, and C, S, and O EDX maps of the GQDs-S composites.

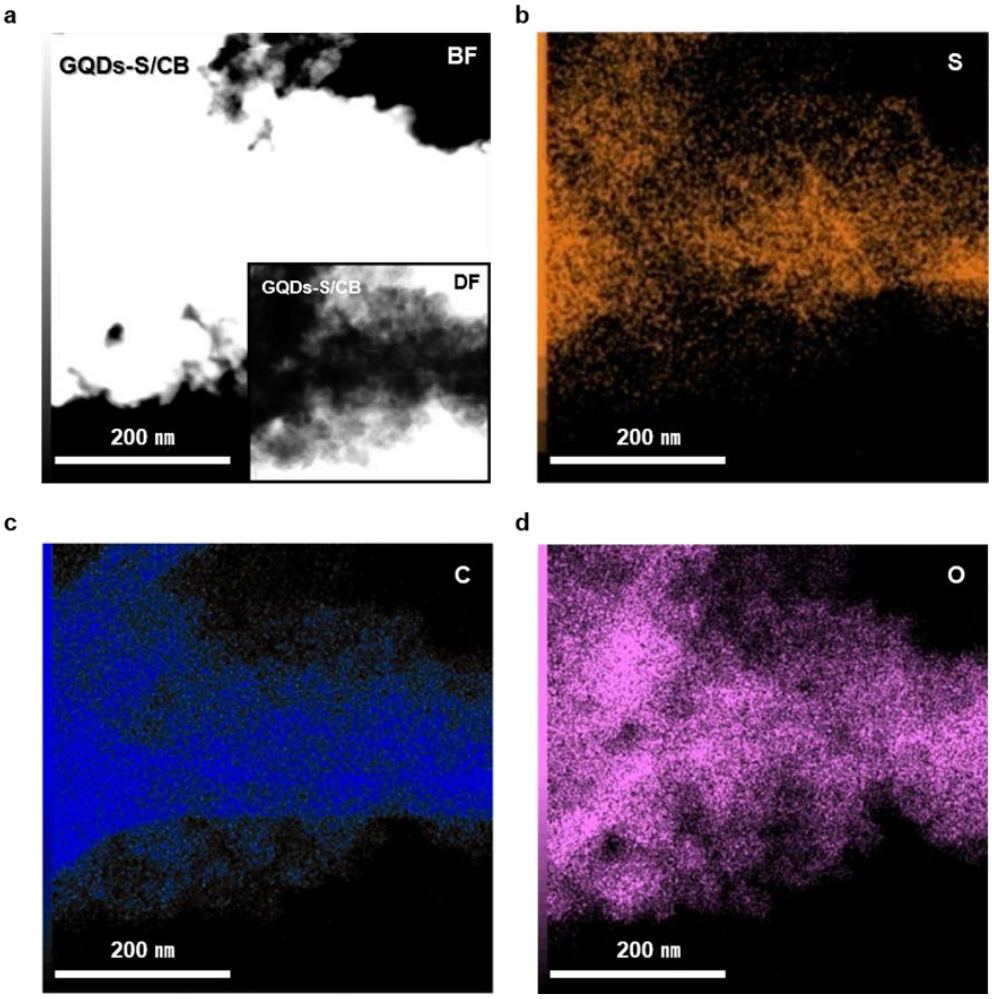

Fig. 4.S2. (Color) Scanning transmission electron microscopy and EDX characterization of the GQDs-S/CB composites. TEM images of the GQS-S/CB composites, and C, S, and O EDX maps of the GQDs-S/CB composites.

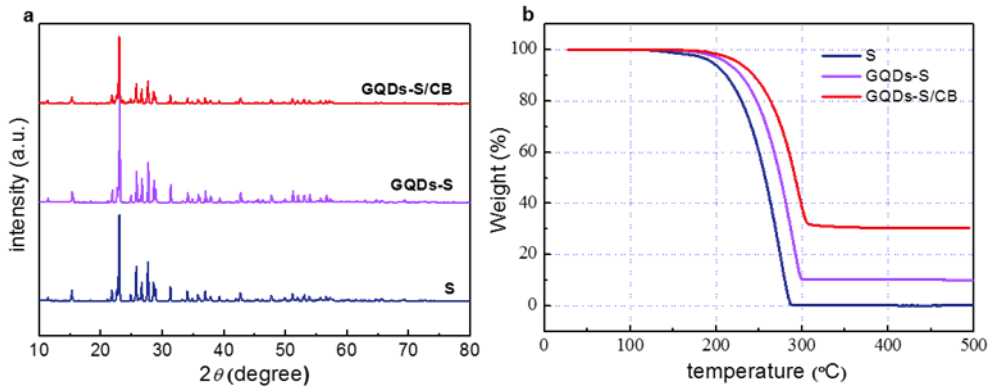

Fig. 4.S3. (Color) X-ray diffraction (XRD) patterns and Thermogravimetric analysis (TGA). XRD of sulphur, GQDs-S, and GQDs-S/CB composites **a**, and TGA collected in N_2 atmosphere with a heating rate of 10℃/min **b**, the S content of the cathode.

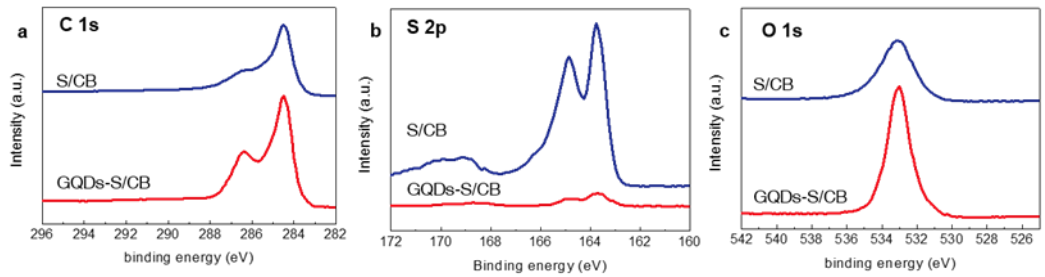

Fig. 4.S4. (Color) X-ray photoelectron spectroscopy of S/CB, and GQDs-S/CB particles. a, C 1*s* peaks, **b,** S 2*p* peaks, and **c,** O 1*s* peaks of S/CB and GQDs-S/CB particles.

Table S1 | Summary of XPS quantitative values of each elements in Figure S4

At. %	C 1*s*	S 2*p*	O 1*s*
S/CB	73.91	12.38	13.70
GQDs-S/CB	83.45	0.64	15.91

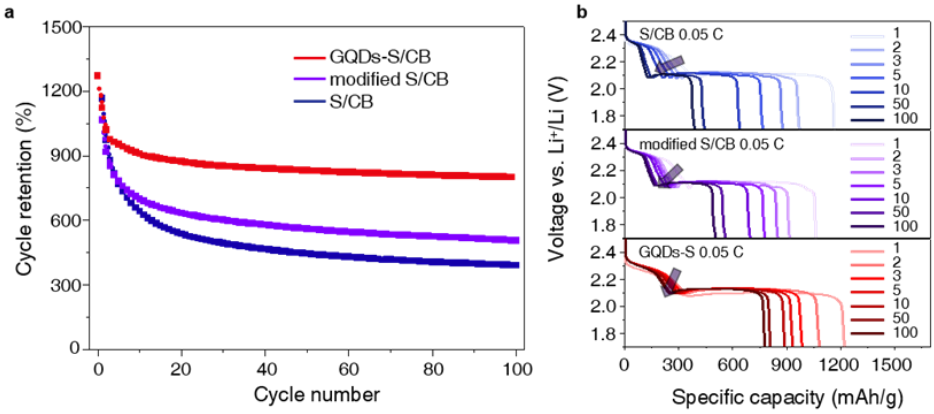

Fig. 4.S5. (Color) a, Cycling performance and b, discharge profile of GQDs-S/CB, modified S/CB, and S/CB at 0.05 *C* for 100 cycles. The GQDs-S/CB electrode shows superior cycle retention compared to S/CB and modified S/CB, which indicates that the surfactant alone does not prevent dissolution of the sulphide discharge-products into the electrolyte.

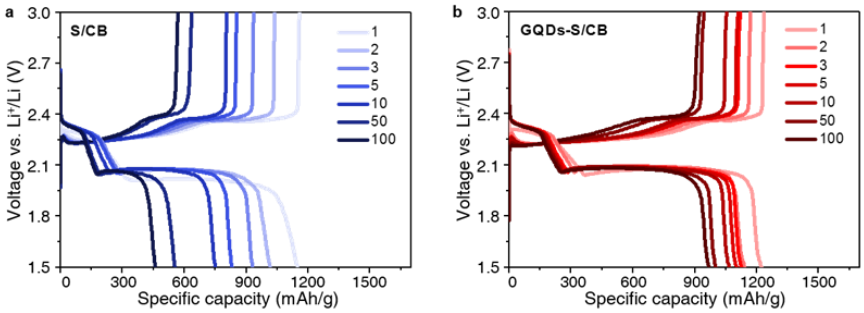

Fig. 4.S6. (Color) Charge-discharge profiles of **a,** S/CB and **b,** GQDs-S/CB at 0.5 *C* for 100 cycles.

Table S2 | Summary of numerical values of each component (U_1,U_2, Q_1, Q_2, and Q_{total}) with selected cycles for S/CB at 0.5 *C*

Cycle number	U_1(V)	U_2(V)	Q_1(mAh/g)	Q_2(mAh/g)	Q_{total}(mAh/g)
1	2.31	2.01	354.86	793.35	1148.21
2	2.39	2.05	295.57	726.53	1022.10
3	2.39	2.05	289.60	635.50	925.10
5	2.38	2.05	280.88	550.37	831.25
10	2.39	2.05	240.52	479.98	720.50
50	2.39	2.05	199.04	355.11	554.15
100	2.39	2.05	180.21	279.36	459.57

Table S3 | Summary of numerical values of each component (U_1,U_2, Q_1, Q_2, and Q_{total}) with selected cycles for GQDs-S/CB at 0.5 *C*

Cycle number	U_1(V)	U_2(V)	Q_1(mAh/g)	Q_2(mAh/g)	Q_{total}(mAh/g)
1	2.33	2.04	370.90	853.24	1224.14
2	2.42	2.06	317.78	825.39	1143.17
3	2.42	2.06	304.93	819.39	1124.32
5	2.42	2.06	291.70	811.01	1102.71
10	2.42	2.06	273.24	803.66	1076.90
50	2.42	2.06	260.21	741.70	1001.91
100	2.42	2.06	259.43	728.81	988.24

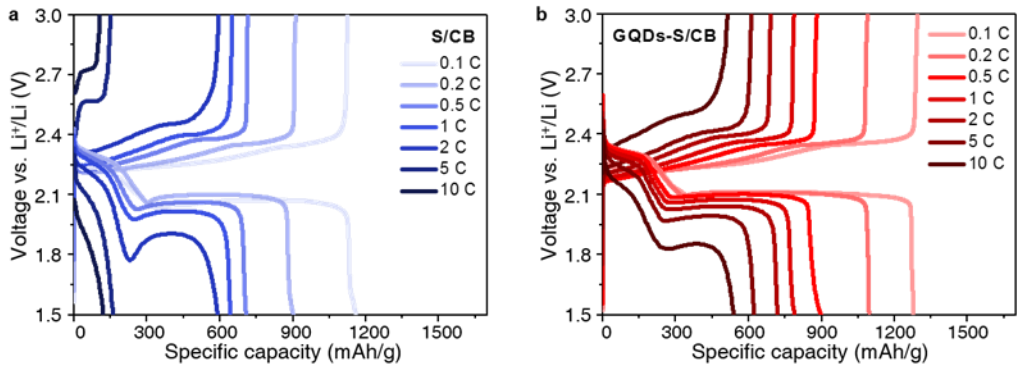

Fig. 4.S7. (Color) Rate performance of a, S/CB and **b,** GQDs-S/CB from 0.1 *C* up to 10 *C*.

Table S4 | Summary of numerical values of each component (U_1,U_2, Q_1, Q_2, and Q_{total}) with various C-rates for S/CB

1 C-rate (1672 mA/g)	U_1(V)	U_2(V)	Q_1(mAh/g)	Q_2(mAh/g)	Q_{total}(mAh/g)
0.1 C-rate	2.34	2.03	344.52	813.52	1158.04
0.2 C-rate	2.43	2.06	300.92	599.87	900.78
0.5 C-rate	2.43	2.03	260.48	447.41	707.95
1.0 C-rate	2.37	1.98	248.95	364.80	613.75
2.0 C-rate	2.33	1.78	229.90	291.41	521.32
5.0 C-rate	2.30	-	160.26≥	-	160.26
10.0 C-rate	2.07	-	120.35≥	-	120.35

Table S5 | Summary of numerical values of each component (U_1,U_2, Q_1, Q_2, and Q_{total}) with various C-rates for GQDs-S/CB

1 C-rate (1672 mA/g)	U_1(V)	U_2(V)	Q_1(mAh/g)	Q_2(mAh/g)	Q_{total}(mAh/g)
0.1 C-rate	2.43	2.07	359.35	917.54	1276.89
0.2 C-rate	2.53	2.09	330.95	764.67	1095.62
0.5 C-rate	2.53	2.09	289.73	606.46	896.19
1.0 C-rate	2.52	2.06	292.58	533.39	825.97
2.0 C-rate	2.51	2.03	285.02	499.82	784.84
5.0 C-rate	2.48	1.97	261.70	359.77	621.46
10.0 C-rate	2.41	1.83	259.28	280.89	540.17

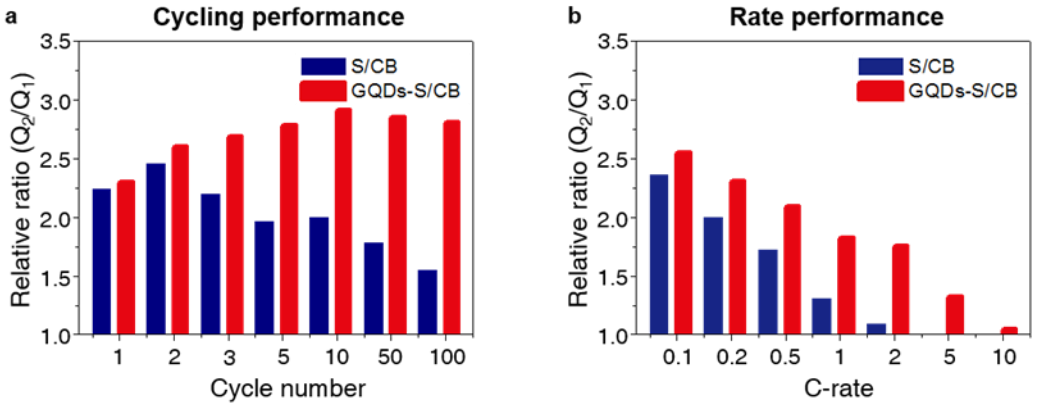

Fig. 4.S8. (Color) Relative ratios of dissolution/precipitation regime capacity (Q_2/Q_1). a, Cycling performance up to 100 cycles. **b,** Rate performance from 0.1 *C* to 10 *C*.

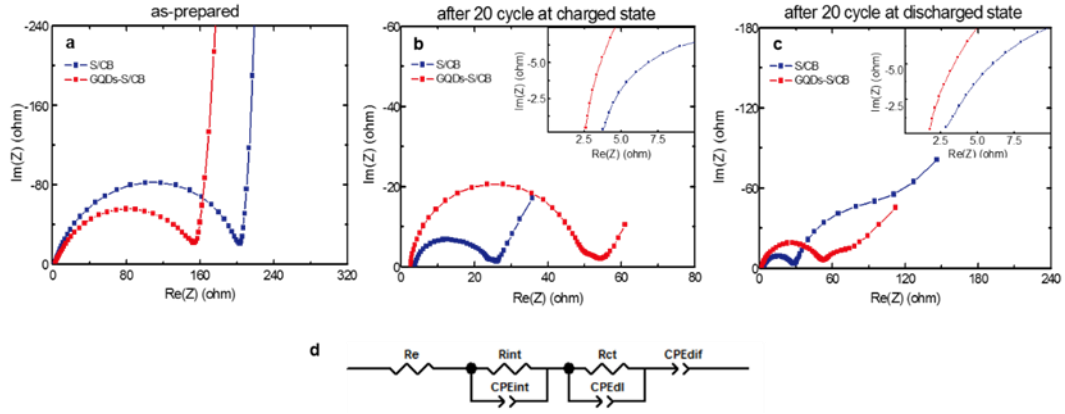

Fig. 4.S9. (Color) Electrochemical impedance spectroscopy (EIS). Lithium/sulphur cells **a,** as-prepared, **b,** fully charged, and **c,** discharged state after 20 cycles. Insets show the high-frequency range. The equivalent circuit model used to analyze the Nyquist plots **d,** charge-discharge states.

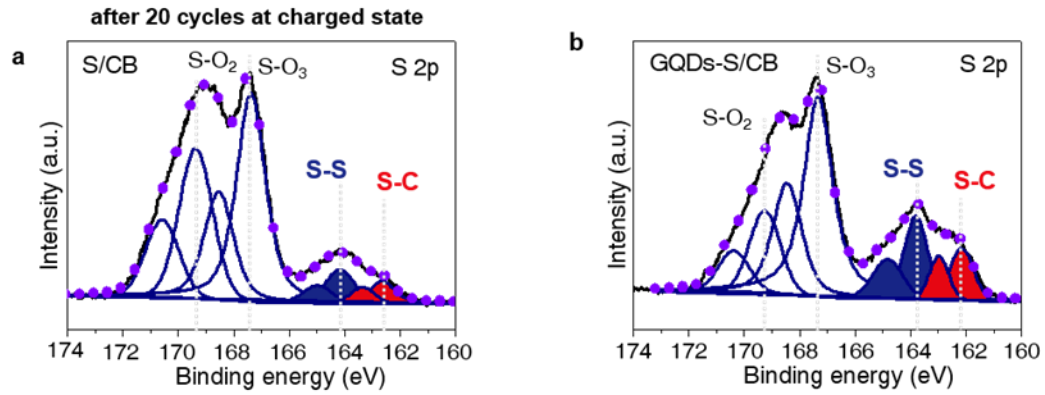

Fig. 4.S10. (Color) High resolution C 1*s* X-ray photoelectron spectroscopy a,b, C 1*s* spectrum of the S/CB and GQDs-S/CB electrodes after 20 cycles in the discharged state. Each spectrum has been fitted with peaks for different bonded carbon (navy line) and the sum of the fitting curves (violet dots) is consistent with the raw data (black solid line).

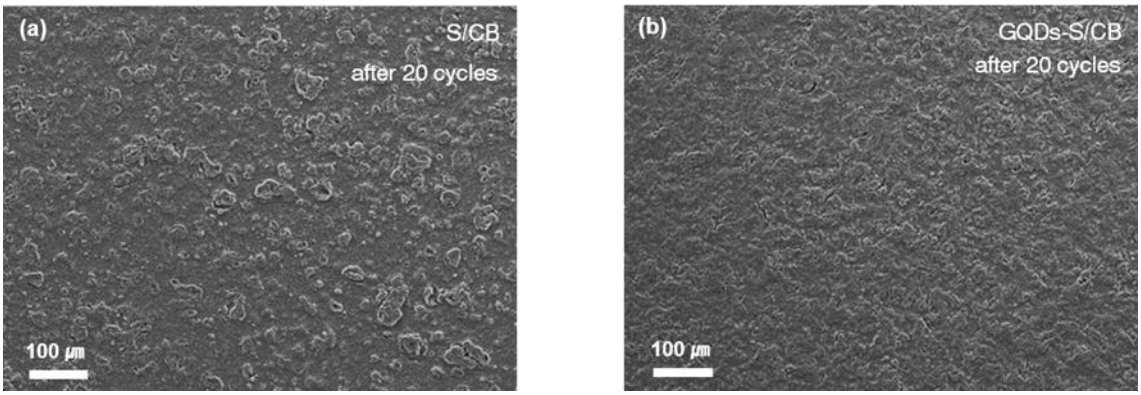

Fig. 4.S11. (Color) SEM images of GQDs-S/CB and S/CB cathode electrodes after electrochemical cycling. a,b, GQDs-S and S electrodes after cycling.

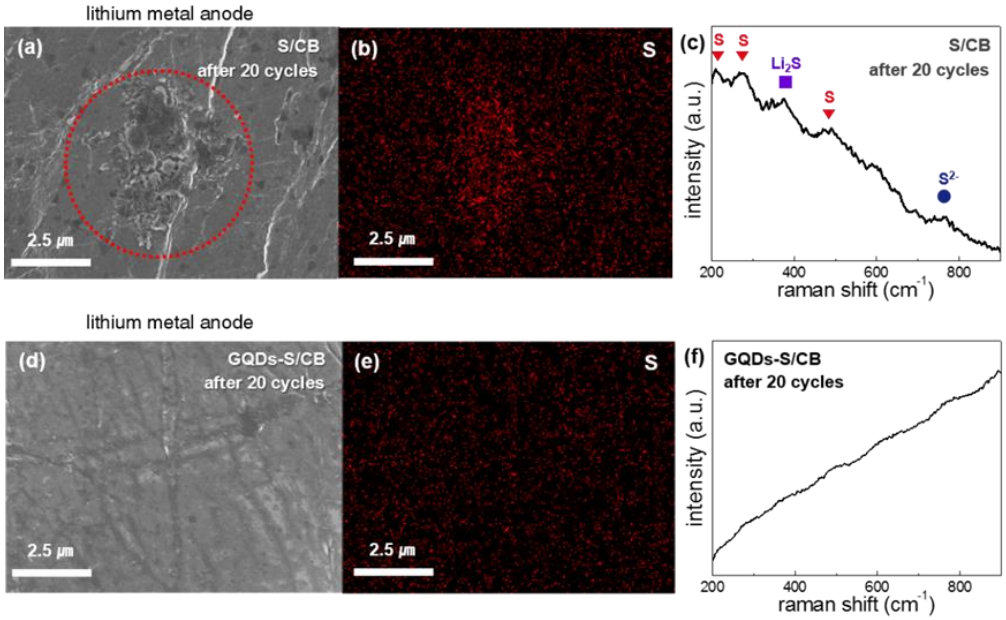

Fig. 4.S12. (Color) SEM images and Raman spectra of lithium anodes after cycling against S/CB and GQDs-S/CB electrodes. a,d, SEM images after 20 cycles. b,e, Sulphur energy-dispersive X-ray spectroscopy maps. c,f, Raman spectra. The S peaks are assigned to 156, 221, 473 cm^{-1}, Li_2S to 378 cm^{-1}, and S^{2-} to 746 cm^{-1} (ref. 2). No peaks are present in the cell containing GQDs-S/CB.

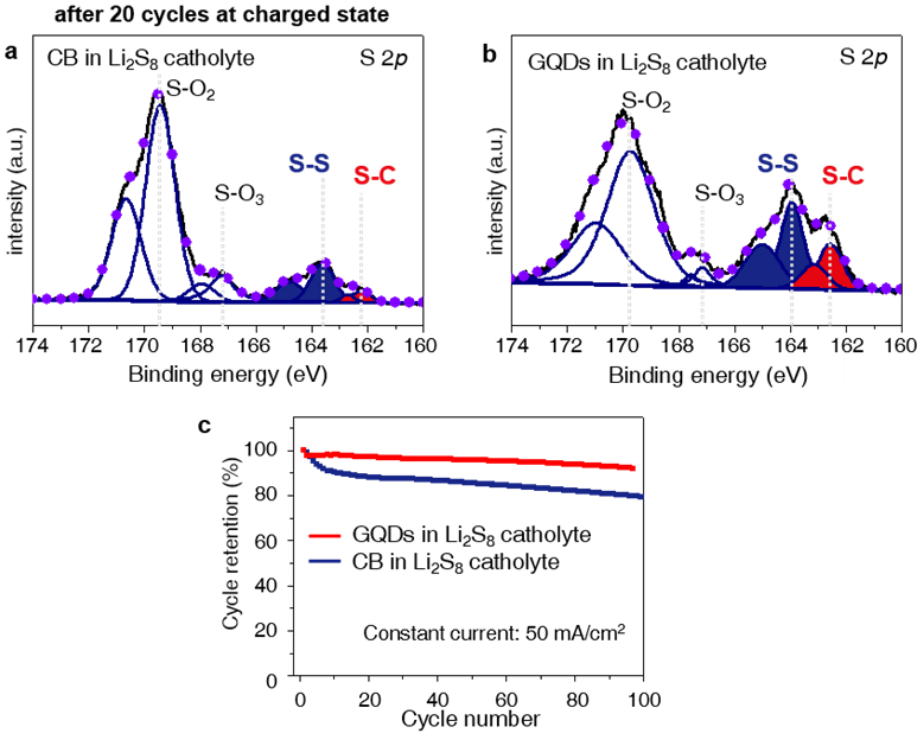

Fig. 4.S13. (Color) High resolution S 2*p* X-ray photoelectron spectroscopy and cycle performance. a,b**,** S 2*p* spectrum of the CB and GQDs electrodes, in the charge state, after 20 cycles. These electrodes were cycled in the Li_2S_8 catholyte. Each spectrum was fitted with functions corresponding to different valencies of sulphur (navy line) and the sum of these fitted curves (violet dots) is consistent with the raw data (black solid line). **c,** Cycle retention of GQDs/CB and CB electrodes in Li_2S_8 catholyte over 100 cycles.

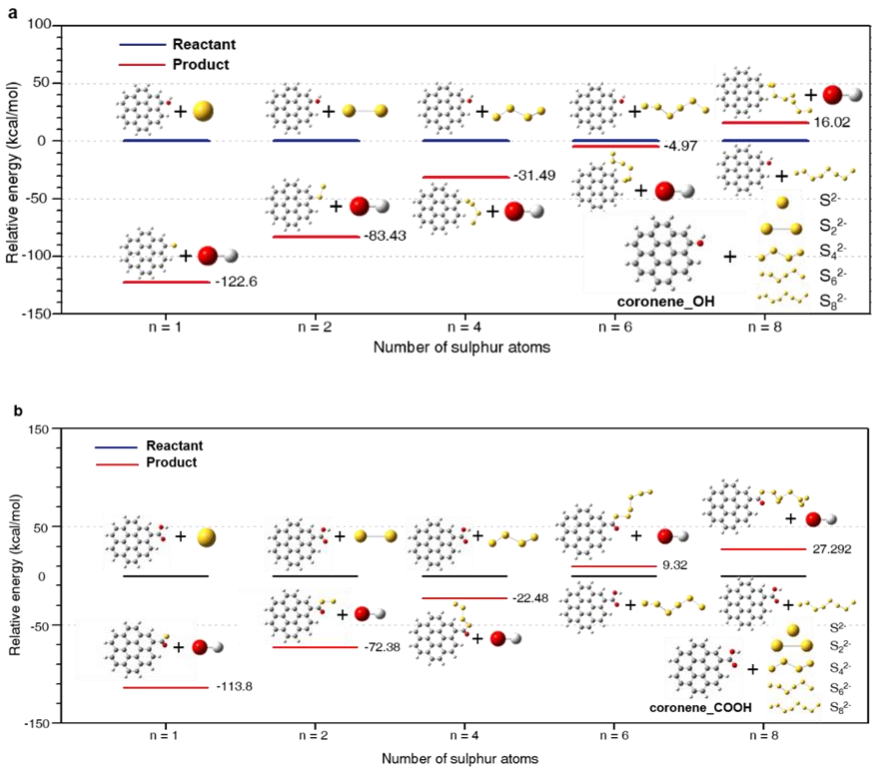

Fig. 4.S14. (Color) The relative energies for the reactant and product in binding of polysulphides to GQDs. A plot of the relative energies for the reactant and product in binding of polysulphides to GQDs, versus the sulphur chain length. The functional groups on GQDs enhance the binding of polysulphides to the carbon due to the substitution of **a**, –OH (C-OH) to S_n^{2-} and **b**, –OH (C-COOH) for S_n^{2-}. Yellow, red, white, and gray represents S, O, H, and C atoms, respectively.

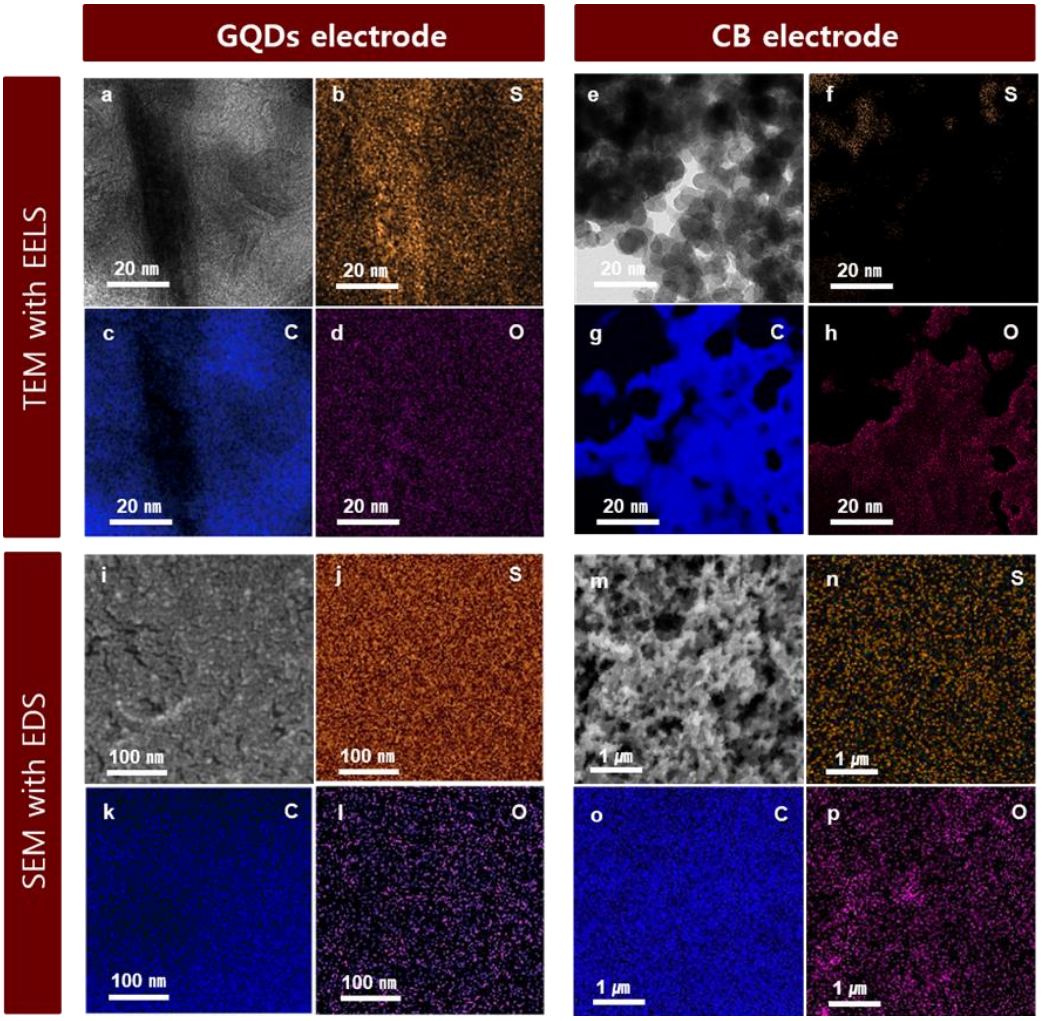

Fig. 4.S15. (Color) TEM and SEM images with EELS and EDX on the GQDs and the CB electrodes in Li_2S_8 catholyte after 20 cycles. a,e Bright field STEM images of the GQDs and CB electrodes. b-d,f-h, Electron energy loss spectroscopy maps of C, S, and O of the GQDs and CB electrode in the Li_2S_8 catholyte. i,m, SEM images of the GQDs and CB electrodes in the Li_2S_8 catholyte after cycling. j-l,n-p, C, S, and O EDX maps of the GQDs and CB electrodes.

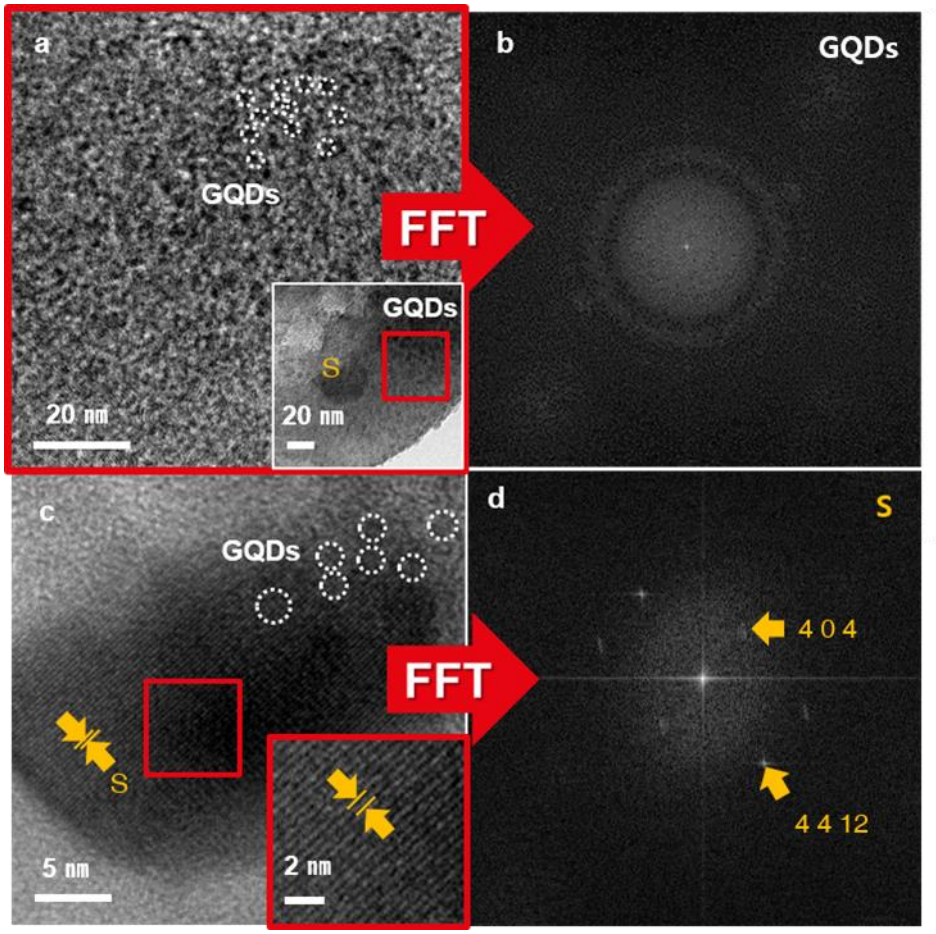

Fig. 4.S16. (Color) HRTEM (high-resolution transmission electron microscopy) images of nano-sized sulphur on GQDs electrode in Li_2S_8 catholyte after 20 cycles. a, TEM image of nano-sized sulphur in the GQD electrode. b, The FFT of the selected region in image, a. The ring pattern of graphene quantum dots. c, Magnification of nano-sized sulphur in image a shows the lattice fringes of sulphur and GQDs. d, The FFT of the selected area in image, c.

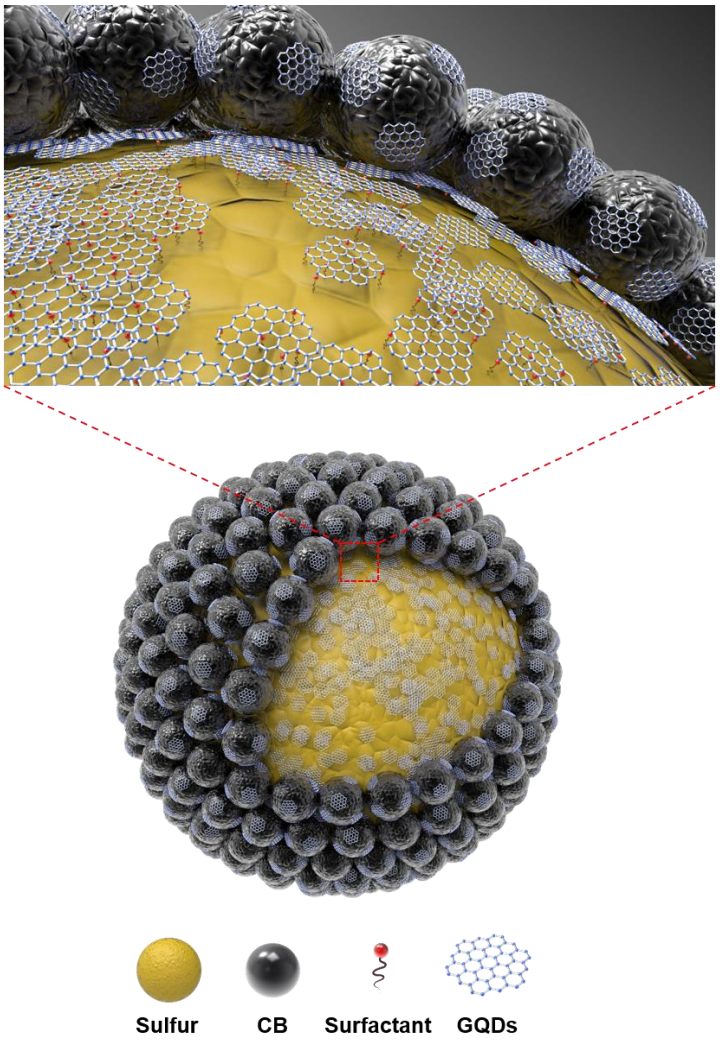

Appendix 4-S1. (Color) Scheme of core-shell structure of GQDs-S/CB particle

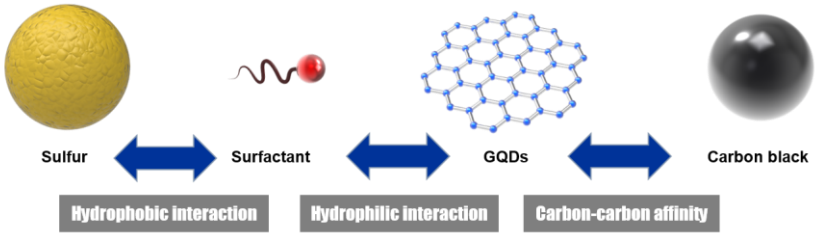

Appendix 4-S2. (Color) Scheme of surface interaction of core-shell structure of GQDs-S/CB particle

4.6. References

1. Armand, M. and Tarascon J. -M., "Building better batteries", *Nature* **451**, 652-657 (2008).
2. Goodenough, J. B., Park, K. -S., "The Li-ion rechargeable battery: a perspective", *J. Am. Chem. Soc.* **135**, 1167-1176 (2013).
3. Marom, R., et al., "A review of advanced and practical lithium battery materials", *J. Mater. Chem.* **21**, 9938-9954 (2011).
4. Cabana, J., et al., "Beyond intercalation-based Li-ion batteries: the state of the art and challenges of electrode materials reacting through conversion reactions", *Adv. Mater.* **22**, E170-E192 (2010).
5. Manthiram, A., Fu, Y. and Su, Y.-S., "Challenges and prospects of lithium-sulphur batteries", *Acc. Chem. Res.* **46**, 1125-1134 (2013).
6. Chung, W. J., Griebel, J. J., et al., "The use of elemental sulfur as an alternative feedstock for polymeric materials", *Nat. Chem.* **5**, 518-524 (2013).
7. Bruce, P. G., Freunberger, S. A., Hardwick, L. J., Tarascon, J. -M., "Li-O2 and Li-S batteries with high energy storage", *Nat. Mater.* **11**, 19-29 (2012).
8. Choi, N. -S., et al., "Challenges facing lithium batteries and electrical double-layer capacitors capacitors", *Angew. Chem. Int. Ed.* **51**, 9994-10024 (2012).
9. Simmonds, A. G., Griebel, J. J., Park, J., et al., "Inverse vulcanization of elemental sulfur to prepare polymeric electrode materials for Li-S batteries", *ACS Macro Lett*. **3**, 229-232 (2014).
10. Mikhaylik, Y. V., Akridge, J. R., "Polysulfide shuttle study in the Li/S battery system",

J. Electrochem. Soc. **151**, A1969-A1976 (2004).

11. Elazari, R., Salitra, G., Garsuch, A., Panchenko, A., Aurbach, D., "Sulphur-impregnated activated carbon fiber cloth as a binder-free cathode for rechargeable Li-S batteries", *Adv. Mater.* **23**, 5641-5644 (2011).
12. Su, Y. and Manthiram, A., "Lithium-sulphur batteries with a microporous carbon paper as a bifunctional interlayer", *Nat. Comm.* **3** 1166-1171 (2012).
13. Zhang, C., et al., "Confining sulfur in double-shelled hollow carbon spheres for lithium-sulfur batteries", *Angew. Chem. Int. Ed.* **51**, 9592-9595 (2012).
14. Zhou, G. and et al., "A graphene-pure sulfur sandwich structure for ultrafast long-life lithium-sulfur batteries", *Adv. Mater.* **26**, 625-631 (2014).
15. Ji, X., Lee, K. T., and Nazar, L. F., "A Highly ordered nanostructured carbon-sulphur cathode for lithium-sulphur batteries", *Nat. Mater.* **8**, 500-506 (2009).
16. Xin, S. et al., "Smaller sulphur molecules promise better lithium-sulphur batteries", *J. Am. Chem. Soc.* **134**, 18510-18513 (2012).
17. Schuster, J., He, G. et al., "Spherical ordered mesoporous carbon nanoparticle with high porosity for lithium-sulphur batteries", *Angew. Chem. Int. Ed.* **51**, 3591-3595 (2012).
18. Ji, L., Aloni, S., Wang, L., Cairns, E. J., Zhang, U., "Porous carbon nanofiber-sulphur composite electrodes for lithium/sulphur cells", *Energy Environ. Sci.* **4**, 5053-5059 (2011).
19. Guo, J., Xu, Y., and Wang, C., "sulphur-impregnated disordered carbon nanotubes cathode for lithium sulphur batteries", *Nano Lett.* **11**, 4288-4294 (2011).

20. Wang, H. et al., “Graphene–wrapped sulphur particles as a rechargeable lithium-sulphur battery cathode material with high capacity and cycling stability”, *Nano Lett.* **11**, 2644-2647 (2011).
21. Ji, L., Rao, M. et al., “Graphene oxide as a sulphur immobilizer in high performance lithium/sulphur cells”, *J. Am. Chem. Soc.* **133**, 18522-18525 (2011).
22. Zu, C., Manthiram, A., “Hydroxylated graphene-sulphur nanocomposites for high-rate lithium-sulphur batteries”, *Adv. Energy Mater.* **3**, 1008-1012 (2013).
23. Evers, S., Nazar, L. F., “Graphene-enveloped sulphur in a one pot reaction: a cathode with good coulombic efficiency and high practical sulphur content”, *Chem. Commun.* **48**, 1233-1235 (2012).
24. Fu, Y. and Manthiram, A., “Orthorhombic bipyramidal sulphur coated with polypyrrole nanolayers as a cathode material for lithium-sulfur batteries”, *J. Phsy. Chem. C* **116**, 8910-8915 (2012).
25. Peng, J. et al., “Graphene quantum dots derived from carbon fibers”, *Nano Lett.* **12**, 844-846 (2012).
26. Ritter, K. A., Lyding, J. W., “The influence of edge structure on the electronic properties of graphene quantum dots and nanoribbons”, *Nat. Mater.* **8**, 235-242 (2009).
27. Pan, D., Zhang, J., Li, Z., Wu, M., “Hydrothermal route for cutting graphene sheets into blue-luminescent graphene quantum dots”, *Adv. Mater.* **22**, 734-738, (2010).
28. Acik, M., Lee, G., Mattevi, C, Pirkle, A., Wallace, R. M., et al., “The role of oxygen during thermal reduction of graphene oxide studied by infrared absorption

spectroscopy", *J. Phys. Chem. C* **115**, 19761-19781 (2011).

29. Gokus, T., Nair, R. R., Bonetti, A., Bohmler, M., Lombardo, A., Noboselov, et al., "Making graphene luminescent by oxygen plasma treatment", *ACS Nano* **3**, 3963-3968 (2009).
30. Yeon, J., Jang, J. et al., "Raman spectroscopy and X-ray diffraction studies of sulphur composite electrodes during discharge and charge", *J. Electrochem. Soc.* **159**, A1308-A1314 (2012)
31. John F. Moulder, William F. Stickle, Peter E. Sobol, Kenneth D. Bomben. Handbook of X-ray photoelectron spectroscopy (Physical Electronics, Inc., 1995).
32. Su, Y.-S., Fu, Y., Cochell, T., and Manthiram, A., "A strategic approach to recharging lithium-sulphur batteries for long cycle life", *Nat. Comm.* **4**, 2985-2992 (2013).
33. Deng, Z., Zhang, Z. et al., "Electrochemical impedance spectroscopy study of a lithium/sulphur battery: modelling and analysis of capacity fading", *J. Electrochem. Soc*. **4**, A553-A558 (2013)
34. Bruckner, J., Soren T. et al., "Lithium sulphur batteries: influence of C-rate, amount of electrolyte and sulphur loading on cycle performance", *J. Power Sources* **268**, 82-87 (2014).
35. S. Kaciulis Spectroscopy of carbon: from diamond to nitride films. *Surf. Interface Anal.* **44**, 1155-1161 (2012).
36. Kummer, K., Vyalikh, D. V., "High-resolution photoelectron spectroscopy of self-assembled mercaptohexanol monolayers on gold surfaces", *J. Electron. Spectrosc. Relat. Phenom.* **163**, 59-64 (2008).

37. Juhye Song, Sung Jun Lee et al., “Thermal reactions of lithiated and delithiated sulphur electrodes in lithium-sulfur batteries”, *ECS Electrochem. Lett.* **3** (4) A26-A29 (2014).

38. Socrates, G. Infrared and Raman characteristic group frequencies tables and charts: Sulphur and Selenium compounds Ch.16 (John Wiley & Sons Ltd, Third edition, 2001).

39. Song, J., Xu. T. et al., “Nitrogen-doped mesoporous carbon promoted chemical adsorption of sulphur and fabrication of high-areal-capacity sulphur cathode with exceptional cycling stability for lithium-sulphur batteries”, *Adv. Funct. Mater.* **24**, 1243-1250 (2014).

40. Berghof, V., Sommerfeld, T., and Cederbaum, L. S., “Sulfur cluster dianions”, *J. Phys. Chem. A* **102**, 5100-5105 (1998).

41. Abrahams, S. C., “The crystal and molecular structure of orthorhombic sulfur”, *Acta Cryst.* **8**, 661-671 (1955).

42. Stephens, P. J., Devlin, F. J., Chabalowski, C. F., Frisch, M. J., “Ab Initio calculation of vibrational absorption and circular dichroism spectra using density functional force fields”, *J. Phys. Chem.* **98**, 11623-11627 (1994).

43. Gaussian 09, Frisch, M. J., Trucks, G. W., Schlegel, H. B., Scuseria, G. E., et al. Gaussian, Inc., Wallingford CT, 2009.

Chapter 5.

Inverse Vulcanization of Elemental Sulfur to Prepare Polymeric Electrode Materials for Li−S Batteries

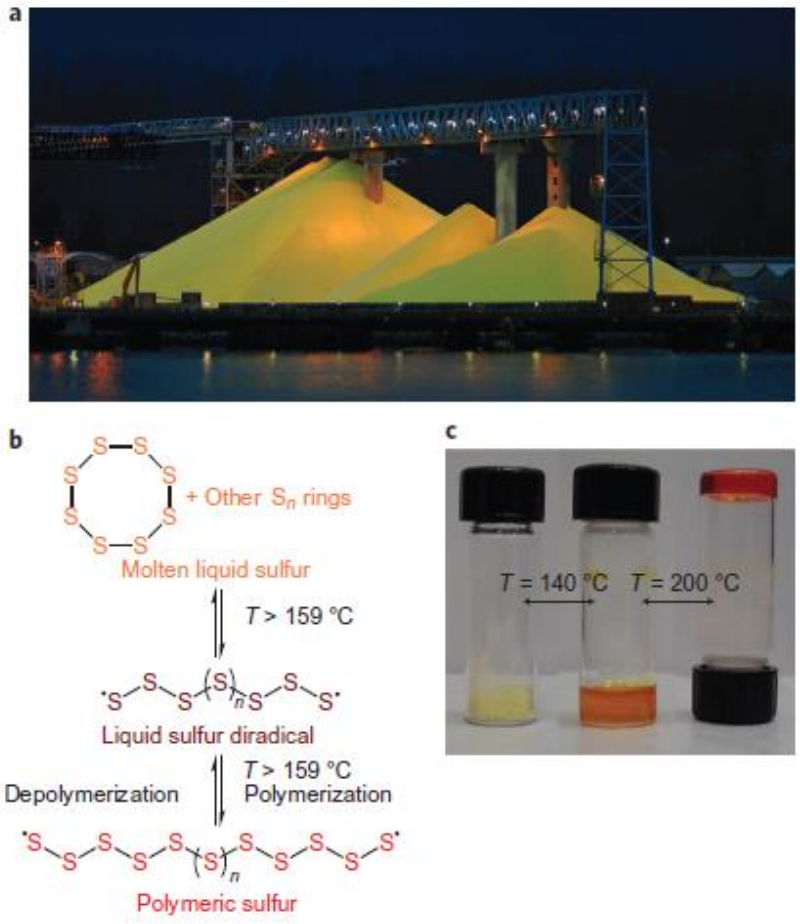

* The work presented in Chap. 5 was published in *Nature Chemistry* **5**, 518-524 (2013) entitled, "The use of elemental sulfur as an alternative feedstock for polymeric materials" Woo Jin Chung, Jared J. Griebel, Eui Tae Kim, Hyunsik Yoon, Adam G. Simmonds, Hyun Jun Ji, Philip T. Dirlam,

Fig. 5.T. (Color) Elemental sulfur as a feedstock. **a**, Example of an exposed deposit of elemental sulfur from hydrodesulfurization in petroleum refining processes. The large abundance of sulfur points to an important opportunity to use this as a new chemical feedstock for polymeric materials. **b**, Schematic for thermal ROP of S_8 into polymeric sulfur diradical forms. c, Bulk forms of S8 powder, molten liquid sulfur and polymeric sulfur formed via thermal ROP. Despite the formation of high molecular weight polymeric sulfur from the ROP of S8, the presence of diradical species results in depolymerization back to monomeric and oligomeric sulfur allotropes.

Richard S. Glass, Jeong Jae Wie, Ngoc A. Nguyen, Brett W. Guralnick, **Jungjin Park**, A´rpa´d Somogyi, Patrick Theato, Michael E. Mackay, Yung-Eun Sung*, Kookheon Char* and Jeffrey Pyun*

And, *ACS Macro Letters* **3**, 229-232 (2014) entitled,

"Inverse Vulcanization of Elemental Sulfur to Prepare Polymeric Electrode Materials for Li−S Batteries"

Adam G. Simmonds,‡ Jared J. Griebel,‡ **Jungjin Park**, Kwi Ryong Kim, Woo Jin Chung, Vladimir P. Oleshko, Jenny Kim, Eui Tae Kim, Richard S. Glass, Christopher L. Soles, Yung-Eun Sung, Kookheon Char,* and Jeffrey Pyun*

5.1. Introduction

5.1.1. Previous studies

Lightweight batteries made from high energy density materials are of specific interest for electric vehicle (EV) applications, such as, plug-in hybrid and electric cars as well as unmanned aerial vehicles. Lithium-sulfur (Li-S) batteries are an ideal candidate for EV applications because of the high theoretical specific capacity of sulfur at 1,672 mAh/g, as well as, the high specific energy of approximately 2600 Wh/Kg. In practice, capacities typically range from 800-1000 mAh/g, which is 4-5 times that of current Li-ion technology.[1,2] The overall electrochemical reaction in the cell is $16\ Li^0 + S_8 \rightarrow 8\ Li_2S$, where metallic Li serves as the anode and elemental sulfur (S_8) serves as the active material in the cathode and is converted into linear polysulfides upon reduction.

While the inherently high specific capacity of S_8 far exceeds that of current Li-ion systems, lithium-sulfur batteries have not achieved widespread commercialization due to limited battery lifetime from either gradual capacity fading or outright failure. Initial capacities around 1,200 mAh/g are fairly common, but retaining this capacity up to several hundred cycles remains challenging. This poor long-term performance has been associated with "shuttling" of linear polysulfides dissolved into the electrolyte medium. A second cause of the limited cycle stability in Li-S batteries arises from the deposition of solid Li_2S discharge products on the cathode.[3] As discharge proceeds, soluble high-order polysulfides are reduced to Li_2S discharge products, which are insoluble in ethereal solvents and deposit as a hard, intractable solid on the cathode surface. Further complications arise during cycling as sulfur undergoes a volume expansion of roughly

80% when forming Li_2S, generating mechanical stress on the cathode framework. Repeated cycling creates cracks in the cathode which, over time, ultimately leads to Li_2S encrusted carbon detaching from the electrode. Once electrically disconnected, the Li_2S is no longer accessible for recharging, resulting in a loss of capacity. Suppressing the cathode damage caused by the Li_2S deposition is essential for extending the long term performance of lithium sulfur batteries. Since the recent advance of Nazar et al.,[4] a number of reports have demonstrated the preparation of sulfur-based nanocomposite materials. Strategies to prepare such nanocomposites aim to encapsulate or sequester the S_8 and its electrochemically generated polysulfides into blends intimately mixed with nanocarbons, or core-shell colloids to create enhanced cathodes for Li-S batteries.[5-10] Cui et al., [11] demonstrated that yolk-shell $S_8@TiO_2$ colloids exhibit high capacity retention and extended lifetimes achieving roughly 700 mAh/g at 1000 cycles at a C/2 rate. Alternatively, the use of sulfide polymers (e.g., DMAcT) has been investigated as a route for electroactive cathode materials.[12] More recently, processing, or carbonization with Li_2S salts has been investigated to create bulk electroactive materials for advanced Li-S cathodes.[13] Recent advances in the utilization of all solid-state Li-S batteries have been reported to obviate the issues associated with liquid electrolytes.[14] All of these systems represent significant advances in the creation of novel electroactive materials to improve the electrochemical performance of cathodes in Li-S batteries. However, challenges still persist in the creation of chemistry and materials that are inexpensive and amenable to large scale production, while retaining high charge capacity and electrochemical stability. Recent efforts by Cui et al. demonstrated the one-pot

dispersion polymerization method to prepare core-shell colloids, exhibiting the enhanced capacity retention up to 1000 cycles.[15]

5.1.2. Material Selections

Herein, we report the synthesis and characterization of poly(sulfur-random-1,3-diisopropenylbenzene) (poly(S-r-DIB)) copolymers and explore composition effects on the electrochemical performance of these copolymers as the active cathode material in Li−S batteries. We previously reported on the synthesis of these copolymers via a process termed inverse vulcanization and demonstrated that Li−S batteries fabricated from these materials exhibited high specific capacity (823 mAh/g at 100 cycles).[15] In this report, we explore for the first time with these sulfur copolymers a direct structure−property correlation of copolymer composition with electrochemical properties to afford optimal polymeric materials for these battery systems. We further demonstrate improved Li−S battery lifetimes out to 500 charge−discharge cycles with excellent retention of charge capacity. The enhanced battery performance observed with these polymeric active materials arises from in situ generation of organosulfur additives (from DIB units) and linear polysulfide segments (Li_xS_y) via electrochemical fragmentation of the initial poly(S-r-DIB) copolymer. We propose that these organosulfur species suppress irreversible deposition of insoluble discharge products (Li_2S_3, Li_2S_2, Li_2S) and are mechanistically distinct from recent Li−S battery systems that nanoencapsulate sulfur to suppress dissolution of linear polysulfides. This sulfur based copolymer is also a new addition to an emerging class of electroactive polymers that have been used as polymeric

electrodes for Li batteries, examples of which include conjugated polymers and nitrosyl radical functional polymers.[16–27] To our knowledge, these novel sulfur copolymers exhibit one of the highest capacities of any wholly polymeric material serving as the active material in batteries cycled to extended lifetimes. The Li−S battery using S8 as the active material in the cathode functions as a liquid electrochemical cell, where discharge causes the reduction of S8 into higher order linear polysulfides (Li_2S_8, Li_2S_6, Li_2S_4) that fully dissolve into the electrolyte medium.3 Continued discharge results in the soluble higher order polysulfides being further reduced to insoluble lower order sulfides (e.g., Li_2S_2, Li_2S) that redeposit onto the carbon-binder cathode framework. Li−S batteries fabricated with poly(S-r-DIB) copolymers as the active cathode material are identical to traditional Li−S batteries using S8, with the exception of soluble organosulfur species (i.e., thiolated DIB units) generated upon discharge of the copolymer. These organosulfur products co-deposit with other insoluble lower order polysulfides onto the carbon-binder cathode framework at the end of discharge, which we propose “plasticizes” these insoluble polysulfide discharge products, enabling more efficient battery cycling. This hypothesis was readily tested by the preparation and electrochemical evaluation of poly(S-r-DIB) copolymers with systematic variation of DIB content. It is important to note that poly(S-r-DIB) copolymers with a high content of sulfur initially exhibit poor solubility toward the electrolyte medium when cast onto the cathode, but form soluble products after discharge to lower polysulfides.

5.2. Experimental section

Materials and instrumentation. Sulfur (S_8, sublimed powder, reagent grade, Aldrich), 1,3-Diisopropenylbenzene (DIB, 97 %, Aldrich), anhydrous Chloroform (Aldrich), Polyethylene (Avg. Mw ~4000 g/mol), Conductive carbon (Super C65, Timcal), Lithium bis(trifluoromethane)sulfonimide (Aldrich), Lithium nitrate (Aldrich), Polypropylene separator (Celgard), Lithium foil (FMC), 1,3-Dioxolane (Novolyte) and 1,2-Dimethoxy ethane (Novolyte) were commercially available and used as received without further purification. The morphology and microstructure of copolymer S-*r*-DIB and conventional S8 cathodes were characterized by field-emission scanning electron microscopy (FESEM) and energy-dispersive X-ray spectroscopy (EDXS) techniques. FESEM observations and EDXS analyses of the cycled cathodes mounted on aluminum alloy stubs were performed using a Hitachi S4700 SEM. The instrument was equipped with a cold field-emission (FE) electron gun and an 80 mm2 active area Oxford Instruments X-Max high-speed silicon drift X-ray detector (SDD). XPS data were collected with monochromatic Al(Kα) radiation using a KRATOS 165 Ultra photoelectron spectrometer.

General procedure for the preparation of poly(sulfur-*random*-(1,3-diisopropenylbenzene)) (Poly(S-*r*-DIB)) copolymers. The preparation of these copolymer materials was conducted using our previously report method.1 A general procedure is listed below along with example protocols on the synthesis of these materials. To a 24 mL glass vial equipped with a magnetic stir bar was added sulfur (S8, masses detailed below) and heated to T = 185 ℃ in a thermostated oil bath until a clear orange colored molten phase was formed. 1,3-Diisopropenylbenzene (DIB, masses

detailed below) was then directly added to the molten sulfur medium via syringe. The resulting mixture was stirred at T = 185 ℃ for 8-10 minutes, which resulted in vitrification of the reaction media. The product was then taken directly from the vial using a metal spatula and removal of the magnetic stir bar for determination of yields after allowing the reaction mixture to cool to room temperature.

a. Preparation of poly(S-*r*-DIB) with 20-wt% DIB: The copolymerization was carried out by following the general method written above with S8 (4.00 g, 15.6 mmol) and DIB (1.00 g, 6.32 mmol) to afford a red solid (yield: 4.98 g).

b. Preparation of poly(S-*r*-DIB) with 30-wt% DIB: The copolymerization was carried out by following the general method written above with S8 (3.50 g, 13.7 mmol) and DIB (1.50 g, 9.48 mmol) to afford a red solid (yield: 5.0 g).

c. Preparation of poly(S-*r*-DIB) with 40-wt% DIB: The copolymerization was carried out by following the general method written above with S8 (3.00 g, 11.7 mmol) and DIB (2.00 g, 12.6 mmol) to afford a red solid (yield: 4.97 g).

d. Preparation of poly(S-*r*-DIB) with 50-wt% DIB: The copolymerization was carried out by following the general method written above with S8 (2.50 g, 9.69 mmol) and DIB (2.50 g, 15.8 mmol) to afford a reddish-brown solid (yield: 4.99g).

Fabrication and testing of Li-S Batteries Poly(S-*r*-DIB) of various copositions were combined with conductive carbon and polyethylene as a binder in a mass ratio of 75:20:5, respectively and ball milled into a slurry with anhydrous chloroform. The slurry was then blade cast onto carbon coated aluminum foil and air dried resulting in a sulfur loading of roughly 0.75 mg/cm2. This cathode was assembled into CR2032 coin cells (MTI) with a

polypropylene separator and a lithium foil anode in an argon filled glove box. The electrolytes used were 0.38 M lithium bis(trifluoromethane)sulfonimide and 0.32M lithium nitrate in a 1:1v/v mixture of 1,3-dioxolane and 1,2-dimethoxy ethane. Battery cycling was done on an Arbin BT2000 battery tester from 1.7 to 2.6 V.

5.3. Results and discussion

5.3.1. Materials characterization

The poly(S-r-DIB) copolymers employed in this study were synthesized by inverse vulcanization through direct dissolution and copolymerization of DIB in liquid sulfur.[15,28,29] This process is essentially a bulk copolymerization of molten sulfur and DIB heated above the floor temperature (T_f) for the free radical ring-opening polymerization (ROP) of S_8 (Figure 5.1). The copolymerization of S_8 with varying DIB feed ratios from 1 to 50% by mass was conducted to prepare sulfur-based copolymer materials, where the incorporation of electroactive S−S bonds was directly controlled. Sulfur copolymers with 50% by mass DIB were found to be soluble in organic solvents (facilitating solution characterizations such as NMR and SEC),[15] while higher compositions of sulfur afforded sparingly soluble materials.

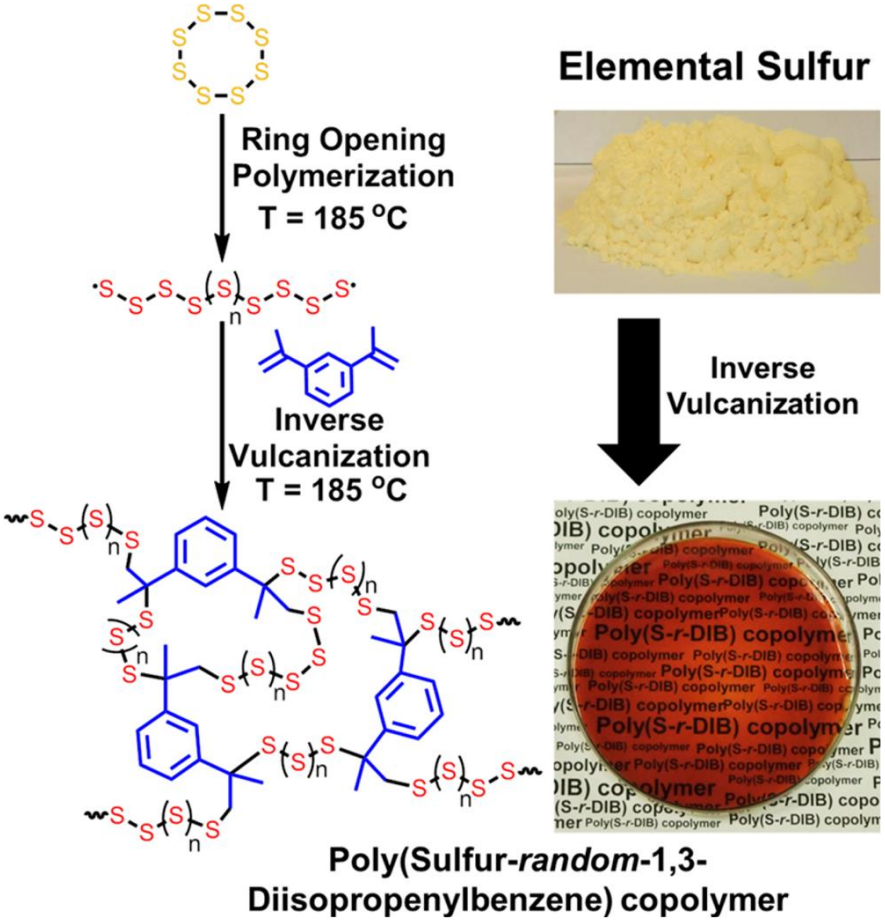

Fig. 5.1. (Color) Synthetic scheme for the inverse vulcanization process yielding poly(sulfur-random-1,3-diisopropenylbenzene) copolymers.

5.3.2. Electrochemical analysis

To investigate composition effects on battery performance, poly(S-r-DIB) copolymers were fabricated into 2032 type battery coin cells and cycled at a rate of C/10 (167.2 mA/g) with lithium foil employed as the anode (Figure 5.2). The sulfur copolymers with 1% by mass DIB exhibited cycling performance comparable to elemental sulfur, whereas copolymers with compositions of 20% or greater by mass DIB exhibited little to no improvement over elemental sulfur. However, poly(S-r-DIB) copolymers with compositions of 5, 10, and 15% by mass DIB all exhibited high initial capacities, low initial capacity loss, and consistently reduced capacity loss per cycle.

From this survey of compositional effects on the electrochemical properties, copolymers with a composition of 10% by mass DIB were found to perform optimally (inset, Figure 5.2). Preliminary studies of this copolymer as an active material in Li−S battery cathodes exhibited a specific capacity of 823 mAh/g at 100 cycles.18 Further optimization of cathode coating methods has yielded significant improvement in both initial capacity and suppression of capacity fading. An initial capacity of 1,225 mAh/g was observed in the Li−S batteries fabricated in the present study and low capacity loss was exhibited as noted by the capacities of 1,005 mAh/g at 100 cycles and 817 mAh/g at 300 cycles with a Coulombic efficiency of 99% throughout. Currently this system has been extended to 500 cycles while retaining a significant capacity of 635 mAh/g (Figure 3). Additionally, these sulfur copolymers were capable of sustaining high capacities at faster C-rates producing over 800 mAh/g at 1C (inset, Figure 5.3). Although, at 2C, the

capacity is significantly reduced as the charge/discharge rate becomes comparable with the inherent rate of diffusion required for the complete sulfur electrochemical conversion processes.

For further insight into the enhanced performance of poly(Sr-DIB) copolymers in Li−S batteries, the normalized charge and discharge profiles of batteries fabricated from copolymers with different DIB concentrations (5−50% by mass) were compared. While changes in the voltage versus normalized capacity curves with DIB content are observed, the curves have the same basic salient characteristics for all compositions. This fact suggests that similar reactions occur for both the S_8 and poly(S-r-DIB) copolymers proving that both S−S and organosulfur moieties in the copolymer were electroactive in both voltage regimes (Figure 5.4).

In the voltage versus normalized capacity plots, the effect of DIB concentration was most evident in the low voltage plateau of the charge and discharge prolfies, where both profiles shifted toward lower voltage with an increase in DIB content (Figure 5.4). This trend provided support for the proposed mechanism of DIB-bound sulfur codeposition within a matrix of lower order sulfide discharge products (i.e., Li_2S_3, Li_2S_2, Li_2S). Initially during discharge of poly(S-r-DIB) copolymers in the high voltage plateau regime, we propose the formation of both higher order organosulfur DIB units and Li_2S_8 (1 and 2 in Figure 5.5a); with further reaction generating organosulfur DIB units (with shortened oligosulfur units) and Li_2S_4 (3 and 4 in Figure 5.5a). Continued discharge into the lower voltage plateau resulted in the conversion of 3 and 4 into fully discharged organosulfur

DIB products and insoluble mixtures of Li_2S_3 and Li_2S_2 (5 and 6 in Figure 5.5a), which codeposited on the cathode, as supported by XPS (see Supporting Information). Furthermore, the improved battery performance for these copolymers was not primarily from the electrochemical properties of organosulfur DIB discharge products, but rather that these organosulfur units function as "plasticizers" in the insoluble Li_2S_3/Li_2S_2 discharge product phase. Hence, we propose that the enhanced cycle stability of these Li−S batteries arises from the presence of these organosulfur units dispersed in the insoluble lower order sulfide phases to suppress irreversible deposition of these discharge products to abate capacity losses. However, at higher compositions of DIB in the copolymer (above 15% by mass), these organosulfur discharge products were presumably more concentrated in the electrolyte and in equilibrium with other free polysulfides, (e.g., Li_2S_3) to reform high order polysulfides (see Figure 5.5b). These high order polysulfides were more soluble in the electrolyte medium and hence, did not efficiently co-deposit with lower polysulfides on the cathode (see Supporting Information, Figure 5.S5), resulting in rapid capacity fading, as shown in Figure 5.2.

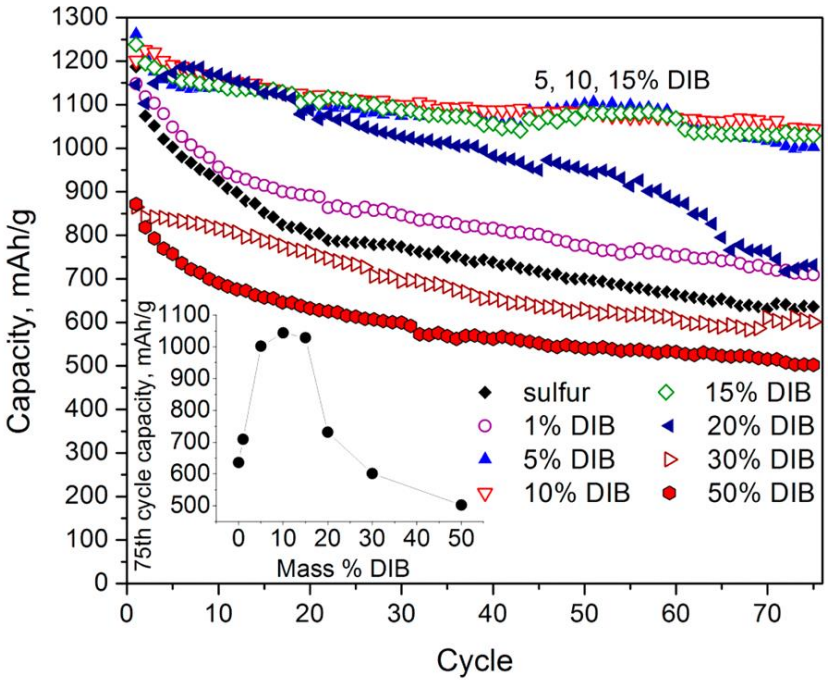

Fig. 5.2. (Color) Cycling performance of Li−S batteries from sulfur copolymers of varying composition (0−50% by mass DIB) up to 75 cycles. Inset figure shows a plot of the specific capacity measured at the 75th cycle against sulfur copolymer composition.

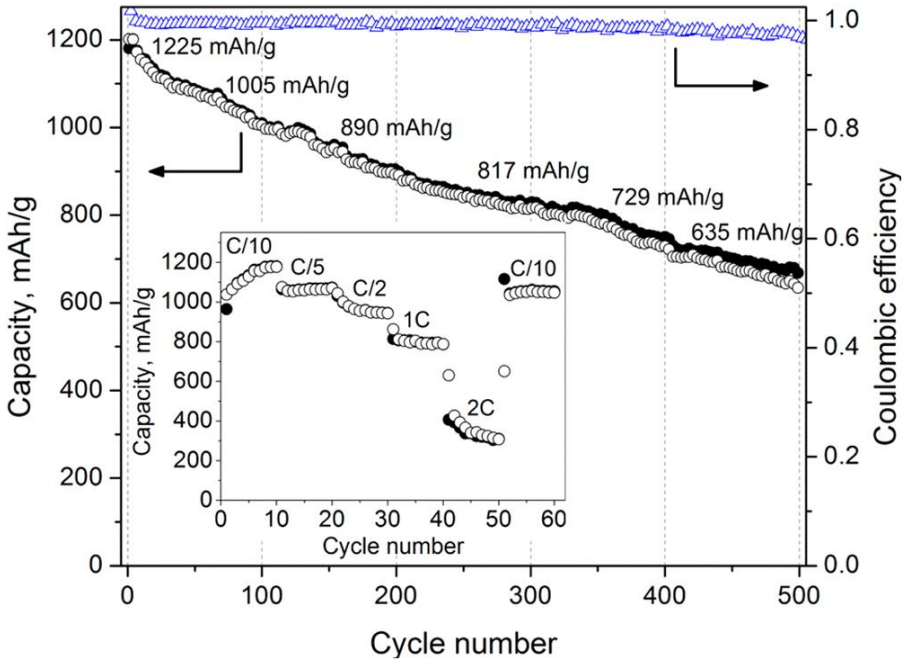

Fig. 5.3. (Color) Cycling performance of Li−S battery from 10% by mass DIB copolymer batteries to 500 cycles with charge (filled circles) and discharge (open circles) capacities, as well as Coulombic efficiency (open triangles). The C-rate capability of the battery is shown in the figure inset.

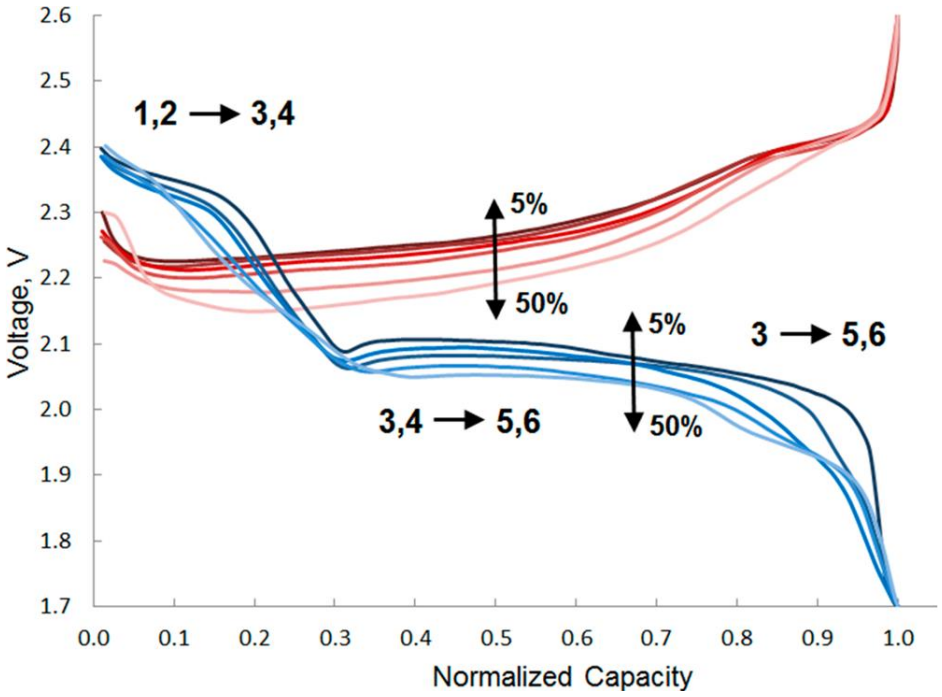

Fig. 5.4. (Color) Normalized charge and discharge profiles of copolymer cathodes with different DIB composition. Charging profiles for 5% (dark red), 10%, 20%, 30%, and 50% (light red) and discharging profiles for 5% (dark blue), 10%, 20%, 30%, and 50% (light blue). Proposed assignments of chemical products formed during the discharge cycles are indicated in Figure 4.5a.

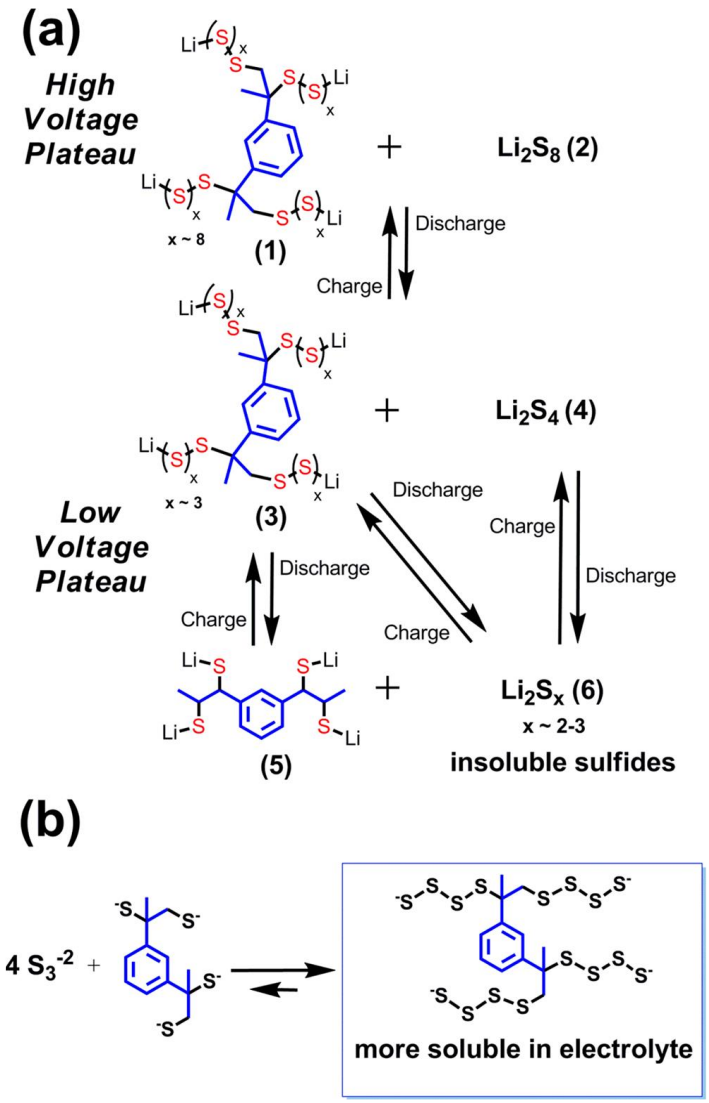

Fig. 5.5. (Color) Figure 5. (a) Proposed electrochemisty of poly(S-r-DIB) copolymers in Li−S batteries; (b) proposed equilibrium between lower polysulfides and organosulfide discharge products, which at higher DIB compositions favors formation of soluble higher order polysulfides. Li+ cations omitted for clarity due to the presence of excess cations in the electrolyte.

5.4. Conclusions

The synthesis of sulfur copolymers via inverse vulcanization for enhanced cathode materials in Li−S batteries is reported. We demonstrate that this inexpensive, bulk copolymerization can sufficiently modify the properties of sulfur to improve the battery performance without the need for nanoscopic synthesis or processing. This system also demostrates for the first time that high capacity polymeric electrodes can be fabricated while also suppressing capacity fading after extended battery performance to 500 cycles.

5.5. Supporting informations

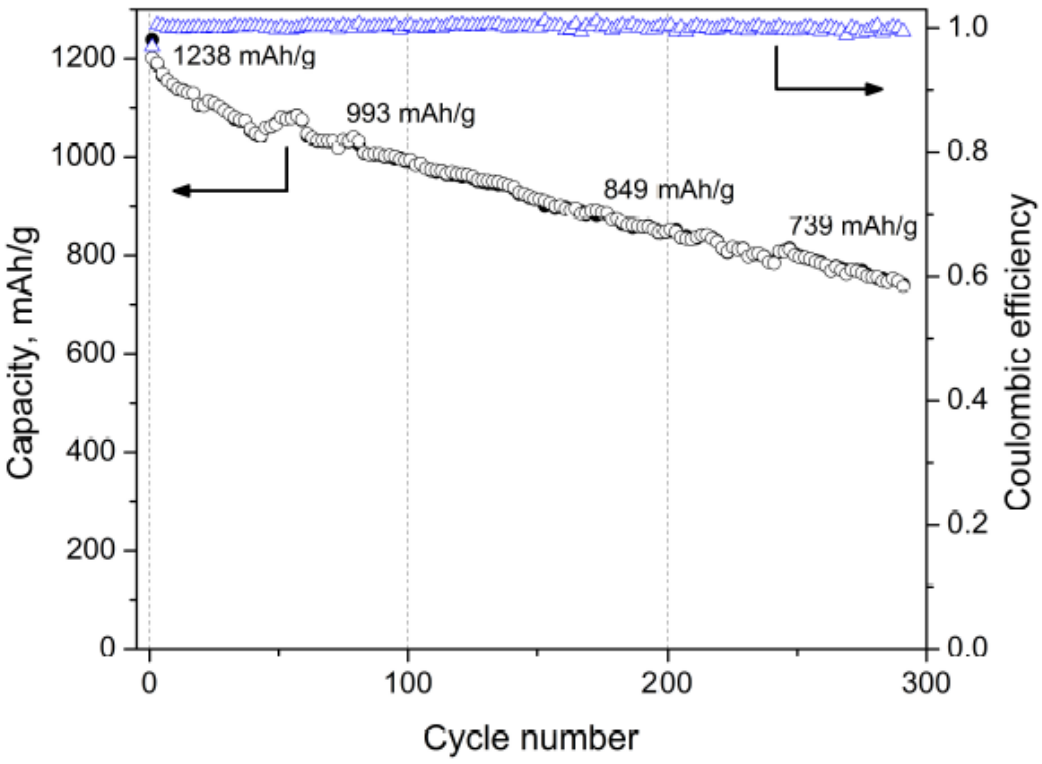

Fig. 5.S1. (Color) Battery cycling performance of poly(S-*r*-DIB) copolymer, 15-wt% DIB to 290 cycles.

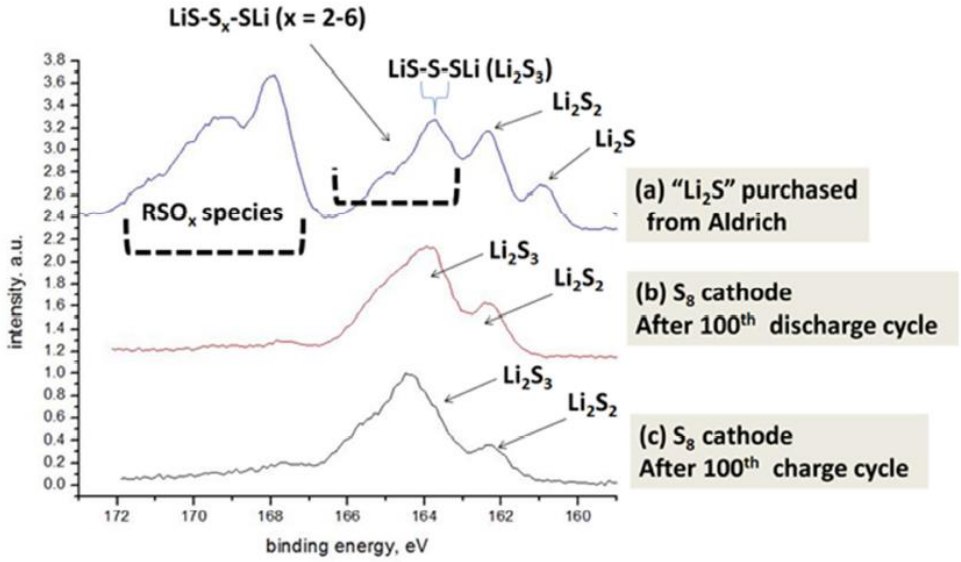

Fig. 5.S2. (Color) S2p XPS spectra of: (a) Li2S reference material purchased from Aldrich (b) Li-S battery cathode fabricated from S8 left in the discharged state after 100 cycles (c) Li-S battery cathode fabricated from S8 left in the charged state after 100 cycles

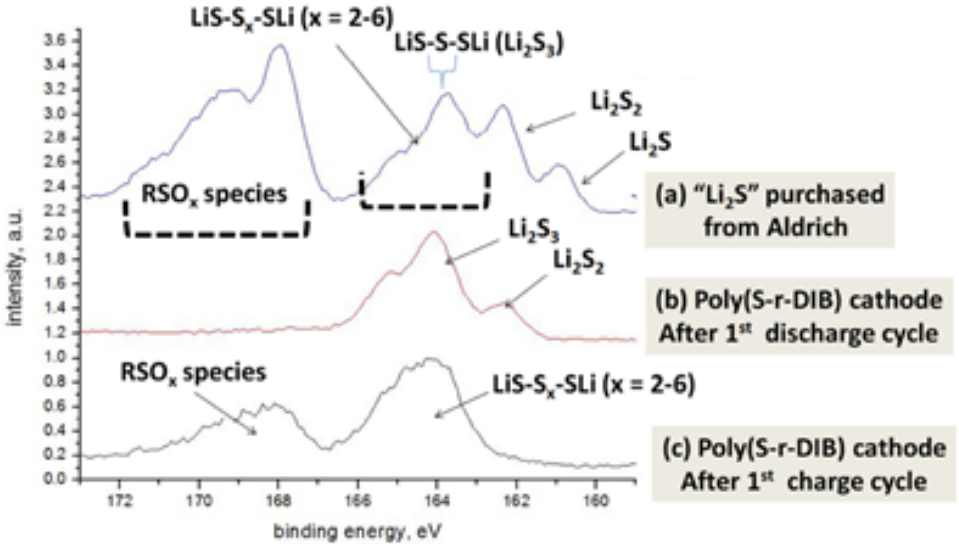

Fig. 5.S3. (Color) S2p XPS spectra of: (a) Li2S reference material purchased from Aldrich (b) Li-S battery cathode fabricated from poly(S-r-DIB) with 10-wt% DIB left in the discharged state after 100 cycles (c) Li-S battery cathode fabricated from poly(S-r-DIB) with 10-wt% DIB left in the charged state after 100 cycles

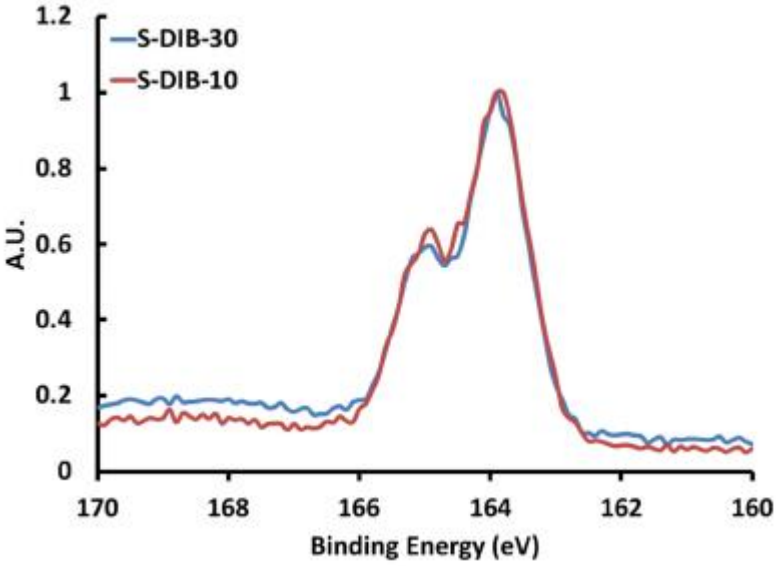

Fig. 5.S4. (Color) S_{2p} XPS spectra of poly(S-*r*-DIB) copolymers (both 10 and 30-wt% DIB)

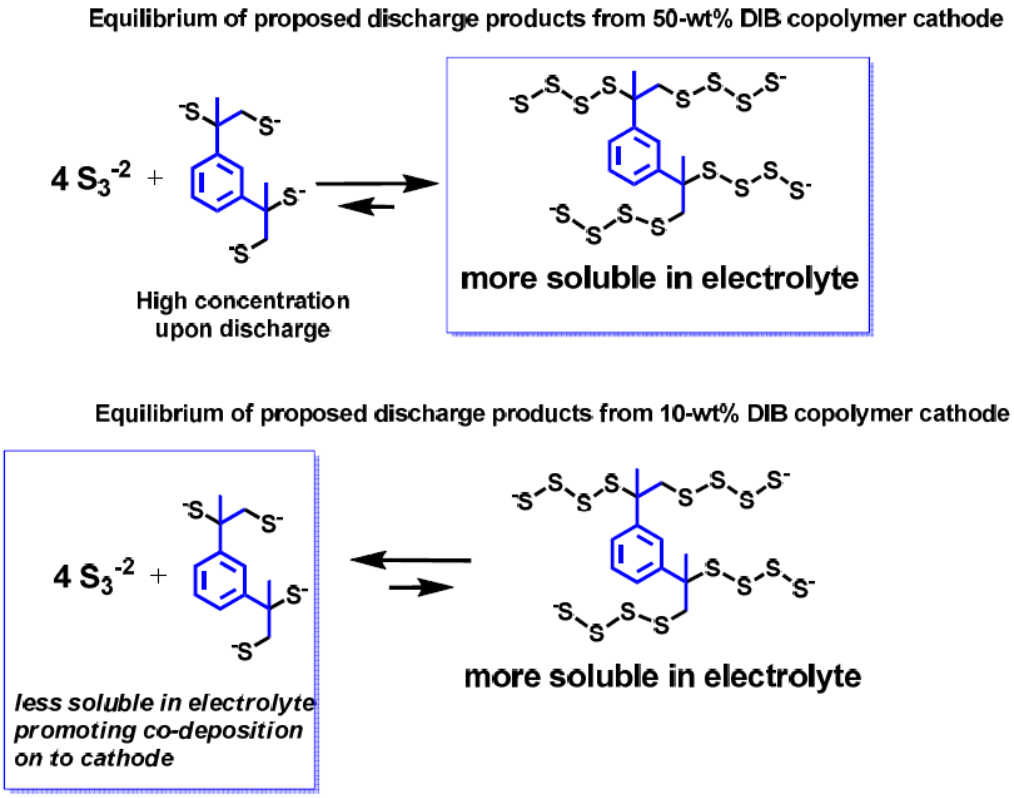

Fig. 5.S5. (Color) Discharge products of free polysulfides and organosulfur DIB discharge products for high (top scheme) and low (bottom scheme) DIB content copolymers. When using high content DIB copolymers, a high concentration of organosulfur species are generated which are in equilibrium with lower sulfide (e.g., Li2S3) to form high order polysulfides, which are more soluble in the electrolyte, do NOT re-deposite onto the cathode and result in charge capacity fading. Conversely, for low DIB content copolymers, a higher concentration of longer polysulfides are present (due to the initially lower concentration of DIB units), which favors disproportation back to insoluble Li2S3

(and other lower sulfides) and organosulfur-DIB discharge products. In the scheme Li+ cations are omitted for clarity due to the presence of excess Li-ions in the electrolyte.

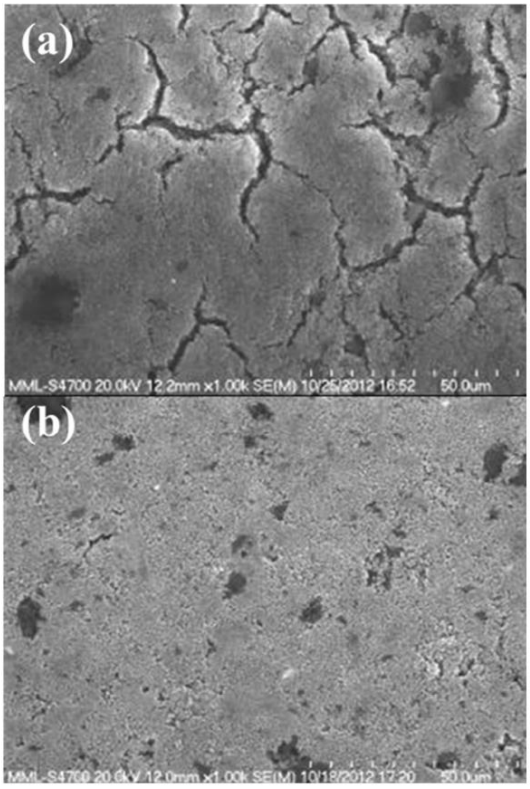

Fig. 5.S6. FE-SEM images in the charged state after solvent-rinsing of cathodes to remove electrolyte salts for (a) Li-S batteries using S8 cathodes at 80 cycles and (b) Li-S batteries using 10% by mass DIB sulfur copolymer cathodes at 120 cycles. Note the cathodes fabricated from sulfur copolymers remain a greater degree of structural integrity after extensive cycling in comparison to cycled S8 batteries.

5.6. References

1. Manthiram, A.; Fu, Y.; Su, Y.-S., *Acc. Chem. Res.* **46**, 1125−1134 (2013).
2. Evers, S.; Nazar, L. F., *Acc. Chem. Res.* **46**, 1135−1143 (2013).
3. Zhang, S. S., *J. Power Sources* **231**, 153−162 (2013).
4. Mikhaylik, Y. V.; Akridge, J. R., *J. Electrochem. Soc.* **151**, A1969−A1976 (2004).
5. Mikhaylik, Y. V., *U.S. Patent* **7**, 354 680, (2005).
6. Ji, X.; Lee, K. T.; Nazar, L. F., *Nat. Mater.* **8 (6)**, 500−506 (2009).
7. Wang, J. L.; Yang, J.; Xie, J. Y.; Xu, N. X., *Adv. Mater.* **14** (13−14), 963−965 (2002).
8. Jayaprakash, N.; Shen, J.; Moganty, S. S.; Corona, A.; Archer, L. A., *Angew. Chem., Int. Ed.* **50 (26)**, 5904−5908 (2011).
9. Wu, F.; Chen, J.; Chen, R.; Wu, S.; Li, L.; Chen, S.; Zhao, T. J., *Phys. Chem. C* **115 (13)**, 6057−6063 (2011).
10. Seh, Z. W.; L., W.; Cha, J. J.; Zheng, G.-y.; Yang, Y.; McDowell, M. T.; Hsu, P.-C.; Cui, Y., *Nat. Commun.* **4**, 1−6 (2013).
11. Moon, S.; Jung, Y. H.; Jung, W. K.; Jung, D. S.; Choi, J. W.; Kim, D. K., *Adv. Mater.* **25**, 6547−6553 (2013).
12. Zhou, W.; Yu, Y.; Chen, H.; DiSalvo, F. J.; Abruna, H. D., *J.Am. Chem. Soc.* **135**, 16736−16743 (2013).
13. Song, M.-K.; Zhang, Y.; Cairns, E. J., *Nano Lett.* **13** (12), 5891−5899 (2013).
14. Li, W.; Zheng, G.; Yang, Y.; She, Z. H.; Liu, N.; Cui, Y., *Proc. Natl. Acad. Sci. U.S.A.* **110**, 7148−7153 (2013).

15. Chung, W.-J.; Griebel, J. J.; Kim, E.-T.; Yoon, H.-S.; Simmonds, A. G.; Ji, H.-J.; Dirlam, P. T.; Glass, R. S.; Wie, J. J.; Nguyen, N. A.; Guralnick, B. W.; Park, J.; Somogyi, A.; Theato, P.; Mackay, M. E.; Sung, Y.-E.; Char, K.-C.; Pyun, J., *Nat. Chem.* **5 (6)**, 518−524 (2013).
16. Liu, M. L.; Visco, S. J.; Dejonghe, L. C., *J. Electrochem. Soc.* **138 (7)**, 1891−1895 (1991).
17. Tatsuma, T.; Sotomura, T.; Sato, T.; Buttry, D. A.; Oyama, N., *J. Electrochem. Soc.* **142 (10)**, L182−L184 (1995).
18. Chao, Z. S.; Lan, Z.; Yu, J., *J. Power Sources* **196 (23)**, 10263−10266 (2011).
19. Kiya, Y.; Henderson, J. C.; Abruna, H. D., *J. Electrochem. Soc.* **154**, A844−A848 (2007).
20. Mike, J. R.; Lutkenhaus, J. L., *ACS Macro Lett.* **2**, 839 (2013).
21. Shao, L.; Jeon, J.-W.; Lutkenhaus, J., *L. Chem. Mater.* **24**, 181−189 (2012).
22. Choi, W.; Harada, D.; Oyaizu, K.; Nishide, H., *J. Am. Chem. Soc.* **133**, 19839−19843 (2011).
23. Suga, T.; Ohshiro, H.; Sugita, S.; Oyaizu, K.; Nishide, H., *Adv. Mater.* **21**, 1627−1630 (2009).
24. Nishide, H.; Oyaizu, K., *Science* **319**, 737−738 (2008).
25. Suga, T.; Pu, Y.-J.; Kasatori, S.; Nishide, H., *Macromolecules* **40**, 3167−3173 (2007).
26. Nishide, H.; Iwasa, S.; Pu, Y.-J.; Suga, T.; Nakahara, K.; Satoh, M., *Electrochim. Acta* **50**, 827−831 (2004).
27. Duan, B.; Wang, W.; Wang, A.; Yuan, K.; Yu, Z.; Zhao, H.; Qiu, J.; Yang, Y., *J. Mater.*

Chem. A **1**, 13261−13267 (2013).

28. Chung, W. J.; Simmonds, A. G.; Griebel, J. J.; Kim, E. T.; Suh, H. S.; Shim, I. -B.; Glass, R. S.; Loy, D. A.; Theato, P.; Sung, Y.-E.; Kookheon, C.; Pyun, J., "///" *Angew. Chem., Int. Ed.* **50**, 11409−11412 (2011).
29. Wang, K.; Groom, M.; Sheridan, R.; Zhang, S.; Block, E. J., *Sulfur Chem.* **34**, 55−66 (2013).

Chapter 6

Sulfur-rich Polymeric Nanocomposites with Reduced GO for Stable and Fast Li-S batteries

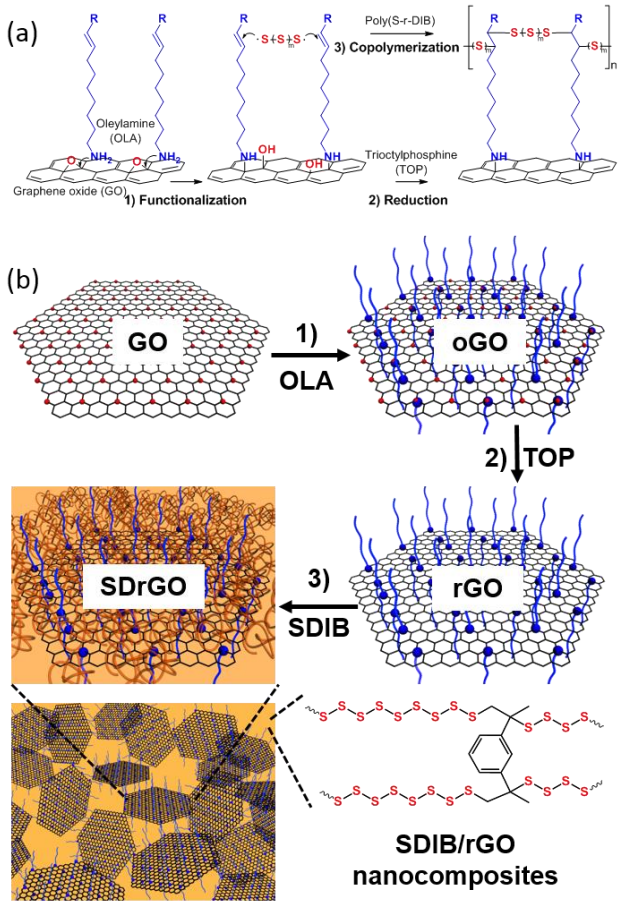

Fig. 6.T. (Color) Schematic illustration of synthesis of poly(S-r-DIB)/rGO nanocomposites (SDrGO)

6.1. 1ntroduction

6.1.1. Previous studies

Lithium-sulfur batteries are expected to achieve a significant breakthrough in energy storages and electric vehicles industry, due to the large specific capacity (1,675 $mAhg^{-1}$) of sulfur cathodes. However, there are still many challenging problems to overcome for the commercialization. The most serious issues in sulfur cathodes come from the electrically insulating property along with the unique electrochemical reaction of sulfur, which result in rapid capacity decaying during the charge/discharge cycles. The intermediate products of sulfur, polysulfides, easily dissolve in the electrolyte, and they continuously diffuse out from the electrode. Moreover, the dissolved polysulfides irreversibly precipitate on the surface when converting into sulfur, or lithium sulfide (Li_2S) during the charge or discharge, respectively. Those electrochemical process involving liquid and solid phases leads to gradual loss of active sulfur with electrical contact due to the decomposition of electrode structure.

To address these issues, a large number of strategies have been developed for a decade. The most representative methods come along with nano-structured carbon/sulfur composite materials. The intimate contact between carbon and sulfur not only facilitate fast electron transfer, but also prevent irreversible dissolution and precipitation of polysulfides by physical encapsulation or chemical association.

6.1.2. Material selections

We recently developed a new chemistry to synthesize high sulfur content copolymers, poly(S-r-DIB) (SDIB), via the inverse vulcanization, and these polymeric materials

exhibited high capacity retention until more than 500 cycles when used as cathode materials in Li-S cells.[1-4] Small contents of monomer (DIB), cross-linked with linear polysulfide chains, act as a binder to prevent irreversible dissolution of polysulfides, and stabilize the lithiated product phases of the cathode. As a result, homogeneous contact between carbon and the copolymers could be retained during the repeated charge/discharge cycles. However, the enhancement of high C-rate capability with SDIB copolymer is still hard to achieve due to the absence of electrically conducting pathway inside the copolymers.

A facile method to include functional nanomaterials within polymeric sulfur matrices were introduced.[5, 6] By using unique dual interaction between oleylamine (OLA) and sulfur, PbS NP/sulfur copolymer nanocomposites were synthesized in a one-pot manner. The double bond in the middle of OLA chain copolymerized with sulfur diradical to form polymeric matrix of the nanocomposites, and at the same time, the amine functional group at OLA chain end attached to the surface of PbS NP to stabilize the interfaces.

Herein we demonstrate an improvement in rate capability of poly(S-r-DIB) cathode by introducing simple nano-scale inclusion of reduced GO (rGO) into SDIB using dual interaction of OLA with sulfur and GO (**Scheme 6-1)**.

For the homogeneous dispersion of rGO in SDIB polymer matrix, GO was modified with oleylamine (OLA), and the OLA modified GO (oGO) was subsequently reduced with trioctylphosphine (TOP), as a reducing agent. Lee et al.[7] reported that these modification and reduction steps afforded good miscibility and processability of rGO in 1,2 dichlorobenzene (DCB). Therefore, simple mixing of rGO and poly(S-r-DIB) at 150 ℃

resulted in the homogeneous nanocomposite materials after purification. Furthermore, the OLA molecules, binding to rGO, copolymerized with SDIB in the mixing step, to generate nano-scale electrical contact between rGO and SDIB polymer.

6.2. Experimental Section

Materials: Graphite powder (<45 microns), sulfur, potassium permanganate (KMnO4), oleylamine (OLA, 70% technical grade), trioctylphosphine (TOP, 90% technical grade), and N,N-dimethylformamide (DMF) were purchased from Sigma-Aldrich. Hydrochloric acid (HCl) was provided from Samchun Chemical. Concentrated sulfuric acid (H2SO4) was obtained from PFP Chemicals. Hydrogen peroxide (H2O2) and 1,2-dichlorobenzene (DCB) was purchased from Junsei Chemical. 1,3-Diisopropenyl benzene (DIB) was obtained from TCI Chemical.

Synthesis of GO, oGO, and rGO: GO was prepared from natural graphite by the modified Hummer's method according to the previous reports.[1] 2 g of graphite and 46 mL of H2SO4 were added into the flask placed in ice bath with stirring. After 10 min, 6 g of KMnO4 was slowly added to the mixture, while being kept below 20 ℃. After 16 h, 92mL of deionized water was slowly added and heated to 35 ℃ for 2 h. The reaction was terminated with 280 mL of deionized water and 5 mL of H2O2 at 60 ℃. The reaction product was filtrated and washed several times with 500 mL of 5 % HCl solution. The fractionated GO dispersion in water (1 mg/mL) were obtained by ultra-sonication at 40 % amp. for 30 min in the presence of ice bath. The final product was freeze-dried for 3 days for further use.

oGO and rGO were prepared following the previous paper by Lee and coworkers.[2] 0.2 g of GO and 2 mL of OLA were added into 50 mL of DMF, and the mixture was subjected to sonication for 1 h, followed by heating at 80 ℃ for 24 h. For purification, 50 mL of ethanol was added and oGO suspension was precipitated by centrifugation at 4500 rpm

for 20 min. This process was repeated twice after the re-dispersion of the precipitates in 20 mL of n-hexane. The final product was dried in vacuum oven overnight. For the preparation of rGO, 0.1 g of oGO and 5 mL of TOP were added into 50 mL of DCB, and the mixture was subjected to sonication for 1 h, followed by heating at 100 ℃ for 24h. The purification and drying process was the same as that for oGO.

Synthesis of SDIB, SrGO and SDrGO nanocomposites: SDIB copolymer was synthesized according to the previous reports.[3] 4.5 g of sulfur and 0.5 g of DIB were heated at 185 ℃ with vigorous stirring until the mixture became homogeneous and vitrified. For SrGO, 0.05 g of rGO and 0.45 g of sulfur were added in 5 mL of DCB, and the mixture was subjected to sonication for 1 h, followed by heating at 150 ℃ for 24 h. After the reaction, 10 mL of methanol was added and the product was precipitated by centrifugation at 4500 rpm for 20 min. The product was dried in vacuum oven overnight. SDrGO was synthesized with 0.05 g of rGO and 0.45 g of SDIB copolymer added in 5 mL of DCB. The reaction and purification steps were the same as that for SrGO.

Characterization: 1H NMR spectra were obtained with a Bruker Avance III 500 MHz spectrometer using CDCl3 as a solvent. Differential scanning calorimeter (DSC) data was obtained using a DSC 4000 (PerkinElmer) at a heating rate of 10 ℃/min under nitrogen atmosphere. Thermal gravimetric analysis (TGA) was carried out by a TGA Q500 (TA Instruments) at a heating rate of 10 ℃/min under nitrogen atmosphere. Elemental analysis was performed using a Flash1112 (CE Instrument, Italy) with CHNS-Porapack PQS columns. X-ray diffraction (XRD) measurements were obtained using a New D8 Advance model (Bruker) at room temperature with a CuKα radiation source at 18 kW. X-

ray photoelectron spectroscopy (XPS) was conducted using Axis-HSi (Kratos) with Mg/Al dual anode at 15 kV and 10 mA. Fourier-transform infrared (FTIR) spectra were obtained with FT-IR/NIR Frontier Spectrum 400 (PerkinElmer). Atomic force microscopy (AFM) was carried out with Nanowizard (JPK Instruments). Raman spectra were taken with T64000 (Horiba) using Ar laser (514 nm). Transmission electron microscopy (TEM) images were recorded on a JEOL-JEM2100 at an operating voltage of 200 kV. For the cross-sectional views of TEM, the samples were placed on a pre-cured epoxy resin, and then embedded by pouring a fresh epoxy resin on the top of the films after drying in a vacuum oven. The resin mixture for molding was prepared by mixing 25.6 g of Embed 812 resin, 13.51 g of dodecenyl succinic anhydride, 10.9 g of Nadic® methyl anhydride, and 1 g of DMP-30. All the components were purchased from Electron Microscopy Sciences. The cured resins were sliced with a microtome (Leica Microsystems). The 70 nm-thick slices were prepared with a diamond-coated knife (DiATOME) at an angle of 6 ° and a cutting velocity of 0.1 mm/s. The slices were suspended in water and supported on a Cu grid.

6.3. Results and discussion

6.3.1. Materials characterization

For the homogeneous dispersion of rGO in SDIB polymer matrix, GO was modified with oleylamine (OLA), and the OLA modified GO (oGO) was subsequently reduced with trioctylphosphine (TOP), as a reducing agent. Lee et al.[7] reported that these modification and reduction steps afforded good miscibility and processability of rGO in

1,2 dichlorobenzene (DCB). Therefore, simple mixing of rGO and poly(S-r-DIB) at 150 ℃ resulted in the homogeneous nanocomposite materials after purification. Furthermore, the OLA molecules, binding to rGO, copolymerized with SDIB in the mixing step, to generate nano-scale electrical contact between rGO and SDIB polymer.

XRD patterns were obtained to confirm the successive modification and reduction of GO. As-synthesized GO has a diffraction peak at 2θ = 11.7 °, corresponding to 7.56 Å of the basal plane distance (001) due to the oxygen containing functional groups in graphene interlayers. After the modification with OLA, the interlayer distance increased to 23.4 Å, which is attributed to the length of alkyl chains of OLA intercalated between the GO interlayers.[8] When oGO reduced with TOP (rGO), a new broad peak centered at 20.8 ° (4.27 Å), closer to that of natural graphite (3.34 Å), appeared in the XRD pattern as a result of re-stacking of reduced graphene interlayers.[7] The AFM height measurements also confirm the OLA grafting on GO after the reduction. The thickness of GO measured by AFM was about 1 nm, while as those of oGO and rGO were roughly 2 to 2.5 nm. The 4 point probe measurement revealed that the electrical resistivity of GO ($7.43X10^5$ Ω·cm) slightly decreased after OLA modification ($3.20 X 10^4$ Ω·cm), and after the reduction, it drastically decreased into 6.06 Ω·cm. Further characterization of rGO were conducted by FTIR, XPS, and TGA as included in supporting information.

As-synthesized rGO was well dispersed in DCB, so the suflur/rGO (SrGO) or SDIB/rGO (SDrGO) composites for cathode materials were obtained by simply mixing of sulfur or SDIB, respectively, with rGO in DCB. The contents of sulfur in SDIB polymer used in the synthesis were 90 wt%, which was proved to exhibit best electrochemical

performance,[4] and 10 wt% of rGO was additionally included in the SrGO and SDrGO nanocomposites. TGA curves confirmed the incorporation of rGO in the nanocomposites after the purification. About 90 wt% and 80 wt% of sulfur was contained in the SrGO and SDrGO nanocomposites, respectively. The STEM images along with the EDS elemental maps were demonstrated to show identical location of both sulfur and carbon signals, and that implies the nano-scale electrical contact between active sulfur of poly(S-r-DIB) and carbon of rGO.

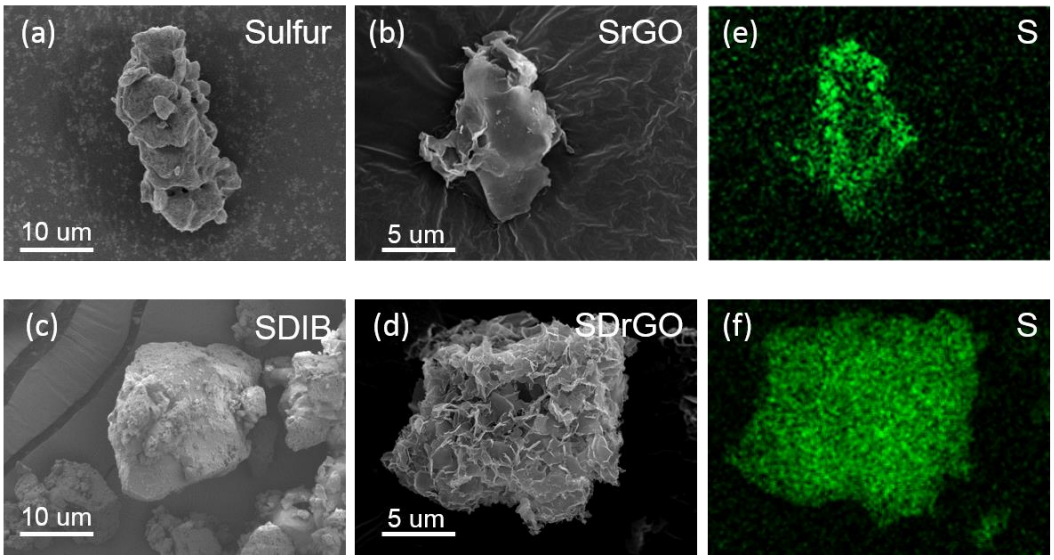

Fig. 6.1. (Color) SEM images of (a) sulfur, (b) SrGO, (c) SDIB, and (d) SDrGO and EDS element sulfur (S) mapping of (e) SrGO , and (f) SDrGO

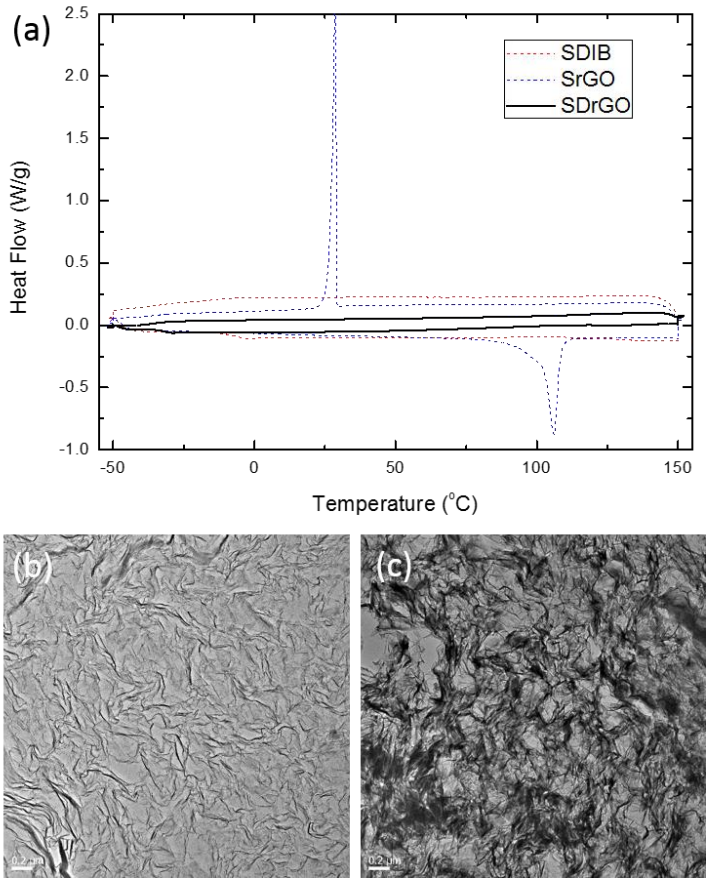

Fig. 6.2. (Color) (a) DSC curves of Poly(S-r-DIB) (SDIB), Sulfur/rGO nanocomposites (SrGO), and Poly(S-rDIB)/rGO nanocomposites (SDrGO) and TEM images of (b) SrGO and (c) SDrGO prepared microtomming method

6.3.3. Electrochemical analysis

The electrochemical analysis applied the SDIB, SrGO, and SDrGO electrodes, which prepared physical mixing with carbon black and binder (pvdf) using mortar mixing. First of all, the cycling performance confirmed all of samples at 0.5 C-rate (1C = 1,675 mA/g) in figure 6.3 a. The SDrGO sample exhibits the highest initial capacity and consistent cycle retention compare with SDIB and SrGO. SDIB samples shows the compatible data tendency vs. previous reported data, sulfur-rich polymerized compound (SDIB) does not show the severe capacity fading caused from irreversible polysulfide dissolution but still have insulative nature of sulfur (~10^{-30} S/cm), so that this sample is hard to fully utilize the sulfur materials at initial cycle. On the contrary, the SrGO sample has relatively higher electrical conductivity than SDIB because of conductive carbon incorporated structure, but does not have polysulfide conservation ability originated from C-S bonding. Such reasons make SrGO high initial utilization of sulfur, and capacity degradation on the cycle operations. Interestingly, SDrGO sample performs relative high sulfur utilization of sulfur (1,180 mAh/g at $1^{st.}$ cycle) and preserved specific capacity (960 mAh/g at $300^{th.}$ cycle) compare with SDIB (985 mAh/g at $1^{st.}$ and 850 mAh/g at $300^{th.}$ cycle) and SrGO (1,219 mAh/g at $1^{st.}$ cycle and 598 mAh/g at $300^{th.}$), which homogeneously incorporated structure and sulfur-rich polymerization of SDrGO sample govern superior battery performance. The specific information can be confirmed the charge discharge profile at $10^{th.}$ cycle, which easily shows the SDIB sample have higher polarization curve on charge-discharge. In figure 5.3 b, the various constant current applied all of samples, which can confirm not only the effects of electronic/ionic

conductivity and following polarization properties but also structural stability on high reactive dynamics. The SDrGO sample also exhibits distinguishable performance than SDIB and SrGO. On the other hand, the severe capacity fading is generated from SrGO sample which involve both of effects the wrapping properties of irreversible polysulfide loss and high electrical contact, confirmed degradation tendency at initial cycle and recovery rate at changed C-rate from 1.0 C to 0.1 C. To analyse more detailed, the charge-discharge profile would be an alternative valuation in figure 6.4. This profile would be confirmed the tendency of capacity degradation. The SDIB and SDrGO samples shows sustainable capacity on dissolution region (from initial to supersaturated point) but declined capacity precipitation region (from supersaturated to end point) on discharge profile by doing gradually increased constant current. On the contrary, SrGO sample shows both of region capacities decreased during various constant current. In addition, SrGO, SDrGO samples exhibit the relative slight polarization but SDIB has higher operpotential applying higher constant current. Those properties would be easily confirm the galvanostatic intermittent titration technique (GITT) and cyclic voltammetry of those samples. GITT can confirm the binding effect of soluble polysulfides on dissolution region. The SDIB and SDrGO sample contain the polarity of reaction, applying rest time compare with SrGO. Those sample chemically synthesized sulfur with DIB, which make a C-S bonding and those bonding would be supported the cycle retention as previous reports. So, the GITT data support the wrapping property of SDIB and SDrGO in dissolution region. In addition, cyclic voltammetry (CV) can also confirm the properties of precipitation region. In this region, the SDIB samples has higer positive

onset potential and lower negative onset potential compare with SrGO, and SDrGO, which can explain that the reaction kinetics of ring (SrGO) and linear (SDrGO) sulfur are increased from the coordinated reduced graphene oxide. The electrochemical impedance spectroscopy (EIS) would support previous claims which samples prepared as coin cell type and before cycle state in figure 6.S9. SDrGO and SrGO charge transfer resistance decreased compared with SDIB.

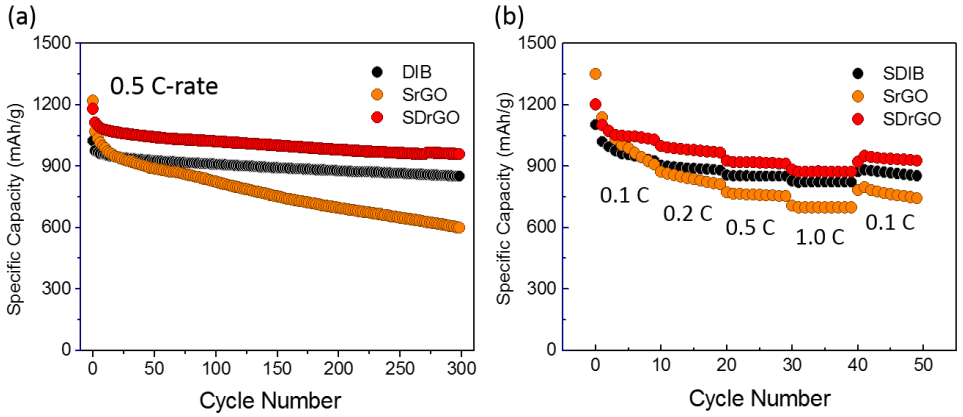

Fig. 6.3. (Color) (a) Cycling and (b) rate performance applying Li-S battery as a cathode materials. The black, orange, and red dots exhibit the performance of SDIB, SrGO, and SDrGO samples.

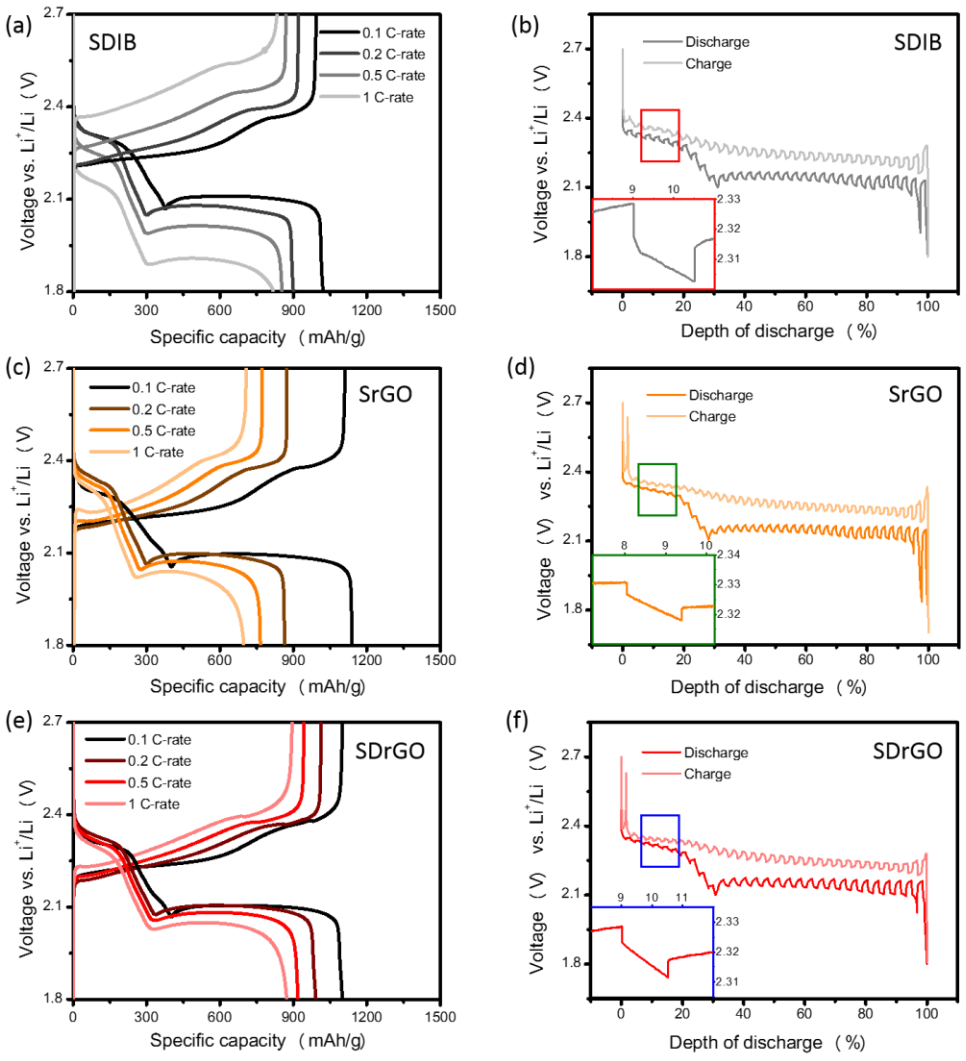

Fig. 6.4. (Color) Charge-discharge profiles (left side) converted from rate performance show the various constanct current (0.1*C*, 0.2*C*, 0.5*C* and 1*C*) of (a) DIB, (c) SrGO, and (e) SDrGO samples and Galvanostatic intermittent titration technique (GITT) plots of (b) SDIB, (d) SrGO, and (f) SDrGO

6.4. Conclusions

In conclusion, the SDrGO chemically synthesized the DIB and sulfur with reduced graphene oxide. To make uniformly incorporated structure, oleylamine (OLA) functionalities are applied on the synthesis method. The S-C boning from DIB support the wrapping of soluble polysulfides and reduced grapehene oxide support the increased electrical conductivity, which make improved cycling and rate performance. Various electrochemical techniques support the deeply understanding for analysing reaction phenomena on this system.

6.5. Supporting Informations

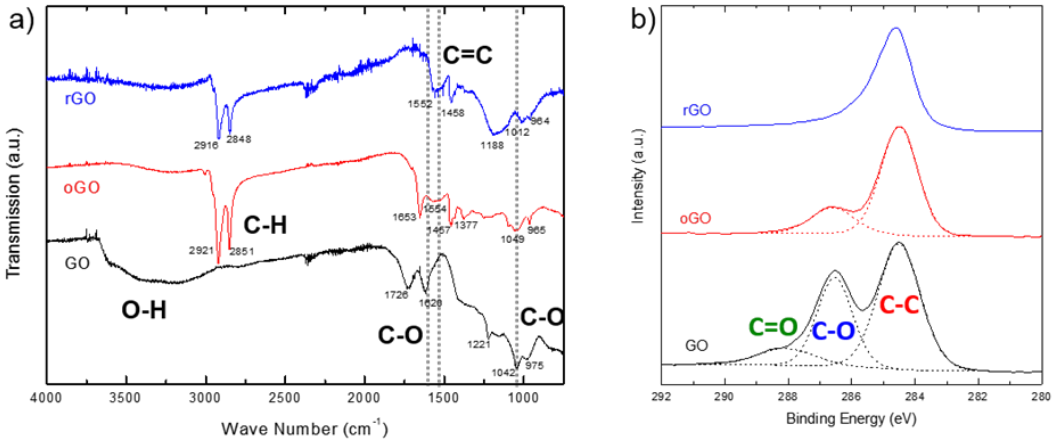

Fig. 6.S1. (Color) a) FTIR spectra and b) XPS spectra at C1s of GO, oGO, rGO.

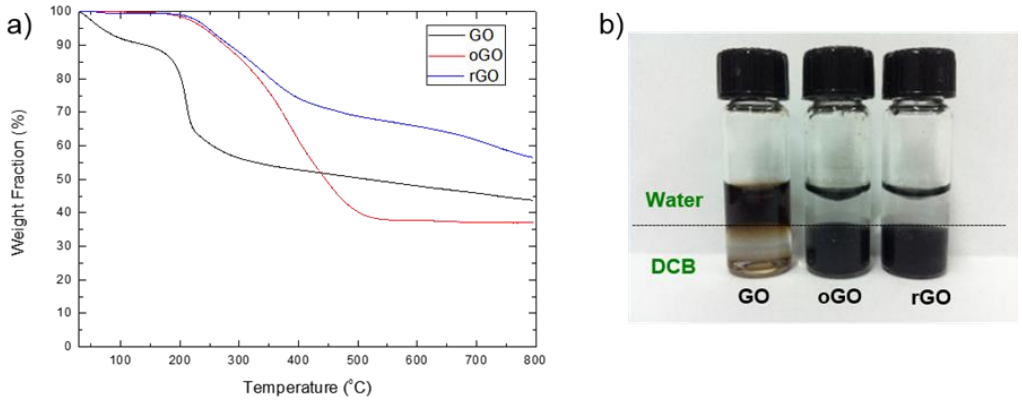

Fig. 6.S2. (Color) a) TGA curves of GO, oGO, and rGO. b) Photo image of GO, oGO, and rGO, dispersed in Water/DCB.

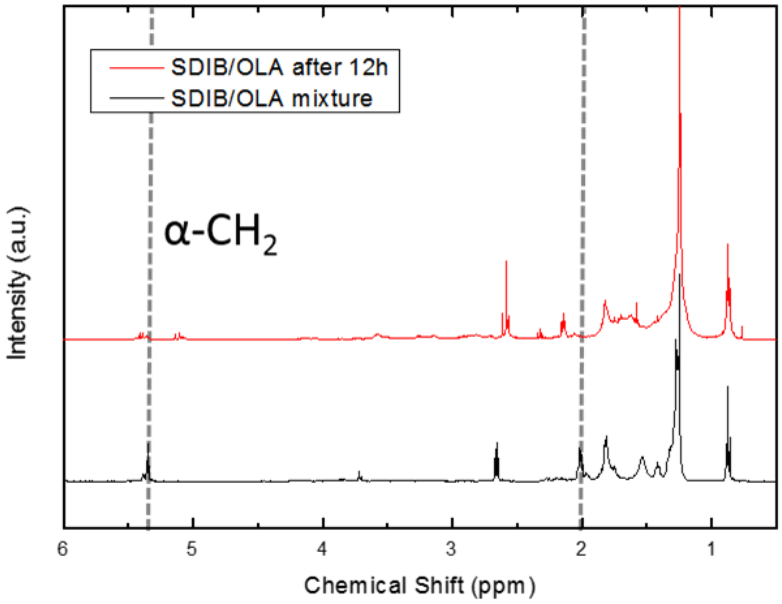

Fig. 6.S3. (Color) ^{1}H NMR shifts of SDIB/OLA mixtures measured before and after the reaction at 150℃ for 12 h

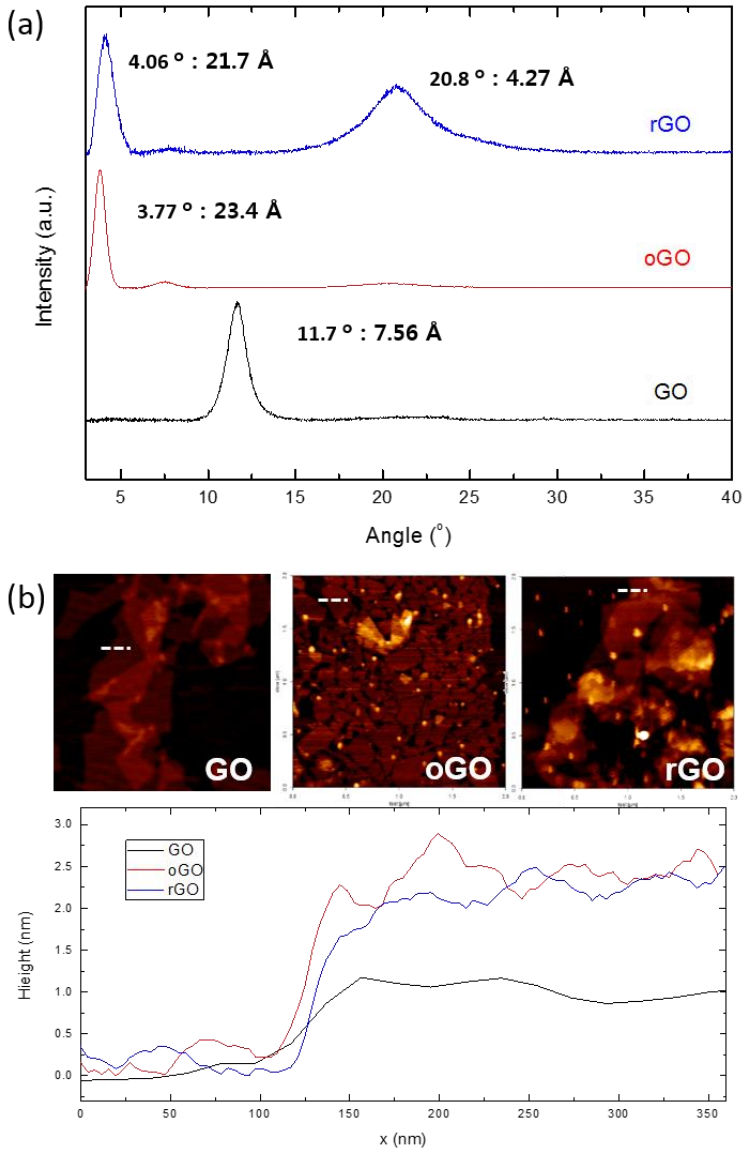

Fig. 6.S4. (Color) (a) XRD patterns and (b) AFM height measurements of GO, oGO, and rGO

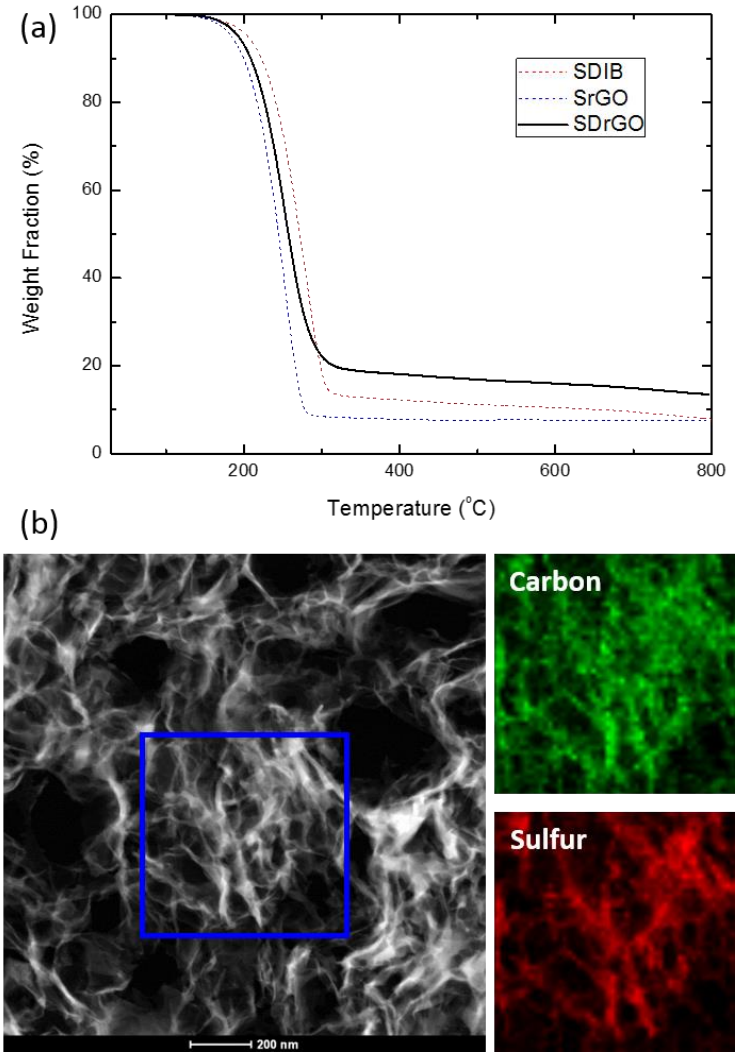

Fig. 6.S5. (Color) (a) TGA curves of Poly(S-r-DIB), Sulfur/rGO nanocomposites, and Poly(S-rDIB)/rGO nanocomposites. (b) STEM image and EDS elemental map of Poly(S-rDIB)/rGO nanocomposites

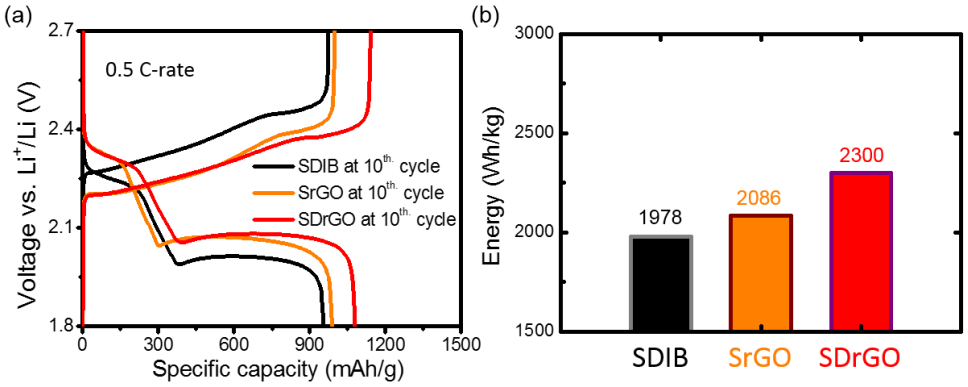

Fig. 6.S6. (Color) Charge-discharge profiles of (black) SDIB, (orange) SrGO, and (red) SDrGO at 10th. cycle applied 0.5 *C*-rate

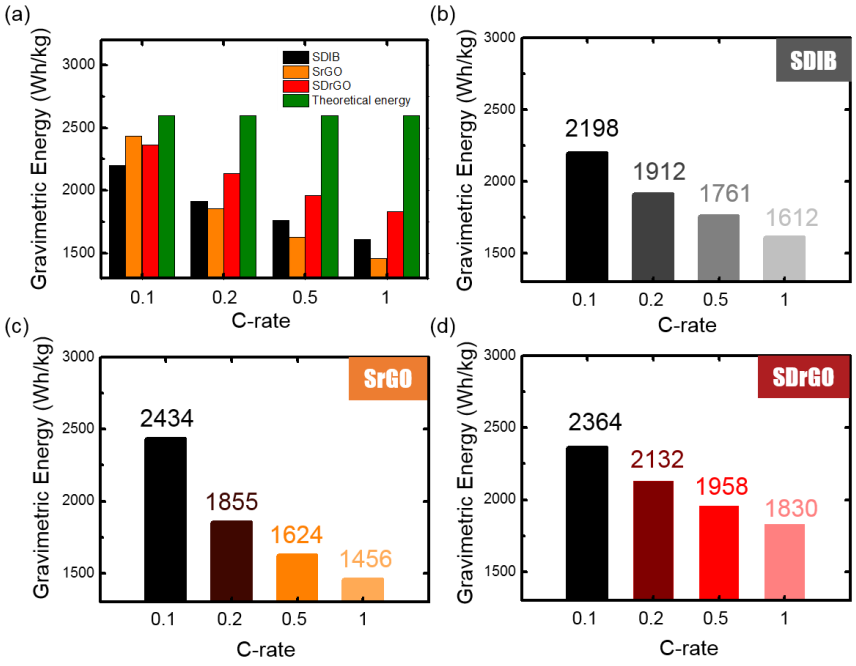

Fig. 6.S7. (Color) Gravimetric enerfy of (black) SDIB, (orange) SrGO, (red) SDrGO, (green) theoretical value at various *C*-rate (0.1 to 1 *C*)

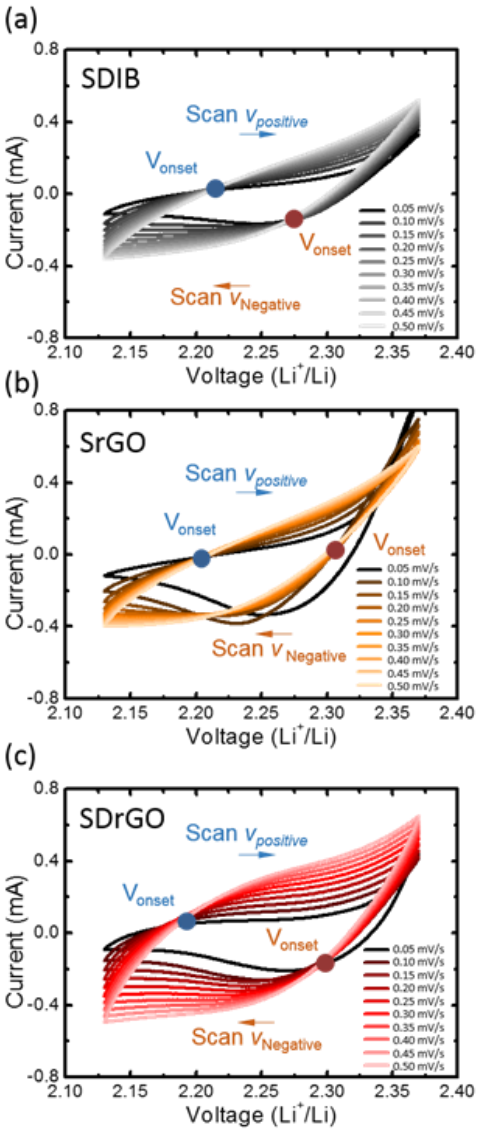

Fig. 6.S8. (Color) Cyclic Voltammetry of a, SDIB, b, SrGO, and c, SDrGO at various scan rate (0.05 mV/s to 0.5 mV/s) (potential windows, from 2.12 to 2.38 V *vs.* Li^+/Li)

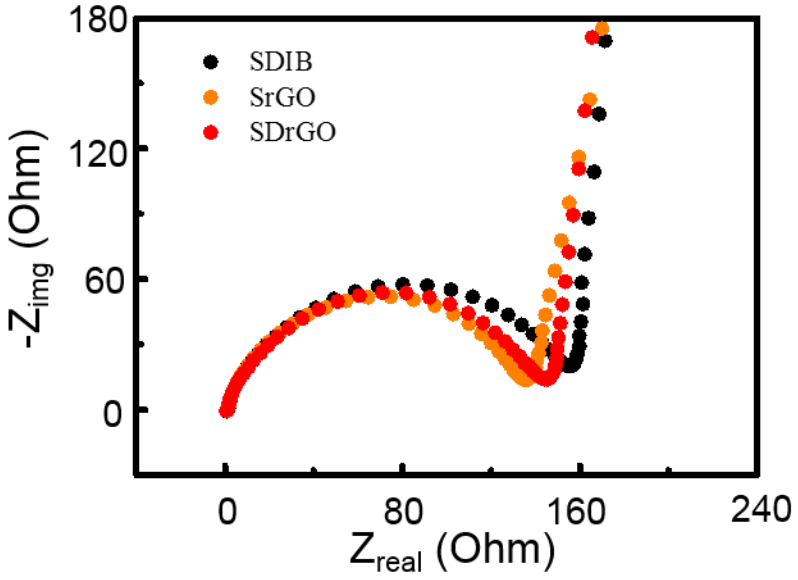

Fig. 6.S9 (Color) Electrochemical impedance spectroscopy (EIS) of (balck) SDIB, (orange) SrGO, and (red) SDrGO.

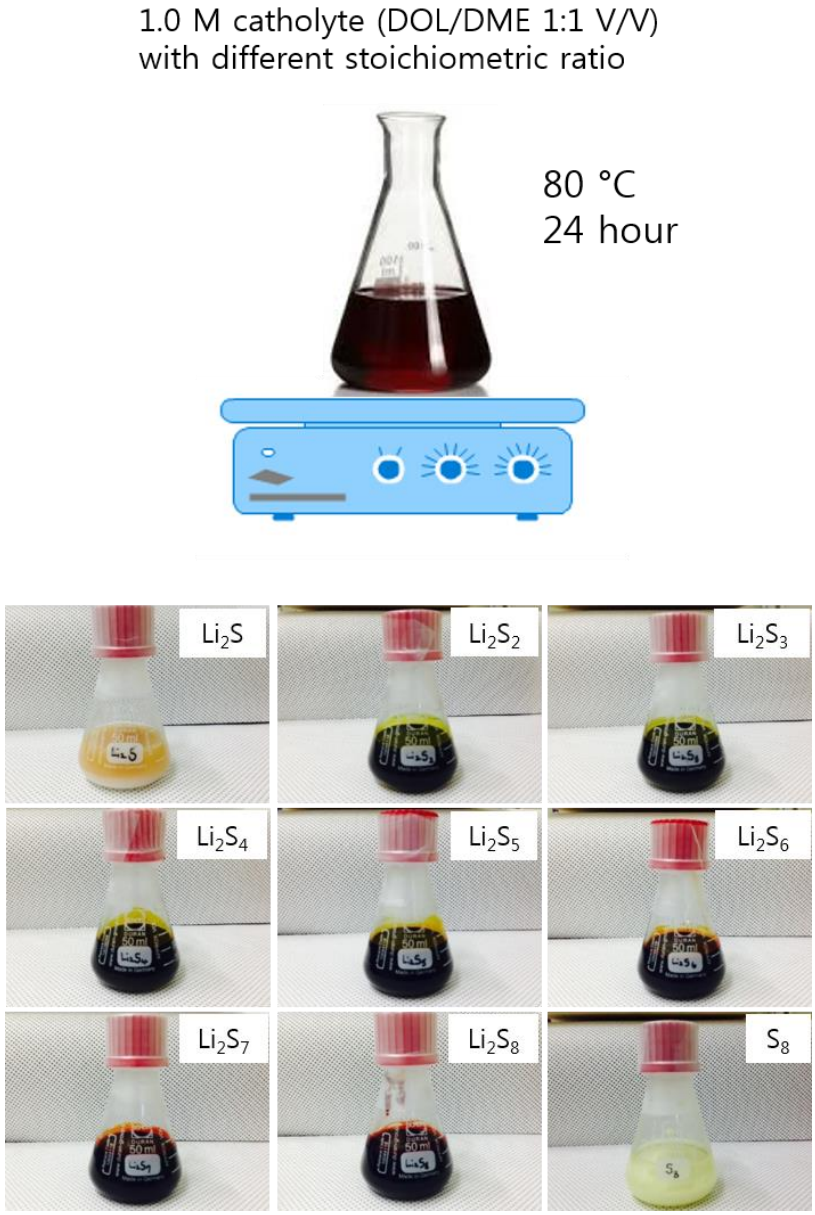

Appendix 6-S1. (Color) Catholyte synthesis

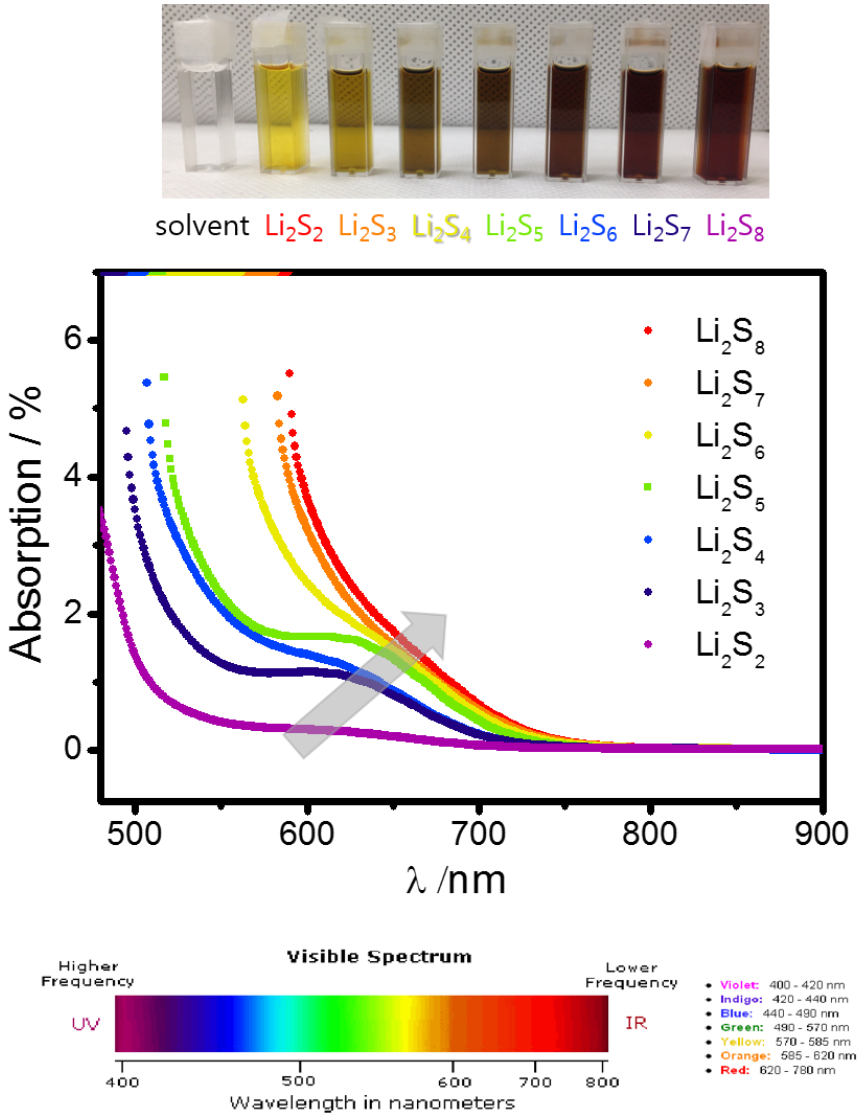

Appendix 6-S2. (Color) Spectra of UV-visible absorption of various polysulfide chain length in catholyte

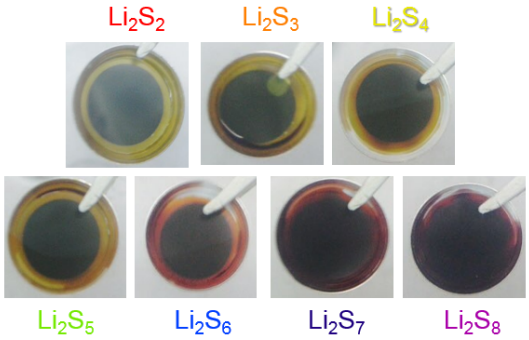

composition	Initial voltage
Li_2S_2	2.189
Li_2S_3	2.191
Li_2S_4	2.208
Li_2S_5	2.220
Li_2S_6	2.296
Li_2S_7	2.352
Li_2S_8	2.393

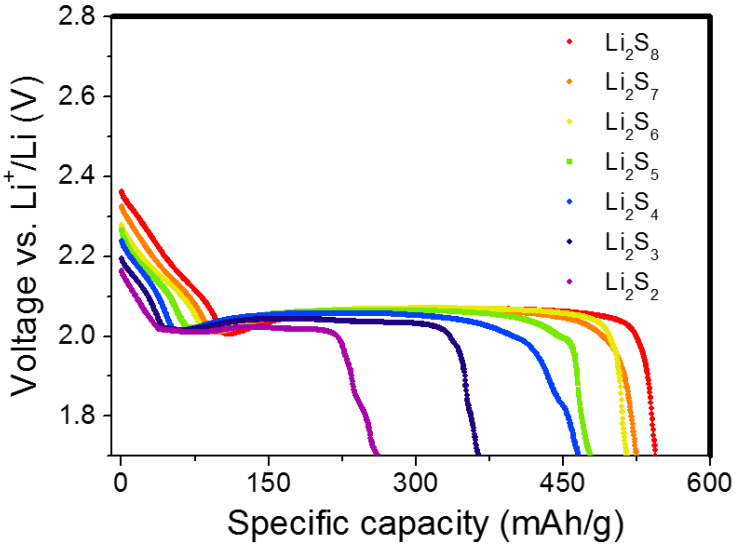

Appendix 6-S3. (Color) discharge profile and open circuit voltage (OCV) of various polysulfide chain length in catholyte

6.6. References

1. W. J. Chung, J. J. Griebel, E. T. Kim, H. Yoon, A. G. Simmonds, H. J. Ji, P. T. Dirlam, R. S. Glass, J. J. Wie, N. A. Nguyen, B. W. Guralnick, J. Park, A. Somogyi, P. Theato, M. E. Mackay, Y. E. Sung, K. Char and J. Pyun, *Nat. Chem.* **5**, 518-524 (2013).

2. P. T. Dirlam, A. G. Simmonds, T. S. Kleine, N. A. Nguyen, L. E. Anderson, A. O. Klever, A. Florian, P. J. Costanzo, P. Theato, M. E. Mackay, R. S. Glass, K. Char and J. Pyun, *Rsc Adv* **5**, 24718-24722 (2015).

3. J. J. Griebel, G. X. Li, R. S. Glass, K. Char and J. Pyun, *J. Polym. Sci. Pol. Chem.* **53**, 173-177 (2015).

4. A. G. Simmonds, J. J. Griebel, J. Park, K. R. Kim, W. J. Chung, V. P. Oleshko, J. Kim, E. T. Kim, R. S. Glass, C. L. Soles, Y.-E. Sung, K. Char and J. Pyun, *ACS Macro Lett.*, **3,** (3) 229–232 (2014).

5. S. Evers and L. F. Nazar, *Chem. Commun.*, **48**, 1233-1235 (2012).

6. L. W. Ji, M. M. Rao, H. M. Zheng, L. Zhang, Y. C. Li, W. H. Duan, J. H. Guo, E. J. Cairns and Y. G. Zhang, *J. Am. Chem. Soc.* **133**, 18522-18525 (2011).

7. T. Q. Lin, Y. F. Tang, Y. M. Wang, H. Bi, Z. Q. Liu, F. Q. Huang, X. M. Xie and M. H. Jiang, *Energy Environ. Sci.* **6**, 1283-1290 (2013).

8. Y. X. Wang, L. Huang, L. C. Sun, S. Y. Xie, G. L. Xu, S. R. Chen, Y. F. Xu, J. T. Li, S. L. Chou, S. X. Dou and S. G. Sun, *J. Mater. Chem.*, **22**, 4744-4750 (2012).

9. C. X. Zu and A. Manthiram, *Adv. Energy Mater* **3**, 1008-1012 (2013).

10. H. L. Wang, Y. Yang, Y. Y. Liang, J. T. Robinson, Y. G. Li, A. Jackson, Y. Cui and H. J. Dai, *Nano Lett*. **11**, 2644-2647 (2011).

11. H. W. Chen, C. H. Wang, W. L. Dong, W. Lu, Z. L. Du and L. W. Chen, *Nano Lett*. **15**, 798-802 (2015).

12. Z. Y. Wang, Y. F. Dong, H. J. Li, Z. B. Zhao, H. B. Wu, C. Hao, S. H. Liu, J. S. Qiu and X. W. Lou, *Nat. Commun*. **5 (**2014).

13. S. Y. Zheng, Y. Wen, Y. J. Zhu, Z. Han, J. Wang, J. H. Yang and C. S. Wang, *Adv. Energy Mater*. **4** (2014).

14. W. J. Chung, A. G. Simmonds, J. J. Griebel, E. T. Kim, H. S. Suh, I. B. Shim, R. S. Glass, D. A. Loy, P. Theato, Y. E. Sung, K. Char and J. Pyun, *Angew. Chem. Int. Edit.* **50**, 11409-11412 (2011).

15. E. T. Kim, W. J. Chung, J. Lim, P. Johe, R. S. Glass, J. Pyun and K. Char, *Polym. Chem.-Uk* **5**, 3617-3623 (2014).

16. J. Liu, H. Jeong, J. Liu, K. Lee, J. Y. Park, Y. H. Ahn and S. Lee, *Carbon* **48**, 2282-2289 (2010).

17. K. K. Yang, S. Liang, L. F. Zou, L. W. Huang, C. Park, L. S. Zhu, J. Y. Fang, Q. Fu and H. Wang, *Langmuir* **28**, 2904-2908 (2012).

Chapter 7.

Copolymerization of Polythiophene and Sulfur to Improve Electrochemical Performance in Lithium-Sulfur Batteries

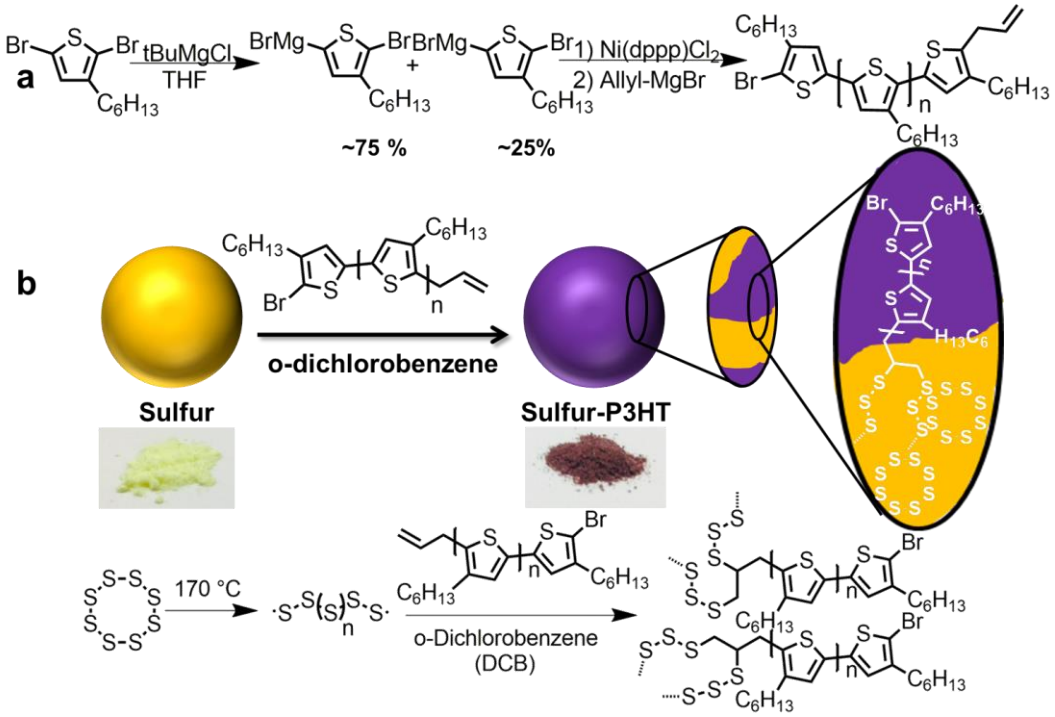

Fig. 7.T. (Color) a) Synthesis of allyl-terminated P3HT applying GRIM polymerization. b) Copolymerization of allyl-terminated P3HT and sulfur.

7.1. Introduction

7.1.1. Previous Studies

Currently, Li-ion rechargeable batteries are considered promising energy storage devices to tackle problems related to the exhaustion of fossil fuels based energy resources.[1] However, Li-ion batteries that commonly contain graphite as an anode and lithium cobalt oxide as a cathode material have a limitation to the specific capacity and energy density. In addition, cobalt containing materials are neither economically nor environmentally friendly. To meet the extensively growing demand of high energy storage devices for electric vehicles, energy storage system (ESS), and artificially bio-medical equipment, the substitution of the currently used electrode materials would be necessary in a timely manner. The lithium sulfur battery with a theoretical specific energy more than six times higher than the current Li-ion battery is one of the most promising candidates to solve these issues, additionally, as sulfur is a very abundant, cheap and non-harmful material.[2,3] However, lithium-sulfur batteries still suffer from several issues, including the insulating nature of sulfur, the volume expansion, unique reaction processes (dissolution/precipitation of active material) during (de-)lithiation, and the so called "shuttle" mechanism,[4,2] which cause capacity decay by irreversible loss of reaction species and/or sites. So far, several approaches were tried to increase the electrical conductivity and prevent the loss of the soluble polysulfides, for instance conductive polymer coating or encapsulating sulfur by various carbonaceous materials such as mesoporous carbon, hollow carbon particles, carbon nanotubes, and graphene based materials, which possibly interact with the polysulfides.[5] Recently, an experimentally

simple approach based on the so-called inverse vulcanization using 1,3-diisoproenylbenzene (DIB) for a radical copolymerization with a molten sulfur radical species resulting in polymeric sulfur materials has been introduced, which exhibited an improved battery performance compared to pure sulfur.[6] The extension of this approach to a tandem inverse vulcanization resulted in an electropolymerization derived polythiophene incorporated in a sulfur-DIB copolymer with a reduced charge transfer resistance.[7]However, the detailed study about the structure and chain length of the resulting oligo- or polythiophenes is not yet reported. Furthermore, the composite material contains a relatively low sulfur loading (50 wt.% after inverse vulcanization), thus it was not practical as a cathode material in lithium-sulfur batteries.

7.1.2. Material Selections

Herein, we are firstly introducing the copolymerization of well-defined allyl-terminated poly(3-hexylthiophene-2,5-diyl) (P3HT) synthesized by Grignard metathesis polymerization with an excess of molten sulfur radicals resulting in the S-P3HT composite, where P3HT copolymers are embedded in a sulfur matrix. This S-P3HT allows the homogeneous incorporation of a well-defined semi-conductive material into sulfur as well as the formation of a stable framework. In this communication, the detailed structure of the S-P3HT composite were studied by various analytical tools, which confirmed the covalent link between sulfur and carbon black in the S-P3HT composite. The covalent linkage led to the enhanced battery performance by effective stabilization of the electrodes during the battery operation. This work clearly demonstrates that the homogeneous composite of P3HT and sulfur at the nanoscale can

be synthesized and assembled into the electrodes for high performance Li-S batteries.

7.2. Experimental Section

Reagents: Tert. butylmagnesium bromide (tBuMgCl**,** 1.0 M in THF), allylmagnesium chloride (2.0 M in THF), [1,3-Bis(diphenylphosphino) propane]dichloronickel(II) ($Ni(dppp)Cl_2$), N-bromosuccinimide (NBS, 99 %), and *o*-dichlorobenzene (DCB, 99 %) were purchased from Sigma Aldrich, 3-hexylthiophene was purchased from TCI. NBS was recrystallized from water. All solvents were dried before use.Polyvinylidene fluoride (PVDF) binder (Sigma Aldrich),Conductive carbon (Super C65, Timcal), Lithium bis(trifluoromethane) sulfonimide (Sigma Aldrich), Lithium nitrate (Sigma Aldrich), Polypropylene separator (Celgard), Lithium foil (FMC), 1,3-Dioxolane (Novolyte) and 1,2-Dimethoxy ethane (Novolyte) were used as received.

Synthesis of allyl-terminated P3HT: The monomer 2,5-dibromo-3-hexlthiophene w as synthesized according to literature. Briefly, NBS (18.25 g, 98,7 mmol) was solv ed in DMF and added to a solution of 3-hexylthiophene (8.00 g, 47.7 mmol) in c hloroform. The reaction was stirred under argon over night at 60 ℃. The reaction mixture was purified first by extracting with diethyl ether and then by column c hromatography (petrolether; R_f of the product: 0.8). The yield of the colorless pro duct was 71%.

^{1}H-NMR (400 MHz, $CDCl_3$): δ [ppm] = 6.80 (s, 1H), 2.53 (t, *J*= 8.0 Hz, 2H), 1.57 (m, 1H), 1.34 (m, 6H), 0.92 (m, 3H).

The polymerization was conducted following a previous description. 2,5-dibromo-3-hexlthiophene (600 mg, 1,84 mmol), 4.2 mlTHF and tBuMgCl (1.75 mmol) were

stirred under argon for 20 h at room temperature. Afterwards the reaction mixture was diluted with 9 ml of THF and 25.6 mg of Ni(dppp)Cl_2 (0.05 mmol) was added to start the polymerization, whereby the reaction mixture turns from slightly yellow to red. Allylmagnesium chloride (1.5 mmol) was added after 10 minutes and the reaction mixture was stirred for further 5 minutes. The polymer was precipitated in methanol. After centrifugation and drying, the polymer was purified by soxhlet extraction using first methanol, then hexane and finally chloroform. Typically, the yield is around 50 %.

^{1}H-NMR (400 MHz, $CDCl_3$): δ [ppm] = 7.01 (s, 31 H), 6.00 (m, 1H), 5.16 (m, 2H), 3.54 (d,*J*= 4.0 Hz 2H), 2.84 (bs, 62H), 1.74 (bs, 63H), 1.45-1.29 (bm, 192 H), 0.95 (bs, 96 H).

^{13}C-NMR: (400 MHz, $CDCl_3$): δ [ppm] =140.0, 133.8, 136.5 (end-group), 130.6, 128.7, 116.3 (end-group), 32.3 (end-group), 31.9, 30.7, 29.6, 29.4, 22.8, 14.2.

SEC: M_n(P3HT)= 9,450 g mol^{-1}, Đ : 1.08.

Elemental analysis: Calculated for allyl-terminated P3HT:C: 72.29, H: 9.43, S: 19.28; found: C: 71.86, H: 10.47, S: 17.67.

Synthesis of S- P3HT: Allyl-terminated P3HT was dissolved in DCB and added to an excess of sulfur, whereby the weight ratio between S and P3HT was varied between S: P3HT of 9.5:0.5, 9:1, 8:2. The reaction mixture was stirred for 1 h at 170 °C. After the complete conversion as detected by NMR, the reaction mixture was quenched in methanol. After centrifugation the product was dried under reduced pressure. The product can be obtained almost quantitatively.

^{1}H-NMR (400 MHz, , $CDCl_3$): δ [ppm] = 6.98 (s, 31 H), 3.2-3.8 (m), 2.80 (s, 62H), 1.74

(s, 63H), 1.45-1.20 (m, 192 H), 0.95 (s, 96H).

^{13}C-NMR: (400 MHz, $CDCl_3$): δ [ppm] =140.0, 133.8, 130.6, 128.7, 120.0 (end-group) 31.9, 30.7, 29.6, 29.4, 29.1 (end-group), 22.8, 14.2

SEC:M_n(S-P3HT)= 10,300 g mol^{-1}, Đ : 1.13

Elemental analysis: Found: C: 67.59, H: 9.43, S: 22.98.

Electrochemical characterization: S-P3HT copolymer containing compositions(S-P3HT/CB P) were mixed with the binder (polyethylene) and conductive carbon (Super P) so that the mixture ratio was fixed to S:(P3HT+conductive carbon):polyethylene=70:25:5. The S-P3HT mixtures were ball milled for 30 minutes to pulverize and homogenize particles and then mixed with binder and carbon. Chloroform (2 ml) was added as a solvent. The slurry was casted on aluminum foil by doctor blading method and dried underair. The sulfur loading was commonly around 1 mg/cm^2. The reference electrodes containing S/P3HT/CB M and S/CB M respectively were prepared in the same waywith the same composition (i.e. S:(P3HT+conductive carbon):polyethylene=70:25:5) and the sulfur loading was commonly around 1 mg/cm^2 as well.

The prepared electrodes were used to assemble CR2032 coin cells in an argon filled glove box. The polypropylene separator was supported by SK innovation corp. The electrolyte composition was 1.0 M lithium bis(trifluoromethane)sulfonamide (LiTFSI), and 0.1 M lithium nitrate in a 1:1 (v/v) mixture of 1,3-dioxolane and 1,2-dimethoxy ethane (Panax Etec, Korea).

The evaluation of the electrochemical performance was conducted by the use of a WBCS3000 battery tester (Won-A Tech, Korea) in avoltage range from 1.7 to 2.8 V *vs*.

Li^+/Li. Electrochemical impedance spectroscopy (EIS) measured at the charged state and the frequency range was fixed to 100kHz to 10mHz at the open circuit voltage (OCV). The AC amplitude was set to be 10 mV. Cyclic voltammetry wasconductedat various scan rates (from 41 μV to 2,080μV) and for each scan rate 5 cycles were operated, whereby only the 5^{th} cycles are shown in Figure 3.

7.3. Results and Discussion

7.3.1. Materials Characterization

Herein, we are firstly introducing the copolymerization of well-defined allyl-terminated poly(3-hexylthiophene-2,5-diyl) (P3HT) synthesized by Grignard metathesis polymerization with an excess of molten sulfur radicals resulting in the S-P3HT composite, where P3HT copolymers are embedded in a sulfur matrix. This S-P3HT allows the homogeneous incorporation of a well-defined semi-conductive material into sulfur as well as the formation of a stable framework. In this communication, the detailed structure of the S-P3HT composite were studied by various analytical tools, which confirmed the covalent link between sulfur and carbon black in the S-P3HT composite. The covalent linkage led to the enhanced battery performance by effective stabilization of the electrodes during the battery operation. This work clearly demonstrates that the homogeneous composite of P3HT and sulfur at the nanoscale can be synthesized and assembled into the electrodes for high performance Li-S batteries.

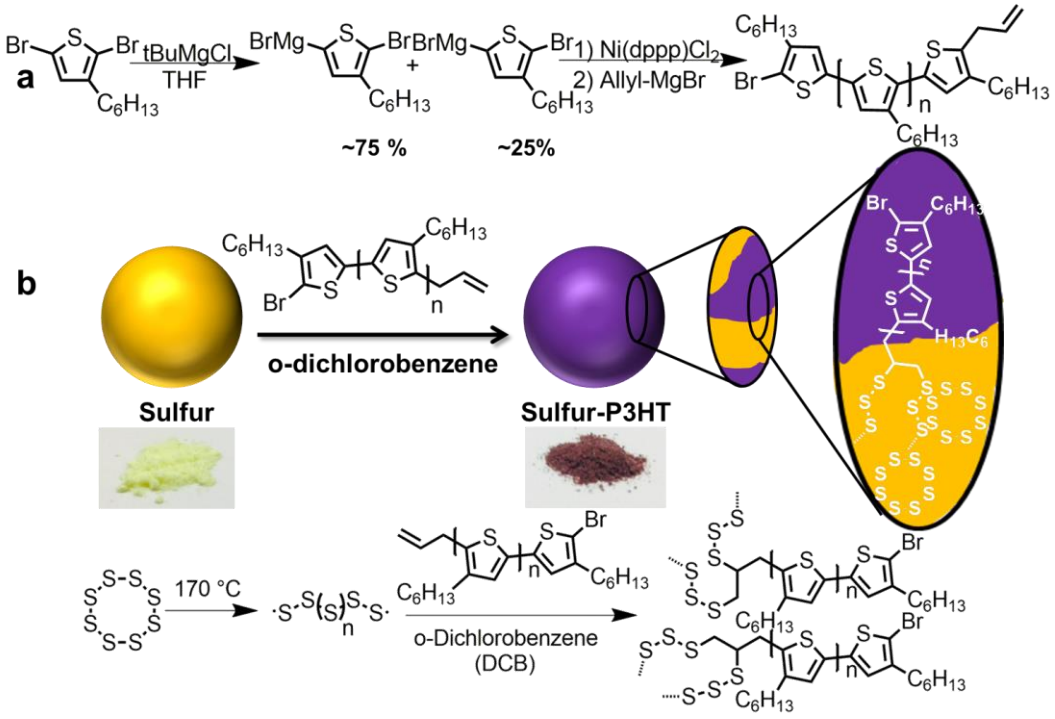

Fig. 7.1. (Color) Synthetic scheme for the inverse vulcanization process yielding poly(sulfur-random-1,3-diisopropenylbenzene) copolymers.

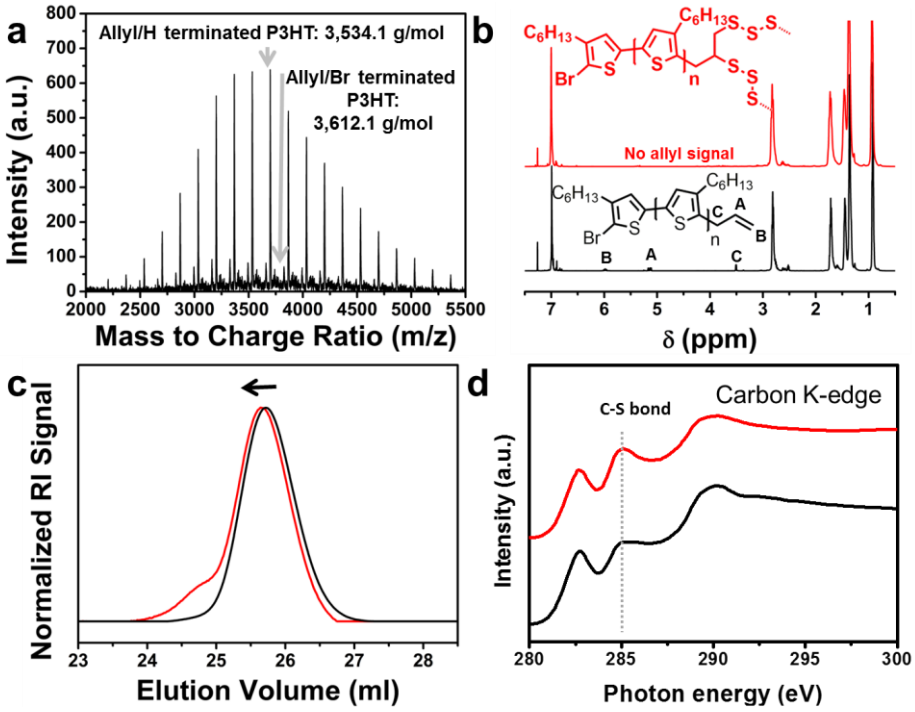

Fig. 7.1. (Color) (a) MALDI-TOF spectrum of allyl-terminated P3HT. NMR spectra (b) and SEC elugram (c) and near edge X-ray absorption fine spectra (NEXAFS) (d) of P3HT/S/CB mixture (black) and S-P3HT/CB copolymer composite (red).

7.3.2. Electrochemical Analysis

In order to investigate the effect of the covalent linkage of P3HT to sulfur on the battery performance, three different electrodes were applied as a cathode material. S, sulfur and P3HT mixture (S/P3HT), and S-P3HT were thoroughly mixed with carbon black to prepare the cathode electrode and each can be abbreviated as S/CB, S/P3HT/CB, and S-P3HT/CB, respectively. In all electrodes, the amount of the conductive material, i.e. the sum of carbon black and P3HT, was set to be 25 wt. %. As shown in Figure 3a, initial specific capacities of S/CB, S/P3HT/CB, and S-P3HT/CB are 1260 $mAhg^{-1}$, 1154 $mAhg^{-1}$, and 1212 $mAhg^{-1}$ at 0.5C (1C is defined as 1675 mA g^{-1}), respectively. Slightly higher initial capacity of S/CB can be achieved due to the higher electrical conductivity of CB than P3HT. However, as cycles go on, S-P3HT/CB exhibits a superior cycling performance compared with S/CB and S/P3HT/CB. S/CB and S-P3HT/CB electrodes show a rapid drop of capacity within the first 20 cycles to 696 mAh g^{-1} and 754 mAh g^{-1}, respectively. In contrast, the capacity of S-P3HT/CB is 877 mAh g^{-1} after 20 cycles and preserved with very little decay upon further cycling. The capacity of S-P3HT/CB after 100 cycles is still achieved with 799 mAh g^{-1} compared to 482 mAh g^{-1} (S/CB) and 544.70 mAh g^{-1} (S/P3HT/CB). P3HT is homogeneously incorporated into the sulfur particles as shown in scanning electron microscopy (SEM) images (see Figure 7.S6), and XRD data (Figure 7.S7). As sulfur and P3HT are intrinsically not miscible, we assume that a homogeneous incorporation might be possible for the S-P3HT copolymer due to a self-assembly of the S-P3HT copolymers on a nanometer scale (as schematically shown in Figure 7.1 b). It seems that homogeneous incorporation of P3HT into sulfur and

corresponding strong interaction between them can stabilize the electrode against irreversible loss of polysulfides during the repeated cycles. The capacity retention can be even slightly increased by increasing the amount of P3HT used during copolymerization as shown in Figure 7.S10, where a capacity of 838 mAh g^{-1} can be obtained for a sample synthesized with a weight ratio S:P3HT 8:2 after 100 cycles.

Figure 7.3 b displays the charge/discharge profiles after 10 cycles, which can provide information about the overpotential of each sample. While S/P3HT/CB exhibits serious increase of overpotential, the S-P3HT/CB electrode shows an similar overpotential to S/CB. The similar overpotential from S-P3HT/CB and S/CB can be understood that lower conductivity of P3HT than CB can be compensated by easily accessible reaction sites as the homogeneous incorporation of P3HT was introduced into the S-P3HT composite at the nanoscale dimension. Electrochemical impedance spectroscopy (EIS) data also confirms the charge transfer kinetics among the electrodes as shown in Figure 7.S6. The semicircle on the Z_{re} axis corresponding to the charge transfer resistance is the smallest for S/P3HT/CB, whereas the semicircle of S/P3HT/CB is significantly larger.

Furthermore, the S-P3HT/CB electrode exhibits an improved C-rate capability as shown in Figure 3c. Significantly higher specific capacities can be obtained for all applied currents in the case of S-P3HT/CB. 739.41 mAh g^{-1} at 1C was obtained in the S-P3HT/CB whereas S/P3HT/CB and S/CB electrodes revealed lower capacities of 527 mAh g^{-1} and 501 mAh g^{-1}, respectively.

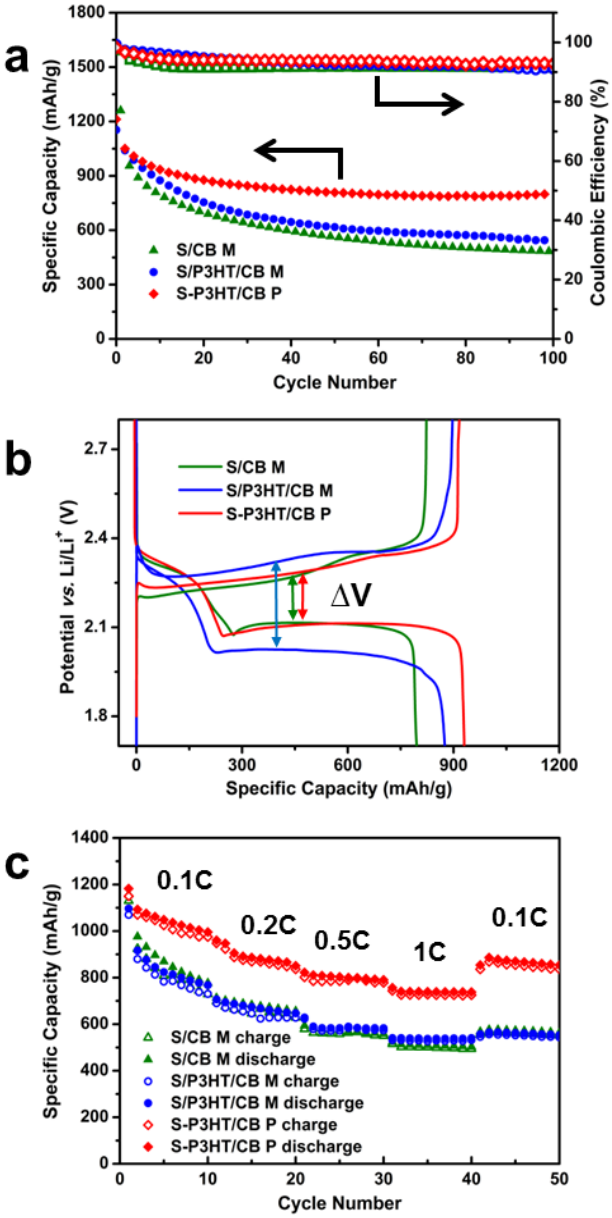

Fig. 7.3. (Color) a) Cycling performance, b) potential profiles and C-rate performance of of S/CB M (green), S/P3HT/CB M (blue) and S-P3HT/CB P (red).

7.4. Conclusions

The structural integrity at the nanoscale of S-P3HT/CB accounts for the enhanced rate capability by shortened diffusion length of reactant. In summary, we introduced the copolymerization of allyl-terminated P3HT with sulfur enabled by a radical reaction between the allyl end-group and a radical sulfur species. This approach allows the covalent linkage of sulfur and P3HT yielding in S-P3HT copolymer homogeneously distributed in a sulfur matrix. The homogeneous incorporation of this semiconducting polymer lowers the electrical resistance, thus, an improved battery performance can be observed for S-P3HT copolymer containing electrodes.

7.5. Supporting Informations

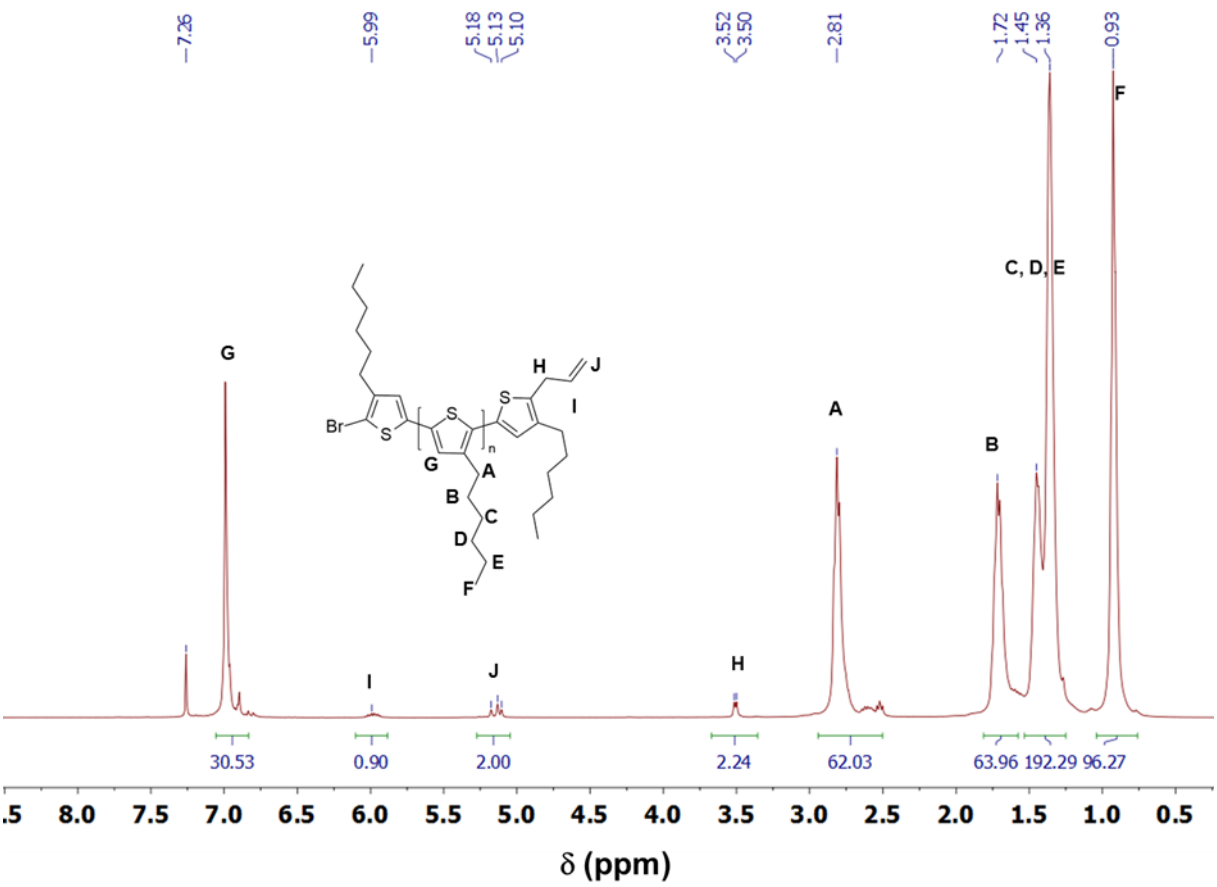

Fig. 7.S1. (Color) ^{1}H-NMR spectrum of allyl-terminated P3HT.

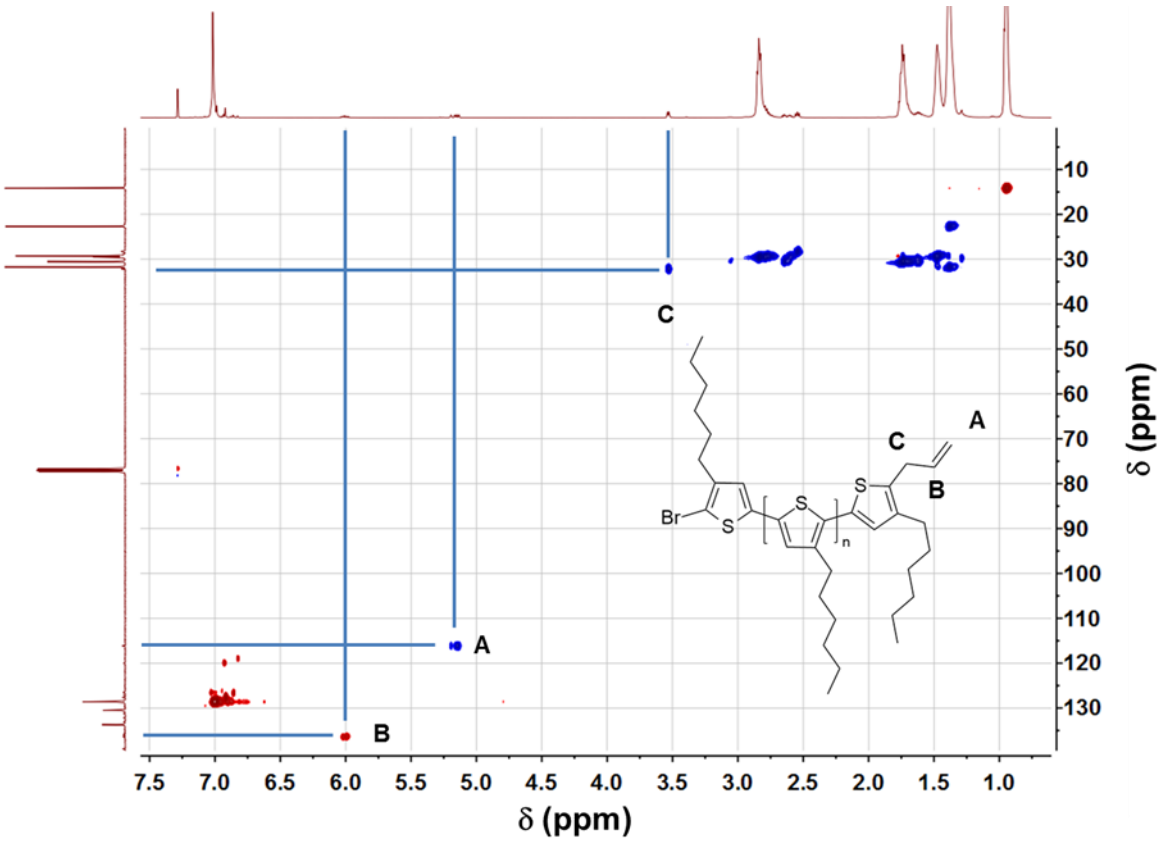

Fig. 7.S2. (Color) Heteronuclear single quantum coherence (HSQC) spectrum of allyl-terminated P3HT.

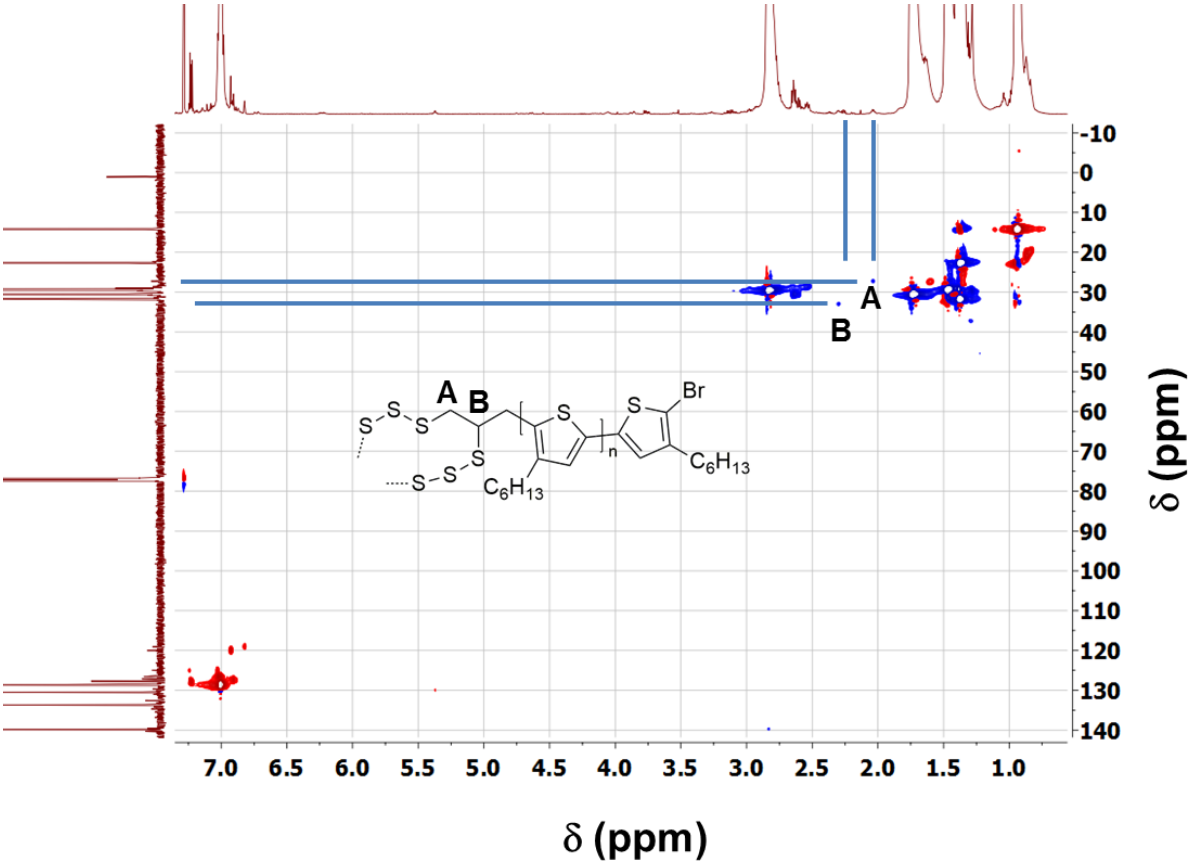

Fig. 7.S3. (Color) Heteronuclear single quantum coherence (HSQC) spectrum of S-P3HT(2).

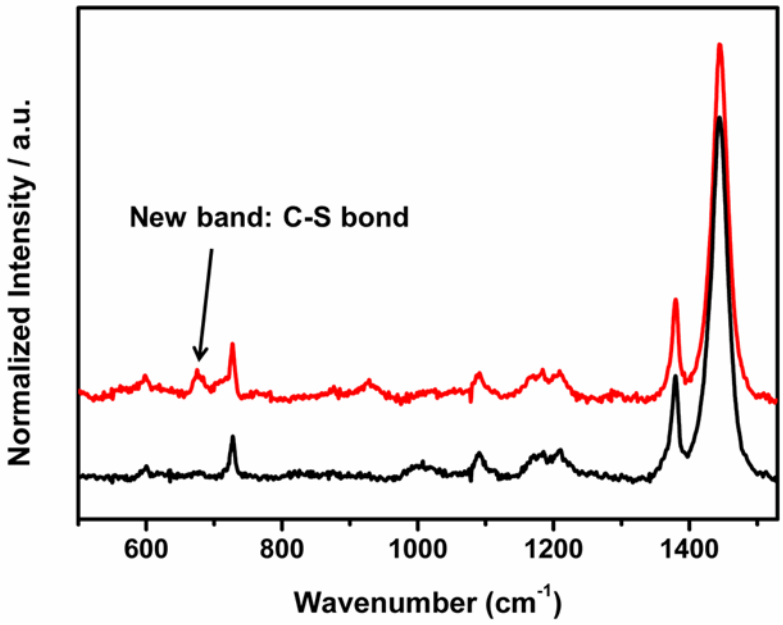

Fig. 7.S4. (Color) Heteronuclear single quantum coherence (HSQC) spectrum of S-P3HT(2).

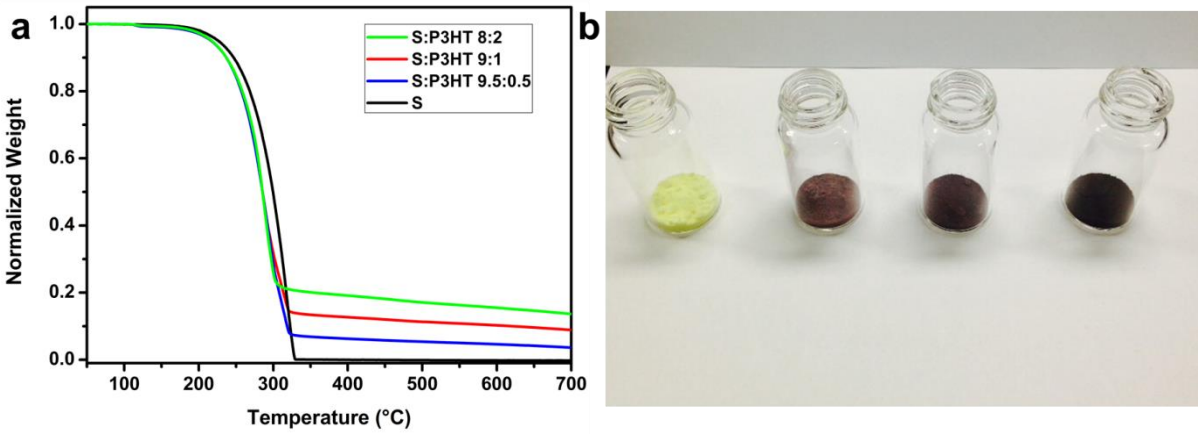

Fig. 7.S5. (Color) a) Thermogravimetric analysis of S:P3HT 8:2 (green), S:P3HT 9:1 (red), S:P3HT 9.5:0.5 (blue) and pure sulfur (black). B) Foto of samples with different P3HT content: from left to right: S, S:P3HT 9.5:0.5, S:P3HT 9:1, S:P3HT 8:2.

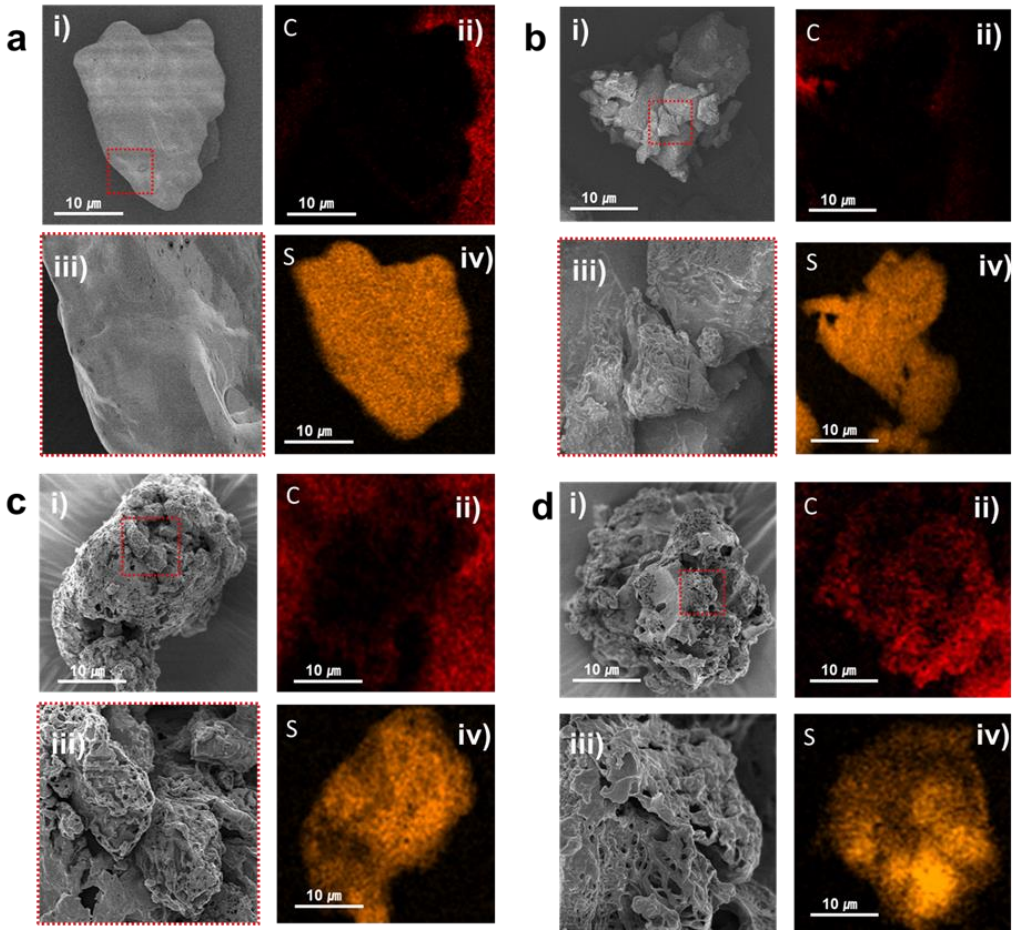

Fig. 7.S6. (Color) Scanning electron micrsocopy image and energy dispersive X-ray spectroscopy analysis of sulfur (a), S-P3HT(0.5) (b), S-P3HT(1) (c), and S-P3HT(2) (d) showing SEM images with low(i) and high (iii) resolution and corresponding elemental mapping of S (ii) and C of SEM image in i) showing an increasing homogeneously C content and decreasing S content with an increasing P3HT content.

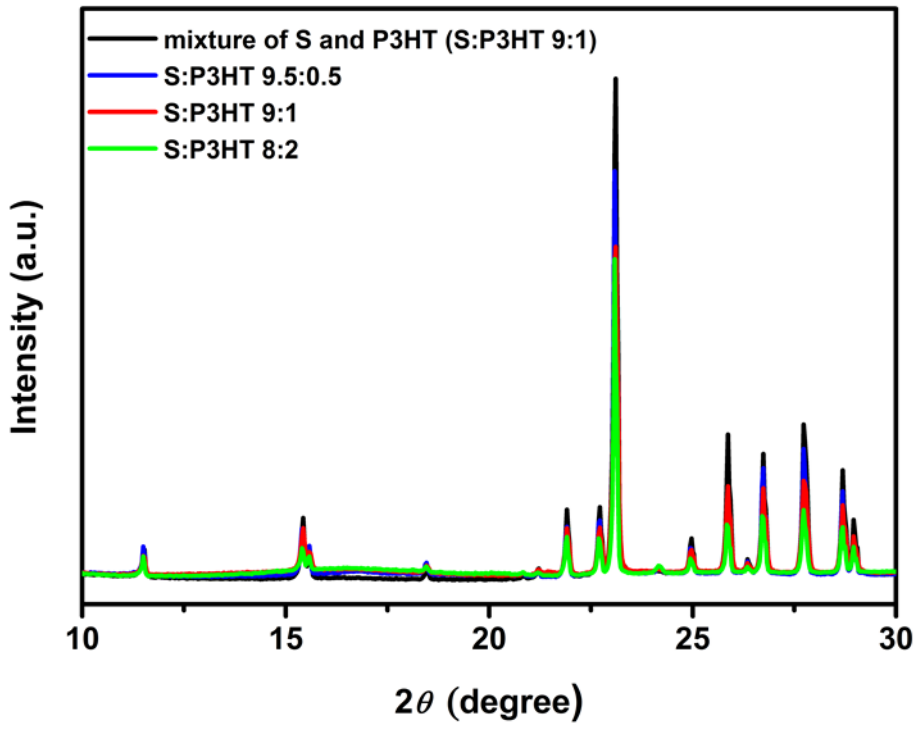

Fig. 7.S7. (Color) XRD patterns for a mixture of S and P3HT as well as for composites containing different ratios of S and P3HT applied during synthesis proving an decreased intensity for incorporated P3HT with increasing P3HT content due to covalent linkage and homogeneous incorporation.

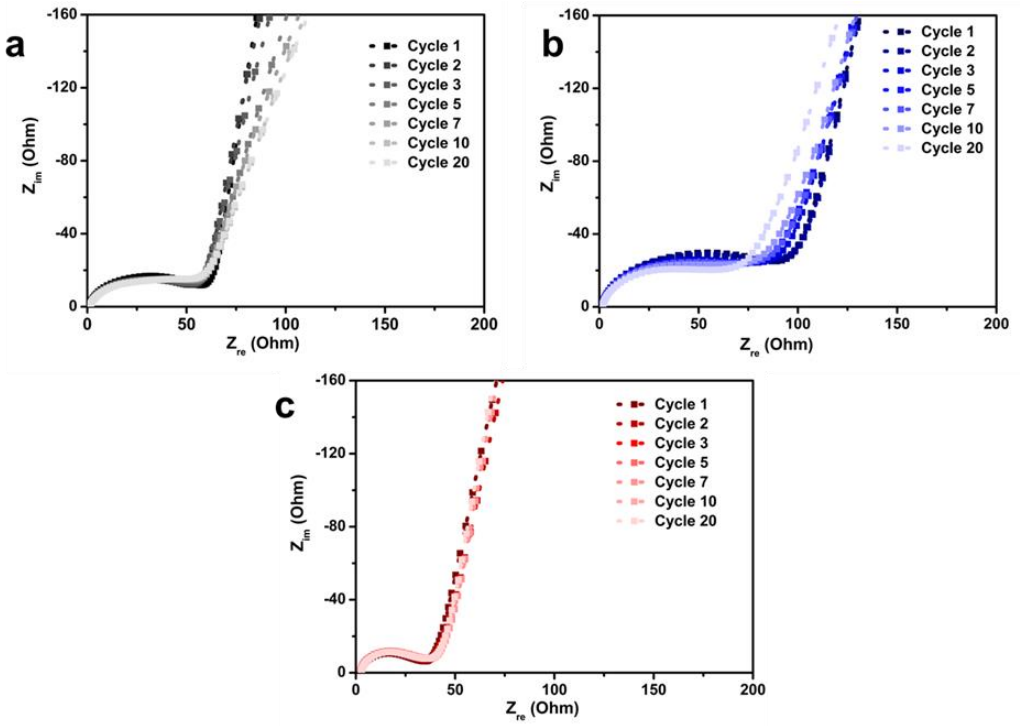

Fig. 7.S8. (Color) Electrochemical impedance spectroscopy of selected cycles of S/P3HT/CB M (a), of S/CB M based electrodes (b), and ofS-P3HT/CB P(c).

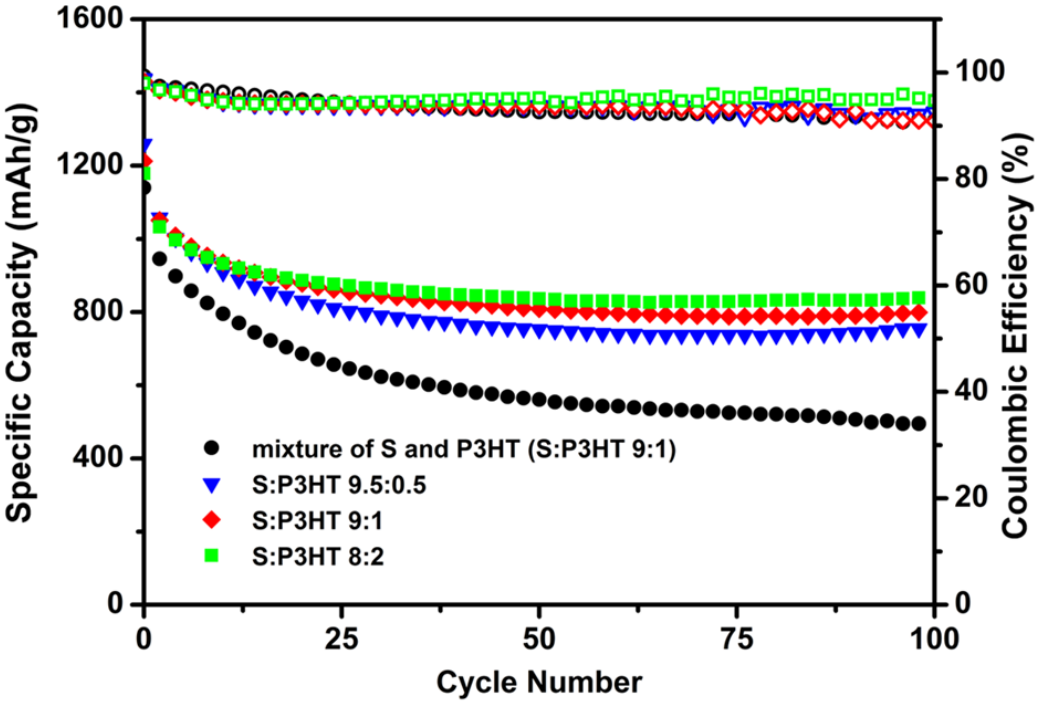

Fig. 7.S9. (Color) Galvanostatic cycling of different S-P3HT copolymer containing compositions and comparison to physically mixed S and P3HT.

7.6. References

1. Armand, M., Tarascon, J.-M., *Nature* **451** (7179), 652–657 (2008).

2. Bresser, D., Passerini, S., Scrosati, B., *Chem. Commun.* **49** (90), 10545 (2013).

3. a) Evers, S., Nazar, L. F., *Acc. Chem. Res.* **46** (5), 1135–1143 (2013). b) Bruce, P. G., Freunberger, S. A., Hardwick, L. J., Tarascon, J.-M., *Nat Mater.* **11** (1), 19–29 (2011).

4. a) Mikhaylik, Y. V., Akridge, J. R., *J. Electrochem. Soc.* **151** (11), 1969–1976 (2004). b) Manthiram, A., Fu, Y., Su, Y.-S., *Acc. Chem. Res.* **46** (5), 1125–1134 (2013).

5. a) Yang, Y.; Yu, G., Cha, J. J.; Wu, H.; Vosgueritchian, M.; Yao, Y.; Bao, Z.; Cui, Y., *ACS Nano* **5** (11), 9187–9193 (2011). b) Wang, J.; Yang, J.; Xie, J.; Xu, N. *Adv. Mater.* **14** (13-14), 963–965 (2002). c) Wu, F.; Chen, J.; Chen, R.; Wu, S.; Li, L.; Chen, S.; Zhao, T., *J. Phys. Chem. C.* **115** (13), 6057–6063 (2011). d) He, G.; Ji, X.; Nazar, L., *Energy Environ. Sci.* **4** (8), 2878 (2011). e) Ji, X.; Lee, K. T.; Nazar, L. F. *Nat Mater.* **8** (6), 500–506 (2009). f) Zheng, G.; Yang, Y.; Cha, J. J.; Hong, S. S.; Cui, Y., *Nano Lett.* **11** (10), 4462–4467 (2011). g) Cao, Y.; Li, X.; Aksay, I. A.; Lemmon, J.; Nie, Z.; Yang, Z.; Liu, J., *Phys. Chem. Chem. Phys.* **13** (17), 7660 (2011). h) Evers, S.; Nazar, L. F., *Chem. Commun.* **48** (9), 1233 (2012). i) Wang, J.-Z.; Lu, L.; Choucair, M.; Stride, J. A.; Xu, X.; Liu, H.-K., *J. Power Sources* **196** (16), 7030–7034 (2011). j) Ma, L.; Zhuang, H.; Lu, Y.; Moganty, S. S.; Hennig, R. G.; Archer, L. A., *Adv. Energy Mater.* **4**, 17 (2014)

6. a) Chung, W. J.; Griebel, J. J.; Kim, E. T.; Yoon, H.; Simmonds, A. G.; Ji, H. J.;

Dirlam, P. T.; Glass, R. S.; Wie, J. J.; Nguyen, N. A.; Guralnick, B. W.; Park, J.; Somogyi, Á.; Theato, P.; Mackay, M. E.; Sung, Y.-E.; Char, K.; Pyun, J., *Nature Chem.* **5** (6), 518–524 (2013). b) Simmonds, A. G.; Griebel, J. J.; Park, J.; Kim, K. R.; Chung, W. J.; Oleshko, V. P.; Kim, J.; Kim, E. T.; Glass, R. S.; Soles, C. L.; Sung, Y.-E.; Char, K.; Pyun, J., *ACS Macro Lett.*, 229–232 (2014).

7. Dirlam, P. T.; Simmonds, A. G.; Shallcross, R. C.; Arrington, K. J.; Chung, W. J.; Griebel, J. J.; Hill, L. J.; Glass, R. S.; Char, K.; Pyun, J., *ACS Macro Lett.*, 111–114 (2015).

8. Nie, Y.; Zhao, B.; Tang, P.; Jiang, P.; Tian, Z.; Shen, P.; Tan, S., *J. Polym. Sci. A Polym. Chem.* **49** (16), 3604–3614 (2011).

9. Loewe, R. S.; Khersonsky, S. M.; McCullough, R. D., *Adv. Mater.* **11** (3), 250–253 (1999).

10. Loewe, R. S.; Ewbank, P. C.; Liu, J.; Zhai, L.; McCullough, R. D., *Macromolecules* **34** (13), 4324–4333 (2011).

11. Jeffries-EL, M.; Sauvé, G.; McCullough, R. D., *Adv. Mater.* **16** (12), 1017–1019 (2004).

12. Jeffries-EL, M.; Sauvé, G.; McCullough, R. D., *Macromolecules* **38** (25), 10346–10352 (2005)

Chapter 8.

Conformal Coating of Sulfur Electrode via Layer-by-Layer Deposition for High Capacity Retention in Li-S Batteries

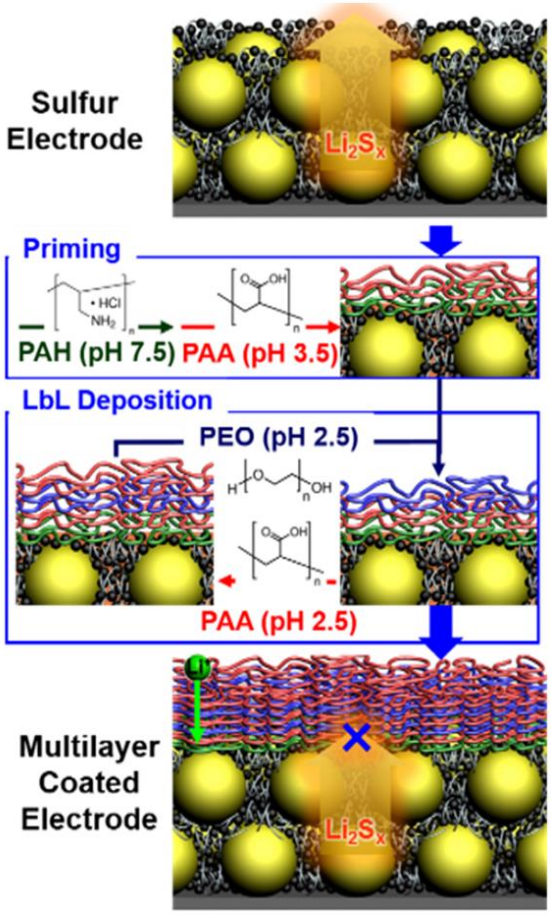

Fig. 8.T. (Color) Schematic illustration of layer-by-layer deposition on sulfur electrodes

8.1. Introduction

8.1.1. Previous Studies

Lithium-sulfur (Li-S) batteries are considered as one of the most promising candidates for the next generation energy storage systems owing to their high theoretical specific capacity (1,675 $mAhg^{-1}$). However, still it is challenging to achieve the theoretical capacity from Li-S batteries because of the irreversible loss of poysulfides, low electrical conductivity of sulfur (~ 10^{-15} Ω·m),[1] volumetric expansion of lithiated discharge products, etc. In particular, the higher order discharge product of the reaction between S_8 and Li_2S, polysulfides, are highly soluble in the electrolyte medium, thus they are continuously dissolved and precipitated on the cathode during the battery operation. When the polysulfides are precipitated as S_8 or Li_2S during the redox reaction, they can be isolated on the cathode without electrical contact. The electrical isolation of active species results in serious loss of capacity by impeding the further electrochemical reaction. Moreover, the diffusion of these polysulfides throughout the solvent phase also results in their migration on to the Li anode side to form of inactive deposits on the surface of Li metal, and that retards charging back to higher order polysulfides (polysulfide shuttle).[2]

In order to solve these issues, much effort has been attempted particularly by tailoring the morphology of active sulfur species in nano-scale. Significant improvement could be provided by the use of sulfur/carbon composites,[3] where nano-sized sulfur was chemically or physically confined by carbonaceous materials. Encapsulation based on which of sulfur has been reported to preserve the polysulfides within the vicinity of the

cathode side as well as enhance the electrical conductivity of the cathode. Recently, the molecular structure of elemental sulfur was modified for novel cathode materials.[4] The high sulfur content copolymers were prepared with small amount of organic cross-linkers, which was bound to linear polysulfide chains and stabilized the interphases between the lithiated and de-lithiated products. Highly stable capacity retention during several hundred cycles was achieved with this extremely simple synthetic chemistry.

From a macroscopic viewpoint of the cathode part, the dissolved polysulfides were able to be confined only to the inside of the cathode part, using an additional interlayer between the cathode and separator.[5] Mostly, interlayers, the layers of carbonaceous materials, or polymer electrolytes, were deposited on separators which were placed facing to the sulfur cathode to prevent the diffusion of polysulfide. When applying the interlayer in the Li-S batteries, conformal contact between the cathode and the interlayer should be taken into account, otherwise, the dissolved polysulfides could be irreversibly lost.

Layer-by-layer (LbL) deposition is known as an effective technique to produce conformal coating layers on various substrates with tunable thickness in a nano-meter scale.[6] There are many options of functional materials for the multilayer deposition by the adsorption of each one on top of the other one using electrostatic attraction, hydrogen bonding, or covalent bonding. Polyethylene oxide (PEO) has been frequently utilized with polyacrylic acid (PAA) to form PEO/PAA hydrogen-bonded multilayers for ion conductive membranes, and especially they exhibited superior lithium ion diffusion characteristics compared to other electrostatic multilayers with cationic polyelectrolytes,

such as polyallylamine hydrochloride (PAH), or polyethylenimine (PEI) to form PAH/PAA, or PEI/PAA multilayers, respectively.[7]

8.1.2. Material Selections

Herein, we demonstrate a new strategy enabling the conformal coating that is directly prepared on the cathode surface by LbL deposition (**Figure 1a**). To the best of our knowledge, utilization of surface protecting layers on the sulfur cathode using LbL deposition has not been introduced. In this work, the polymer multilayers were designed to have a composition of PAH/PAA/$(PEO/PAA)_n$ (n=1, 3, and 5), and deposited on to the typically prepared sulfur cathode. The multilayer coated cathodes effectively prevented irreversible loss of polysulfides while providing Li ionic conduction, whereby the capacity retention is significantly enhanced during the repeated cycles.

8.2. Experimental Section

Materials: Polyallylamine hydrochloride (PAH, Mw = 15 000 g mol -1), polyacrylic acid (PAA, Mw = 50 000 g mol -1), polyethylene oxide (PEO, Mw = 300 000 g mol -1), and bis(trifluoromethane)sulfonamide lithium salt (LiTFSI) were purchased from Sigma-Aldrich.

Preparation of sulfur electrodes: The sulfur powder (325 mesh) was purchased from Alfa Aesar. Super P carbon and polyvinylidene fluoride (PvdF) were provided from SK innovation. The slurry mixture was prepared by mortar mixing of sulfur (60 wt%) , super P (20 wt%), and PvdF (20 wt%), and then casted on an aluminum foil using a doctor blade, followed by drying in a vacuum oven for 12 hours.

Layer-by-layer deposition: The polymer solutions for layer-by-layer deposition were prepared by dissolving polymers in 18MΩ Milli-Q wtater (1 mg mL -1), and pH of each solution was adjusted using 0.1 M of HCl and NaOH. The rinsing solutions corresponding to each polymer solution with the same pH were prepared with Milli-Q water. LiTFSI (0.1 M) was added to all polymer and rinsing solutions. For the deposition of priming layers, the sulfur electrodes were initially dipped into PAH (pH = 7.5) solution for 5 min and then spun at 1500 rpm for 30 s, followed by rinsing with the Milli-Q water of the same pH at the same rpm. The PAA (pH = 3.5) solution was spun at the same condition, and then washed with the rinsing solution with the same pH. The layer-by-layer deposition was conducted on top of the priming layers with PEO (pH = 2.5) and PAA (pH = 2.5), by dipping for 5 min in each polymer solution and 1 min in rinsing solution, respectively. The cycle was repeated for the required number of bi-layers. After deposition, the electrodes were dried overnight in vacuum oven at 50 ℃.

Morphology Characterization: Water contact angles were measured using a DE/DSA100 contact angle analyzer (Fruss Inc.). Scanning electron microscopy (SEM) images were obtained with JSM-6701F (JEOL). X-ray photoelectron spectroscopy (XPS) was conducted using Axis-HSi (Kratos) with Mg/Al dual anode at 15 kV and 10 mA.

Electrochemical Characterization: All electrodes were punched into circular disks (~11mm) and assembled in a 2032 type coin cell. The electrolyte was prepared with 0.1 M lithium nitrate (LiNO3) and 1.0 M lihtium bistrifluoromethane-sulfonimide (LiTFSI) in dioxolane (DIOX) and dimethyl ether (DME) 1:1 volume ratio mixture (PanaxEtec, Korea). Electrochemical properties were measured with a WBC300 cycler (Won-A Tech,

Korea). The potential window was fixed to 1.7 V-2.8 V vs. Li+/Li. The electrochemical impedance spectroscopy (EIS) was performed at open-circuit voltage between 100,000 to 0.1 mHz with fluctuations of 10 mV.

8.3. Results and Discussion

8.3.1. Materials Characterization

In general, the first adhesion layer is very critical on the growth of LbL multilayers. Particularly, the direct LbL deposition of hydrophilic $(PEO/PAA)_n$ multilayers on the typically prepared cathode surface, due to the hydrophobicity and lack of uniformity of the cathode surface. Therefore prior to LbL deposition, PAH/PAA priming layers were spin-coated using aqueous solutions of PAH (pH 7.5) and PAA (pH 3.5) with 0.1 M of LiTFSI added salt. The reason for the priming effect of the PAH/PAA layer is that their weak positive/negative charges and high ionic strength of their solutions sufficiently screen the long-range electrostatic repulsions and thereby enhance the hydrophobic attractions of the adsorbed chains to the surface.[8] Furthermore, spin-assisted polyelectrolyte adsorption generates more flat and uniform surfaces compared to those formed by dipping method, because the spinning of the substrates induces shear force on the adsorbing polymer chains so that they densely cover the surface.[9]

After the deposition of the priming layer (PAH/PAA) on the cathode, PEO/PAA multilayers were alternatively adsorbed by dipping method using PEO and PAA solutions, both of which were prepared by adding 1 M of LiTFSI and adjusting the pH at 2.5 to induce hydrogen bonding between ether oxygen of PEO and protonated carboxylic acid of PAA.[10] From these conformal coating procedure on top of the cathode, PAH and PAA

polymer chains were sequentially adsorbed on to the hydrophobic substrates, and the following LbL multilayers of PEO/PAA stably grew on them without delamination.

In order to be sure of uniform polymer layers on the mixed surfaces of the cathode, it should be confirmed that the LbL multilayers adsorb and grow on each of the cathode components. The surface of sulfur cathode is composed of 3 different materials, sulfur powder (60 wt%), carbon black (20 wt%), and polyvinylidene fluoride (pvdf) binders (20 wt%), which are randomly mixed on the surface. The cathode components were separated and prepared into 2 substrates, the sulfur substrate and the carbon+binder substrate, and employed in the multilayer adsorption procedure as described above for the sulfur cathode coating. The polymer adsorption behaviors on different substrates were investigated by contact angle measurements (**Figure1b**). All of the substrates were initially very hydrophobic (104.1, 164.9 and 144.4 ° for sulfur, carbon+binder and sulfur+carbon+binder substrates (sulfur cathode), respectively), but during the sequential deposition of the polymers up to PEO/PAA 5 bilayers, the contact angles of them significantly decreased into 24.7, 13.4, and 16.2 °, respectively. More hydrophilic surfaces of carbon+binder substrate and the cathode than that of sulfur substrate could be explained by much more porous and rough surface morphologies of them. The surface and cross-sectional SEM images of bare cathode confirms the porous and rough morphologies, in which the carbon black particles with 50 nm of diameter mostly cover the surface (**Figure1c, 1d**). After PEO/PAA 5 bilayer deposition, the surface looked dominantly passivated with polymer layers of 2 μm thickness as observed in the SEM image, and they deeply penetrated inside the cathode through the pores (**Figure1e, 1f**).

The LbL deposition without priming layers, however, didn't show such morphological changes. The successful conformal coating on the sulfur cathodes with PAH/PAA/(PEO/PAA)n multilayers were also confirmed with further characterization included in Supporting information.

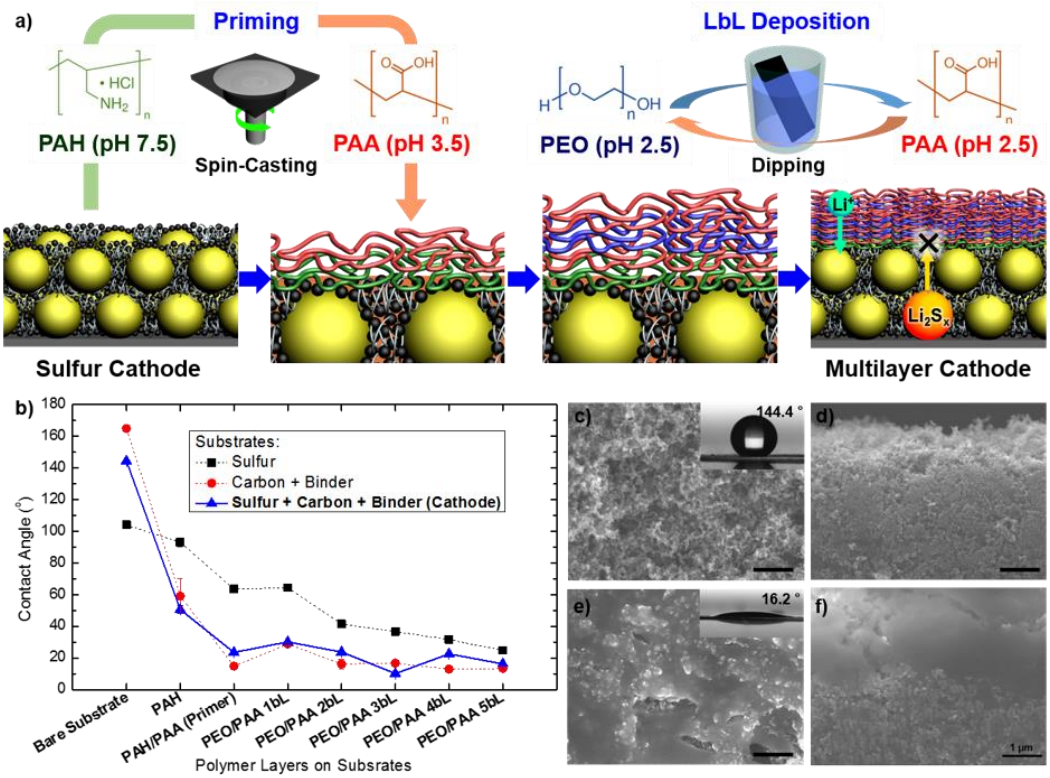

Fig. 8.1. (Color) a) Schematic illustration of priming and layer-by-layer deposition on sulfur cathodes. b) Contact angles as a function of adsorbed polymer layers on the substrates of sulfur, carbon + binder, and sulfur + carbon + binder (sulfur cathode). c) SEM image of bare sulfur cathode and photo image of water droplet on it for contact angle measurement. d) Cross-sectional SEM image of bare sulfur cathode. e) SEM image of 5 bilayer coated cathode and photo image of water droplet on it for contact angle measurement. f) Cross-sectional SEM image of 5 bilayer coated cathode.

8.3.2. Electrochemical Analysis

The electrochemical stability of the multilayer coated cathodes was investigated using galvanostatic cyclings at a 0.5 C rate (1 C = 1675 mAg^{-1}). The charge/discharge voltage profiles of the cathodes as different thickness of bilayers are shown in **Figure 2a**. The region of the upper plateau at ~2.4 V in the discharge profile is originated from the dissolution reaction, where the solid sulfur is reduced to soluble polysulfides (S_8 to S_n^{2-}, n=8-4).[11] In this region, the decrease of capacity during initial 10 cycles can be denoted as "ΔQ", which mainly resulted from the irreversible loss of active sulfur due to that of soluble polysulfides, thus ΔQ is directly related to the surface protecting characteristics of the cathodes. The ΔQ value of the bare cathode is the largest (164 $mAhg^{-1}$), and it decreased to 106, 92, and 81 $mAhg^{-1}$, for 1, 3, and 5 bilayer coated cathodes, respectively. Such decrease of ΔQ values as a function of the bilayer thickness indicates the effective prevention of polysulfide loss can be achieved by the multilayer coatings. Meanwhile, slight increase in charge-discharge overpotential was found in 5 bilayer coated cathode in Figure 2a. The increase of overpotential can be originated from the interruption of lithium ion conductivity by thicker multilayers on the cathode. In this regard, it should be noted that there is a trade-off point between ΔQ and overpotential, suggesting that the surface protecting layer has optimum thickness.

The discharge capacities of the cathodes as multilayer coating are presented in **Figure 2b**. As elucidated by the decrease of ΔQ, the multilayer coated cathodes exhibited higher discharge capacity up to 100 cycles, while as the bare sulfur cathode shows rapid capacity fading even after initial 10 cycles. As discussed above, the thickness of the multilayer has

the optimum for the cathode to reveal the best electrochemical performance. In our system, 3 bilayer coated cathode exhibited the best capacity retention (806 $mAhg^{-1}$) after 100 cycles, 70.27 % vs initial capacity, while 42.46 %, 48.24 %, and 64.37 % could be obtained in the bare, 1 bilayer, and 5 bilayer coated cathodes, respectively.

The cycling performances of the cathodes were also measured without addition of $LiNO_3$ in the electrolytes (**Figure2c**), which is a common additive to suppress the shuttle effect of the polysulfides, although all the other electrochemical characterizations in this work were conducted with $LiNO_3$ salts. The Li-S batteries without $LiNO_3$ are prone to the chemical reaction between polysulfides and Li anode,[12] thus cycling under the absence of $LiNO_3$ are informative to study the effect of protecting layers on the loss of polysulfides during the repeated cycles. The bare cathode shows the deteriorated discharge capacity (141.32 mAh/g) and Coulombic efficiency (28.17% at 84 th. cycle). The poor Coulombic efficiency is caused by shuttle effect, which results from the disproportionate reaction of polysulfides with Li metal anode. After the 84th cycle, the bare electrode did not operate because the shuttle effect is too severely evolved.[2] On the other hand, the bilayer coated electrodes (PEO/PAA 1, 3, and 5 bL) exhibit the improved capacity (618.47 $mAhg^{-1}$, 744.91 $mAhg^{-1}$, and 715.33 $mAhg^{-1}$) and higher Coulombic efficiency (77.1%, 83.83%, and 86.70%) compared with the bare electrode (141.32 $mAhg^{-1}$, 28.17%). The good capacity retention and high Coulomic efficiency even without LiNO3 additives confirm that the bilayer coating is effective on the protection of the cathode against the loss of polysulfides during the battery operation.

The electrochemical impedance spectroscopy (EIS) of multilayer coated cathodes was compared with that of the bare sulfur cathode (**Figure 3a, 3b**). The EIS was recorded at the pristine state, the 1st charged state, and the 10th charged state. The impedance of the bare cathode drastically decreases after 10 cycles, which is attributed to the decrease in the interphase contact resistance and its related capacitance in the cathode.[13] Continuous leakage of polysulfide during the repeated cycles resulted in the extended electrical contact of the carbon framework and structural rearrangement in the cathode. On the other hand, the changes in the impedance of the multilayer coated cathodes are negligible, and that is the evidence of stable cathode structure preserved during the cycles by preventing polysulfide diffusion with the multilayer coating.

Because the severe capacity fading of the cathodes were dominantly occurred during the initial 10 cycles, the changes in surface morphologies of the cathodes after the cycles were investigated by SEM (**Figure 3c, 3d**). There were several micrometer sized sulfur particles isolated from the surface of the bare cathode, where soluble polysulfides were diffused into the electrolyte and re-precipitated on the surface. These sulfur particles are electrochemically inactive, due to lack of electrical contact with the carbons, and that leads to the decrease in the capacity. On the other hand, multilayer coated cathodes preserved initial morphologies after initial 10 cycles owing to complete protection of intermediate polysulfides in their structures.

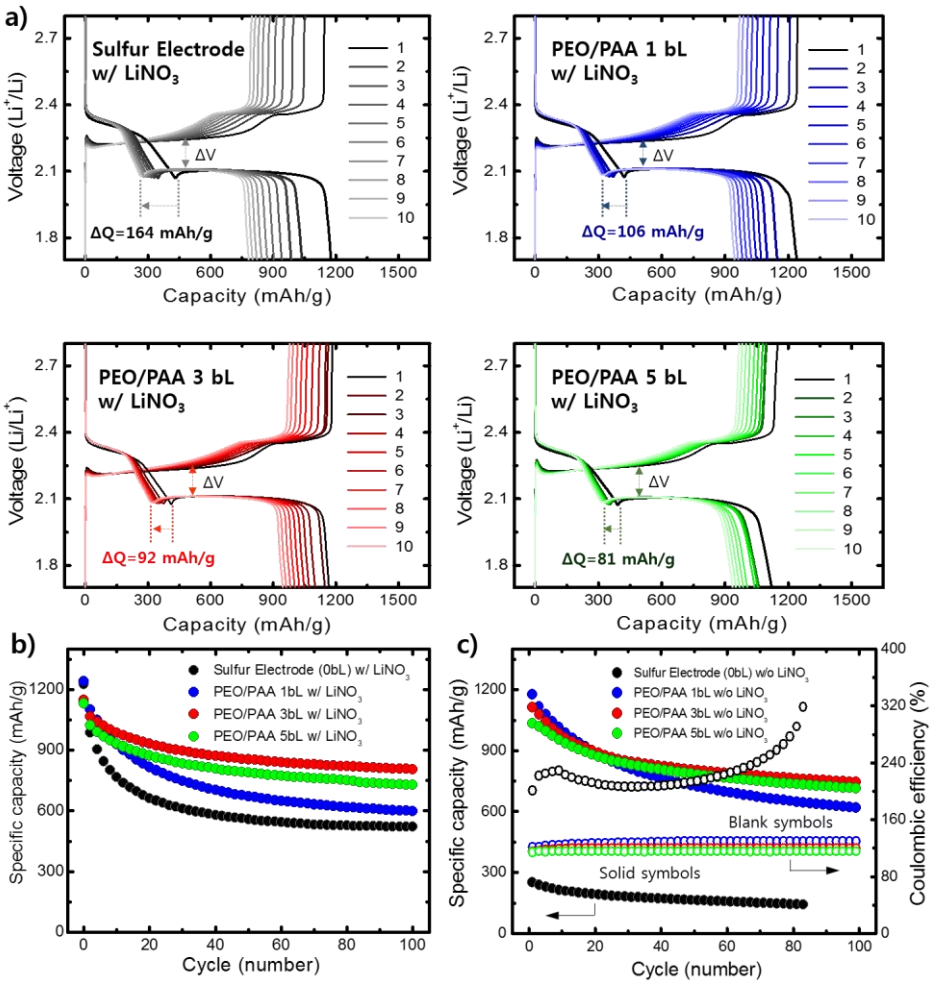

Fig. 8.2. (Color) a) Charge/discharge voltage profiles of sulfur cathode and 1, 3, and 5 bilayer coated cathodes. b) Cyclic performances of sulfur cathode and 1, 3, and 5 bilayer coated cathodes. c) Cyclic performances of sulfur cathode and 1, 3, and 5 bilayer coated cathodes without addition of $LiNO_3$ salts in the electrolytes.

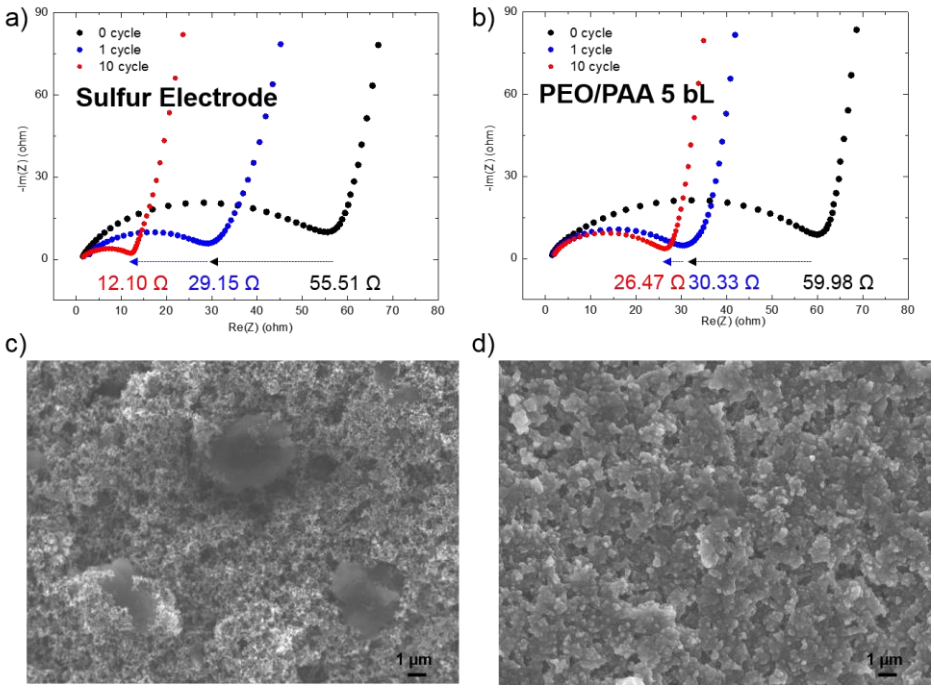

Fig. 8.3. (Color) a) Electrochemical impedance spectroscopy of sulfur electrode and b) 3 bilayer coated electrode measured before cycling and after 1 and 10 cycles. c) SEM images of sulfur electrode and d) 3 bilayer coated electrode after 10 cycles.

8.4. Conclusions

In conclusion, PEO/PAA multilayers on sulfur cathode effectively improved the capacity retention of lithium-sulfur batteries, by successful protection of polysulfide from irreversible loss. This simple and inexpensive method is expected to be widely utilized in various types of electrochemical devices. Future work for further optimization of electrochemical performance is currently underway by nanostructural tailoring of surface layers.

8.5. Supporting Informations

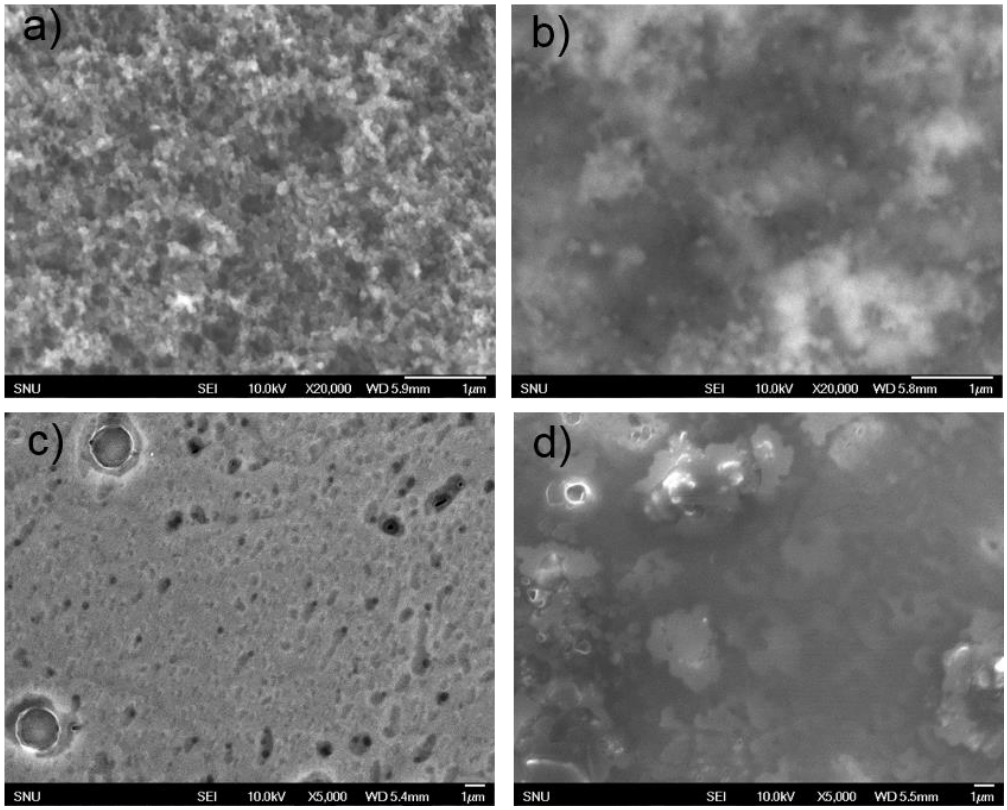

Fig. 8.S1. SEM images of a) bare carbon+binder substrate b) 5 bilayer coated carbon+binder substrate c) bare sulfur substrate d) 5 bilayer coated sulfur substrate.

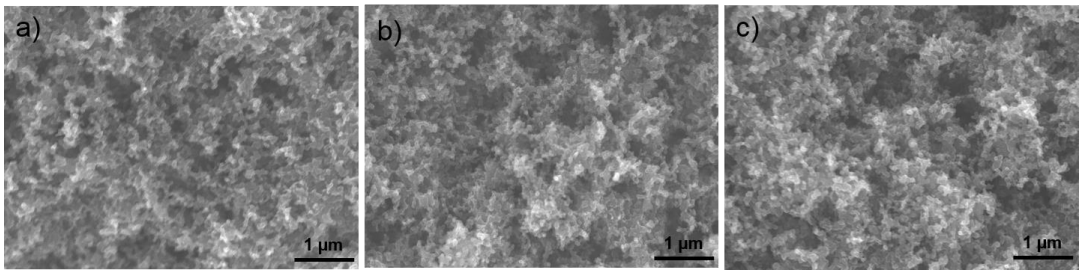

Fig. 8.S2. SEM images of sulfur cathode after PEO/PAA a) 1 bilayer, b) 3 bilayers, c) 5bilayers deposition without priming layer (PAH/PAA).

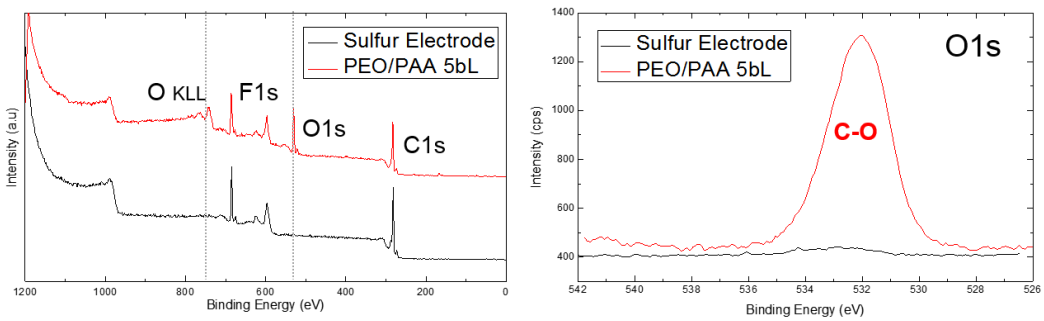

Fig. 8.S3. (Color) XPS spectra of bare sulfur electrode and PEO/PAA 5 bi-layer coated sulfur electrode.

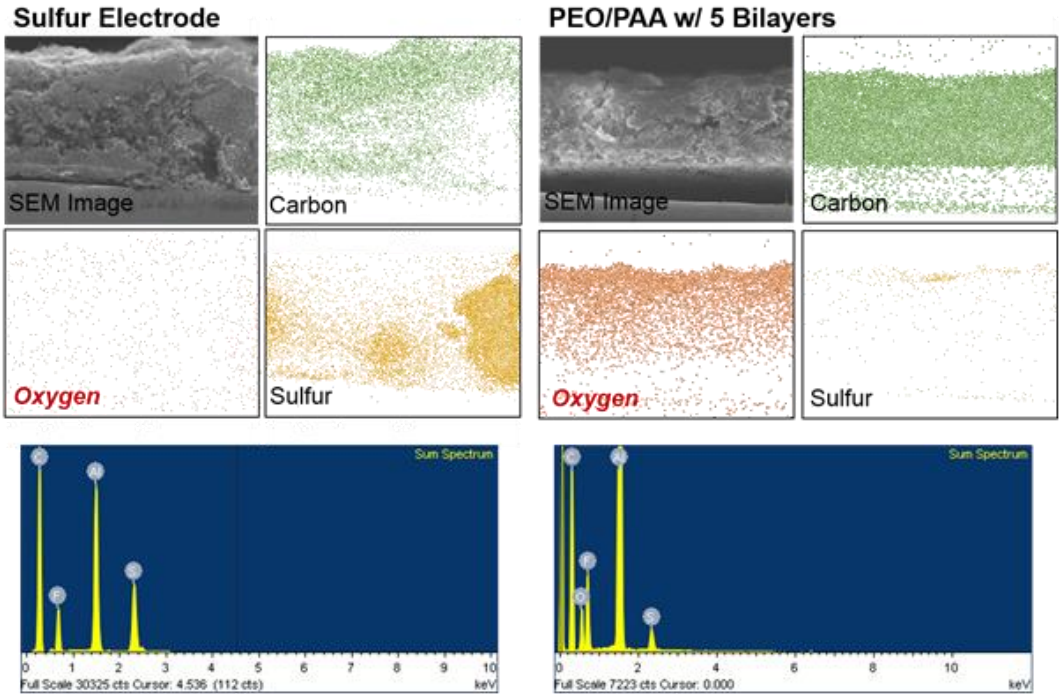

Fig. 8.S4. (Color) EDS spectra and elemental maps of bare sulfur electrode and PEO/PAA 5 bi-layer coated sulfur electrode.

Element [wt%]	Bare Electrode	PEO/PAA 5 bi-layer Electrode
C	72.41	53.07
O	-	10.72
F	15.07	18.67
Al	7.95	16.54
S	4.24	1.00
Totals	99.67	100.00

Table 8-S1. Weight fractraction of elements estimated from EDS spectra of bare sulfur electrode and PEO/PAA 5 bi-layer coated sulfur electrode.

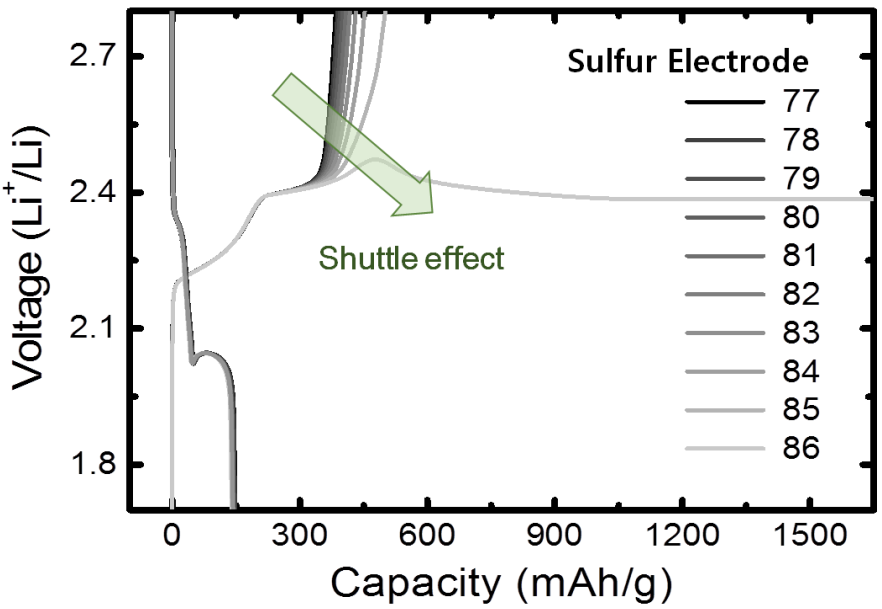

Fig. 8.S5. (Color) a) Charge/discharge voltage profiles of sulfur electrode, which shows the conventional Shuttle effect ongoing cycling.

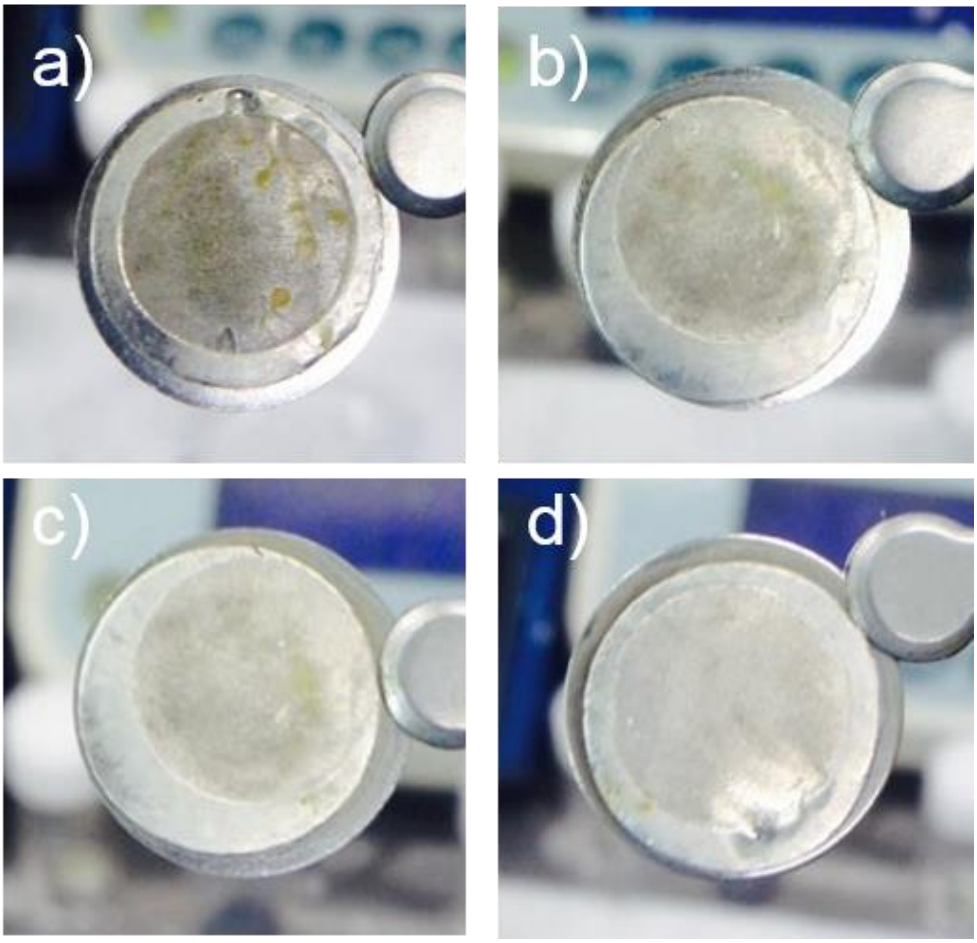

Fig. 8.S6. (Color) Photo images of Li anodes disassembled after 10 cycles with a) bare sulfur electrode, b) 1 bilayer coated electrode, c) 3 bilayer coated electrode, and d) 5 bilayer coated electrode.

8.6. References

1. P. T. Dirlam, A. G. Simmonds, R. C. Shallcross, K. J. Arrington, W. J. Chung, J. J. Griebel, L. J. Hill, R. S. Glass, K. Char, J. Pyun, *Acs Macro Lett.* **4**, 111 (2015).

2. Y. V. Mikhaylik, J. R. Akridge, *J. Electrochem. Soc.* **151**, A1969 (2004).

3. H. W. Chen, W. L. Dong, J. Ge, C. H. Wang, X. D. Wu, W. Lu, L. W. Chen, *Sci Rep-Uk* **3** (2013); Y. Z. Fu, A. Manthiram, *J. Phys. Chem. C* **116**, 8910 (2012); N. Jayaprakash, J. Shen, S. S. Moganty, A. Corona, L. A. Archer, *Angew. Chem. Int. Ed.* **50**, 5904 (2011); K. T. Lee, R. Black, T. Yim, X. L. Ji, L. F. Nazar, *Adv. Energy Mater*. **2**, 1490 (2012); W. Y. Li, Q. F. Zhang, G. Y. Zheng, Z. W. Seh, H. B. Yao, Y. Cui, *Nano Lett*. **13**, 5534 (2013); S. Moon, Y. H. Jung, W. K. Jung, D. S. Jung, J. W. Choi, D. K. Kim, *Adv. Mater.* **25**, 6547 (2013); L. F. Xiao, Y. L. Cao, J. Xiao, B. Schwenzer, M. H. Engelhard, L. V. Saraf, Z. M. Nie, G. J. Exarhos, J. Liu, *Adv. Mater.* **24**, 1176 (2012); J. moon, J. Park, I. Jo, S.-H. Yu, C. Jeon, J. Lee, S.-P. Cho; Y.-E. Sung, and B. H. Hong, *Nanoscale* DOI: 10.1039/c5nr01951f (2015).

4. W. J. Chung, J. J. Griebel, E. T. Kim, H. Yoon, A. G. Simmonds, H. J. Ji, P. T. Dirlam, R. S. Glass, J. J. Wie, N. A. Nguyen, B. W. Guralnick, J. Park, A. Somogyi, P. Theato, M. E. Mackay, Y. E. Sung, K. Char, J. Pyun, Nat Chem 2013, 5, 518; P. T. Dirlam, A. G. Simmonds, T. S. Kleine, N. A. Nguyen, L. E. Anderson, A. O. Klever, A. Florian, P. J. Costanzo, P. Theato, M. E. Mackay, R. S. Glass, K. Char, J. Pyun, *Rsc Adv.* **5**, 24718 (2015); J. J. Griebel, G. X. Li, R. S. Glass, K. Char, J. Pyun, J *Polym. Sci. Pol. Chem.* **53**, 173 (2015); A. G. Simmonds, J. J. Griebel, J. Park, K. R.

Kim, W. J. Chung, V. P. Oleshko, J. Kim, E. T. Kim, R. S. Glass, C. L. Soles, Y. E. Sung, K. Char, J. Pyun, *ACS Macro. Lett.* **3**, 229 (2014).

5. S. H. Chung, A. Manthiram, *J. Phys. Chem. Lett.* **5**, 1978 (2014); M. Gu, J. Lee, Y. Kim, J. S. Kim, B. Y. Jang, K. T. Lee, B. S. Kim, *RSC Adv.* **4**, 46940 (2014); J. Q. Huang, Q. Zhang, H. J. Peng, X. Y. Liu, W. Z. Qian, F. Wei, *Energ Environ. Sci.* **7**, 347 (2014); Y. S. Su, A. Manthiram, *Nat Commun*. 3 (2012); H. B. Yao, K. Yan, W. Y. Li, G. Y. Zheng, D. S. Kong, Z. W. Seh, V. K. Narasimhan, Z. Liang, Y. Cui, *Energ Environ. Sci.* (2014), 7, 3381; G. M. Zhou, S. F. Pei, L. Li, D. W. Wang, S. G. Wang, K. Huang, L. C. Yin, F. Li, H. M. Cheng, *Adv. Mater.* **26**, 625 (2014).

6. T. K. Hong, D. W. Lee, H. J. Choi, H. S. Shin, B. S. Kim, *ACS Nano* **4**, 3861 (2010); B. S. Kong, J. X. Geng, H. T. Jung, *Chem. Commun.* 2174 (2009); S. W. Lee, B. S. Kim, S. Chen, Y. Shao-Horn, P. T. Hammond, *J. Am. Chem. Soc.* **131**, 671 (2009); R. Lingstrom, L. Wagberg, *J. Colloid Interf. Sci.* **328**, 233 (2008); D. Yoo, S. S. Shiratori, M. F. Rubner, *Macromolecules* **31**, 4309 (1998).

7. D. M. DeLongchamp, P. T. Hammond, *Chem. Mater.* **15**, 1165 (2003); D. M. DeLongchamp, P. T. Hammond, *Langmuir* **20**, 5403 (2004); T. R. Farhat, P. T. Hammond, *Adv. Funct. Mater.* **15**, 945 (2005).

8. J. Park, P. T. Hammond, *Macromolecules* **38**, 10542 (2005)

9. J. Cho, K. Char, Langmuir 2004, 20, 4011; J. Cho, K. Char, J. D. Hong, K. B. Lee, Adv Mater 2001, 13, 1076; J. Cho, S. H. Lee, H. M. Kang, K. Char, J. Koo, B. H.

Seung, K. B. Lee, *Polymer* **44**, 5455 (2003).

10. J. Seo, J. L. Lutkenhaus, J. Kim, P. T. Hammond, K. Char, *Macromolecules* **40**, 4028 (2007); J. Seo, J. L. Lutkenhaus, J. Kim, P. T. Hammond, K. Char, *Langmuir* **24**, 7995 (2008).

11. Y. S. Su, Y. Z. Fu, T. Cochell, A. Manthiram, *Nat. Commun.* **4,** (2013).

12. S. S. Zhang, *Electrochim. Acta* **70**, 344 (2012).

13. Z. F. Deng, Z. A. Zhang, Y. Q. Lai, J. Liu, J. Li, Y. X. Liu, J Electrochem Soc 2013, 160, A553.

국문초록

기술 발전에 의한 에너지 소비가 증가됨에 따라, 이를 충족 시킬 수 있는 새로운 개념의 친환경적인 에너지 변환 및 저장 장치의 개발이 필요시 되고 있다. 최근 다양한 연구 그룹에서 이러한 문제를 해결하기 위한 시도들이 있는 가운데, 높은 에너지 변환 효율과 낮은 환경 오염을 갖는 리튬 이온 이차전지가 전기화학 에너지 저장 장치로서 주목 받고 있다. 그 중 리튬 황 이차 전지는 음극을 리튬 금속, 양극은 황을 이용하는 전지로서 고용량 산화/환원 조합을 갖고 있다. 양극 재료 로서 사용되는 황은 값이 저렴 할 뿐만 아니라, 원유를 정제할 때 나오는 부산물로서 재사용이 필요시 된다. 리튬 황 이차 전지는 이러한 장점에도 불구하고, 아직 까지 해결해야 할 문제가 남아 있다. 가장 대표적인 문제는 황의 낮는 전자/이온 전도도, 그리고 배터리 충방전시 발생하는 비가역적인 용량 감소 및 부피 팽창이다. 본 연구에서는 다양한 탄소 질 물질을 이용한 문제 해결 및 성능 향상을 도모 하고자 하였다.

1장에서는 리튬 황 배터리의 연구 경향 및 이론을 기반으로 한 반응 메커니즘을 설명한다. 이차 전지의 이해도를 높이기 위해 특정 기본 용어를 설명하고, 리튬을 기본으로 하는 이차전지의 흐름에 대해 간략

하게 명시한다. 또한, 리튬 황 배터리의 장정 및 단점에 대해 언급하고, 이를 해결 하기 위한 다양한 그룹에서 진행 되고 있는 접근법에 대해 보여준다. 마지막으로 본 연구에 적용한 배터리 성능 분석에 관한 실험 조건과 진보된 분석기기에 대해서 보고한다.

2장에서는 리튬 황 배터리의 전기화학 성능을 평가하는 중요한 파라미터 (ΔV, Q_1, 그리고 Q_2) 에 대해서 보고 한다. 충전곡선과 방전곡선 사이에 발생할 수 있는 분극 현상 (ΔV), 그리고 방전시 발생하는 반응 메커니즘으로 구분한 설퍼의 용해 영역에서의 용량 (Q_1)과 설퍼의 석출 영역에서의 용량 (Q_2)들의 경향성 및 비율을 이용한 성능 분석을 진행 하였다. 이러한 요소의 중요성을 확인 하고자 충방전 속도와 전도성 탄소, 및 전도성 탄소 표면의 산소기능기의 양을 조절한 조건에서 실험을 진행 하였다. 이 장에서 정의된 요소 (ΔV, Q_1, and Q_2)들을 통해서 새롭게 디자인된 다양한 연구의 성능 평가에 적용하고자 하였다.

3장에서는 설퍼와 그래핀 산화물 (graphene oxide)을 합성하였다. 이는 그래핀 산화물이 설퍼 입자를 효과적으로 감싸면서 기존에 보고된 충방전 과정 중 발생 하는 비가역적인 황의 용량 감소를 줄이고자 하였다. 또한 그래핀 산화물 표면의 산소 기능기들과 전해액에 녹아 있는

다황화물 (polysulfide) 간의 상호 작용을 통한 성능 향상을 도모 하였다. 이러한 합성방법을 통해 향상된 배터리의 사이클 특성과 율속 특성을 전기화학적 방법을 기반으로 하는 분석을 통해 확인 하였다.

4장에서는 그래핀 산화물 (graphene oxide)의 크기를 양자점 (quantum dot) 까지 줄이고, 그에 따른 황과 탄소의 핵 껍질 구조 (core shell structure)를 디자인 함으로서 전기화학적 성능 향상을 보았다. 이는 그래핀 산화물의 크기를 감소 시킴에 따른, 산소 기능기를 극단적으로 증가 시키기 위함이고, 핵 껍질 구조는 용해성 다황화물의 비가역적 손실을 막아주기 때문이다. 이러한 결과를 통해서 사이클 특성 및 율속 특성이 향상 되었음을 확인 할 수 있었다. 또한 성능 향상과 함께 탄소 황 간의 결합 (C-S bonding) 이 탄소 표면에서 새롭게 생성되는 것을 확인 할 수 있었고, 또한 탄소 황 결합이 존재하는 그래핀 양자점 (graphene quantum dot) 표면에서 황 원소가 상대적으로 더 많이 흡착되는 것을 확인할 수 있었다. 이는 X-ray photoemission spectroscopy (XPS)와 transmission electron microscopy (TEM) 분석 기기를 통해서 확인 하였다. 이러한 실험적 근거를 보충하기 위해 density functional theory (DFT) 계산을 진행하였다.

5장에서는 가교제 (cross linker, diisopropenylbenzene, DIB)를 통한 역가확 (inverse vulcanization) 방법을 통해 황 중합체 (polymeric sulfur)를 합성하였고 이를 리튬 황 배터리에 처음으로 도입해 보았다. 이러한 역가황 방법은 다량의 황 중합체를 간단하고, 효과적으로 합성하는 방법이다. 이렇게 합성된 황 중합체를 리튬 황 배터리에 적용시켜 보았을 때 우수한 사이클 특성을 갖는 것을 확인 할 수 있었다. 이는 가교제와 황 간의 반응을 통한 탄소 황 결합 (C-S bonding)이 생성되는 것을 확인 하였고 이는 500사이클 이상에서도 높은 성능 향상을 보였다.

6장에서는 5장에서 보고된 황 중합체에 환원된 그래핀 산화물 (reduced graphene oxide)을 도입하여 물질을 합성 하였다. 황 중합체와 탄소와의 친화성을 향상 시키기 위해 환원된 그래핀 산화물에 올레일아민 (oleylamine) 처리를 해 주었다. 이를 통해 황중합체가 균일하게 환원된 그래핀 산화물과 분산되어 있는 것을 확인 할 수 있었다. 이는 황 중합체가 갖는 높은 사이클 특성과 함께 빠른 율속 특성에서도 우수한 성능 향상을 가져 왔다.

7장에서는 전도성 고분자 poly (3-hexylthiophene-2,5-diyl)

(P3HT) 을 통한 황과의 혼성중합 (copolymerization)을 디자인 하였다. 이는 P3HT의 allyl end-group과 황 라디칼 반응을 통하여 이루어진다. 이러한 중합체는 탄소 황 결합 (C-S bonding)을 하게 되고 이는 근접 끝머리 X선 흡수 미세 구조(NEXAFS)를 통해서 확인 할 수 있다. 이렇게 만들어진 황 고분자 혼성중합체는 고체 내부의 전자 확산 거리가 짧아 짐에 따른 증가된 율속 성능 향상을 보인다.

8장에서는 폴리에틸렌옥사이드 (PEO)/ 폴리아크릭 에시드 (PAA)를 통한 레이어 바이 레이어 (layer by layer) 방법을 통해 탄소 황 전극을 코팅하였다. 이는 리튬 이온전도도가 있는 막을 전극 위에 코팅함으로서 리튬 이온은 투과 가능하지만, 용해성 다황화물은 투과 하지 못하는 막을 디자인 하였다. 이는 배터리 충방전시 일어날수 있는 황의 비가역적인 감소를 막기 위함이다. 이를 통해 리튬 황 배터리의 사이클 특성이 향상됨을 확인 함과 동시에 리튬 나이트레이트 ($LiNO_3$) 첨가제가 없이도 높은 쿨롱 효율을 보였다.

주요어: 리튬 황 배터리, 탄소질 물질, 역가황, 황중합체, 탄소 황 상호 작용, 전기화학

학 번 : 2011-31304

Appendix : List of Publications and Presentations

A.1. Publications (International):

1. **Jungjin Park**, Chunjoong Kim*, and Yung-Eun Sung*, "The electrochemical analysis using critical parameters in Li-S battery," *Bulletin of the Korean Chemical Society. Accepted*, (2015). Chaper 2

2. Joonhee Moon‡, **Jungjin Park**‡, Insu Jo, Seung-Ho Yu, Cheolho Jeon, Jouhahn Lee, Sung-Pyo Cho, Yung-Eun Sung*, Byung Hee Hong*, "An Electrochemical Approach to Graphene Oxide Coated Sulfur for Long Cycle Life," *Nanoscale* DOI: 10.1039/c5nr01951f (2015). Chaper 3

3. Joonhee Moon‡, **Jungjin Park**‡, Chunjoong Kim, Jin Hyoun Kang, Eunhak Lim, Kwi Ryong Kim, Jaesung Park, Kyung Jae Lee, Seung-Ho Yu, Jung-Hye Seo, Jouhahn Lee, Jiyoung Heo, Nobuo Tanaka, Sung-Pyo Cho, Jeffrey Pyun, Jordi Cabana, Yung-Eun Sung*, and Byung Hee Hong*,, "High-Performance of Lithium-Sulphur Batteries with a Sulphur Cathode Functionalized with Graphene Quantum Dots" *Submitted* (2015). Chaper 4

4. **Jungjin Park**‡, Joonhee Moon‡, Chunjoong Kim, Jordi Cabana, Byung Hee Hong,* and Yung-Eun Sung*, "Graphene Quantum Dots: Induced C-S Bonding Suitable for High Sulphur/Sulphide Utilization," *Submitted.* Chaper 4

5. Eui Tae Kim‡, **Jungjin Park**‡, Chunjoong Kim, Yung-Eun Sung*, Jeffrey Pyun* and Kookheon Char, "Sulfur-rich Polymeric Nanocomposites with Reduced GO for Stable and Fast Li-S batteries" *Submitted* (2015). Chaper 6

6. Bernd Oschmann‡, **Jungjin Park**‡, Chunjoong Kim, Kookheon Char, Yung-Eun Sung, Rudolf Zentel "Copolymerization of Polythiophene and Sulfur to Improve Electrochemical Performance in Lithium-Sulfur Batteries, *Submitted* (2015). Chaper 7

7. Eui Tae Kim‡**, Jungjin Park**‡, Chunjoong Kim, Yung-Eun Sung*, Jeffrey Pyun*, and Kookheon Char*, "Conformal Coating of Sulfur Electrode via Layer-by-Layer Deposition for High Capacity Retention in Li-S Batteries" *Submitted* (2015). Chaper 8

8. Woo Jin Chung, Jared J. Griebel, Eui Tae Kim, Hyunsik Yoon, Adam G. Simmonds, Hyun Jun Ji, Philip T. Dirlam, Richard S. Glass, Jeong Jae Wie, Ngoc A. Nguyen, Brett W. Guralnick, **Jungjin Park**, A´rpa´d Somogyi, Patrick Theato, Michael E. Mackay, Yung-Eun Sung*, Kookheon Char* and Jeffrey Pyun*, "The use of elemental sulfur as an alternative feedstock for polymeric materials," *Nature Chemistry* **5,** 518-524 (2013).

9. Adam G. Simmonds‡, Jared J. Griebel‡, **Jungjin Park**, Kwi Ryong Kim, Woo Jin Chung, Vladimir P. Oleshko, Jenny Kim, Eui Tae Kim, Richard S. Glass, Christopher L. Soles, Yung-Eun Sung, Kookheon Char,* and Jeffrey Pyun*, "Inverse Vulcanization of Elemental Sulfur to Prepare Polymeric Electrode Materials for Li−S Batteries," *ACS Macro Letters* **3**, 229-232 (2014).

10. Kyung Jae Lee, Seung-Ho Yu, Jung-Joon Kim, Dae-Hyeok Lee, **Jungjin Park**, Soon Sung Suh, Jong Soo Cho, Yung-Eun Sung*, "$Si_7Ti_4Ni_4$ as a buffer material for Si and its electrochemical study for lithium ion batteries," *J. Power Sources.* **246**, 729-735 (2014).

A.2. Presentations (International):

1. **Jungjin Park**, Kwi Ryong Kim, Seung-Ho Yu and Yung-Eun Sung*****, "Improved Cycle Performance of Sulfur-Carbon Nanofiber Composite for Li-S battery," *International Meeting on Lithium Batteries*, Jeju, Korea, June 2012.

   [Poster by J. Park]

2. **Jungjin Park**, Kwi Ryong Kim, Kyung Jae Lee, Seung-Ho Yu, Dong Young Chung and Yung-Eun Sung, "Graphene Quantum Dots (GQDs) Surface Functionalization to Enhance the Cycle Stability and Electron Pathway on Lithium Sulfur Batteries," *International Meeting on Lithium Batteries*, Como, Italy, June 2014.

   [Poster by J. Park]

A.3. Presentations (Domestic):

1. **Jungjin Park**, Joonhee Moon, Kwi Ryong Kim, Byung Hee Hong and Yung-Eun Sung,* "Graphene Oxide-Coated Polymer Sulfur Materials for Lithium Sulfur Batteries" *The Korean Society of Industrial and Engineering Chemistry*, Jeju, Korea, May 2013.

   [Poster by J. Park]

2. **Jungjin Park,** Kwi-Ryong Kim, Kyung-Jae Lee and Yung-Eun Sung,* "Confinement and nucleation site effects of grapheme quantum dots (GQDs) on Lithium Sulfur Battery" *The Korean Society of Industrial and Engineering Chemistry*, Jeju, Korea, May 2014.

   [Poster by J. Park]

3. **Jungjin Park**, Eui Tae Kim, Jeffrey Pyun, Kookheon Char, and Yung-Eun Sung,* "Surface Modification of Sulfur Electrodes via Layer-by-Layer Deposition for the High Cycle Retention in Li-S Batteries" *The Korean Society of Industrial and*

Engineering Chemistry, Busan, Korea, April 2015.

[Poster by J. Park]

4. **Jungjin Park**, Eui Tae Kim, Jeffrey Pyun, Kookheon Char, and Yung-Eun Sung,* "Co-polymerization of sulfur and carbon for improving electrochemical performance in Li-S battery" *The Korean Electrochemical Society*, Kwangju, Korea, April 2015.

[Poster by J. Park]